Infrastructure Technology Institute
McCormick School of Engineering and Applied Science
Northwestern University

Condition Monitoring of Urban Infrastructure: Effects of Ground Movement on Adjacent Structures

Final Report

by

Richard Finno

October 26, 2012

DISCLAIMER

The contents of this report reflect the views of the authors, who are responsible for the facts and the accuracy of the information presented herein. This document is disseminated under the sponsorship of the Department of Transportation University Transportation Centers Program, in the interest of information exchange. The U.S. Government assumes no liability for the contents or use thereof.

NORTHWESTERN UNIVERSITY

Hypoplastic Constitutive Law Adapted to Simulate Excavations in Chicago Glacial Clays

A DISSERTATION

SUBMITTED TO THE GRADUATE SCHOOL

IN PARTIAL FULFILLMENT OF THE REQUIREMENTS

for the degree

DOCTOR OF PHILOSOPHY

Field of Civil Engineering

By

Fernando Sarabia

EVANSTON, ILLINOIS

June 2012

Abstract

Hypoplastic Constitutive Law Adapted to Simulate

Excavations in Chicago Glacial Clays

Fernando Sarabia

Economic considerations drive the more effective use of space in urban areas, promoting the construction of taller buildings with deeper basement structures. The crowded nature of urban environments imposes strict restrictions to the tolerable performance of these new constructions.

These restrictions are translated in the need for the development of more precise tools that can be used by engineering practitioners to predict construction induced deformations. Geotechnical finite element simulations are a common technique to estimate construction performance. This methodology can be enhanced by the use of optimization routines to calibrate the constitutive model parameters with existing data.

This thesis introduces enhancements to existing techniques that improve the agreement between model predictions and both, laboratory test data and field performance observations. Specifically, the finite element simulation strategy adopted in this research incorporated the use of an advanced soil model that is conceptually capable of capturing the nonlinear nature of soil stiffness from the very small to large strain levels.

The techniques incorporated in this research were developed to be used for the prediction of deformations of deep excavations in the Chicago area. The parameters of the selected model were either directly estimated from existing laboratory test data or computed using optimization techniques that used sophisticated triaxial test results as target observations. The procedures used to estimate the model parameters incorporated techniques to account for natural variation in degree of soil plasticity, density and degree of overconsolidation of the different Chicago glacial till layers.

The validity of the estimated parameters is evaluated by simulating a top-down excavation performed at the One Museum Park West project in Chicago and comparing the model predictions with the collected performance monitoring data. The project site used as a test bed for this research was heavily instrumented during construction with inclinometers, optical survey points and strain gauges. The collected information was compared to model predictions at a section along the north side of the excavation. This research also developed finite element modelling strategies to incorporate the nonlinear behavior of the structural elements in a basement construction; specifically, the creep and shrinkage effects of the supporting slabs in top-down excavation and the nonlinear bending stiffness of the retaining walls.

The results of this comparison showed reasonable agreement between the computed and observed lateral wall movements at all stages of the excavation. The lack of agreement between the computed and measured ground surface settlements is attributed to the heterogeneous nature of a surficial granular fill encountered at the site.

The relative importance of utilizing a soil model able to capture small strain stiffness nonlinearity, slab creep and shrinkage effects and wall nonlinear bending stiffness was demonstrated by performing parametric evaluations with and without incorporating these effects into the finite element model and comparing the results with the observed performance. Specifically, these parametric evaluations showed that when at the OMPW site small strain stiffness nonlinearity is ignored, the computed ground movements in the hard glacial layers next to the toe of the wall are overpredicted; if the time dependant slab deformations (i.e., creep and shrinkage) are ignored, the lateral wall movements are underpredicted; and not accounting for the nonlinear bending stiffness of the retaining does not significantly change the computed ground movements.

Contents

Abstract 3

List of Tables 8

List of Figures 10

Chapter 1. Introduction 18

Chapter 2. Technical Background 25

2.1. Introduction 26

2.2. Performance of Stiff Earth Retention Systems 26

2.3. Optimization Methods 33

2.4. Summary 36

Chapter 3. Optimization and Inverse Calibration 38

3.1. Inverse Calibration 39

3.2. Summary 44

Chapter 4. One Museum Park West 45

4.1. Introduction 46

4.2. Site Description 47

4.3. Soil Conditions 52

4.4. Ground Water Conditions 55

4.5. Project Description 62

4.6. Construction Activities and Performance Monitoring Data 76

4.7. Summary 105

Chapter 5. HC Model Calibration Using Triaxial Test Data 107

5.1. Introduction 108

5.2. Hypoplastic Soil Model for Clays (HC Model) 118

5.3. HC Model Adapted for Chicago Clays 130

5.4. Triaxial Testing Optimization 150

5.5. Summary 187

Chapter 6. Finite Element Simulation of OMPW 190

6.1. Finite Element Model 191

6.2. OMPW Computed versus Observed Performance 212

6.3. Summary 222

Chapter 7. Summary and Conclusions 224

Bibliography 229

Appendix A. Triaxial Test Data versus Finite Element Simulations 234

List of Tables

4.1	Depth of timber piles in MSE wall	50
4.2	Chicago bedrock ground water table elevation	57
4.3	Estimated soil permeability per soil layer	61
4.4	Slab thickness and concrete design strength per basement level	67
4.5	OMPW secant pile wall dimension and reinforcing	70
4.6	Construction activities at Section No. 2	81
5.1	List of oedometer and k_o triaxial tests on Chicago clays	133
5.2	List of triaxial test used for optimization	152
5.3	Stages for the finite element simulation of triaxial tests used for Lurie samples	154
5.4	Stages for the finite element simulation of triaxial tests used for Ford and Block 37 samples	154
5.5	Stages for the finite element simulation of triaxial tests used for OMPW samples	155
5.6	Correlations used to estimate the HC model parameters	158
5.7	Correlations used to estimate the HC model parameters	159

5.8	Maximum and minimum reported values for each of the optimized HC model parameters	161
5.9	Optimized Parameters after the First Optimization Cycle	165
5.10	Residual error for each laboratory test	168
6.1	Soil properties for soil layers included in the OMPW finite element model	193
6.2	Mohr Coloumb model parameters (with stress dependant stiffness) used for the urban fill	193
6.3	HC model parameter for the glacial till layer at OMPW site	195
6.4	Creep correction factors	198
6.5	Shrinkage correction factors	200
6.6	Composite beam model parameters for the secant portion of the retaining wall	205
6.7	Composite beam model parameters for the tangent portion of the retaining wall	206
6.8	Construction steps included in the OMPW finite element simulation	208

List of Figures

2.1 Maximum lateral wall movement, system stiffness, and factor of safety against basal heave. Finite element solutions compared with field measurements (after Clough et al. [1989]) 27

2.2 Summary of measured settlements caused by the installation of concrete diaphragm walls (after Clough and O'Rourke [1990]) 28

2.3 Categories used to subdivide excavation performance data (after Long [2001]) 29

2.4 Normalized maximum lateral movement versus depth for Set 2b (after Long [2001]) 31

2.5 Normalized maximum lateral movement versus system stiffness for Set 2b (after Long [2001]) 32

4.1 Photograph of One Museum Park West (right) and One Museum Park East (left) 47

4.2 Pre-construction Plat of Survey 49

4.3 Roosevelt approach embankment. Cross section looking East. (Dimensions in feet) 51

4.4	Elevation contour map showing pre-construction ground surface elevation	53
4.5	Normalized undrained shear strength from vane shear tests versus I_p (from Terzaghi et al. [1996])	55
4.6	Chicago Deep Tunnel (from MWRD)	56
4.7	Measured versus predicted water pressure at Soldier Field and 14^{th} & State Subway Station	58
4.8	Foundation Plan	63
4.9	North-South section along basements (looking West). (Dimensions in feet)	66
4.10	Detail of typical slab-wall connection.	67
4.11	Basement slab penetrations or glory holes	68
4.12	Typical cross section of secant pile wall	69
4.13	Secant pile wall drill rig operations	71
4.14	Cross section of temporary cofferdam	72
4.15	Plan view of temporary cofferdam	73
4.16	Top-down construction	74
4.17	Instrumentation Location Diagram	76
4.18	Strain gauges attached to basement slab reinforcing steel	78
4.19	Top-down construction sequence	80
4.20	Top-down construction sequence (Events at Station No. 2)	82

4.21	Settlement before the beginning of the installation of the deep foundation (day 243)	87
4.22	Settlements during the water main repairs (day 200 to 214)	88
4.23	Settlement after the installation of perimeter walls and foundations (day 340)	89
4.24	Settlements during the installation of deep foundations (day 243 to 340)	90
4.25	Settlement after the excavation of the cofferdam (day 424)	91
4.26	Settlements during the excavation of the cofferdam (day 382 to 423)	92
4.27	Settlement before the beginning of the main excavation (day 529)	93
4.28	Settlement after the installation of basement slab B1 (day 641)	94
4.29	Settlement after the installation of basement slab B2 (day 788)	95
4.30	Settlement after the installation of basement slab B3 (day 816)	96
4.31	Settlement after the installation of basement slab B5 (day 1012)	97
4.32	Settlement after the installation of basement slab B4 (day 1019)	98
4.33	Increment in horizontal movements and settlement at Section No. 2 from the beginning of the main excavation (day 529)	101
4.34	Strain gauge data collected in Section No. 2	102
4.35	Horizontal Movements at the slab levels along Section No. 2	104
5.1	Definition of model parameters: N, λ^* and κ^* (from Mašín [2005])	121

5.2	Matsuoka-Nakai failure surface incorporated into the hypo-plastic soil model (from Niemunis [2002])	123
5.3	Influence of ϕ_c and the ratio $(\lambda^* - \kappa^*)/(\lambda^* + \kappa^*)$ on the SOM surface (from Mašín and Herle [2005])	124
5.4	Measured versus computed triaxial test results simulated using the MCC (CC), HC and 3SKH models (after Hájek et al. [2009])	125
5.5	Stress response for different values of ρ introduced by the *intergranular strain* concept (after Niemunis [2002])	127
5.6	Relation between the rate of *intergranular strain* and stretching tensor (after Niemunis [2002])	129
5.7	Vertical effective stress versus void ratio for Chicago clays tests listed in Table 5.1	134
5.8	Normalized compressibility for Chicago clays tests listed in Table 5.1	135
5.9	Sibari consolidation test data (from Baudet [2001])	136
5.10	Relationship between void ratio at Liquid Limit e_L, N_o and λ^* for Sibari ($\blacklozenge$) and Bothkennar ($\diamond$) clay (from Baudet [2001])	137
5.11	Oedometer tests on intact and reconstituted Chicago clays (from Cho [2007])	138
5.12	Normalized compressibility for Chicago Clays	139
5.13	Relationship between void ratio at Liquid Limit e_L, N_o and λ^* for Chicago clays	141
5.14	Friction angle versus plasticity index (after Mitchell and Soga [2005]	143

5.15	Normalized shear strength versus natural water content (after Finno and Chung [1992])	144
5.16	Shear Wave Velocity Vs_{HH} and Vs_{VH} measured at the OMPW project site	148
5.17	Relationship between model parameter m_R/r and void ratio (OMPW data)	149
5.18	Global Error Parametric Evaluation (Surface: $r^* = 0.59$)	162
5.19	Global Error Parametric Evaluation (Surface: $\beta^* = 0.21$)	163
5.20	Global Error Parametric Evaluation (Surface: $\chi^* = 0.11$)	164
5.21	Residual error histogram	167
5.22	Typical fit, Shear degradation and stress path, TestID: B37TC2	170
5.23	Typical fit, Stress versus strain, TestID: B37TC2	171
5.24	Non-typical fit, Shear degradation and stress path, TestID: B37RTXE4	172
5.25	Non-typical fit, Stress versus strain, TestID: B37RTXE4	173
5.26	Typical fit, Shear degradation and stress path, TestID: LB3TC3	174
5.27	Typical fit, Stress versus strain, TestID: LB3TC3	175
5.28	Non-typical fit, Shear degradation and stress path, TestID: LB3RTE2	176
5.29	Non-typical fit, Stress versus strain, TestID: LB3RTE2	177
5.30	Typical fit, Shear degradation and stress path, TestID: FB1TC1	178
5.31	Typical fit, Stress versus strain, TestID: FB1TC1	179
5.32	Non-typical fit, Shear degradation and stress path, TestID: FB1RTE1	180

5.33	Non-typical fit, Stress versus strain, TestID: FB1RTE1	181
5.34	Typical fit, Shear degradation and stress path, TestID: O2P3TC	182
5.35	Typical fit, Stress versus strain, TestID: O2P3TC	183
5.36	Non-typical fit, Shear degradation and stress path, TestID: O1P2TC	184
5.37	Non-typical fit, Stress versus strain, TestID: O1P2TC	185
6.1	OMPW basement excavation finite element model	191
6.2	Moment versus Curvature Diagram for Retaining Wall	201
6.3	Finite Element Analysis Sketch to Verify Composite Member Properties	203
6.4	Measured versus computed deflection and settlement along ST-2	213
6.5	Measured versus predicted horizontal ground movements at each slab level along ST-2	215
6.6	Measured versus predicted deflection and settlement along ST-2 ignoring small strain stiffness)	217
6.7	Measured versus predicted deflection and settlement along ST-2 ignoring slab creep and shrinkage	219
6.8	Measured versus predicted deflection and settlement along ST-2 ignoring wall nonlinearity	221
A.1	Stress versus strain, TestID: B37DRTE1	235
A.2	Shear degradation and stress path, Stress versus strain, TestID: B37DTC1	236

A.3	Stress versus strain, TestID: B37RTE1	237
A.4	Stress versus strain, TestID: B37RTXE4	238
A.5	Stress versus strain, TestID: B37STC1	239
A.6	Stress versus strain, TestID: B37TC2	240
A.7	Stress versus strain, TestID: B37TC3	241
A.8	Stress versus strain, TestID: B37TC4	242
A.9	Stress versus strain, TestID: FB1RTE1	243
A.10	Stress versus strain, TestID: FB1TC1	244
A.11	Stress versus strain, TestID: FB1TC2	245
A.12	Stress versus strain, TestID: FB2TC2	246
A.13	Stress versus strain, TestID: LB3RTE1	247
A.14	Stress versus strain, TestID: LB3RTE2	248
A.15	Stress versus strain, TestID: LB3TC2	249
A.16	Stress versus strain, TestID: LB3TC3	250
A.17	Stress versus strain, TestID: O1P1RTE	251
A.18	Stress versus strain, TestID: O1P2TC	252
A.19	Stress versus strain, TestID: O2P1RTE	253
A.20	Stress versus strain, TestID: O2P3TC	254
A.21	Stress versus strain, TestID: O3P4TC	255
A.22	Stress versus strain, TestID: O3P5RTE	256
A.23	Shear degradation and stress path, TestID: B37DRTE1	257

A.24	Shear degradation and stress path, TestID: B37DTC1	258
A.25	Shear degradation and stress path, TestID: B37RTE1	259
A.26	Shear degradation and stress path, TestID: B37RTXE4	260
A.27	Shear degradation and stress path, TestID: B37STC1	261
A.28	Shear degradation and stress path, TestID: B37TC2	262
A.29	Shear degradation and stress path, TestID: B37TC3	263
A.30	Shear degradation and stress path, TestID: B37TC4	264
A.31	Shear degradation and stress path, TestID: FB1RTE1	265
A.32	Shear degradation and stress path, TestID: FB1TC1	266
A.33	Shear degradation and stress path, TestID: FB1TC2	267
A.34	Shear degradation and stress path, TestID: FB2TC2	268
A.35	Shear degradation and stress path, TestID: LB3RTE1	269
A.36	Shear degradation and stress path, TestID: LB3RTE2	270
A.37	Shear degradation and stress path, TestID: LB3TC2	271
A.38	Shear degradation and stress path, TestID: LB3TC3	272
A.39	Shear degradation and stress path, TestID: O1P1RTE	273
A.40	Shear degradation and stress path, TestID: O1P2TC	274
A.41	Shear degradation and stress path, TestID: O2P1RTE	275
A.42	Shear degradation and stress path, TestID: O2P3TC	276
A.43	Shear degradation and stress path, TestID: O3P4TC	277
A.44	Shear degradation and stress path, TestID: O3P5RTE	278

CHAPTER 1

Introduction

> A builder must refer constantly to examples of practical application without neglecting theoretical design. He who is guided simply by one or the other will seldom escape sad disappointment.
>
> Collin, 1846

The importance of the theoretical and practical aspects in geotechnical practice has been understood from the early days. The parallel development of the theoretical and practical aspects of geotechnology resulted in the creation of classic soil mechanics, the basis of today's practice. However, in the last two decades, the development of computer science has forever changed the way in which engineering is practiced. The easy access to computers with efficient and fast processing power has promoted an explosive development of numerical techniques that can be used to analyze geotechnical problems.

These numerical techniques include, for instance, finite element procedures to solve the partial differential equations that describe the behavior of multi-phase soil-like materials. Modern finite element codes routinely solve boundary value problems where the non-linear relation that controls the deformation of soil upon the application of new loading is computed keeping a simultaneous consideration for the water migration from areas of high to areas of low hydraulic head as dictated by the laws postulated by Darcy.

Technology has also enhanced the ability to conduct sophisticated tests of soil samples in the laboratory environment and to collect very precise information on the soil behavior from the very small to the large strain levels. This new information has resulted in a better

understanding of the mechanics that describe the behavior of soils; and, in the formulation of many theoretical constitutive soil models than can allegedly capture multiple aspects of these recent findings. Technology has not only affected the quality and precision of the collected data in the laboratory environment, but also in the construction field. New technology allows for the continuous collection and storage of large amounts of information that can be transferred in real-time to remote data centers for evaluation and analysis.

Unfortunately, this explosive growth of technology and knowledge has not been directly paralleled by the enhancement in the geotechnical practice. There is a slow absorption among practitioners of this overwhelming amount of new information and there is much confusion and misunderstanding on how these new theoretical and computational tools can enhance the conditions at the construction site.

Consequently, this work attempts to utilize the techniques that allow for the rapid and practical development of soil mechanics from its beginnings: the observational method. The observational method was introduced by Karl Terzaghi (Peck [1969a]) as a method to achieve safe and economic designs by learning and making adjustment to the designs from a close observation of performance. This same observational approach or "learn-as-you-go" method is applied in this study, but this time utilizing newly available technologies.

Multiple attempts have been made by researchers to utilize laboratory and field construction performance data to extract the parameters that define the constitutive behavior of soil models using optimization techniques. Such attempts have resulted in the proper simulation of laboratory tests results or field construction performance; however, these

studies typically fail to replicate with a single set of model parameters, both sets of observations (laboratory and field performance data). This disagreement is often attributed to the disturbance existing in the soil specimens used for testing.

In this thesis, it is hypothesized that in addition to sample disturbance, this disagreement may also be caused by the selection of constitutive models that are unable to capture the complex soil response observed in the field and laboratory environment, specially, at small strain levels.

The main objective of this study is the calibration of the constitutive soil model parameters for the simulation of excavations in Chicago glacial clays using finite element methods. To make the results of this research accessible to the engineering practitioner, the potential candidates for constitutive soil models were restricted to models that have been implemented in commercial computer codes.

The soil model used in this study is the one developed by Mašín [2006] (HC model) based on hypoplastic laws. This model is conceptually capable of capturing the nonlinear response of soils from the very small to large strain levels.

To minimize disturbance effects, laboratory test results primarily performed on block samples, and to a much lesser degree, pitcher samples are utilized to perform the initial calibration of the soil model parameters. The model parameters are estimated using optimization techniques.

The calibrated soil model is used to simulate a top-down excavation performed at the One Museum Park West (OMPW) project in Chicago, Illinois. The site used as test bed for comparison between the computed and observed performance was heavily instrumented during construction. The utilized instrumentation included inclinometers, optical survey

points and strain gauges. The computed performance obtained using finite element procedures is compared to all the collected performance monitoring data at one section along the north wall of the project site.

In addition to the computation of parameters for the HC soil model, this thesis also proposes finite element modelling strategies to incorporate the nonlinear behavior of the structural elements in a basement construction. In particular, the creep and shrinkage effects of the supporting slabs in top-down excavation and the nonlinear bending stiffness of the retaining walls are explicitly accounted for in the finite element modelling.

Finally, the relative importance of utilizing a soil model able to capture small strain stiffness nonlinearity, slab creep and shrinkage effects and wall bending stiffness is demonstrated by performing parametric evaluations with and without incorporating these effects into the finite element model and comparing the results with the observed performance.

Chapter 2 presents a review of existing technical information that was used as background for this study. Existing optimization procedures that have been successfully used in geotechnical problems are reviewed and the reported performance of the construction of excavations similar to the one used as the test bed for this study are summarized.

Chapter 3 described the gradient based optimization techniques utilized in this study.

The methodology presented in this thesis is tested against field data collected during the construction of the One Museum Park West (OMPW) project in Chicago, Illinois. Chapter 4 presents the soil, ground water conditions, construction activities and performance monitoring data collected during the construction of OMPW.

Chapter 5 presents the hypoplastic constitutive soil model (Mašín [2006]) used in this research and describes the criteria followed for its selection. The theoretical and physical meaning of the constitutive parameters of the model is discussed. The procedures used to calibrate the model parameters using a combination of correlations to existing data and optimization techniques that use triaxial test data as target observations are also described. The methodology used to extend the applicability of the selected model to the different glacial till layers, with different composition is also presented.

Chapter 6 presents details of the finite element procedures used to simulate the excavation of the OMPW basement structure. Special attention was given to the modelling of the structural elements of the OMPW basement, such as the nonlinear bending stiffness of the retaining wall and the time dependent deformation (i.e., creep and shrinkage) of the supporting concrete slabs. The results the finite element simulation of the OMPW excavation, using the model parameters derived in Chapter 5, are presented alongside the construction performance data for comparison. Parametric evaluations tailored to

establish the relative importance of small strain nonlinearity, slab creep and shrinkage and the nonlinear bending stiffness of the wall elements are also presented in Chapter 6. And finally, Chapter 7 summarizes this work and presents the conclusions derived from this research.

CHAPTER 2

Technical Background

2.1. Introduction

This thesis is focused on the extraction of constitutive soil model parameters of the hypoplastic constitutive soil model developed by Mašín [2006] utilizing high quality laboratory test data an excavation in the Chicago, Illinois. Consequently, this chapter references existing work performed in the areas of numerical optimization methods in geotechnical engineering, and in the expected performance of excavations.

2.2. Performance of Stiff Earth Retention Systems

This section reviews the existing information on earth retention system performance included in the literature and selects the information that can be used as comparison for the case study used in this thesis (i.e., OMPW project).

A large database of the performance of retention systems is available in the literature. The most well known studies arguably are the ones published by Peck [1969b] and Clough and O'Rourke [1990]. The database presented by Peck [1969b] includes flexible retention systems, while the one presented by Clough and O'Rourke [1990] includes both, flexible and stiff retention support systems.

As it will be described in detail in the following chapter, the construction of the OMPW basement structure consists of a stiff secant pile wall supported by reinforced concrete slabs. The excavation is performed in the top down manner, i.e., each slab is cast in place against the existing subgrade and the excavation is advanced under each of the newly placed slabs in a mining operation. The soil conditions at the OMPW site consists of superficial granular fill underlain by clay strata that gets stronger and stiffer with depth. The toe of the secant pile wall is keyed into a very stiff to hard glacial till layer.

Consequently, given that the OMPW retention system has a high structural stiffness, the performance of the OMPW site cannot be directly compared to the performance from the case studies collected by Peck [1969b].

Clough et al. [1989] using finite element techniques suggested that the maximum magnitude of lateral ground movements for arising from an excavation in soft to medium clays could be estimated using the factor of safety against basal heave and the system stiffness, as shown in Figure 2.1. This figure also includes the data used to validate the analysis. The results from this study were also reported in Clough and O'Rourke [1990].

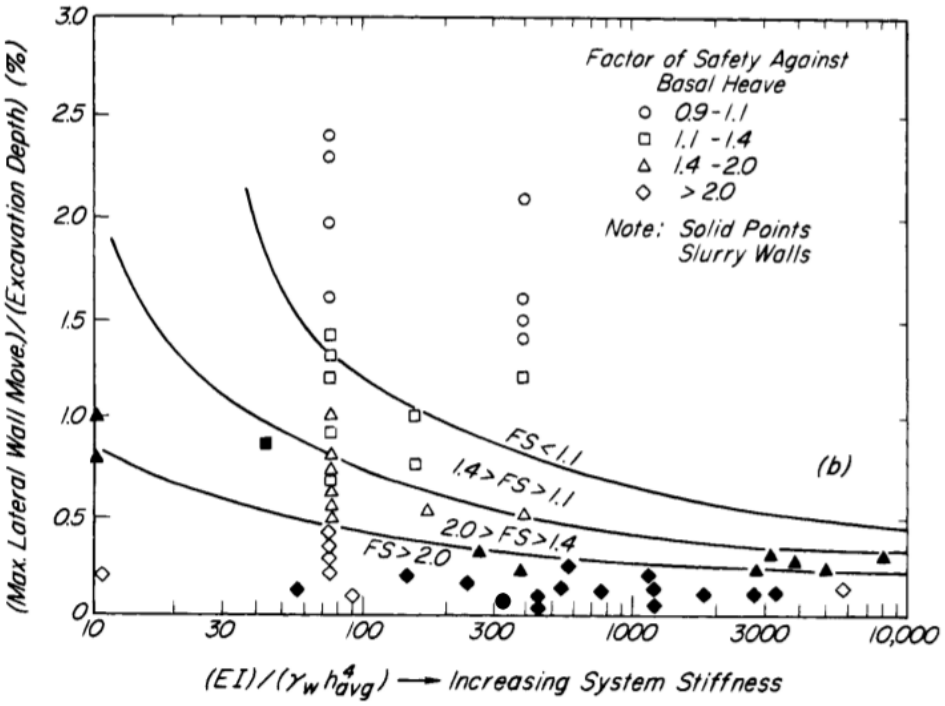

Figure 2.1: Maximum lateral wall movement, system stiffness, and factor of safety against basal heave. Finite element solutions compared with field measurements (after Clough et al. [1989])

The study presented by Clough et al. [1989] does include stiff retention systems (see solid points in Figure 2.1). This figure suggests that the average ratio of δ_v/H for stiff retention systems (slurry walls) is approximately 0.2% and is independent of the system stiffness. It should be noted that the ground movements presented by Clough and O'Rourke [1990] reportedly do not include ancillary construction activities; consequently, any ground movement not caused directly by the main excavation was not included in Figure 2.1. Ground movement caused by ancillary construction activities can be significant. For instance, Figure 2.2, shows ground movements caused the installation of slurry walls. Even though secant pile walls, and not slurry walls, were used at the OMPW site, Figure 2.2 can be used to provide a first-order estimate the ground movement caused by the installation of the perimeter walls.

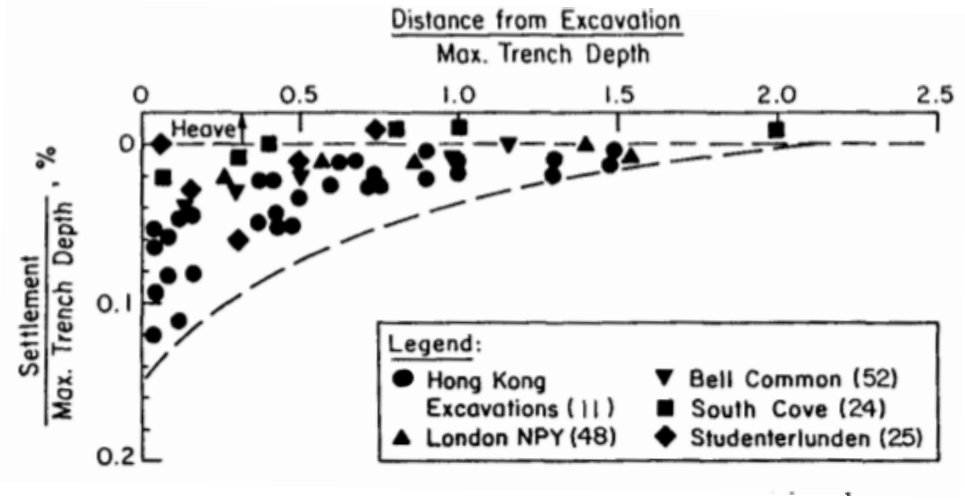

Figure 2.2: Summary of measured settlements caused by the installation of concrete diaphragm walls (after Clough and O'Rourke [1990])

The work performed by Peck [1969b] and Clough et al. [1989] was continued by Long [2001]. Long [2001] compiled data from 296 individual case histories. However, Long [2001] did not separate ancillary movements from movement associated with the main excavation. These case histories were categorized in terms of ground and support conditions, as shown in Figure 2.4.

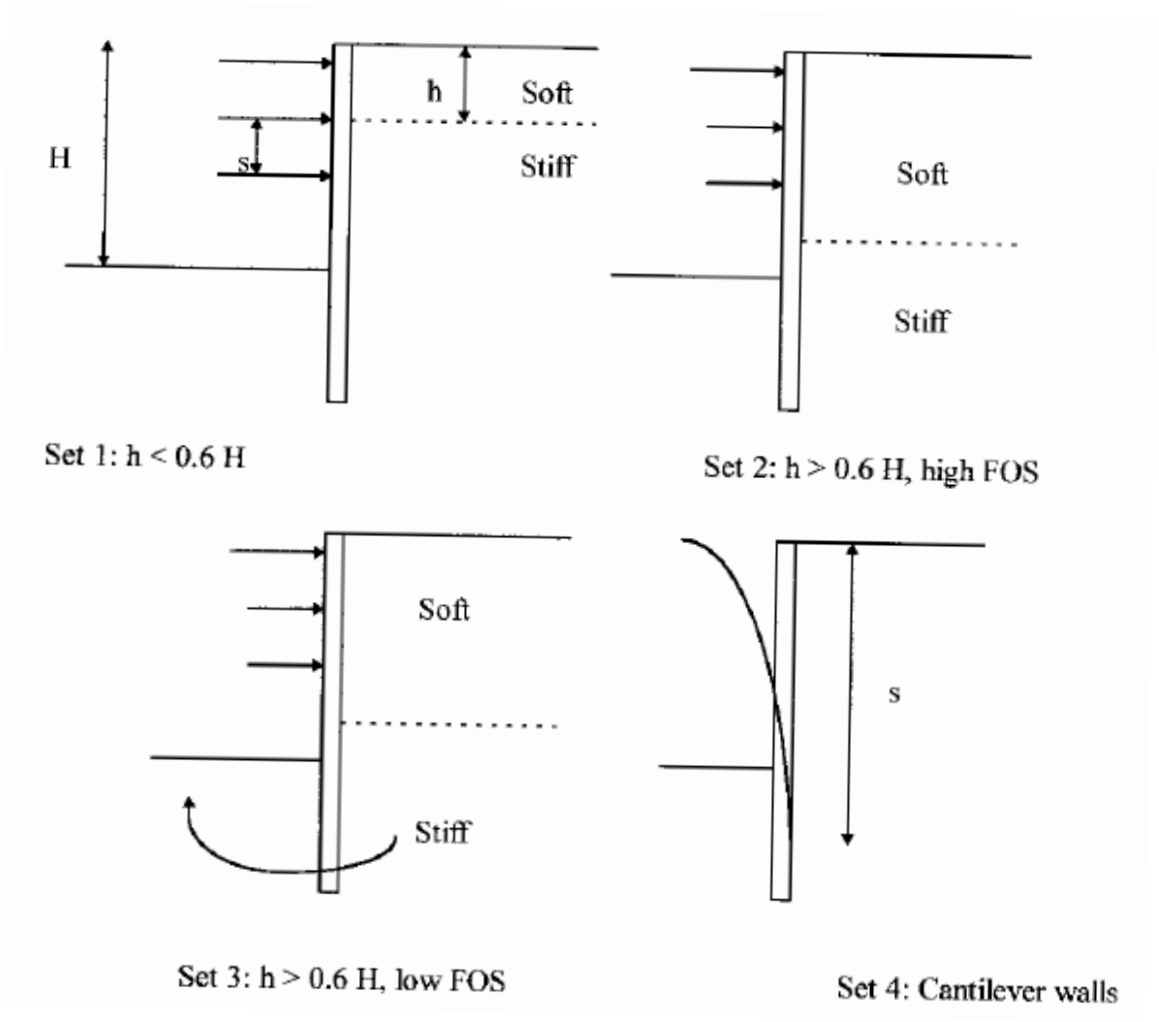

Figure 2.3: Categories used to subdivide excavation performance data (after Long [2001])

These categories include:

- Set 1: Cases where the ground conditions comprise predominantly stiff/medium dense soils and the thickness of soft soils h is $< 0.6H$
- Set 2: Similar to Set 1, but where h is $> 0.6H$
- Set 3: Similar to Set 2, but with a low factor of safety against basal heave
- Set 4: Cantilever walls (s is defined as retained height plus fixity depth)

Sets 2 and 3 were subdivided into two subsets: a) and b). Set 2a and 3a correspond to the condition where the transition from soft to stiff clays occur above the bottom of the excavation, so that $H > h > 0.6H$. Set 2b and 3b corresponds to the condition where the transition from soft to stiff clays occurs deeper, below the bottom of the cut, so that $h > H$.

Long [2001] explained that it is not possible to calculate the factor of safety against basal heave at full depth in cases where the retaining wall is keyed into a hard soil layer using methods such as that of Bjerrum and Eide [1956]. However, Long [2001] suggested that logic and experience confirm that the high factor of safety exists and it is likely higher than 3.0.

The OMPW site has a high factor of safety against basal heave at full depth and soft clays are present at dredge level. Consequently, the performance of the OMPW site can be compared to the data presented by Long [2001] under Set 2b.

The normalized maximum movement (lateral and settlement) for all cases that correspond to Set 2b (case that resembles that conditions at OMPW) is displayed in 2.4. The presented graph shows a slight trend or inverse correlation between excavation depth and movement; however, a large scatter is observed in the data set.

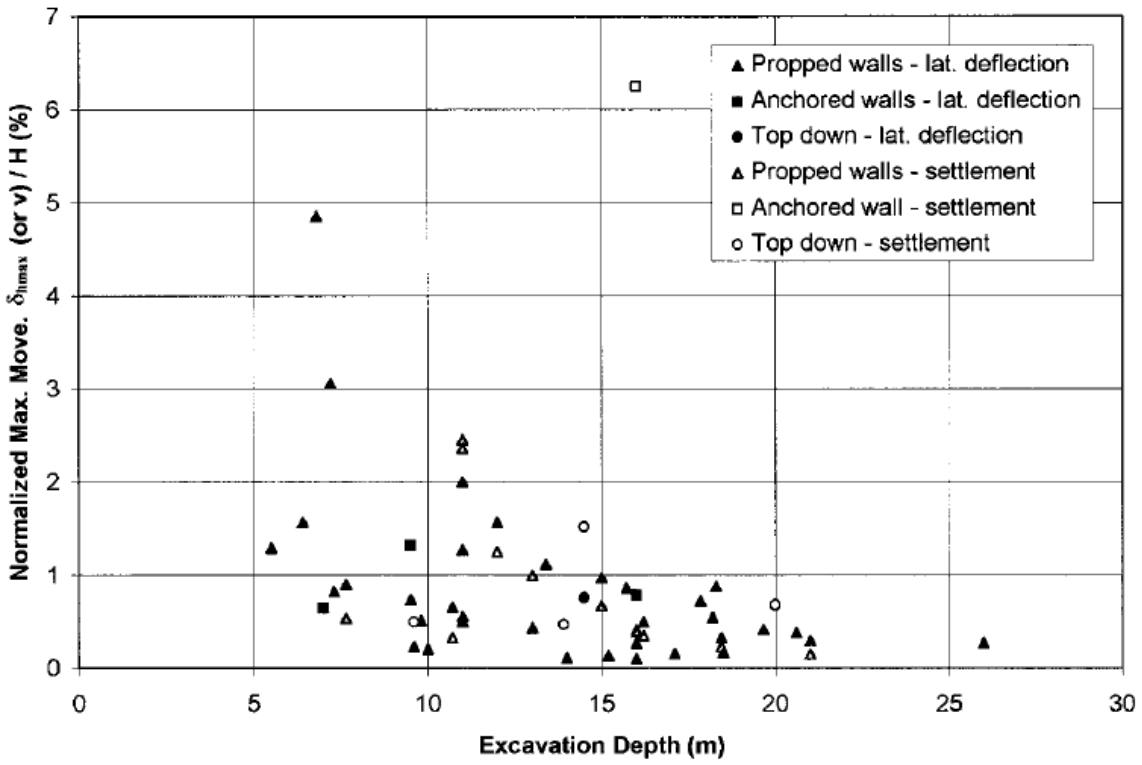

Figure 2.4: Normalized maximum lateral movement versus depth for Set 2b (after Long [2001])

Figure 2.5 presents this same data, but in a normalized maximum lateral movement versus system stiffness, following the same definition of system stiffness originally presented by Clough et al. [1989]. This figure, for reference, also displays the curve recommended by Clough et al. [1989] for factor of safety against basal heave of 3. If the factor of safety against basal heave greater than 3.0, as suggested by Long [2001], it is clear that the curve presented by Clough et al. [1989] largely underestimates the maximum displacement for many of the case histories. The data presented by Long [2001] show sites with ratios

of movement to excavation depth as high as almost 5 %; however, most of the data show a ratio of less than 1.5% and an average value of approximately 0.75 %. It is also interesting to note that the performance of top down constructions do not show less ground movements when compared with propped and anchored walls. However, it is important to recall that the data presented by Long [2001] does include ancillary ground movements and the correlations and data presented by Clough et al. [1989] does not.

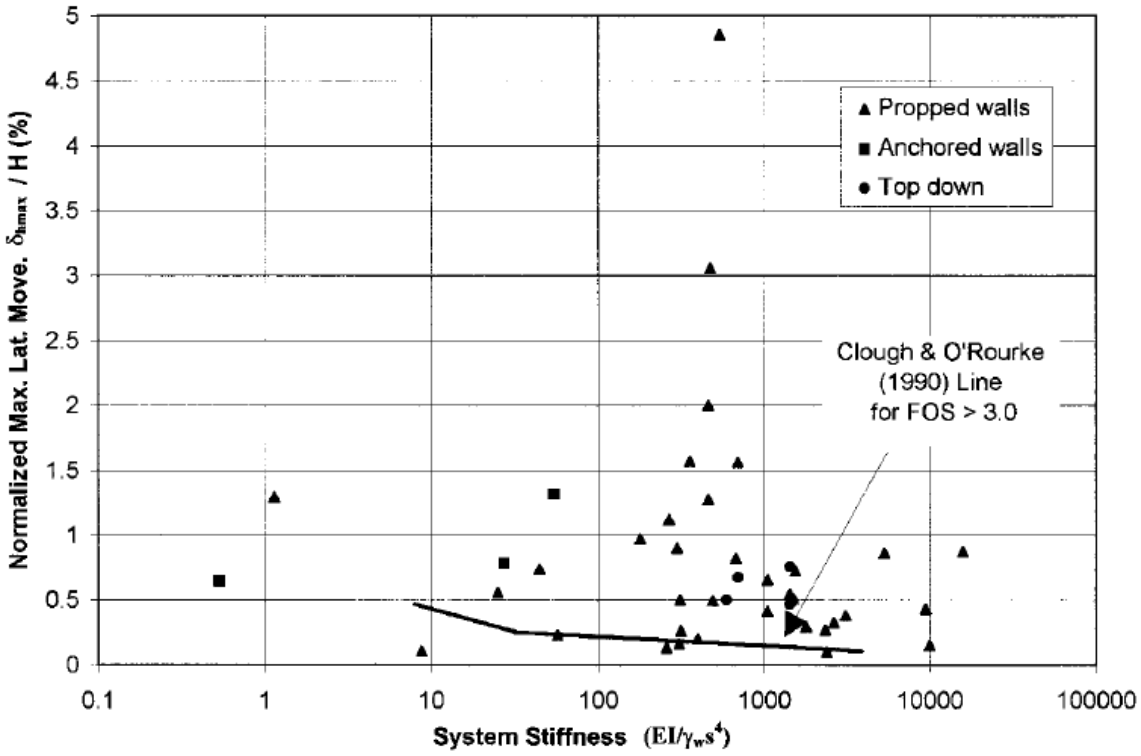

Figure 2.5: Normalized maximum lateral movement versus system stiffness for Set 2b (after Long [2001])

Long [2001] hypothesized that a possible explanation for the unexpected poor performance of the top down excavation could be attributed to thermal shrinkage effect in the concrete slabs.

2.3. Optimization Methods

As explained by Rechea et al. [2008], inverse analysis techniques have been applied to geotechnical problems since the 1980s to extract constitutive model parameters from laboratory, in-situ and field performance data (e.g., Gioda and Maier [1980], Cividini et al. [1981]).

Two main types of inverse analysis that have been applied to geotechnics: gradient based methods and genetic algorithms. In both methods, the problem is solved by minimizing an objective function defined as the weighted difference between calculated and target observations.

Most gradient based methods are variations or improvements of the original Gauss-Newton method. In these methods, the model parameters are continuously adjusted until a convergence criterion is met. The magnitude, by which the parameters are adjusted after each iteration, is computed utilizing the first order derivative matrix (Jacobian) and/or the second order derivative matrix (Hessian) of the objective function. The derivatives are typically estimated numerically, by applying a perturbation to the model parameters. The selected perturbation typically follows a forward or central difference scheme.

The advantages of the gradient based methods are that it is highly efficient and has rapid convergence when the initial trial is close to the optimum solution. But, one disadvantage is that the global minimum may not be reached if the initial trial is located in the vicinity

of a local minimum. Consequently, the application of gradient based methods is more advantageous for problems whose objective function topology is understood and reasonable initial estimates of the model parameters can be provided prior to executing the inverse analysis. Examples of inverse calibration studies using gradient based optimization routines include: Ledesma et al. [1991],Dziadziuszko et al. [2000],Finno and Calvello [2005], Calvello and Finno [2004],Rechea Bernal [2006],Svoboda and Mašín [2008] and Svoboda and Mašín [2011].

The principles of genetic algorithms were originally proposed by Goldberg [1989] and Renders [1994]. A genetic algorithm is an optimization method inspired by Darwin's theory of evolution. Its search routine does not rely on computing derivatives to calculate the trial set of model parameters. Instead, a genetic algorithm optimization method starts by evaluating the objective function on a random set of model parameters distributed across the investigated model parameter domain. Each set of model parameters is called an "individual". After the initial evaluation is performed, a subset of "individuals" that provide the best fit are "selected" to "breed" the next generation and the rest of parameters are eliminated. Reproduction of the new generation is created using "genetic operators," which are numerical operators that allow transforming existing solutions into new ones. After each iteration or generation, the average fit of the population increases. The process is repeated until a certain convergence criteria is met, at which time the existing "individuals" are no longer providing a better fit between calculated and target observations.

One advantage of using genetic algorithms is that its search routine is not affected by the presence of areas of local minima; hence its search routine is global within the specified

domain. In addition, genetic algorithms are recognized for being highly efficient in large, discrete, non-linear problems. One of the disadvantages of using genetic algorithms is that, because of the random nature of the search routine, there is no certainty that the optimal solution may be encountered; instead, only a set of solutions close to the "true" solution may be reported. Other drawbacks of genetic algorithms include the need to define the model parameters domains or search ranges prior to executing the inverse calibration routine. In addition, genetic algorithms typically require high computational cost (large number of function evaluations) when compared with gradient based methods. Examples of inverse calibration studies using genetic algorithms include Levasseur et al. [2008] and Rechea et al. [2008].

The actual inverse calibration methods utilized in this research are described in the Chapter 3.

2.4. Summary

The reported performance of stiff earth retention systems similar to the one at OMPW reported in the literature was reviewed in chapter. The data available in the literature for support systems with a high factor of safety against basal heave (presumably equal to or higher than 3.0) and stiff structural support systems show a highly scattered relation between the anticipated normalized maximum ground movement (δ_h/H) and the excavation depth. In addition, these same cases show a normalized maximum ground movement that seems to be independent of system stiffness as proposed by Clough et al. [1989]. Data shown by Long [2001] indicates that there is not a clear improvement of performance when comparing top-down constructions to propped or braced excavations constructed with bottom-up techniques. Long [2001] hypothesized that this could be attributed to concrete creep in the slabs that serves as the lateral support for the wall.

This chapter also discusses available techniques for solving inverse calibration problems. These techniques include gradient based methods and genetic algorithms. Both methodologies utilize iterative procedures to find the optimum solution that minimizes the error estimated by the objective function. The objective function is defined by the difference between calculated values and physical observations.

Gradient based methods estimate the trial solutions based on the numerical evaluation of the Jacobian or Hessian of the objective function using a forward or central difference scheme. These methods are recognized to have fast convergence, but may not achieve the global minimum unless the initial trial is located close the optimum solution.

Genetic algorithms do not rely on numerical derivatives to estimate the trial solutions; instead, random sets of solutions are evaluated over a predefined domain after each iteration. Subsets of these solutions that provide the best fit are kept and the remainder is eliminated. The solutions that are kept are used to produce a new set of trial solutions. The overall fit of the trial solutions improve after every iteration. Genetic algorithms are recognized for being very efficient when dealing with large nonlinear problems; however, they typically involve a large computational effort.

CHAPTER 3

Optimization and Inverse Calibration

3.1. Inverse Calibration

In an optimization routine, finite element simulations are created to predict the target observations. Therefore, every observation is paired with a computed value obtained from the finite element simulations. An objective function, that quantifies the error between the observed and computed values, is established based on a weighted least squared method. The error computed by the objective function is minimized through a series of iterations using a gradient based method.

Herein, the error minimization routine is based on an implementation of the Levenberg-Marquardt algorithm (LMA), originally published by Levenberg [1944] and later on, independently published by Marquardt [1963]. LMA is a modification of the Gauss-Newton algorithm that includes a damping mechanism that slows the convergence but makes it more suitable for not well-defined functions. LMA has been implemented as the preferred optimization routine in popular optimization computer codes, such as UCODE (Poeter and Hill [1999]), and has been successfully used in the geotechnical field by other researchers (Rechea Bernal [2006] and Svoboda and Mašín [2008] and Svoboda and Mašín [2011]).

A gradient based optimization routine was selected instead of genetic algorithms, because gradient based routines typically prove to be computationally less expensive for the type of problems solved herein (Rechea Bernal [2006]).

The implementation of LMA used in this study is the one developed by the Applied Mathematics Division at the Argonne National Laboratory to solve non-linear systems of equations and non-linear least square problems named MINIPACK. Additionally, a computer routine in the Python Programming Language (`http://www.python.org/`) was

developed to control the data management and the iterative execution the finite element simulations. Since MINIPACK is written in FORTRAN, for convenience, a wrapper to MINIPACK that ports MINIPACK from FORTRAN into Python provided by Scipy (`http://www.scipy.org/`) was utilized. MINPACK, Scipy and Python are freely distributable open source computer codes, portable to different operating systems.

3.1.1. Variable scaling

Model parameters selected for optimization could have different measuring units or could have values that largely differ in magnitude. In these cases, it is recommended to use a scaling function prior to incorporating the model parameter in the optimization routine Hill [1998]. The scaling functions will convert the model parameters into values with comparable magnitudes.

The linear scaling function listed in the equation below was used in this study:

$$x_o^* = \frac{x_o - x_{min}}{x_{max} - x_{min}} \tag{3.1}$$

Where x_o is the variable to be scaled, x_{max} and x_{min} and the maximum and minimum anticipated values for x_o, and x_o^* is the scaled variable. It should be noted that scaling only converts the different variables into parameters with similar magnitudes, but it does not bound their value to a x_{max} and x_{min}. Consequently, during optimization x_o can adopt values smaller or larger than x_{max} and x_{min}, respectively.

3.1.2. Objective Function

The objective function captures the error or discrepancy between the target observations and the model predictions. Calvello [2002] and Rechea Bernal [2006] utilized the objective function as incorporated into the optimization computer code UCODE, defined as:

$$S(b) = \sum_{k=1}^{M*N} w_k (e_k)^2 \tag{3.2}$$

Where b is a vector containing the parameter being optimized, $M * N$ is the total number of observations (M observations in N different instruments), w_k and e_k are the weighting factor and the residual for the k^{th} observation.

The residual e_k, as shown in Equation 3.3, is the difference between the actual observation value (y_k) and its model prediction ($f(b)_k$).

$$e_k = \|y_k - f(b)_k\| \tag{3.3}$$

The weighting factor, w_k, is related to the inverse of the k^{th} measurement error variance:

$$w_k = \frac{1}{\sigma_k^2} \tag{3.4}$$

This factor, in a sense, scales the error of each measurement with respect to the maximum accuracy of the equipment or instrument used to collect the observation.

In the work presented by Rechea Bernal and Calvello, a few observations were carefully selected prior to their incorporation into the optimization routines. Clearly, this careful selection of observations is critical to the proper convergence and success of the optimization process. Conversely, it is also clear that the overall performance of the selected objective function can be biased by a large error caused by a single or a few ill-posed observations.

Selecting the suitability of an observation for use in the optimization process can be a difficult task. Even, when all precautions are taken, it is at times quite complex to determine a priori if certain observations are in fact a true reflection of the performance of the observed process or if they are in full or in part a consequence of some type of instrument or human error.

The difficulty in selecting the most suitable observations for optimization and the elimination of an ill-posed observation from the pool of target observations depends on type and number of observations. Considering that this study aims at utilizing large amounts of data of multiple sources as targets for optimization, a variation to the objective function used by Rechea Bernal and Calvello is developed and implemented in this thesis.

This variation will ideally prevent the whole optimization process to be compromised in case one or few inadequate observations are inadvertently mixed with the dataset. This variation consists of capping the magnitude of the computed residual for each observation to a value that ranges between zero and one. This is accomplished by using the following residual function and the objective functions:

$$S(b) = \frac{\sum_{i=1}^{N} W_i e_i^2}{\sum_{i=1}^{N} W_i} \tag{3.5}$$

$$e_i = \sum_{j=1}^{M} \tanh\left(\frac{v_j \left\| y_j - f(b)_j \right\|}{v_j \left\| y_j \right\|}\right) \tag{3.6}$$

In this re-defined residual function, e_i, the parameter v_i corresponds to the weight factor for each observation, and is equivalent to w_i defined in Equation 3.4. W_i is the weight factor that can be applied to the set of observations obtained from a single instrument or test. This second weight factor is not necessarily incorporated to capture the possible error of the measurement, but to incorporate a mechanism to modify the objective function to favor certain type of observations. This weighting factor, W_i is highly empirical and could be hypothetically used, for instance, to give more weight to an observation collected with high quality workmanship over those with questionable or unknown quality. It could also be used to, for instance, attempt to obtain a better match of the performance data (e.g., and inclinometer) over a laboratory test result (e.g., triaxial test).

The modified definition of the residual presented herein will limit the ability of one or few ill-posed observations to alter the topology of the objective function. In addition, the contribution of the computed residual of an ill-posed observation on the value of the objective function is inversely proportional to the number of observations; consequently, the larger the number of observations, the more unlikely it becomes for a few ill-posed observations to skew the topology of the objective function.

3.2. Summary

In this chapter the inverse calibration techniques utilized to perform the optimization of the finite element model parameters used in this research were discussed. The Levenberg-Marquardt algorithm (LMA) was selected as the preferred optimization method. LMA has been implemented as the preferred optimization routine in other popular optimization computer codes such as UCODE (Poeter and Hill [1999]) and has been successfully used in the geotechnical field by other researchers (Rechea Bernal [2006] and Svoboda and Mašín [2008] and Svoboda and Mašín [2011]). A gradient based optimization routine was selected instead of genetic algorithms, because gradient based routines typically prove to be computationally less expensive.

A new formulation to assemble the objective function and the residual between observations and predictions was introduced. The proposed method was adopted to reduce a potential disruption of the overall optimization convergence or to prevent the modification of the topology of the objective function caused by a single or a few corrupted observations that could be accidentally included in the pool of observations.

CHAPTER 4

One Museum Park West

4.1. Introduction

The performance data obtained at OMPW and results of laboratory tests from samples collected at several sites in Chicago were utilized to validate the optimization procedures proposed in this thesis. This chapter describes site and soil conditions and construction activities during the excavation of OMPW basement structures. The validation and optimization procedures that included the laboratory test data are discussed in Chapter 5. The actual validation of the selected model parameters using the OMPW test data are presented in Chapter 6.

OMPW, as shown in Figure 4.1, is a 53-story reinforced residential concrete tower with four or five basement levels that extends approximately 15 to 21m below existing grade. The OMPW earth retention system was designed to serve as a permanent multi-level underground parking structure and to protect, during and after the excavation, a bridge approach embankment and public utilities located adjacent to the project site. The retaining wall consisted of a stiff secant pile wall and the excavation was performed using top-down construction methods.

The OMPW construction performance data are used to validate the proposed numerical techniques, but also to identify sources of ground movements in stiff retention systems that at times are underestimated or ignored during the design process.

Figure 4.1: Photograph of One Museum Park West (right) and One Museum Park East (left)

4.2. Site Description

4.2.1. Location

The OMPW project site is located in the south end of the Chicago business district in the state of Illinois. As shown in Figure 4.2, the project site is bounded to the north by the Roosevelt Road existing bridge approach embankment, to the west by Indiana Avenue, to the south by an open undeveloped lot and to the east by the One Museum Park East

(OMPE) project. The OMPE project consists of a 62 story high rise structure, built before the OMPW project. The OMPE structure contains two basement levels extending to a maximum elevation of 1m CCD. The OMPE structure is supported on deep caisson foundations.

4.2.2. Site Conditions

Prior to the beginning of the construction of the OMPW project, the project site was vacant. The ground surface elevation of the project site ranged between 5 to 6.5m CCD, whereas the top of the Roosevelt Road embankment was encountered at an elevation that ranged from 8.5 to 11m CCD. Indiana Avenue slopes downward from north to south, meeting Roosevelt Road level to the north, and the project site level at the very south-west corner of the project lot.

4.2.3. Existing Structures

A cross section of the Roosevelt Road bridge approach embankment is shown in Figure 4.3. The southern face of the Roosevelt Road embankment was built using a Mechanically Stabilized Earth (MSE) Wall system. The MSE wall was built using granular backfill and a pre-cast concrete face and it is supported on timber piles.

As it can be seen in Figure 4.3, the MSE wall is only 3.65m wide. The actual depths of the timber piles vary across three distinctive zones: A, B and C (see Figure 4.2). The actual depths of the timber piles below the MSE wall footing are listed in Table 4.1. The tip of these timber piles extends 2 to 3m below the bottom of the OMPW basement excavation and 8 to 9m above the bottom of the perimeter wall.

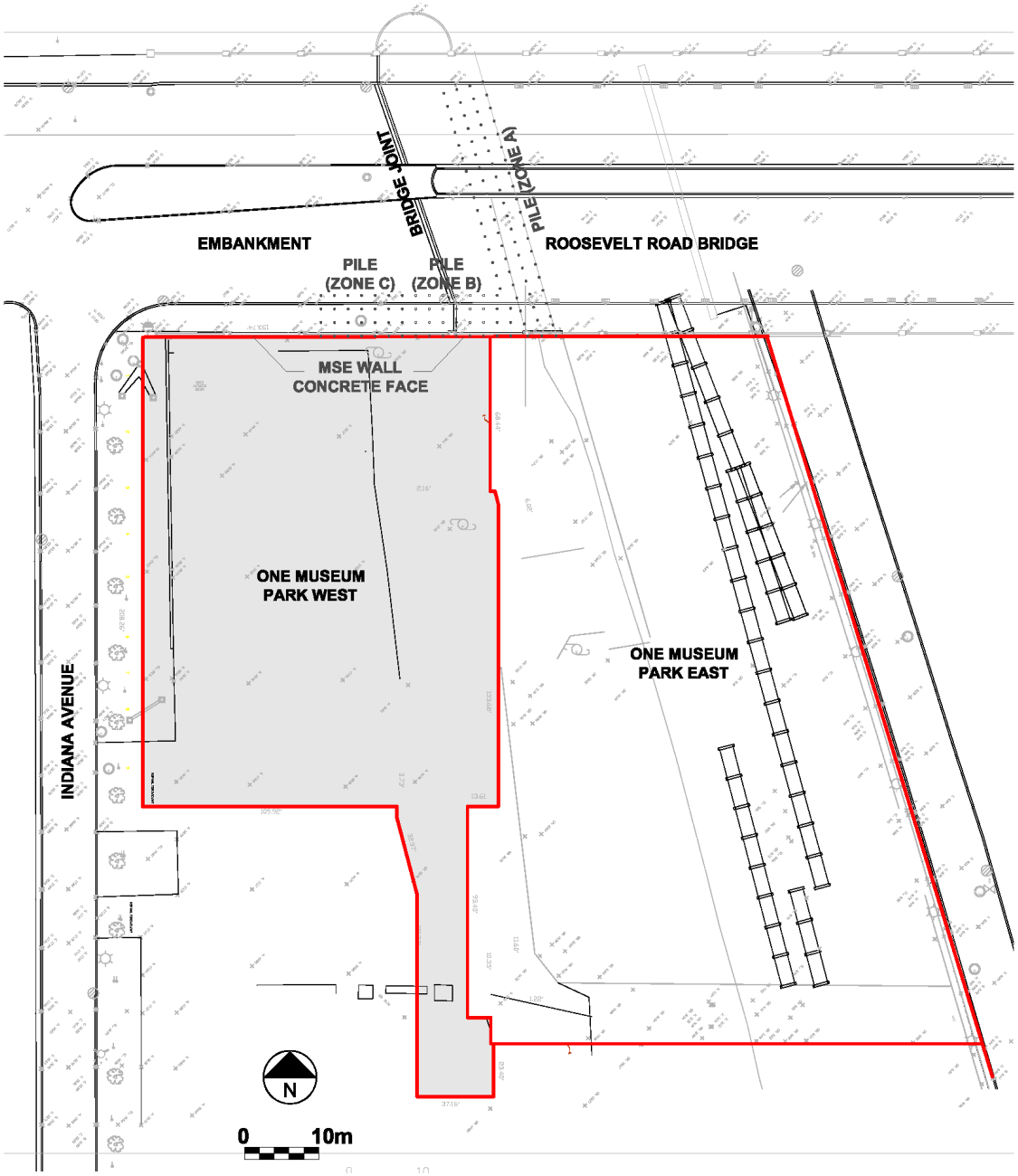

Figure 4.2: Pre-construction Plat of Survey

It is important to emphasize that it is only the face of the Roosevelt Road approach embankment that is reinforced and supported on timber piles. The remainder of the embankment has no deep supports or reinforcing and consists simply of compacted granular backfill.

Zone	Pile Depth, m
A	13.7
B	15.2
C	16.8

Table 4.1: Depth of timber piles in MSE wall

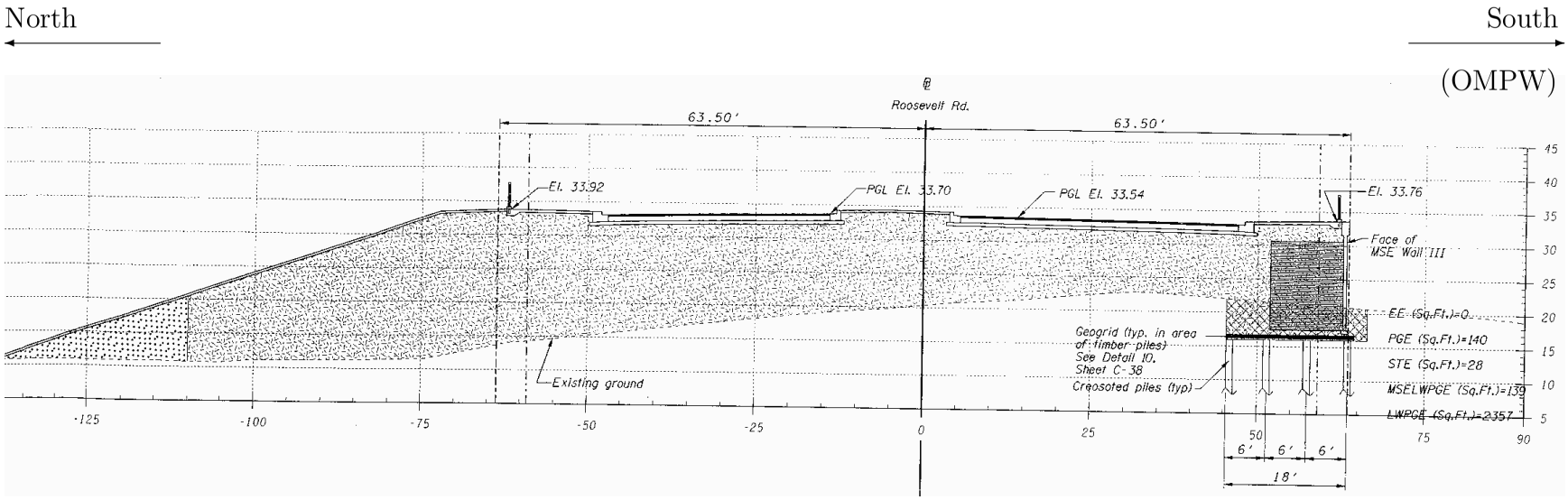

Figure 4.3: Roosevelt approach embankment. Cross section looking East. (Dimensions in feet)

4.3. Soil Conditions

The Chicago soil stratigraphy have been extensively studied by Bretz [1939], Otto [1942], Peck and Reed [1954] and Finno and Chung [1992]. These studies explain that the Chicago soil stratigraphy is formed by glacial till layers above the underlying bedrock. Four of these till layers are subglacial tills (tills formed underneath glacier) and include (in order of deposition): the Valparaiso, Tinley, Park Ridge and Deerfield formations. The density and strength of these layers is directly related to the height of the glacier as the soil was deposited, the drainage conditions, permeability, and the amount of time the ice remained in place. These layers have in general, rather uniform soil properties reflected in the soil water content. Above these subglacial till, the Blogdett formation, a layer of supraglacial till is encountered. Supraglacial tills form in front of the glacial as a result of ice melt-off and re-sidementation of clay particles. These types of formations, as evidenced by the Blodgett formation, are typically highly heterogeneous in composition. This heterogeneity is reflected in, among other things, highly variable water contents.

The stratigraphy and geologic formations at OMPW, interpreted from the boring logs performed at the project site, are shown in Figure 4.4. The exploration program performed at OMPW also included retrieving soil samples for visual inspection and routine laboratory testing. In-situ vane shear and Menard Pressuremeter test were performed.

After the completion of the OMPW project a second exploration program was performed. This second exploration program was performed approximately 75m west of the project site. The program included retrieving 7.6cm diameter Pitcher samples for specialized laboratory testing, performing additional Menard Pressuremeter tests and conducting

cross-hole seismic tests. The results of these specialized tests are also included in this study as targets for optimization.

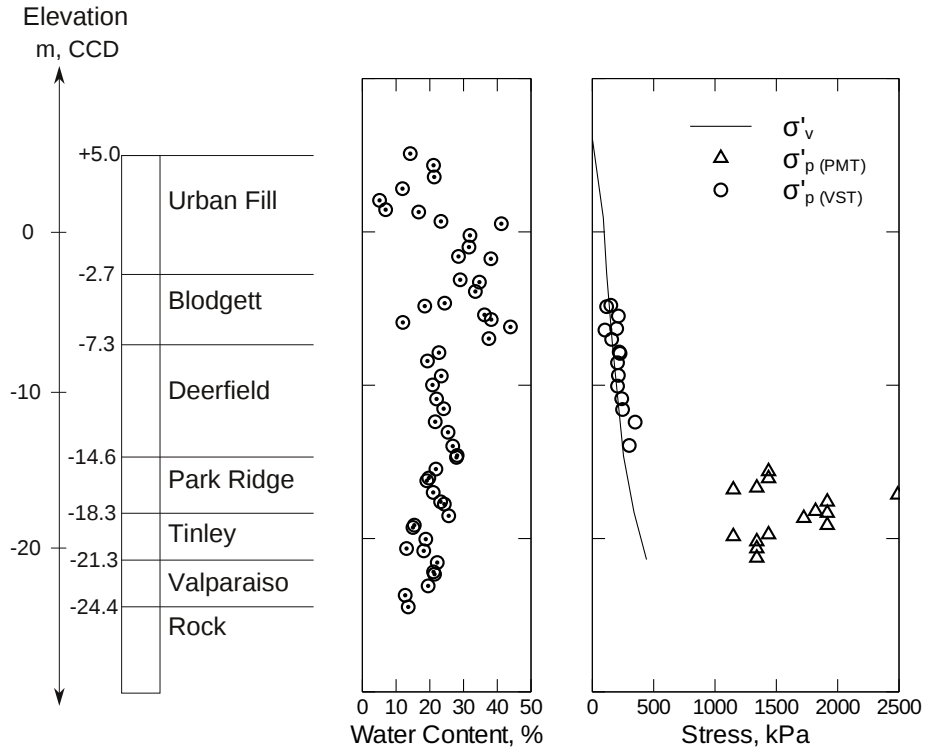

Figure 4.4: Elevation contour map showing pre-construction ground surface elevation

The most compressible clay layers at the site are the Deerfield and Blodgett strata. High compressibility is expected in supraglacial tills, such as the Blodgett formation, as these type of tills are typically encountered in a normally or lightly overconsolidation state. On the other hand, the low degree of overconsolidation observed in the Deerfield formation is rather unusual. This low overconsolidation ratio was attributed by Otto to poor drainage conditions and a short time of the glacial loading. The actual elevation,

thickness, composition and degree of overconsolidation of each till layer vary across the Chicago area.

The soil properties of the clay materials, for both the Deerfield and Blodgett Formations, have been extensively studied using sophisticated laboratory testing procedures by Finno and Chung [1992], Holman [2005], Cho [2007] and Kim [2011]. These studies have included performing a large number of triaxial and consolidation tests. Some of these laboratory test results are also included in this study as targets for the optimization process. A detailed description of all data utilized in the optimization routines is included in Chapter 5.

Figure 4.4 also displays the measured water content with depth. This figure only includes information from the boring logs performed toward the north end of the property. Special attention was given to the north portion of the project site, as it will be explained in the following sections.

In addition to the water content, the maximum past pressure was estimated for all soil layers utilizing the available in-situ information. Mesri [1975] shows that the vane shear strength is directly related to the preconsolidation pressure and the plasticity index of the soil, as shown in Figure 4.5. Consequently, the preconsolidation pressure for the Blodgett and Deerfield layers was estimated using vane shear test results performed in these layers. In addition, Lukas and de Bussy [1976] showed that the preconsolidation pressure is similar in magnitude to the creep pressure measured in the Menard pressuremeter tests. The creep pressure measured in the pressuremeter tests performed in the Park Ridge and Tinley formations was used to evaluate the preconsolidation pressure in those layers.

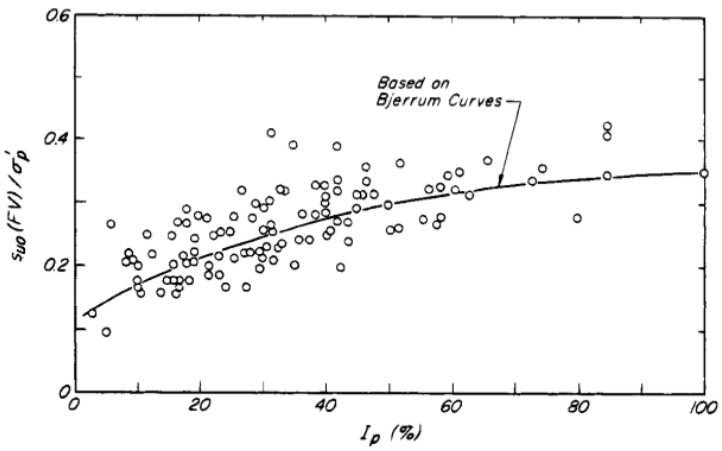

Figure 4.5: Normalized undrained shear strength from vane shear tests versus I_p (from Terzaghi et al. [1996])

The preconsolidation pressure estimated from the vane shear tests results and Menard pressuremeter tests are shown in Figure 4.4. These estimates, when compared to the estimated vertical effective stress (also displayed in the same figure) show the low overconsolidation ratio in the Blodgett and Deerfield formation (between 1 and 1.5) and the higher overconsolidation ratios in the Park Ridge and Tinley formation (between 2 and 5).

4.4. Ground Water Conditions

The ground water conditions in Chicago are greatly influenced by Lake Michigan, the Chicago River and man-made hydraulic structures, especially the Chicago Deep Tunnel. Figure 4.6 shows the location of the Chicago Deep Tunnel. Construction for the Chicago Deep Tunnel started in 1975 as part of the Tunnel and Reservoir Plan (TARP). The system consists of 3 to 10m diameter tunnels located approximately 100m below street level. Part of the system runs underneath both branches of the Chicago River.

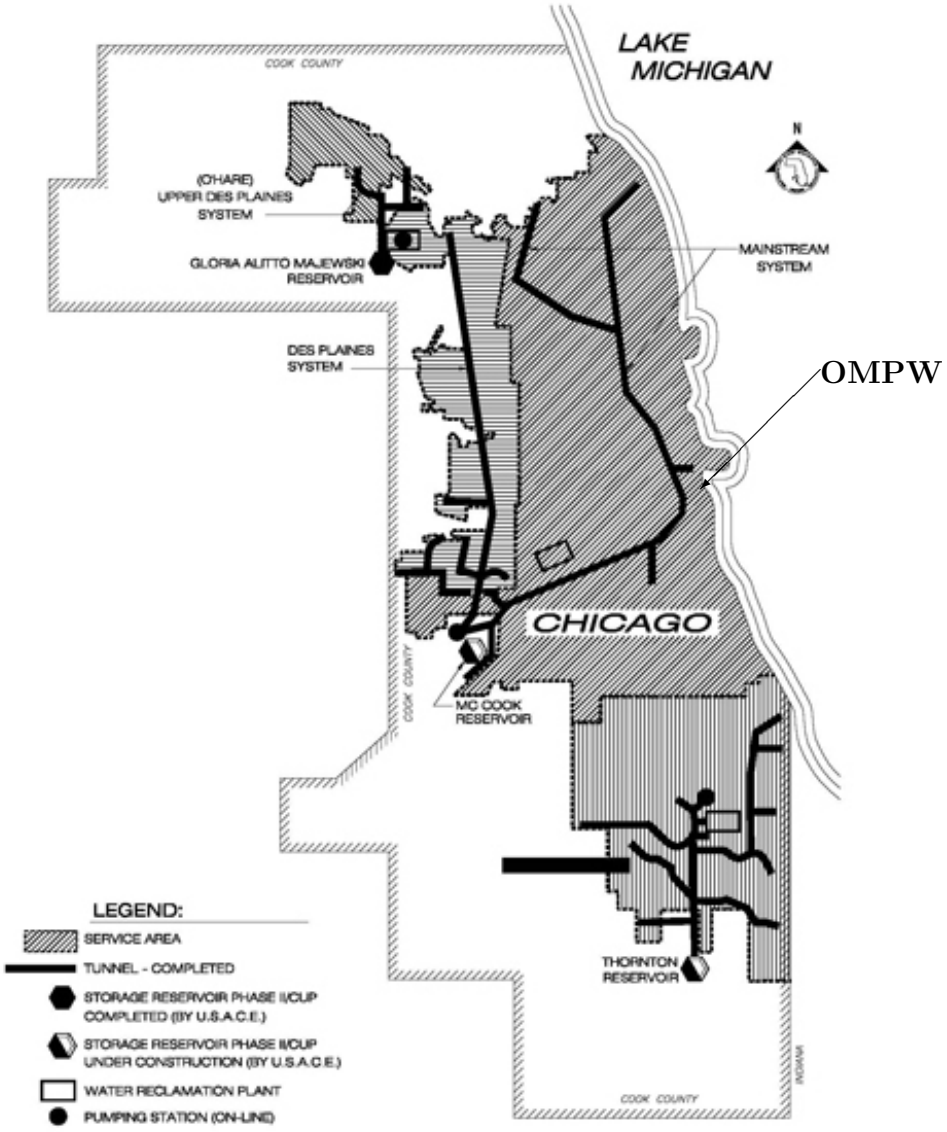

Figure 4.6: Chicago Deep Tunnel (from MWRD)

The construction of the tunnel and the semi-continuous water pumping of them has generated a decrease in the water head at the top of the bedrock formation. Measurements of water levels in the upper strata of the bedrock performed in the Chicago loop in the last decade (after the completion of the tunnel) in project sites located between Lake Michigan and the Deep Tunnel branches show an almost constant water elevation – independent of time and location – of -14.5m CCD. This constant water head suggests that the bedrock water level has reached a hydraulic equilibrium and it is encountered in a steady state condition. Table 4.2 shows a sampling of these observations.

Location	Water Elevation, m CCD	Date
18th St. And Calumet Av.	−13.4	2004/09/27
111 S Wacker Dr.	−15.2	1998
79 E Wacker Dr.	−14.7	2008/01/06
1 N Wacker Dr.	−14.5	1999
Roosevelt Rd. And Michigan Av.	−14.9	1997/01/11
79 East Wacker Dr.	−14.7	2005/06/14
300 N LaSalle St.	−14.1	2005/01/11

Table 4.2: Chicago bedrock ground water table elevation

Typical measurements of the phreatic surface made within the superficial urban fill material roughly coincide with the river or lake levels (0 to 1.5m CCD). A comparison of the current ground water head encountered at the top of rock with the phreatic surface in the superficial fill, show that the water pressures in the natural glacial tills are controlled by a steady state downward seepage, as will be subsequently discussed.

Pore water pressure measurements in the glacial till layers collected at two project sites located in the vicinity of the OMPW project provide further evidence of this downward

seepage. Figure 4.7 shows the pore water pressures measured at Soldier Field and Howard-Dan Ryan station project (located at 14^{th} and State street). These measurements were performed using vibrating wire piezometers installed in the soft to medium clay layers. In this figure, the downward seepage is evidenced by the deviation of the measured pore water pressure from the theoretical hydrostatic water pressure distribution.

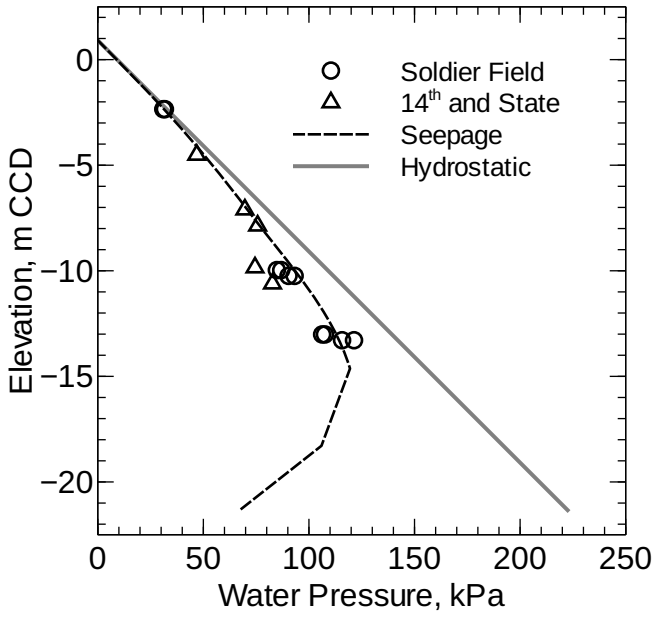

Figure 4.7: Measured versus predicted water pressure at Soldier Field and 14^{th} & State Subway Station

The ground water conditions adopted for the analysis of the OMPW project are those described by a steady state downward seepage driven by a ground water head of -14.5m at the top of bedrock and a phreatic surface of 0.5m in the fill material.

The actual pore water pressure in all clay layers can be readily computed if one-dimensional (vertical) flow is assumed. To compute the actual pore water pressures the permeability of all soil layers need to be measured or estimated.

As explained by Mesri et al. [1994], the permeability of young clay deposits exists in a very narrow range independent of their composition ($5 * 10^{-10}$ to $5 * 10^{-9} m/s$). The siltier materials will typically come to equilibrium after natural deposition at small void ratios, but large void sizes. On the other hand, more plastic soils will reach equilibrium at high void ratios but smaller void sizes. Because the void ratio and void size have opposites effects on the permeability, the permeability of siltier clays are often similar in magnitude to those of the more plastic ones. Consequently, the permeability of the softest and youngest silty clay deposit (i.e., Blodgett till) was assumed to be encountered in this range and to be equal to $5 * 10^{-9} m/s$.

No information is available to reliably estimate the permeability of the deeper glacial till layers at the OMPW site. Consequently, the permeability of these layers was estimated using the following indirect approach.

First, it is assumed that the glacial till layers are similar across neighboring sites; specifically, it was assumed that the permeability of the glacial till layers at OMPW were similar to the ones at the Soldier Field and 14^{th} and State projects. Given this assumption, the permeability of the deeper till layers was back calculated from the piezometer data presented in Figure 4.7. The back calculation of permeability is performed following an iterative procedure in which the pressure distribution is computed using trial sets of permeability (for all till layers, expect for the Blodgett formation). The pressure distribution is then computed using the Darcy equations for one-dimensional flow listed below:

$$q = -k_i * \Delta h_i / H_i \tag{4.1}$$

In Equation 4.1, q, k_i, Δh and H_i are the hydraulic flux, permeability, change in total hydraulic head and thickness of the i^{th} layer, respectively. It should be recalled the in one-dimensional steady state flow, the hydraulic flux (q) is identical in all layers. The trial sets of permeability are changed until a good match between the calculated and reported water pressures are obtained and the permeability in all layers is estimated.

In this back analysis, the hydraulic boundary conditions at Soldier Field and 14^{th} & State project were assumed to be equal to the typical values encountered in the Chicago area; that is, a ground water head of -14.5m at the top of bedrock and a phreatic surface of 0.5m in the fill material.

Clearly, assuming that the permeability of the different tills layers remains constant across neighboring sites can be questioned. However, it should be noted that the differences between boring logs performed at the OMPW and the ones performed at the Soldier Field and 14^{th} and State projects, show differences in the soil formations that are comparable to the changes in soil properties observed across the borings performed at OMPW alone. Consequently, the error introduced in this analysis by this assumption may not be greater than the error that is introduced by the OMPW soil heterogeneity.

This proposed back analysis resulted in the estimated permeability listed in Table 4.3.

For practical purposes, the permeability of the granular urban fill, the Valparaiso formation (formed of gravel and boulders) and the underlying fractured bedrock can be assumed to be almost free draining when compared to the rest of the clay till layers.

Consequently, a permeability of $10^{-3}m/s$ (several orders of magnitude higher than the typical permeability of the clay layers) was adopted for subsequent analyses.

Layer	Permeability, m/s
Urban Fill	$1.0 * 10^{-3}$
Blodgett	$5.0 * 10^{-9}$
Deerfield	$1.7 * 10^{-09}$
Park Ridge	$4.2 * 10^{-10}$
Tinley	$2.5 * 10^{-10}$
Valparaiso	$1.0 * 10^{-3}$

Table 4.3: Estimated soil permeability per soil layer

4.5. Project Description

4.5.1. Structural System

The structural frame for the 53 story tower was built with reinforced concrete and it is supported by a central concrete core composed of shear walls that provide lateral resistance to wind loading. The core is connected to a reinforced concrete structural frame consisting of columns and beams. The floors are formed of reinforced structural slabs reinforced in two directions.

4.5.2. Foundations

The foundation system is shown in Figure 4.8 and consists of a combination of drilled pier foundations and a perimeter secant pile wall. The central core, sustaining the heaviest loads, is supported on straight piers (or caissons) that bear on the top (no socket) of rock. The remainder of the tower, sustaining lesser loads, is supported on a combination of straight and belled caissons and a perimeter secant pile wall.

4.5.2.1. Straight Caissons. The straight caissons are designed to transmit an allowable bearing pressure of 8,600kPa to the underlying bedrock formation encountered at an approximate elevation of -24.4m, CCD. The shafts are reinforced with high strength concrete ($f'c$ =69MPa) and a full length reinforcing cage. The shafts are approximately 14m long and extend from the bottom of the tower core (-10.5m, CCD) to the top of the rock formation (-24.4m, CCD). The shafts diameters varied from 2.44 to 2.75m under the core, and from 1.37 to 2.28m under the rest of the parking structure.

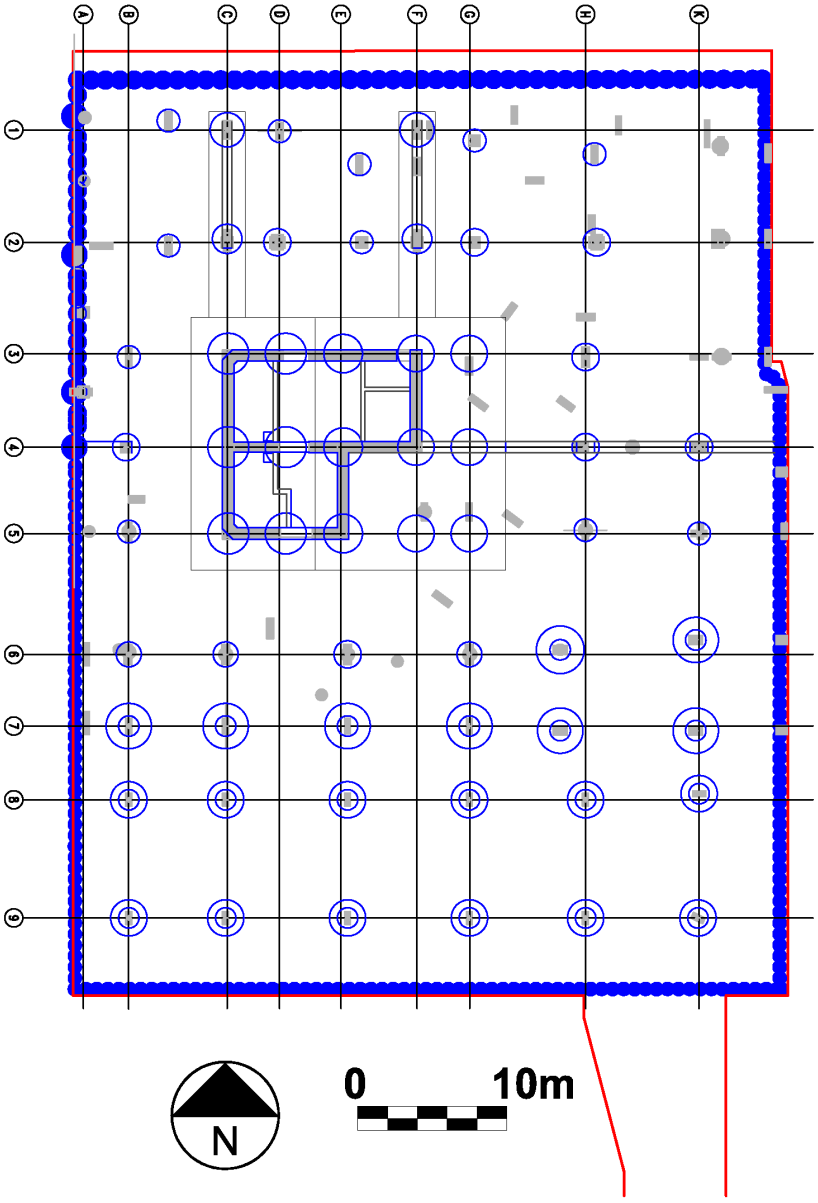

Figure 4.8: Foundation Plan

The shafts were excavated using a temporary steel casing that extends from ground surface into the underlying natural clays at an approximate elevation of -10.5m CCD. The excavation of the caissons was performed under a full head of synthetic slurry. After completion of the excavation, the reinforcing steel cage was lowered into the slurry and the concrete was poured into the shaft using a tremie pipe. Immediately after concrete set up, the slurry and concrete laitance was removed from the top of the caisson and a pre-cast reinforced concrete column was lowered in the temporary casing and connected to the top of the caisson. The column extended to ground surface. The annulus between the pre-cast columns and the temporary casing was filled with sand and the temporary casing was removed from the ground. A few small diameter caissons were extended to the ground surface and did not require dropped-in pre-cast columns.

4.5.2.2. Belled Caissons. The belled caissons were designed to transmit an allowable bearing pressure of 1,077kPa to a layer of over-consolidated glacial tills encountered at an approximate elevation of -16.7m, CCD. The shafts were reinforced with normal strength concrete ($f'c$ =41.4MPa) and partial length reinforcing cage. The shafts were 1.37m in diameter and the bells varied in diameter from 2.44 to 3.20 m. The shafts were excavated using a temporary casing that extended from ground surface into the underlying natural clay. No slurry was used.

Pre-cast columns were also dropped-in to extend the shaft to ground surface. The annulus was backfilled with sand, and the temporary casing was pulled out of the ground.

4.5.3. Basement Structure

Figure 4.9 shows a North-South cross section across the basement structure. The basement was designed as a continuous ramp that revolves around the tower core. The basement slab meets with the street level along the south property line. The basement slabs are relatively flat along the north and south perimeter walls. The steepest ramp descents are observed along the east and west perimeter walls. The basement structure contains five levels along the northern portion of the project site, and four levels along the southern portion.

The basement floors consist of structural slabs and a slab on grade. The slabs are connected to the perimeter walls using steel dowels, as shown in Figures 4.10. This type of connection allows for the development of bending moments in the slabs at the connections with the walls.

The structural slabs are 25.4 cm thick and the slabs on grade in level B4 and B5 is 20.3 cm thick. Table 4.4 depicts the typical slab thickness and concrete design compressive strength for each of the basement levels.

It should be noted, that the concrete utilized for all the basement slabs did not include any additive or special mix design to prevent excessive shrinkage or creep. It should also be noted that the slab on grade was not designed for uplift pressures as it was placed over a drainage blanket 15 cm thick with a sump and pump system provided to prevent hydrostatic pressures.

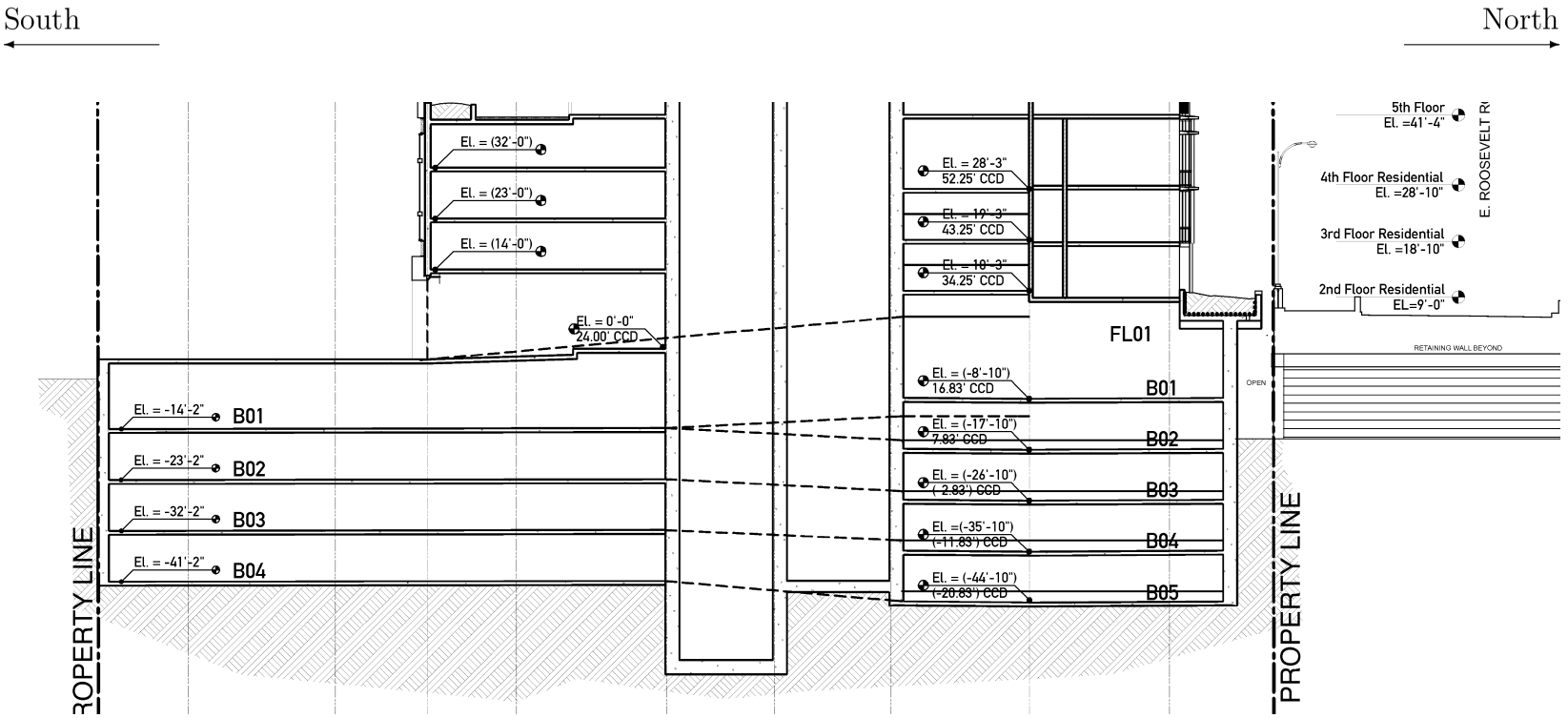

Figure 4.9: North-South section along basements (looking West). (Dimensions in feet)

Basement Level	Slab Thickness, cm	Concrete Strength, MPa
1st Floor	30.5	55.1
B1	25.4	41.3
B2	25.4	41.3
B3	25.4	41.3
B4	25.4/20.3	41.3/34.5
B5	20.3	34.5

Table 4.4: Slab thickness and concrete design strength per basement level

Figure 4.10: Detail of typical slab-wall connection.

The basement slabs were poured in sections that extended from the perimeter wall to the central core. The slabs were always formed on a thin mud mat layer (approx. 15 cm thick) poured on the excavated sub-grade. In general, the slabs were formed and poured shortly after the excavation of each section. The basement slabs contained two large penetrations that allowed the removal of spoil during the excavation. These penetrations (or glory holes) were not poured until the end of the excavation of all basement levels. Figure 4.11 shows the location of the glory holes.

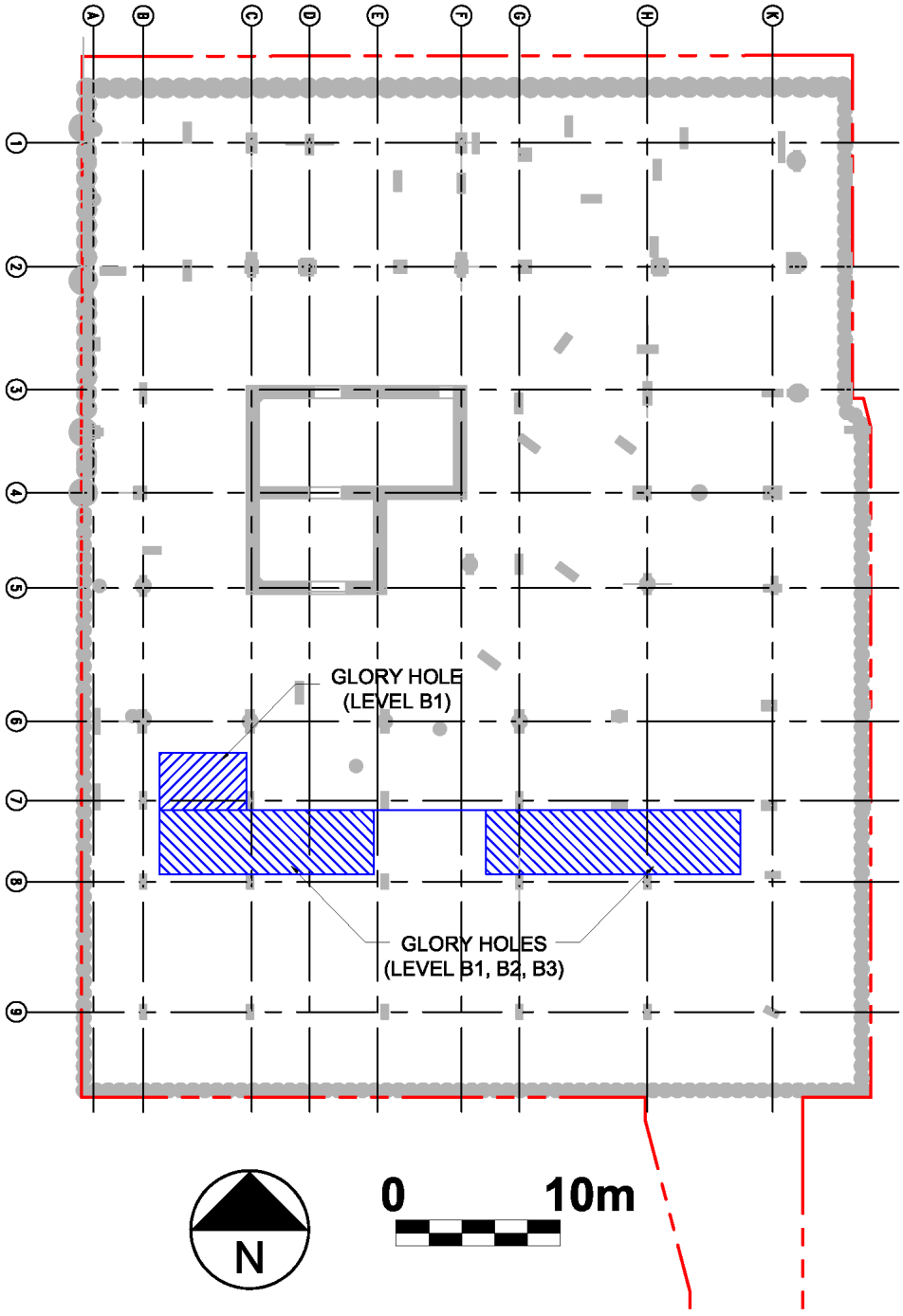

Figure 4.11: Basement slab penetrations or glory holes

4.5.4. Secant Pile Walls

The perimeter secant pile walls were designed to serve as both temporary and permanent lateral supports as part of the earth retention system, in addition to supporting vertical loads. A typical section of the secant pile wall is shown in Figure 4.12. The secant pile wall is formed by series of vertical shafts adjacent to one another. The center to center spacing of the piles is less than the pile diameter, creating an overlap that make the piles secant to one another. The purpose of these overlaps is to improve the water tightness of the wall. Each shaft is provided with a steel beam that increases the flexural stiffness of the walls.

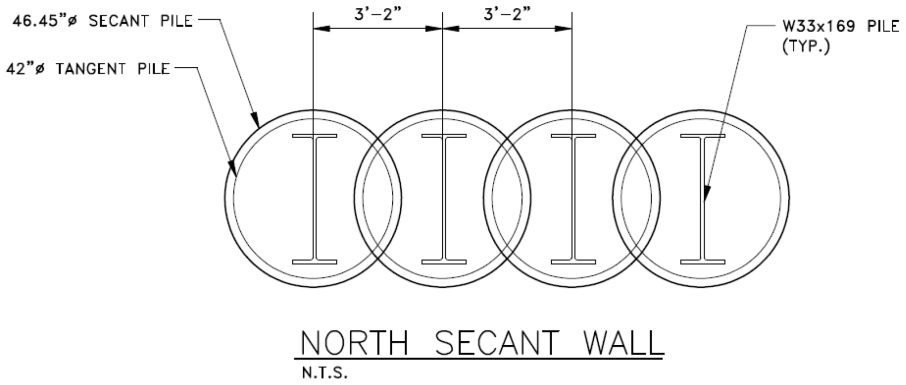

Figure 4.12: Typical cross section of secant pile wall

The secant piles were installed with the drill rig shown in Figure 4.13.1. The rig is provided with an external casing with cutting teeth and an internal auger. The shafts are initially advanced by rotating the external casing attached to the kelly bar. Consequently, the pile diameter is equal to the outside diameter of the external casing. The casing is capable of cutting through concrete of the adjacent piles to create the pile overlap. After

the casing has advanced a few feet, the casing is detached from the kelly bar, as shown in Figure 4.13.1. Next, the internal auger is used to remove the spoil inside the casing, as shown in Figure 4.13.2. After the spoil has been removed, the external casing is re-attached to the kelly bar. This procedure is repeated several times, until the casing reaches an elevation slightly deeper than the proposed bottom of basement. A water tight system, and consequently the pile overlap, was not needed below the bottom of the basement. For this reason, the remainder of the pile is advanced using only the internal auger. In this lower portion of the wall, the pile diameter is equal to the outside diameter of the auger and the shafts are designed to be tangent to one another.

Table 4.5 shows the diameter of the secant piles (above and below the dredge line), pile spacing and amount of reinforcing steel of the secant pile wall across the perimeter of the project site. Figure 4.5 lists the zones with different pile designs and indicates the different pile diameters and type of reinforcing steel. Figure 4.11 can be utilized as a reference for the location of the column lines.

Wall	Column Line	Shaft Diameter,m	Shaft Spacing,m	Steel Section
North	A-H.8	1.18/0.97	0.97	W33x169
West	0-3.1	1.18/0.97	0.97	W33x169
West	3.1-7.1	0.88/0.74	0.74	W24x94
West	7.1-10	0.88/0.74	0.74	W24x84
South	A-B.9	0.88/0.74	0.74	W24x76
South	B.9-H.8	0.88/0.74	0.74	W24x84
South	H.8-L	0.88/0.74	0.74	W24x76
East	3.1-9	0.88/0.74	0.74	W24x76
East	9-10	0.88/0.74	0.74	W24x84

Table 4.5: OMPW secant pile wall dimension and reinforcing

(4.13.1) External casing released (4.13.2) Internal auger

Figure 4.13: Secant pile wall drill rig operations

The bottom of the secant pile wall varies in elevation from -18.3 to CCD along the north property line to -17.7m CCD, along the south property line.

4.5.5. Internal Cofferdam

An internal circular cofferdam was built in the center of the project site. Figure 4.14 shows a cross section of the cofferdam. As shown in the figure, the internal cofferdam was built using steel sheet-piles (section PZC-18) and four levels of steel ring beams. Each bracing level was installed immediately after reaching the bracing level elevation. The excavation within the cofferdam extended to the top of the core foundations, at elevation, -10.5m, CCD. The location of the circular cofferdam is shown in Figure 4.15. The cofferdam was built to the construct building core using a bottom-up construction method.

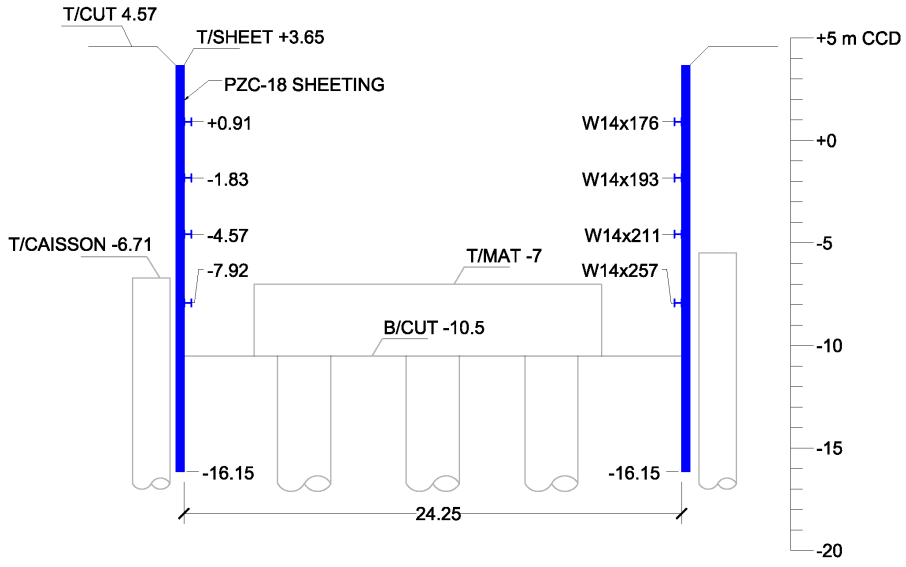

Figure 4.14: Cross section of temporary cofferdam

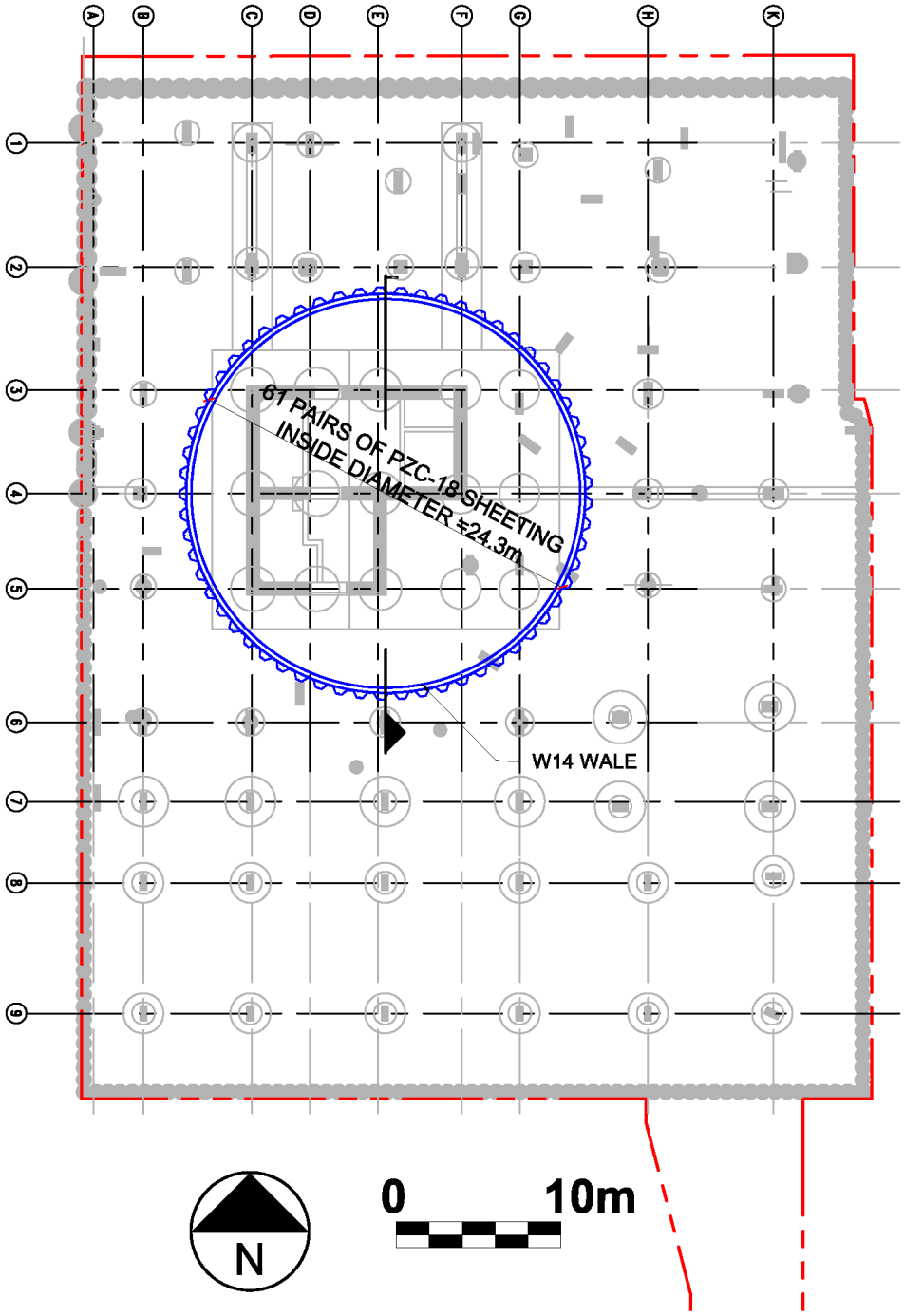

Figure 4.15: Plan view of temporary cofferdam

4.5.6. Top-down Construction

The basement structure at OMPW, with the exception of the building core, was excavated and built using the top-down construction method. In top-down construction, the basement slabs are formed and poured on the existing subgrade. Figure 4.16 shows the reinforcing steel of a new slab being formed. The right side of the photograph shows the front face of the excavation.

Figure 4.16: Top-down construction

The excavation is performed beneath the structural slabs in a mining operation. Low clearance equipment is used to transport the spoil to the glory hole areas. Long reach excavators located outside the excavation removed the spoil through the glory holes. The excavation was advanced until the elevation of the next basement level was reached. A thin layer of lean concrete (mud mat) was poured to create a smooth surface, which served as a form to pour the concrete slabs. This process was repeated several times until the final basement level was completed. In general, the slabs were poured immediately after exposing the excavated subgrade. At the OMPW project, the excavation was performed following the direction of the parking ramps. After the excavation of each basement level, the sheet pile wall used for the construction of the cofferdam was cut and the basement slabs were connected to the core.

4.6. Construction Activities and Performance Monitoring Data

4.6.1. Instrumentation Program

Responses to the construction activities were monitored using strain gauges, survey points and inclinometers. Figure 4.17 shows the location of the available instrumentation.

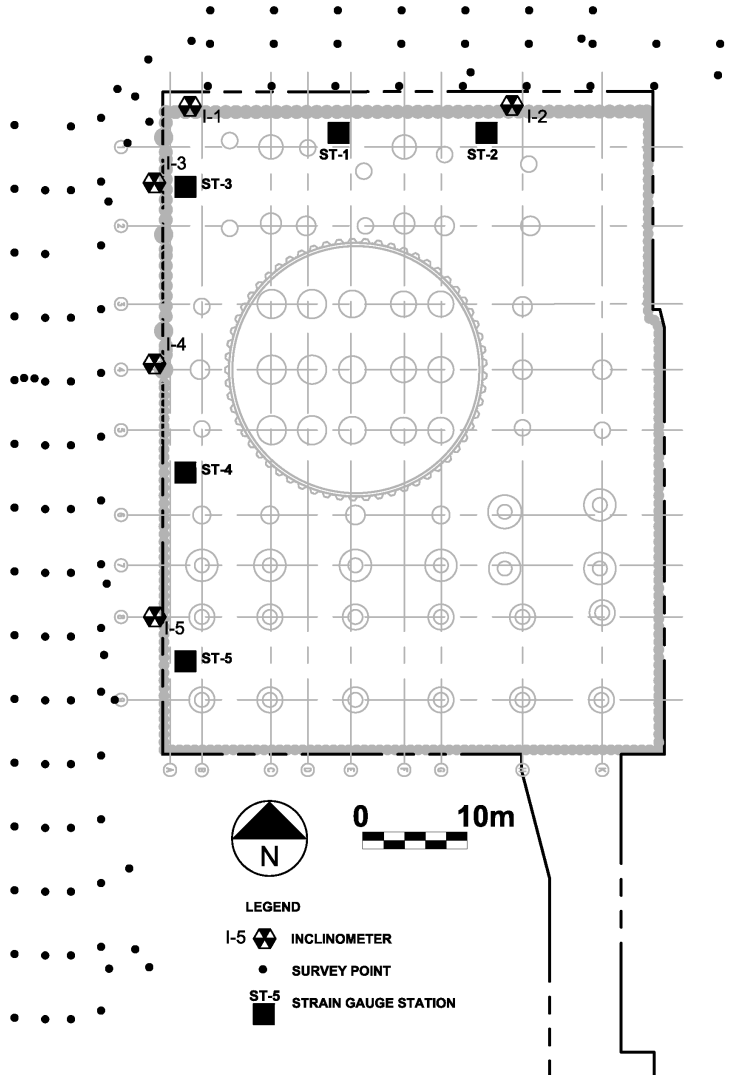

Figure 4.17: Instrumentation Location Diagram

The survey points are shown in Figure 4.17 and consisted of markings on the sidewalks and pavement that surrounded the project site. The survey points were established and monitored throughout the entire construction process.

The location of the five inclinometers is identified in Figure 4.17 as I-1 through I-5. The inclinometers were placed approximately 1m behind the wall and were extended from ground surface to elevation -22m CCD. The inclinometers also were installed at the beginning of construction. However, these inclinometers were damaged shortly after their installation during the installation of the secant pile walls. The inclinometers were replaced immediately before the commencement of the excavation of basement level B1 and before the placement of slab level B1. It should be noted that the naming convention adopted for this project assigned the same level name (e.g., B1) to the excavation level and the slab placed immediately below it. Therefore, for instance, slab level B1 is located below excavation level B1.

Four strain gauges were embedded in each of the slabs at the locations denoted as ST-1 through ST-5. The strain gauges were installed in pairs, side by side. Each pair of strain gauges consisted of one strain gauge located on the top and one strain gauge on the bottom rebar. Figure 4.18 shows the typical arrangement of the strain gauges in each monitoring section.

4.6.2. Sequence of Events

A chart summarizing the sequence of the construction activities is shown in Figure 4.19. For convenience, the abscissa in the figure is expressed in number of days – and not in dates. Day zero was arbitrarily assumed to be January 1, 2007.

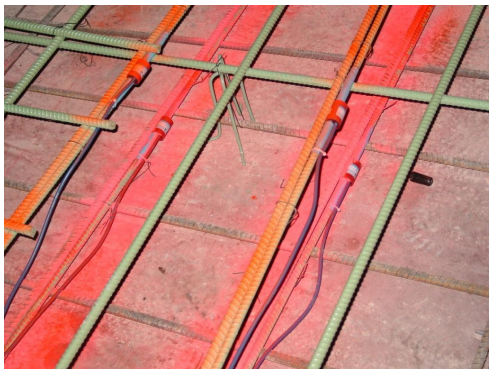

Figure 4.18: Strain gauges attached to basement slab reinforcing steel

As it can be in Figure 4.19, the construction activities at OMPW commenced on day 90 with the installation of the basement perimeter walls. Prior to performing any excavation, the secant pile walls and caissons were installed from existing ground surface (day 90 to 339). The secant pile walls construction started first. During the installation of the secant pile walls, repairs to the water main along Indiana avenue (day 203 to 214) were performed. These repairs included replacing a portion of water pipe. When approximately 68 % of the secant pile walls had been installed, the straight and belled caissons construction started on day 243.

The completion of the deep foundation system was followed by the construction of the building core using bottom up methods. The central core was excavated using a circular cofferdam, consisting of a sheet-pile wall and horizontal ring beams for internal bracing. Prior to the installation of the sheetpile wall, the urban fill was potholed along the sheetpile wall driving line using a backhoe (day 339 to 360). After potholing, the sheetpile walls were driven in place (day 360 to 382). After driving the sheeting, the excavation inside the cofferdam was performed (day 382 to 432). The excavation inside the cofferdam was

extended to the elevation of the bottom of the mat under the core. After completing the cofferdam excavation, the mat, and building core was formed and poured (day 452 to 529).

After the construction of the building core was finished, the construction of the remainder of the parking structure was performed. This process started with the excavation of the site grade to the elevation of basement level B1 day (529 to 626). Day 529 can be considered as the starting day of the main excavation. During the excavation of basement level B1, floor level F1 (above grade) was formed and poured (540 to 579).

After the completion of the excavation of basement level B1, the B1 slab was cast on the existing grade (day 626 to 641), connecting the perimeter secant pile walls and the central core of the building. The remainder of the basements was constructed using top-down methods. The top-down construction of the remaining portions of the basements was performed from day 626 to 1019. The small openings in the slabs (glory holes) that were utilized to remove the excavated materials through a mining operation were closed at the end from day 1032 to 1046.

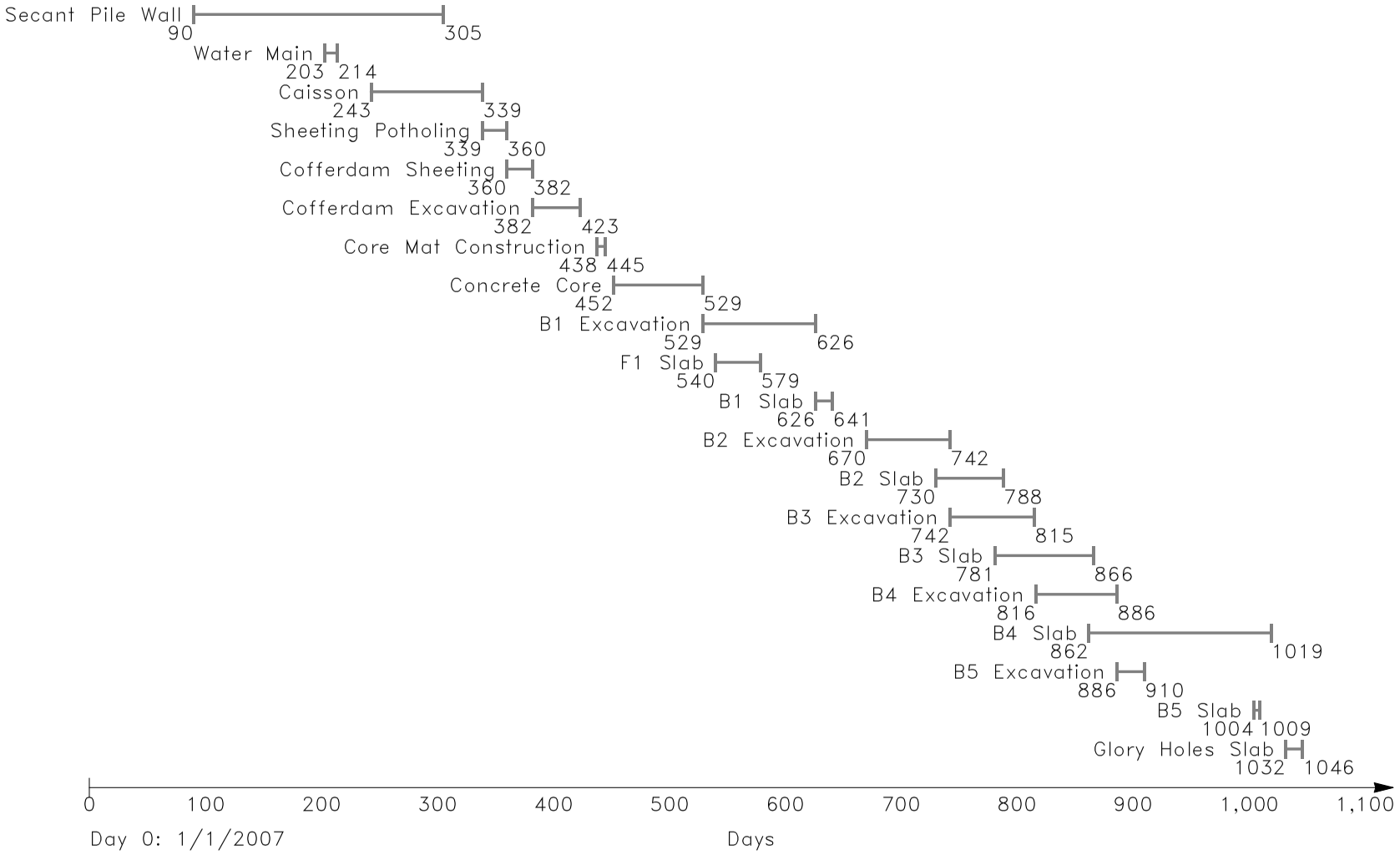

Figure 4.19: Top-down construction sequence

Special attention was given to Section No. 2, as this section is used as the basis to evaluate the numerical methods proposed in this work. Whereas Figure 4.19 describes the general sequence of events at the site, Table 4.6 lists the days when the excavation was performed and the slab were installed directly along Section No. 2.

Activity	Day Start	Day Finish
Excavation of level B1	529	536
Installation of Slab F1	549	579
Installation of Slab B1	641	648
Excavation of level B2	730	732
Installation of Slab B2	739	746
Excavation of level B3	780	787
Installation of Slab B3	813	820
Excavation of level B4	858	876
Installation of Slab B4	884	891
Excavation of level B5	893	897
Installation of Slab B5	1004	1011

Table 4.6: Construction activities at Section No. 2

Figure 4.20 shows the construction events along Section No. 2, listed in Table 4.6, in relation to the construction events of the whole construction site.

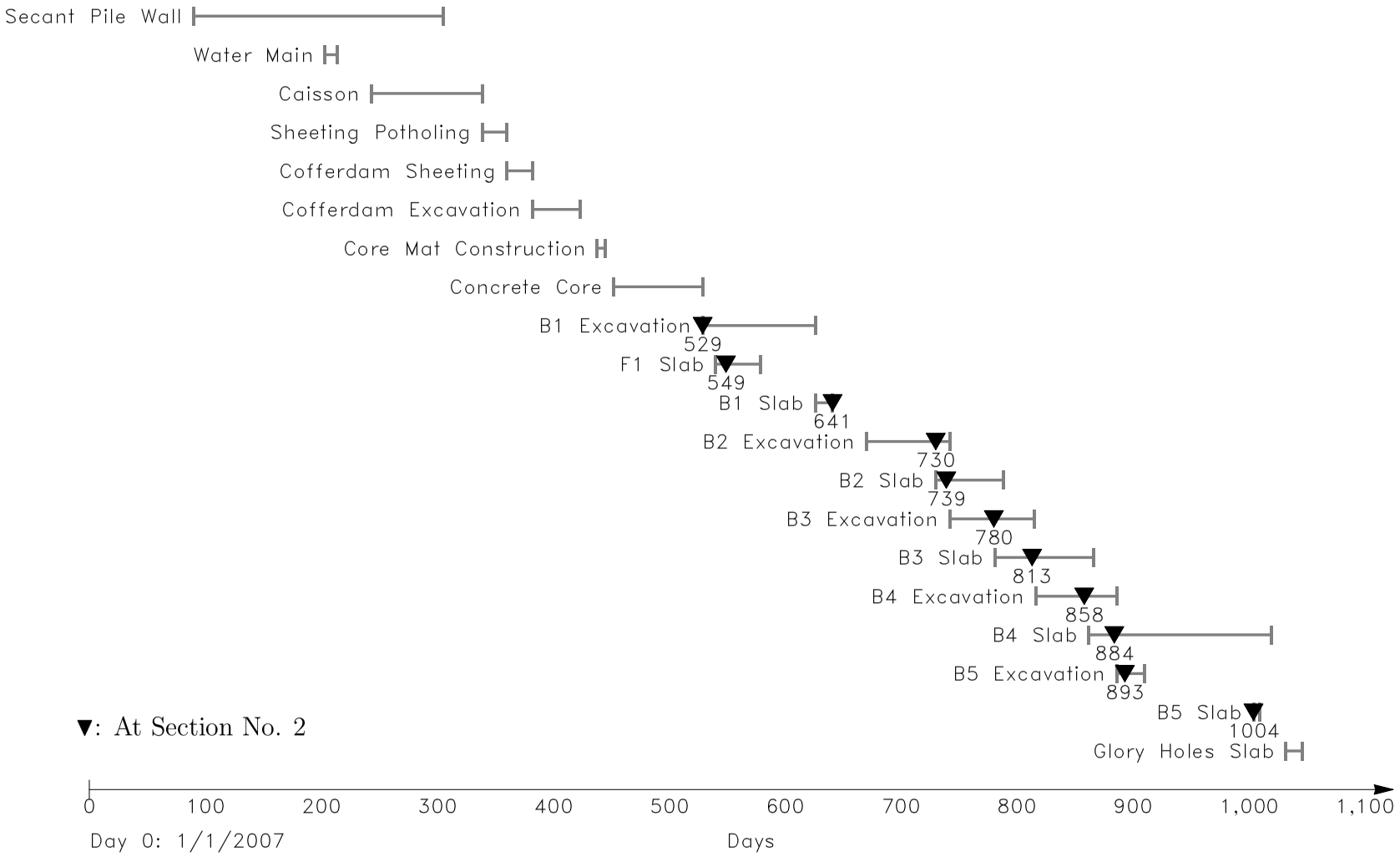

Figure 4.20: Top-down construction sequence (Events at Station No. 2)

4.6.3. Performance

The performance of the retention system was analyzed in terms of the magnitude of the observed vertical and horizontal movements and their relation to the different construction activities.

The vertical movements recorded at the survey point locations were utilized to create settlement contour maps at dates when important construction activities were completed. These contour maps are displayed as Figures 4.21 through 4.32.

Figure 4.21 shows the measured settlements before beginning the installation of the deep foundations (day 243). At this point, the installation of 92 % (47 of 51 piles), 94 % (60 of 64 piles), 87 % (78 of 90 piles) and 100 % (85 of 85 piles) of the secant piles along the north, south, west and east walls had been installed, respectively. 14 of the 20 secant piles to be installed were located in the northwest corner of the site, in an area bounded by column line B and column line 4. Consequently, all the recorded settlement measured along the north perimeter of the site, and the west perimeter (south of column line 4) can be assumed to capture the secant pile installation effects.

The maximum measured settlements along the north perimeter is approximately equal to 1.5 cm and it is equal to the average wall installation ground movements reported by Clough and O'Rourke [1990] (i.e., 0.075% of the trench depth). This is slightly unexpected, since the installation effects data presented by Clough and O'Rourke [1990] is based on slurry walls. One could argue that when comparing the installation effects caused by a secant pile wall to those of a slurry wall, the ground movements caused by the installation of a secant pile wall should be smaller, since the installation of secant piles use a steel liner and have a much smaller excavated area at any given time. However, the optical

survey data does support this perception, and shows that installation effect of secant pile and slurry walls could be similar in certain cases.

The maximum measured settlement registered along the west wall, south of column line 4, on day 243 is approximately 4cm. This amount of movement appears to be large when compared to the movements observed along the north wall (i.e., 1.5cm); however, it should be noted, as displayed in the construction schedule shown in Figure 4.19 that the water main located along Indiana Avenue was repaired between day 203 and 214. This repair consisted of excavating a trench to replace a section of the water pipe. The incremental movement that occurred exclusively during the duration of the water main repairs was extracted and is shown in Figure 4.22. It can be seen that the water main repairs are partly responsible for 2cm of the 4cm of the total recorded movement. In addition, construction problems were reported during the installation of the secant piles along the southern portion of the site. Namely, water infiltration into the pile was observed during the pile excavation. This water infiltration occurred because a saturated sand layer near the bottom of the piles was penetrated during the pile installation. It is interesting to note that if the movements caused by the water main repairs are subtracted from the total 4cm of movements registered along the south portion of the west wall, the installation induced movements along the west wall become similar to the ones observed along the north wall.

Figure 4.23 shows that the settlement after completing the installation of the deep foundations and perimeter secant pile wall (day 339). Considering that the installation of the secant pile wall was almost complete on day 243, the deep foundations installation effects can be estimated by subtracting the ground movements recorded on day 243 from the

ones recorded on day 339. These deep foundations installation effects are displayed in Figure 4.24. The installation of deep foundations caused an additional 1.5 to 3.5cm of movement along the north wall and 1.5 to 3cm of movement along the west wall (south of column line 4). The ground movements along the west wall, north of column line 3, show a maximum movement of 4.5cm; however, these movements include the combined effect of the installation of the deep foundations and perimeter walls. The larger movements, caused by the foundation construction, recorded along the north wall when compared to the ones along the west wall are expected; and they are likely driven by the larger concentration of deep foundations toward the north end of the project site and the higher stability number in the softer clays due to the surcharge imposed by Roosevelt Road.

Figure 4.25 shows the total settlements after the installation and excavation of the cofferdam (day 423). In a similar manner, the ground movements caused by the excavation of the cofferdam are isolated by subtracting the ground movement recorded in days 382 from the ones on 423, as they mark the beginning and end of the excavation of the cofferdam. The cofferdam excavation effects are displayed in Figure 4.26. The excavation of the cofferdam caused an additional 1.5cm of movement along the west wall and negligible movement along the north wall. Larger ground movements along the west wall are expected as they are closer to the cofferdam.

Figure 4.27 shows the total settlements immediately before the commencement of the main excavation. It is interesting to note that more than 10 and 6cm of movement along the west and north walls, respectively, occurred before the main excavation even started. Figure 4.28, 4.29, 4.30, 4.31 and 4.32 shows settlements after the excavation and installation of the basements slabs B1, B2, B3, B5 and B4, respectively. These figures show

that the maximum total settlement along the west and north perimeter of the site was approximately, 14cm and 10cm, respectively. However, only 6cm and 8cm of settlement (along the west and north perimeter of the site) are attributed to main excavation. The difference is attributed to other construction activities, performed prior to the excavation.

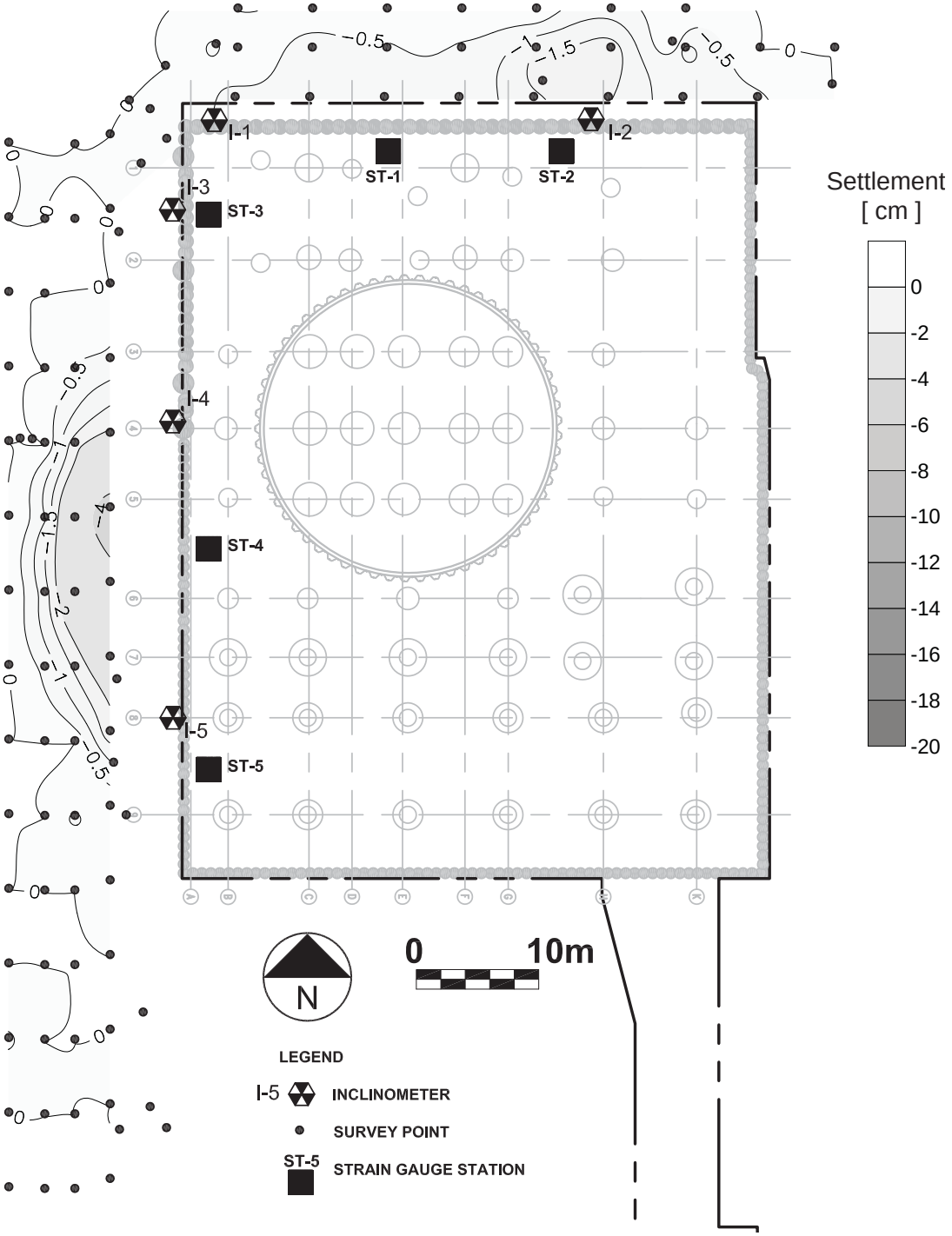

Figure 4.21: Settlement before the beginning of the installation of the deep foundation (day 243)

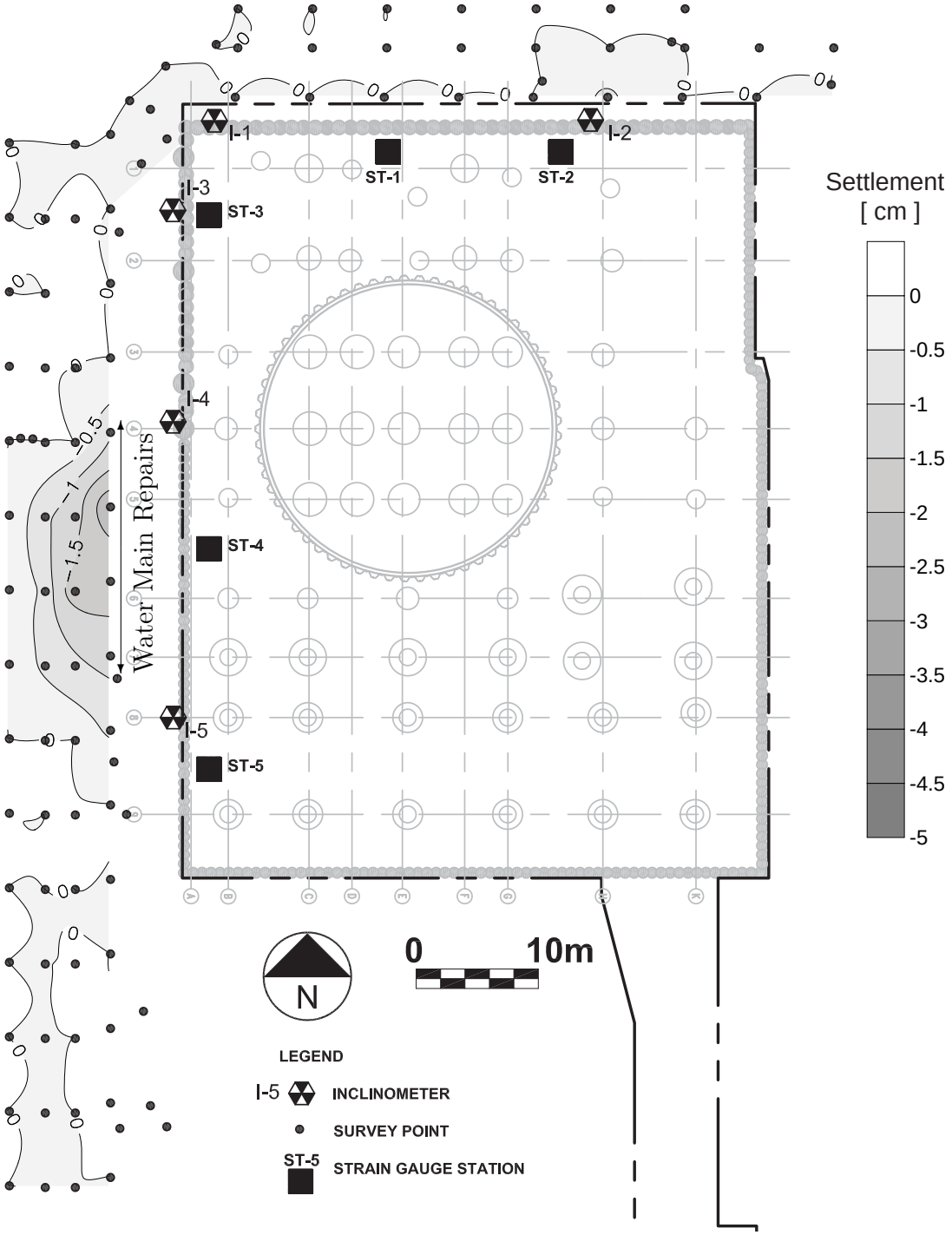

Figure 4.22: Settlements during the water main repairs (day 200 to 214)

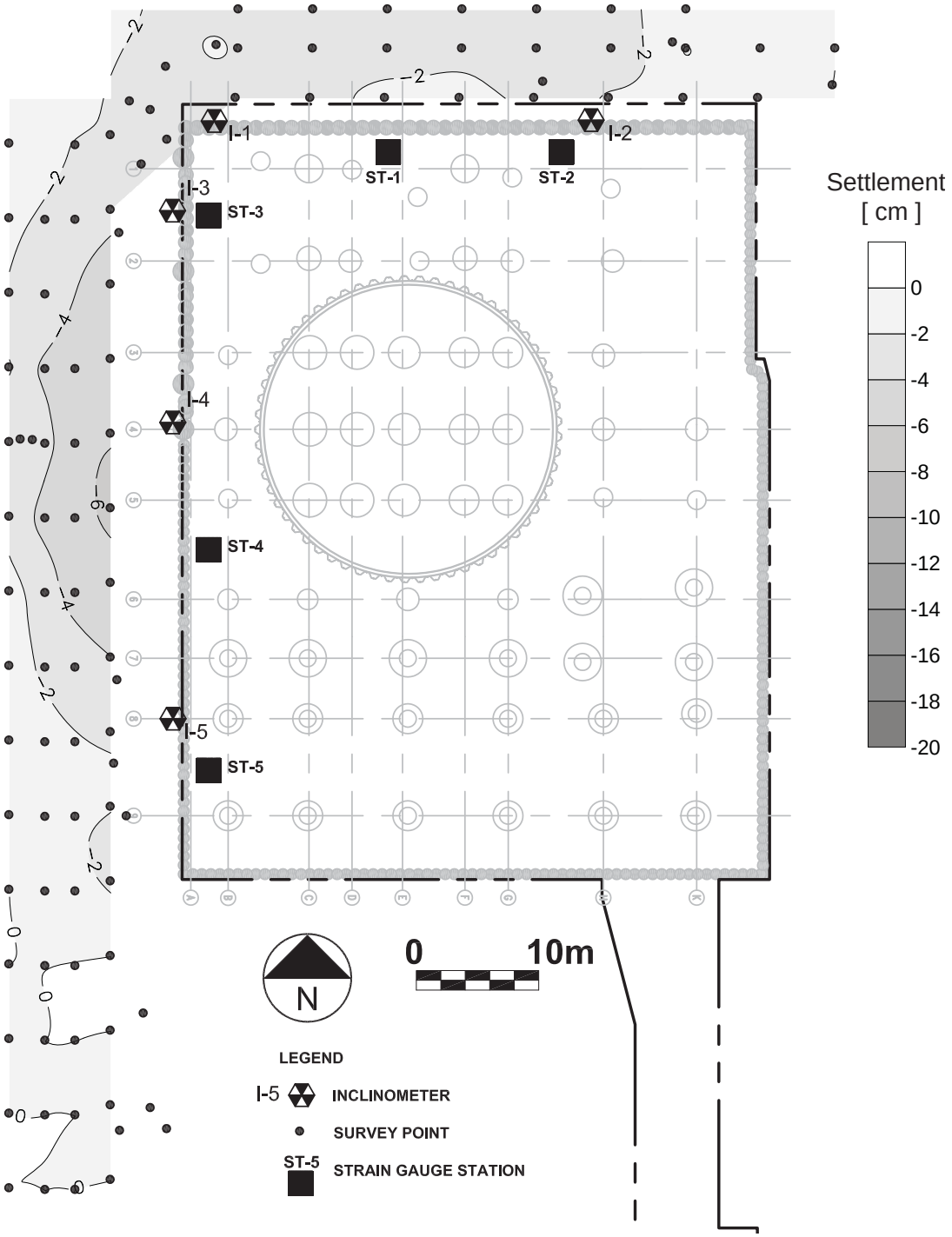

Figure 4.23: Settlement after the installation of perimeter walls and foundations (day 340)

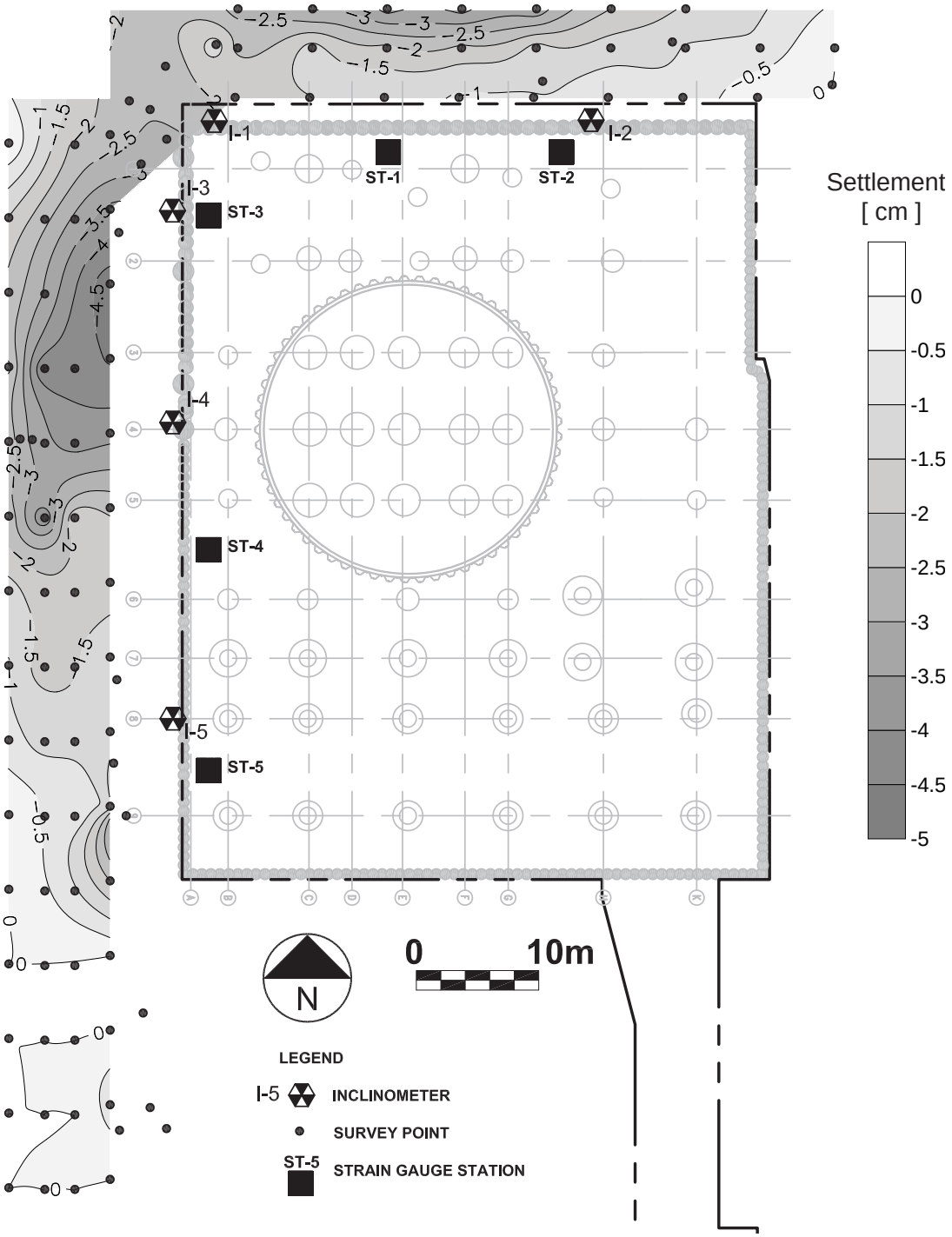

Figure 4.24: Settlements during the installation of deep foundations (day 243 to 340)

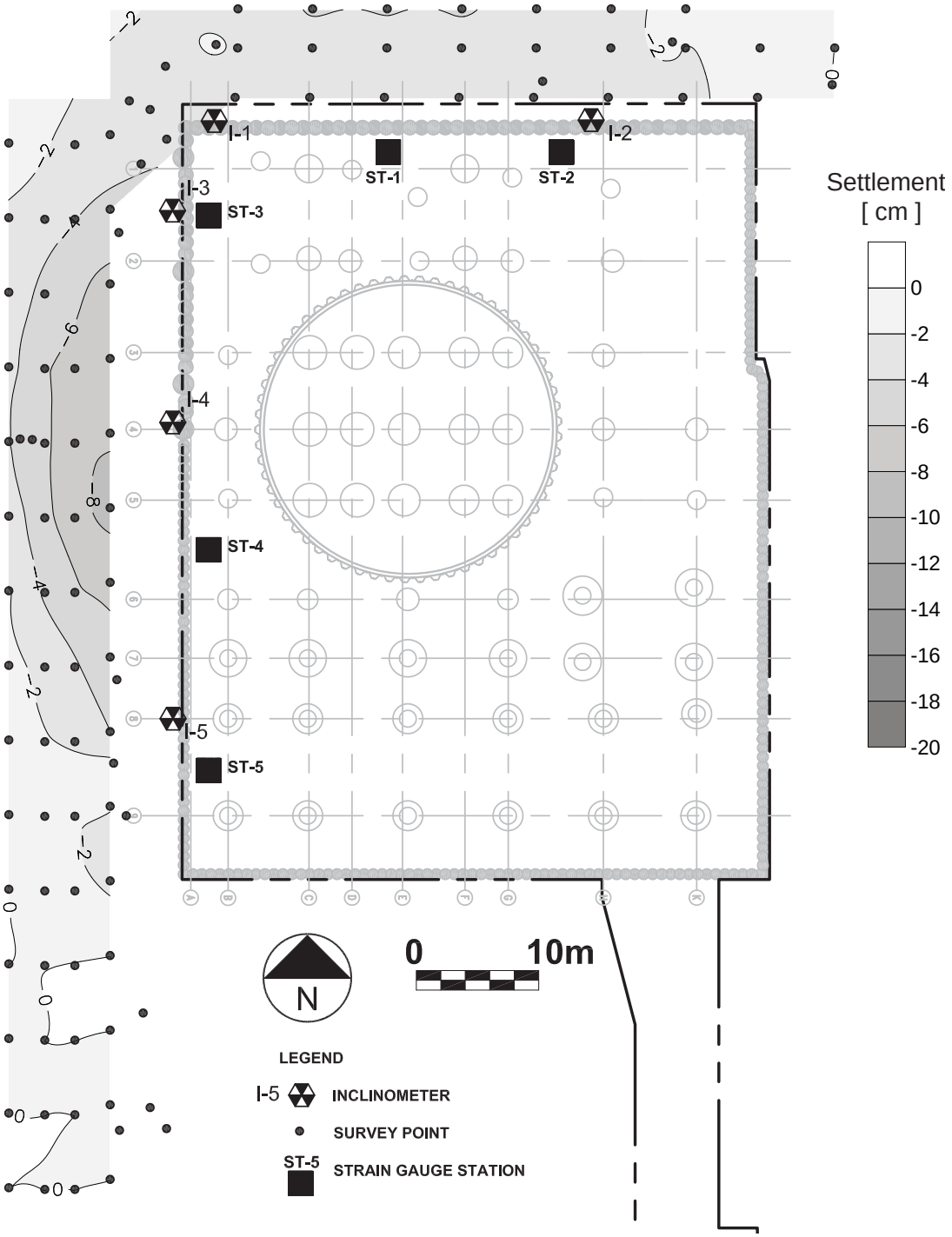

Figure 4.25: Settlement after the excavation of the cofferdam (day 424)

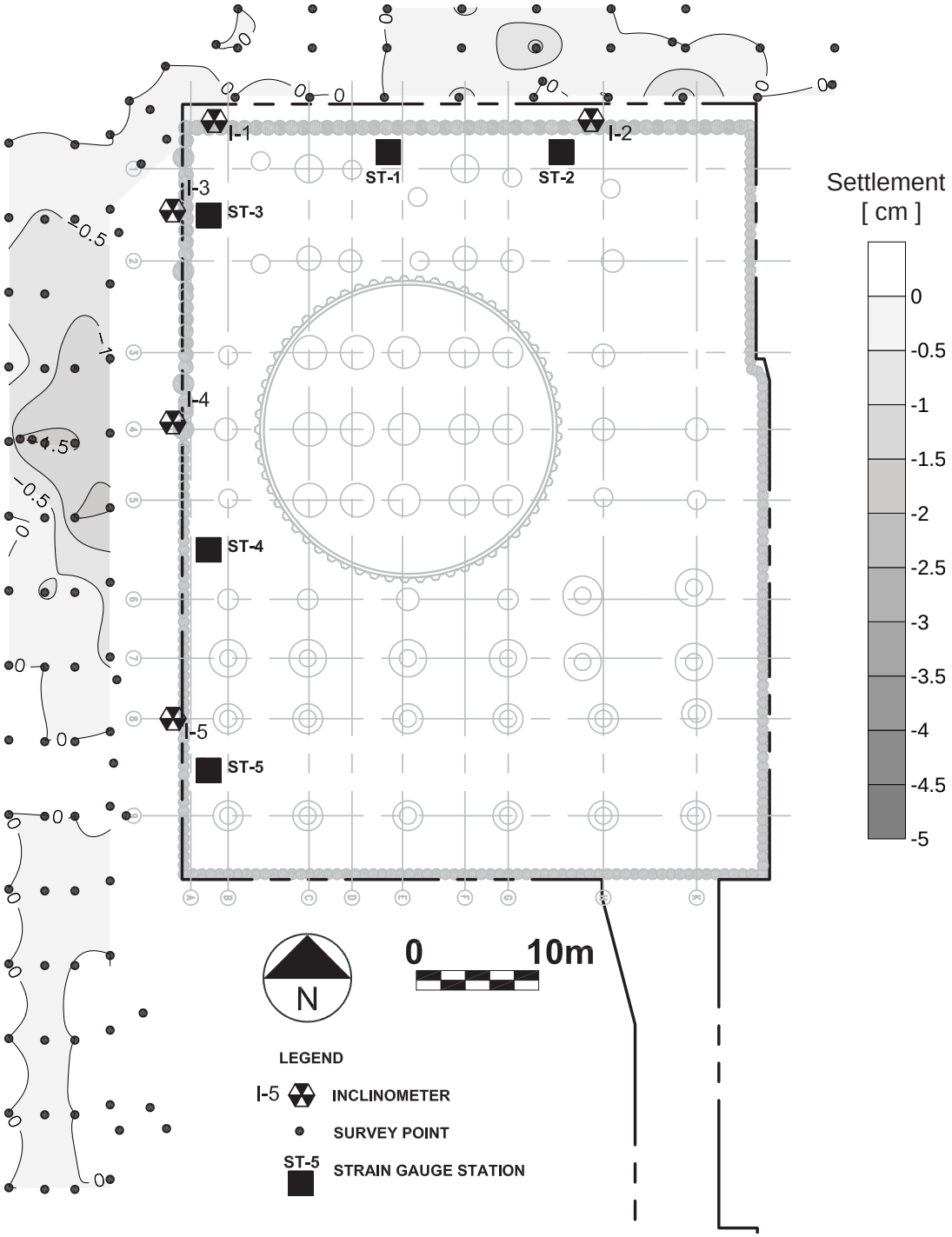

Figure 4.26: Settlements during the excavation of the cofferdam (day 382 to 423)

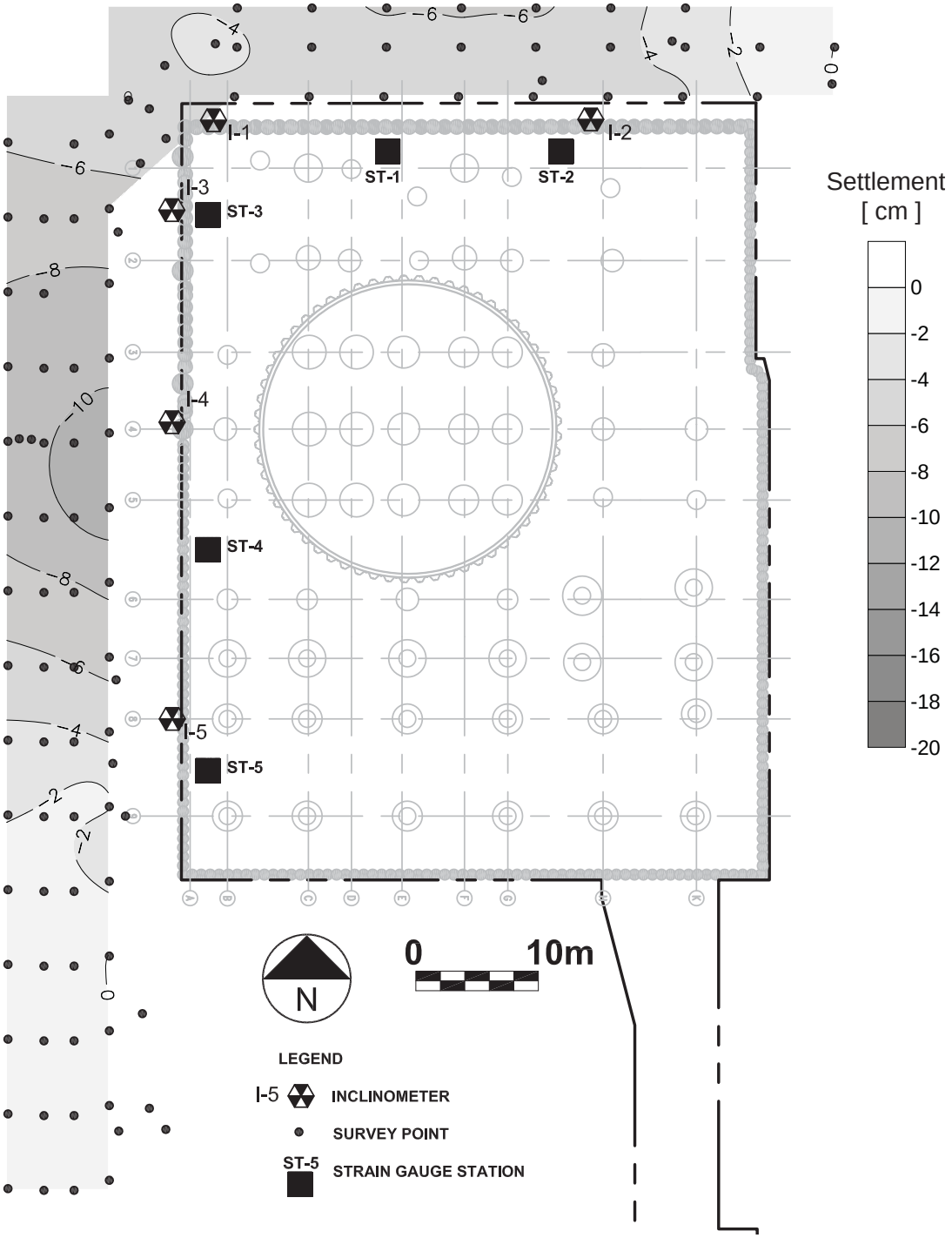

Figure 4.27: Settlement before the beginning of the main excavation (day 529)

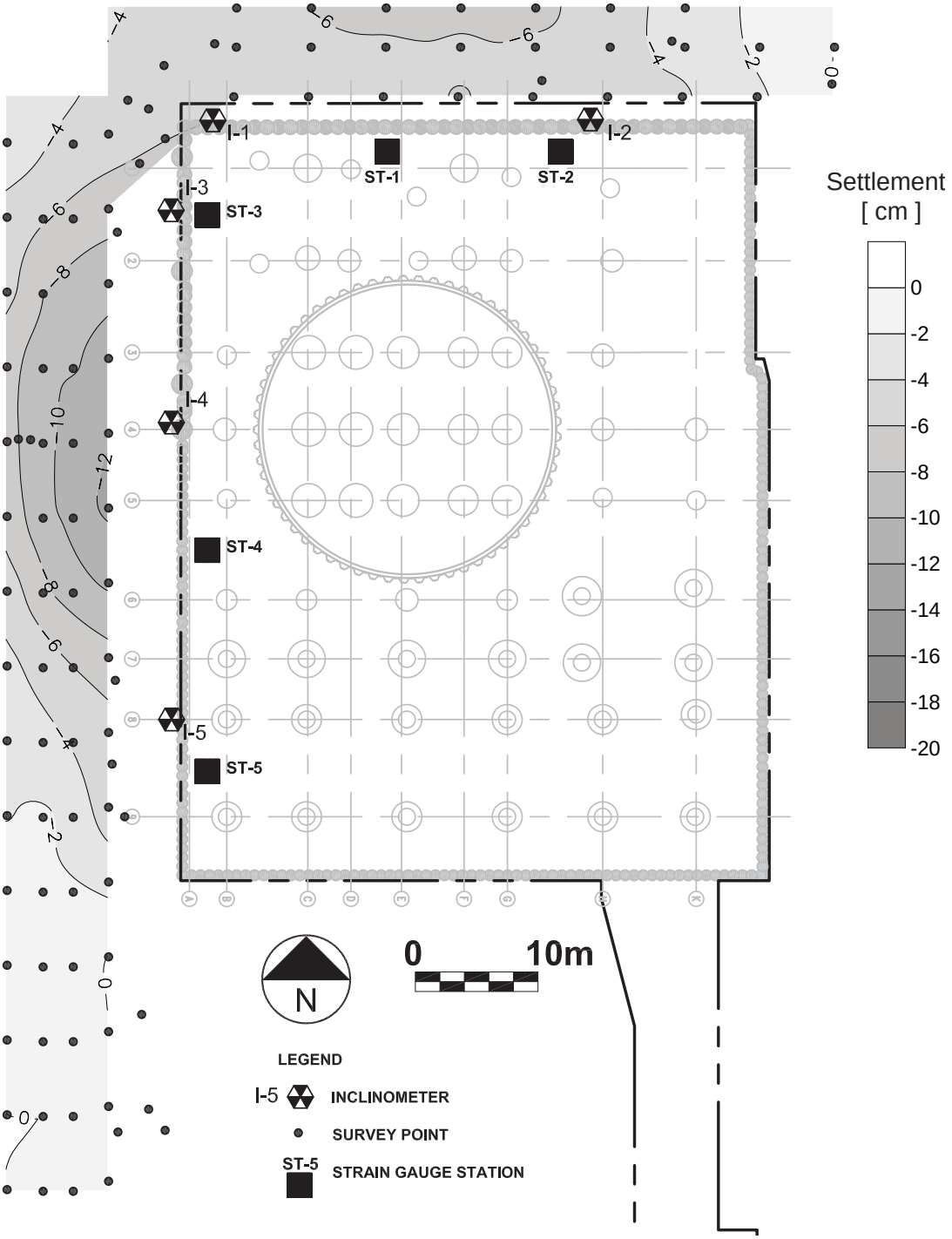

Figure 4.28: Settlement after the installation of basement slab B1 (day 641)

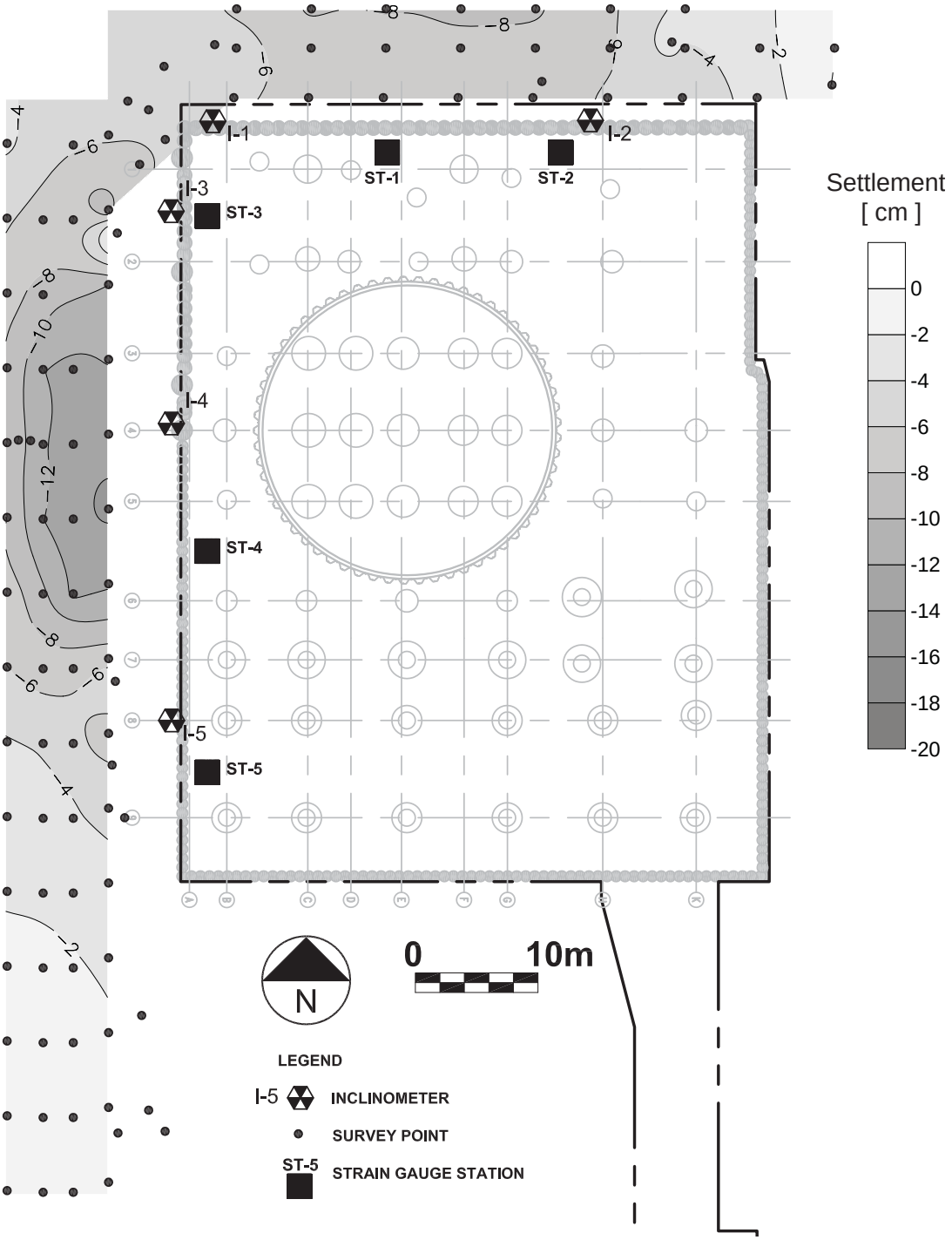

Figure 4.29: Settlement after the installation of basement slab B2 (day 788)

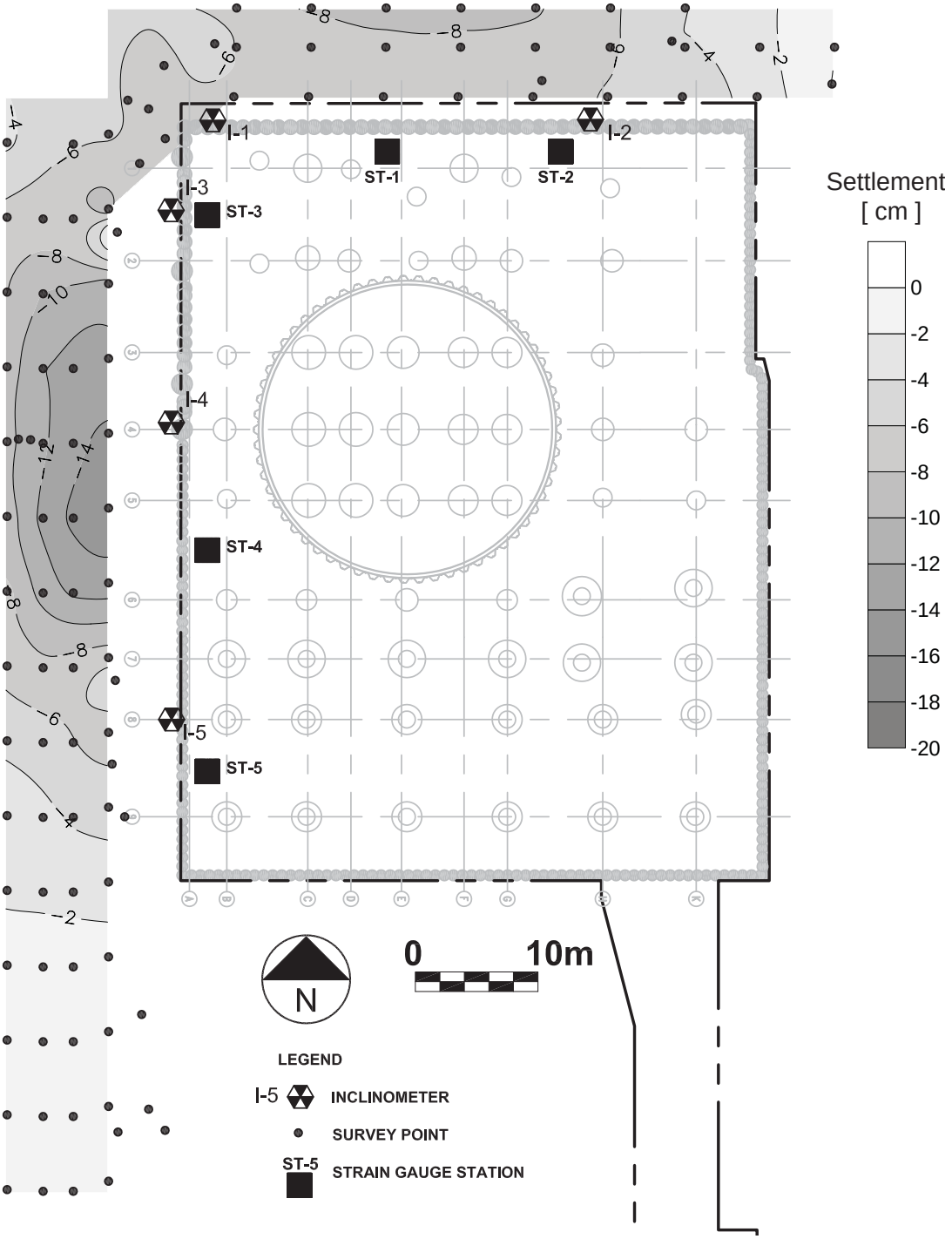

Figure 4.30: Settlement after the installation of basement slab B3 (day 816)

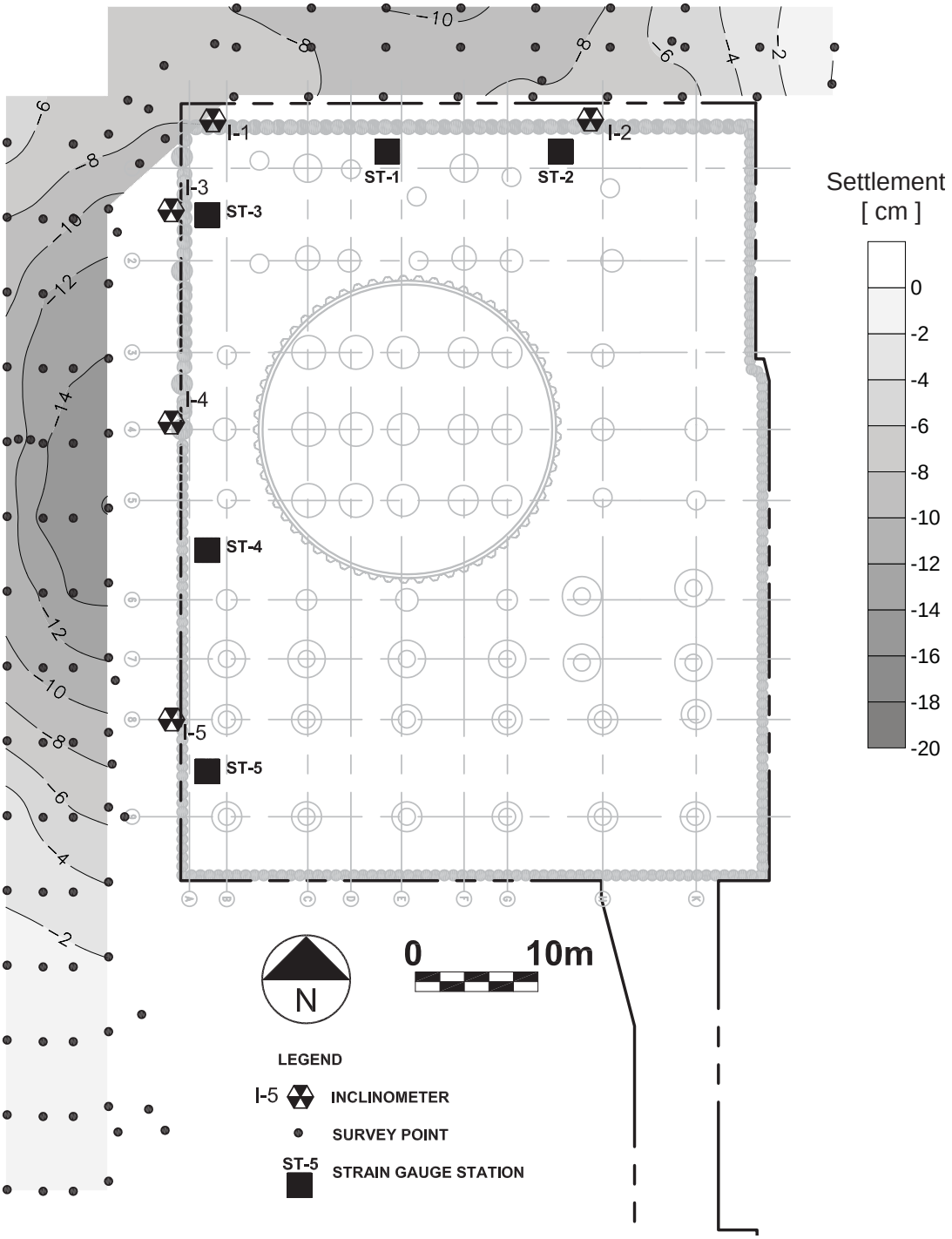

Figure 4.31: Settlement after the installation of basement slab B5 (day 1012)

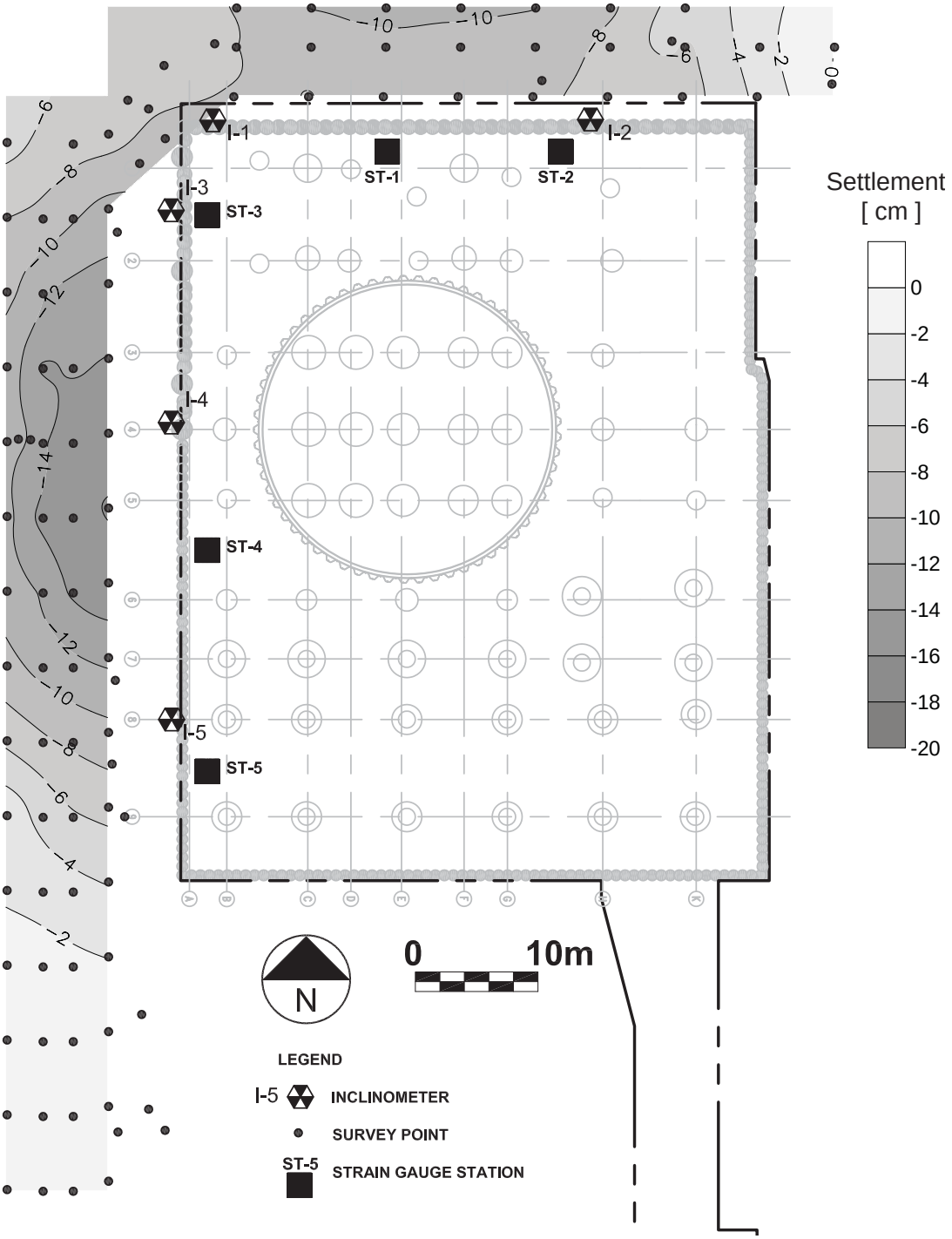

Figure 4.32: Settlement after the installation of basement slab B4 (day 1019)

Special attention is given to Section No. 2 along the north wall. As it was discussed before, the distance between the cofferdam and the north wall, and in particular, the distance from the cofferdam to Section No. 2 was sufficient to prevent significant settlements along the north perimeter of the site during the excavation of the cofferdam, this can be seen in Figure 4.26. Consequently, if Section No. 2 is analyzed, it could be argued that the performance of the north secant pile wall along Section No. 2 was not greatly influenced by the presence of the cofferdam.

Inclinometer data was also used to monitor the performance of the construction activities. Unfortunately, continuous inclinometer records (horizontal ground movement) only exist from the beginning of the mass basement excavation (day 529).

Figure 4.33 shows the horizontal ground movement from the day the main excavation started (day 529). In addition, this figure also shows the increment in vertical movements from the survey point data from day 529. The two closest pairs of survey points (located east and west of Station No 2) were used to represent the settlement in this section. If the magnitude of the horizontal movements caused by the main excavation is compared to magnitude of the incremental settlements, for every state, this agrees with observation made by Clough and O'Rourke [1990] who reports a ratio of horizontal to vertical ground movement from 0.75 to 1.

The maximum recorded horizontal movement was approximately 3cm. This corresponds to approximately $0.3\%H$, if H (excavation depth) is measured from the site grade and $0.2\%H$, if H is measured from the top of Roosevelt Road. This range shows a performance similar to the slurry wall cases reported by Clough et al. [1989]. Clough et al. [1989] reports a typical range of $0.1\%H$ to $0.25\%H$. If ancillary ground movements are considered the

range will vary from $0.65\%H$ to $0.9\%H$, depending upon the selection of H. This range agrees with the data presented as Case 2b by Long [2001]. The database presented by Long [2001] included ancillary data. In particular, Long's Case 2b corresponds to stiff retention systems with a high factor of safety against basal heave and the transition from soft to hard clays located above the dredge level. The data for Case 2b showed a maximum typical ratio of $1.5\%H$ and average value of $0.75\%H$.

In addition to the inclinometer records, the strain gauge data was also used to compute displacements. The installed inclinometers were only read until day 1123, approximately 77 days after the completion of the excavation; however, the strain gauge data records extend more than one year after the completion of the construction. The recorded strains collected from the strain gauges in Section No.2 are displayed in Figure 4.34. The strains, presented in Figure 4.34 were computed from the raw data as recommended by the manufacturer (Geokon [2010]), to compensate for the difference between thermal expansion of steel (strain gauges) and concrete (slab), following the equation below:

$$\epsilon_{actual} = (R1 - R0) * C + (T1 - T0) * K_{steel} \tag{4.2}$$

Where ϵ_{actual} corresponds to the computed strain, $R1$ and $R0$ correspond to the current and raw initial strain measurement, C is a calibration factor, $T1$ and $T0$ correspond to the current and initial measured temperature, respectively, and K_{steel} corresponds to the coefficient of thermal expansion of steel (assumed to be $12.2 ppm/C$). The strains shown in Figure 4.34 capture the deformation caused by changes in temperature, concrete creep and shrinkage and the direct application of load.

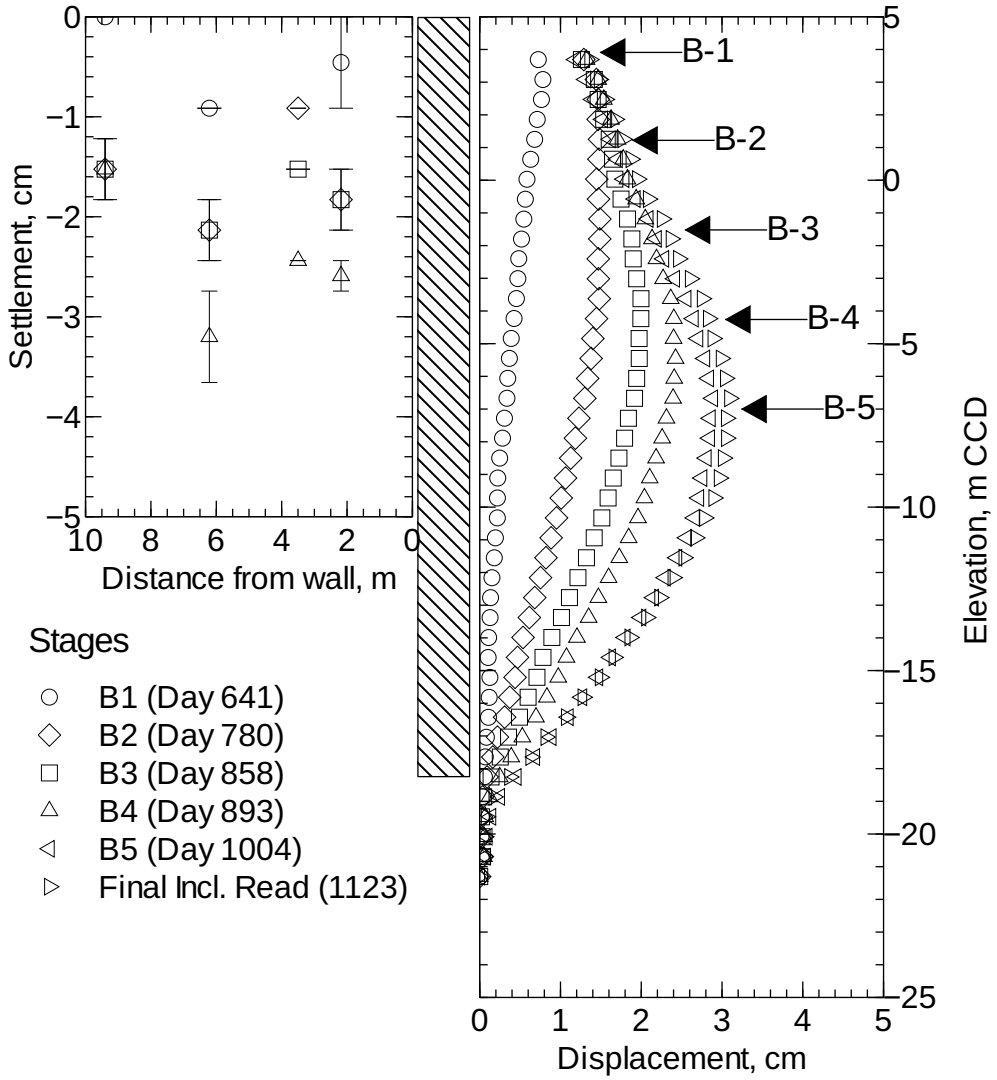

Figure 4.33: Increment in horizontal movements and settlement at Section No. 2 from the beginning of the main excavation (day 529)

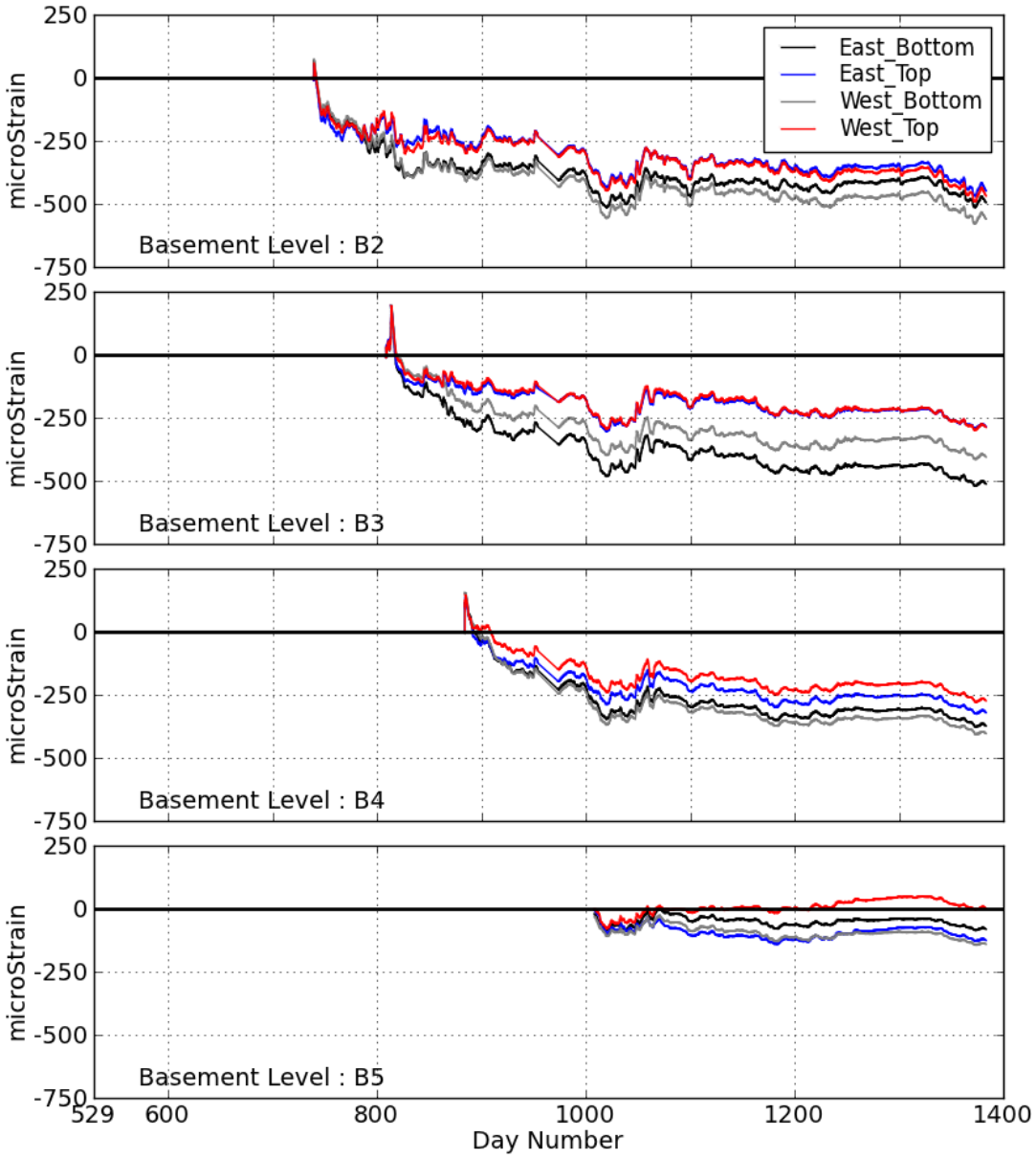

Figure 4.34: Strain gauge data collected in Section No. 2

If it is assumed that the recorded strains are constant along the slabs, the computed strains can be converted into slab deformations by multiplying the recorded strains by an effective slab length. The determination of this effective slab length is not straightforward, as it depends on the way in which the loads across the slabs are transferred to columns, the concrete core and the perimeter walls. After a trial and error process, it was determined that the effective length that provides the best agreement between the computed deformation using strain gauges and slab displacements using the inclinometer data is approximately 18m. The computed displacements using strain gauge data (assuming an effective slab length of 18m) is plotted alongside the slab displacement measured using inclinometers in Figure 4.35. It should be noted that the distance (in the north-south direction) from the north perimeter walls to the concrete core is 17.98m. Hence, this coincidence suggests that concrete core acts like a rigid support along to the southern end of the slabs in the vicinity of Section No. 2.

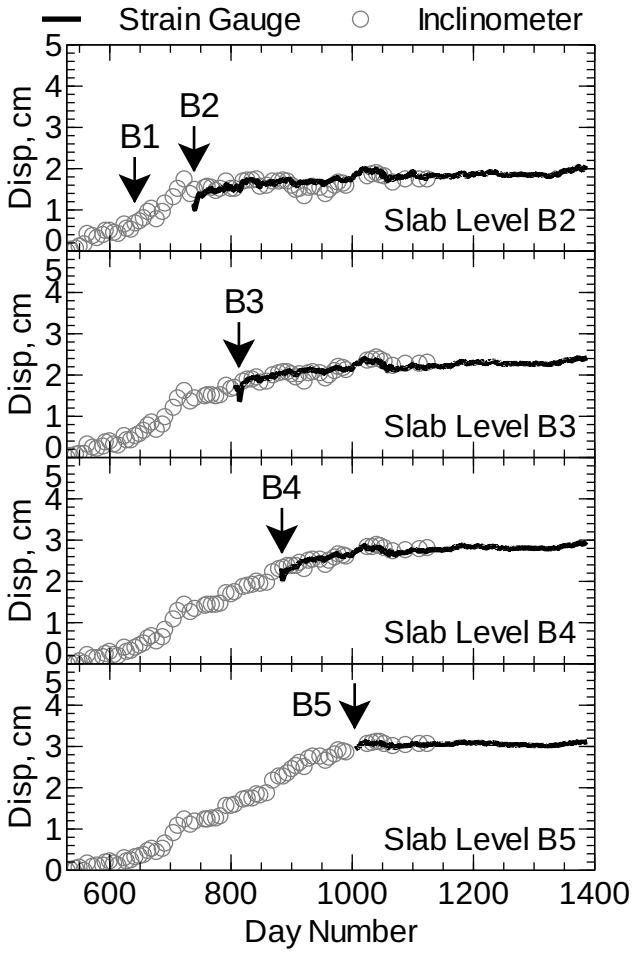

Figure 4.35: Horizontal Movements at the slab levels along Section No. 2

4.7. Summary

The soil and ground water conditions at the OMPW project site were presented in this chapter. The construction activities and the collected performance monitoring data were also presented and discussed.

The soil conditions at the OMPW site consist of a surficial granular fill underlain by layers of glacial tills. The glacial tills show an increasing degree of overconsolidation with depth. The ground water conditions correspond to the ones of steady state downward seepage. These conditions are primarily driven by the continuous pumping of the deep Chicago tunnels.

The construction at the OMPW project site consisted of a 5-level basement structure adjacent to an approach embankment (Roosevelt Road). The construction of the basement structure, with exception of the central core area, was performed using top down methods. This means that the perimeter and deep foundations were built first. After the installation of these vertical elements, the first slab was poured at the existing subgrade level. The excavation of the first basement level was performed underneath the newly placed slab in a mining operation. Once the excavation reached the next basement level, a new slab was poured to provide additional support to the perimeter wall. This process was repeated multiple times until the final basement level was built. The central core was built using a circular sheet pile wall cofferdam following bottom-up construction methods. The concrete core was built before the main excavation started.

The performance monitoring instrumentation consisted of optical survey points, inclinometers and strain gauges installed in the slabs. The survey points provided a complete record of ground movements from the beginning to the end of the construction. This data

allowed one to clearly identify the effect of each of the construction activities, specifically the effects of installing the perimeter wall, the deep foundations, and the excavation of the central cofferdam and the installation of each floor slab. Inclinometer and stain gauge data were available to monitor the effects of the construction activities only during the main excavation.

The observed performance at OMPW agrees with the performance data presented in the literature for similar structures and soil conditions. Specifically, the computed normalized ground movements, equal to $0.65\%H$ to $0.9\%H$, if the ancillary movements are considered, and equal to $0.2\%H$ to $0.3\%H$, if no ancillary movements are considered, agree with the ranges reported in the literature. In addition, observed performance at the OMPW site also supports the observation made by Long [2001] that indicates that there is not a clear improvement on the performance top-down constructions when compared to the performance of propped or braced excavations. If the movements arising from the ancillary construction activities could be prevented, then the benefits of the very stiff support system would be realized and the total ground movements arising from the excavation process would be relatively small.

CHAPTER 5

HC Model Calibration Using Triaxial Test Data

5.1. Introduction

Previous attempts using optimization techniques have been successful matching the response of one or few pieces of data or observations. Specifically, optimization techniques have been used to match laboratory test results or the field performance collected during one or some stages of construction (e.g., Calvello [2002]). However, these same studies have failed to predict both laboratory and performance monitoring data with the same set of constitutive model parameters.

Reasons for the inability to predict all observations is unclear and several hypotheses can be made. It is possible that the discrepancy could be attributed to the disturbance of the soil samples used for laboratory testing. It is also possible that the constitutive soil model selected for optimization is incapable of accurately predicting multiple complex stress paths (measured in the field and in the laboratory) with a single set of parameters. If the latter is true, the optimized parameters would only be valid for predicting the response of the soil subjected to stress paths similar to those used as the target for optimization. This, of course, depends on the capabilities of the constitutive model, as well as the optimization methodology.

In this research, it is hypothesized that if high quality laboratory tests data are utilized in conjunction with an advanced soil model capable of capturing the complex soil behavior observed in the field and laboratory environment, it may be possible to predict field and laboratory performance with a single set of parameters. The framework proposed in this research differs from previous attempts in that the laboratory testing results will not be ignored to favor a better match of the field observations. Laboratory experiments used

in this thesis primarily were conducted on specimens cut from block samples taken from excavation in the Chicago area.

This research is focused on predicting the performance of excavations. In order to increase the likelihood of succeeding at capturing the soil response, in the broad scale proposed in this research, one must understand the key aspects of soil behavior that control the performance of excavations. Such aspects should be carefully considered when selecting the candidate constitutive soil model for the finite element simulations.

To increase the likelihood of accurately predicting the performance of the proposed construction from early stages of the optimization process — where only laboratory tests are available — information captured by the selected laboratory tests and employed in the optimization routines, should be relevant and sufficient to properly calibrate the selected soil model.

Key aspects of soil behavior that control the performance of excavations through clays are discussed in this following section.

5.1.1. Change in Stress Level and Overconsolidation Ratio

During an excavation, stresses are relieved in the resisting soil next to the toe of the retaining wall. In particular for excavations that require long periods of time, such as in a top down construction, such stress relief translates into large changes in density and overconsolidation ratio (OCR) after the excess pore water pressures dissipate. Consequently, to properly predict soil deformations under such conditions one must select a constitutive soil model for clays that is capable of predicting changes in stiffness resulting from changes

in stress, density and OCR. This condition rules out the potential use of any constitutive model that is not based on critical state soil mechanics.

5.1.2. Small Strain Non Linearity Effects

Understanding small strain behavior is a key element to the successful design and the accurate prediction of soil deformations under working conditions (Burland [1989]). There is sufficient evidence to show the importance of including the soil response at small strains in finite element predictions. This evidence suggests that incorporating small strain stiffness allows accurate prediction of the distribution of ground movements behind the retaining wall (e.g., Hashash and Whittle [1993], Finno and Tu [2006]). Accurate prediction of the ground surface settlement profile is necessary to predict the potential distress of adjacent structures and utilities during an excavation (e.g., Boone [1996]; Son and Cording [2011]; Finno et al. [2005]).

Many cases reported in literature, where the small-strain non-linearity is not properly accounted, show good agreement between the computed and observed wall movements. However, results from the same computations do not accurately reflect the distribution of settlements. Factors that explain this disagreement between the observations and model predictions include that the settlement measurements collected at ground surface are influenced by volume changes of surficial soils caused by seasonal drying and wetting cycles, seasonal temperature changes, presence of surficial uncontrolled granular fills, presence of slabs, pavements or underground structures and dilation of surficial granular soils. It

is difficult, if not impossible, to capture all these factors with numerical methods. However, in addition to all these factors, it is also possible that the disagreement may also be attributed to the inaccurate representation of the soil at small strain levels.

The study of ground surface settlement is often further hindered by the lack of good quality field data. This deficiency arises mainly because of the difficulty of obtaining and maintaining survey points in crowded urban areas. In this study, optical survey points extending approximately 10m behind the perimeter walls, as shown in Chapter 4, were established and monitored during the course of the project. Even though this limited number of observations is not sufficient to fully define the excavation-induced settlement profile, the available pool of observations will be used to benchmark the model predictions and draw pertinent conclusions.

The second possible effect of the small-strain non-linearity on the performance of an excavation includes the inward movement of the toe of a support wall in stiff support systems. Economic considerations promote the design of deeper and deeper basement structures to increase the effective use of space. In Chicago, and in cities with similar geology, this practice has resulted in the design of stiffer retaining walls that are "keyed" into stiffer soil deposits. In Chicago, this stiffer till layer has been at times (dangerously) accounted for as an almost rigid soil support that prevents movements of the toe of the retaining wall. Observations of ground movements collected with inclinometers that extend below the toe of the wall level, such as the ones performed during the OMPW project, suggests that ground movement of the toe of the wall — even if relatively small — are not negligible and play a key role in the overall performance of the retaining system. In this thesis, it is hypothesized that because the overall magnitude of movement of the toe

of the wall is relatively small, it is not possible to properly estimate the ground movements at these depths, unless the soil stiffness at small-strain levels is properly modelled.
In summary, the effects of small strain non-linearity may not only affect the ground surface settlements, but also the lateral wall movements at deeper depths.

5.1.3. Use of High Quality Data

There are many factors that influence the shear modulus and degradation of soil at very small and small strain levels. The most relevant factors are sample disturbance, current state and stress history, stress path directions and reversals, anisotropy and aging/creep. Sample disturbance is the greatest impediment to accurately measure the soil stiffness at small strain levels and it is also an important factor that makes it difficult to predict excavation performance using constitutive models calibrated to match laboratory data. Disturbance is caused by many factors, including but not limited to, borehole instability, reduction of effective stress, shear strains induced by tube penetration and sample extrusion and trimming (Hight [2001]). Disturbance causes a variety of different effects on soft soils, but typically, results in a flatter modulus degradation curve due to progressive destructuring and shrinkage of the yield surface (Clayton et al. [1992]). However, it is also possible for the modulus of a somewhat disturbed sample to increase after reconsolidation due to a significant reduction of the void ratio.
Since one of the objectives of this research is to determine if all collected data (soil testing and performance monitoring data) can be described by finite element simulations with a single set of parameters, it is crucial that disturbance effects be eliminated or greatly reduced. Therefore, for that purpose, this research uses the test results performed

on soft Chicago clays by Holman [2005], Cho [2007] and Kim [2011]. They performed triaxial and consolidation tests on specimens from high quality block samples obtained from excavations in the Chicago area. This research also uses tests results performed on specimens of the deeper and stiffer Chicago soil deposits extracted using a Pitcher sampler.

5.1.4. Dynamic Shear Modulus and Soil Anisotropy

The dynamic shear modulus, G_0, represents the initial shear modulus prior to any significant deformation; and consequently, it represents the maximum shear modulus before any shear stiffness degradation occurs.

The formulations presented in the literature suggest that the maximum shear modulus can be estimated with parameters derived from the density and states of stresses of the soil mass. For example, Hardin and Black [1968] showed that the greatest impact on the dynamic shear modulus of clays are the mean effective normal stress, p', the void ratio, e, and the overconsolidation ratio, OCR. Houlsby and Wroth [1991] suggested that the shear modulus of clays could be adequately defined by employing only the mean effective normal stress p' and the OCR. These general concepts have been modified by researchers to incorporate anisotropic states of stress and the deviatoric stress (e.g., Rampello et al. [1997]). Further modifications that specifically target Chicago clays have also been presented by Kim and Finno [2011].

Certain soils may show different values of shear modulus at small strains, G_{HH} and G_{VH}, when measured in two orthogonal directions. The degree of this cross-anisotropy depends on the type of depositional environment, stress history and soil type.

Considering that the initial stiffness is a key factor when attempting to characterize soil stiffness at small strains, the selected soil model should be able to estimate it accurately. In addition, if the simulated soil exhibits a high degree of cross-anisotropy, the selected model should also be able to capture this behavior.

5.1.5. Stress Path and Recent Stress History Effects

Recent stress history effects refers to a difference in soil response arising from different stress paths experienced by a soil specimen prior to shearing. In a laboratory environment, two hypothetical soil samples consolidated to the same density and stress, could have different responses during shearing, depending upon the stress path followed during sampling, trimming, saturation, consolidation and creep.

For instance, Cho et al. [2007] showed the effects of the sample swelling during saturation. Swelling during saturation (at low effective stresses) increased the strains that accumulate when reconsolidating to the in-situ vertical effective stress and lowered the shear wave velocity, thereby inferring a change in the original structure of natural clay. It was observed that sample swelling during saturation can significantly change the soil stiffness at small strains.

Stress path directions and stress reversals also have a significant influence on the stiffness degradation of clays. Atkinson et al. [1990] indicated the softest response with the most rapid degradation occurred in the stress path that continues in the same direction as the consolidation stress path (0° rotation). The stiffest response occurred for stress paths in the opposite direction as the consolidation stress path (180° rotation). The stress path direction effects in Chicago soft clays for triaxial tests following different drained and

undrained stress probes have been studied and presented by Holman [2005], Cho [2007] and Kim [2011].

The influence of stress path directions and reversals on very small and small strain response has been incorporated into some small strain constitutive models for clays, such as the one proposed by Stallebrass and Taylor [1997]. Stallebrass and Taylor [1997] used concepts of kinematic regions of very small and small strain stiffness as proposed by Jardine [1992]. As shown by Stallebrass and Taylor [1997], the incorporation of this phenomenon in the constitutive soil models shows dramatic improvements in the predicting capabilities in the small strain region. This suggests that the proper incorporation of this phenomenon in the selected constitutive model, in the same or a similar manner, is very important.

5.1.6. Constitutive Soil Model Selection Criteria

Because one of the objectives of this research is to develop a tool or guideline to perform geotechnical finite element simulation of excavations that is accessible to engineering practitioners, the potential candidates for constitutive soil models was restricted to models that have been implemented in commercial computer codes.

Nonlinear constitutive soil models that were considered included the Soft Soil model (SS), the Hardening Soil model (HS) and the Hardening Soil Model with Small Strain (HSSMALL). These three models are described and explained in PLAXIS [2010]. The SS model consists of an extension of the Modified Cam Clay model (Roscoe and Burland [1968]) to include material-rate dependency. Even though this model complies with soil behavior described by critical state soil mechanics, it was disregarded because it was not formulated to capture the anisotropic and non-linear stiffness at small strain levels. The HS model

was also disregarded for the same reason, in addition to not being critical-state soil mechanics based. A modified version of the HS model (i.e., HSSMALL) was given additional attention. The HSSMALL model includes significant improvements when compared to its predecessor. This formulation allows one to predict the non-linear response at small strains. At large strains the stiffness of this model degrades back to the one of the HS model. The HSSMALL model was also ultimately discarded because the implementation cannot capture the dependency stiffness on density and stress path direction.

Two additional advanced models suitable for modelling clays available for use with commercial computer codes through the soilmodels.info project (`www.soilmodels.info`) were considered. These models include the 3-SKH model (Stallebrass [1990] and Stallebrass and Taylor [1997]) and a hypoplastic model developed by Mašín [2006] (HC). These two models provide several attractive features. The 3SKH is a bounding surface model that at normally consolidated states degrades to the Modified Cam Clay model. Two kinematic surfaces are defined inside the bounding surface. One surface is introduced to control the region where pure elastic deformations take place, and the second surface is introduced to determine the area affected by recent stress history. The 3SKH model is defined by nine model parameters and theoretically is able to capture most of the features listed on the previous sections.

The HC model is not developed using the elasto-plastic framework, but it is based on the hypoplastic laws presented by Kolymbas [1991]. The HC model is also defined by nine soil model parameters. The numerical framework utilized for the development of the 3SKH and the HC models are very different; however, they were both developed to capture the same key features of soil behavior, including those postulated by critical state soil

mechanics by using density (or void ratio) as a state variable to predict the soil response at various degrees of overconsolidation. Both models, in a slightly different manner, also capture recent stress history effects and small strain non-linearity. The similarities shared by the two models are reflected in that the two models use some parameters with the same physical definition and both models have very similar responses to certain stress paths (Hájek et al. [2009]).

When attempting to decide between the HC and 3SKH, the HC seemed to have certain advantages that were considered significant. First, the yield surface of the 3SKH model in the octahedral plane is circular and independent of the Lode angle (identical to the yield surface in Cam Clay), whereas the HC model accounts for stress anisotropy and reaches failure at states similar to the ones described by Matsuoka and Nakai [1974]. In addition, the definition of low strain stiffness incorporated in HC includes the cross-anisotropy referenced in Section 5.1.4, while the dynamic stiffness incorporated in the 3SKH model simply follows the isotropic definition suggested by Viggiani and Atkinson [1995].

5.2. Hypoplastic Soil Model for Clays (HC Model)

For the reason explained in Section 5.1, and other reasons included in this section, the HC model was selected for characterizing all Chicago clays, both soft and stiff. The purpose of this section is to briefly describe the formulation and capabilities of the HC model as it relates to the key aspects of soil behavior the affect or control the performance of excavations mentioned before. The different model parameters and their physical meaning are also discussed.

5.2.1. Hypoplastic Law

The HC model was developed based on the hypoplastic laws presented by Kolymbas [1991]. As explained in Kolymbas [2000], constitutive models based on hypoplasticity do not distinguish between elastic or plastic deformations and do not include the concepts of yield surface or plastic potentials. Hypoplastic models obey a single equation that defines the relation between stress and strain based on the direction of loading and other state variables. Since the implementation of hypoplastic laws do rely on yield or bounding surfaces, the use of complex mapping algorithms is not needed, consequently, their implement into numerical codes is easier than complex elasto-plastic models.

The direction dependant stiffness is intrinsic to the formulation of hypoplastic models. As explained by Niemunis [2002], hypoplastic soil models are defined in an incremental form by equation 5.1:

$$\dot{T} = L : D + N\|D\| \tag{5.1}$$

In this equation, $\dot{T}$ is the Jaumann rate of the Cauchy stress tensor (T). D is the Euler stretching tensor (change in strain tensor) and $\|D\|$ represents the Euclidean norm of D and $\vec{D}$. The terms L and N define the constitutive relation and are fourth and second order tensors, respectively.

In this section, the tensorial operations, including the ones included in Equation 5.1 are defined in indicial notation as follows: $A : B = A_{ij}B_{ij}$, $C : A = C_{ijkl}A_{kl}$, $A \otimes B = A_{ij}B_{kl}$ and $A \cdot B = A_{ij}B_{jk}$, where A and B are second order tensors and C is a fourth order tensor.

Such formulation allows for a clear distinction of the dependency of the stiffness tensor on the direction of loading, the backbone of all hypoplastic models. This dependence becomes evident by simplifying Equation 5.1 to one dimension. If only one dimension is considered, Equation 5.1 can be expressed as:

$$\dot{T} = \begin{cases} (L+N)D & \text{for } D > 0 \\ (L-N)D & \text{for } D < 0 \end{cases} \tag{5.2}$$

In this one dimensional case, the tangential stiffness tensor, M, is defined by $L + N$ if the stretching tensor is positive (in the same direction of the strain tensor) and the stiffness tensor becomes $L - N$, when there is a reversal in strains and the stretching tensor becomes negative.

5.2.2. HC Reference Model Parameters

The stiffness at large strains in the HC model, as explained by Mašín [2006], is controlled by a reference model. Equation 5.3 shows the basic formulation of the reference mode. This reference model consists of a modification of Equation 5.1, to include two scalar factors, f_s and f_d, called the barotropy and pyknotropy scalar factors.

$$\dot{T} = f_s L : D + f_s f_d N \|D\| \tag{5.3}$$

These factors introduce density as an additional state parameter that controls changes in stiffness. In particular, the barotropy factor enforces the relationship between the natural logarithm of the mean normal stress and the void ratio, as presented by Butterfield [1979]. The pyknotropy factor enforces the effects of density within the framework of critical state failure.

This reference model is defined by five soil model parameters: N, λ^*, κ^*, ϕ_c and r. As shown in Figure 5.1, the compression parameter λ^*, defines the gradient of the isotropic normal compression line in the $ln(1+e) - \ln(p')$ space. The swelling parameter κ^*, defines the gradient of the isotropic unloading line in the $ln(1+e) - \ln(p')$ plot. The model parameter N, defines the natural logarithm of the specific volume $(1+e)$ on the isotropic normal compression line at $p' = 1kPa$ in $ln(1+e) - \ln(p')$ space. The parameter p_e^* is a state parameter, termed the equivalent mean normal stress, and it is equal to the mean effective normal stress of the current state when projected (at constant void ratio)

into the isotropic normally consolidated line. The state parameter p_{cr} is equal to the mean effective normal stress when the current state is projected into the critical state line.

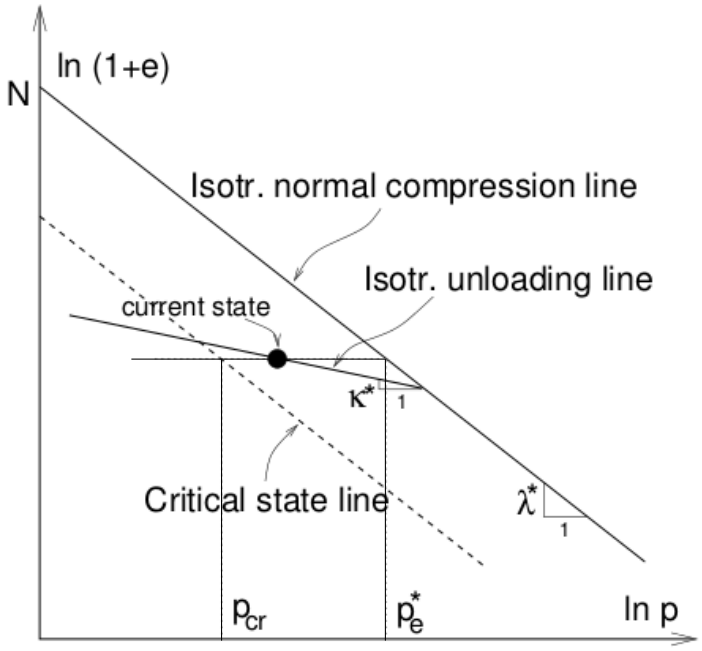

Figure 5.1: Definition of model parameters: N, λ^* and κ^* (from Mašín [2005])

The critical state friction angle (ϕ'_c) defines the friction angle at critical state. The model parameter r, is defined as the ratio between the initial bulk modulus (K_i) and the initial shear modulus (G_i) for a soil sheared starting from an isotropic normally consolidated state. It should be noted that the reference model describes the behavior of the model at large strains; consequently, the initial bulk and shear modulus, the basis of the definition of the model parameter r, are not the ones measured at small strain levels. In fact, except

for r, the large strain parameters are similar in definition to the model parameters of the version of the Modified Cam Clay model presented by Butterfield [1979].

5.2.3. Failure Surface and Bounding Surface

The definition of failure and bounding surfaces belongs to the formulation of elasto-plastic models and it is not part of the formulation of hypoplastic soil models. However, the definition of failure and bounding surfaces are useful concepts that can be used to compare the HC model to well known elasto-plastic models. Consequently, attempts have been made to extract these surfaces from the hypoplastic model definition.

The failure surface can be extracted by imposing the condition $\dot{T} = 0$ on Equation 5.3. In this equation, the pyknotropy factor, f_d, ensures that when $\dot{T} = 0$ all states of stress belong to the Matsuoka-Nakai failure surface (Matsuoka and Nakai [1974]). Niemunis [2002] compared the failure surface implemented in the HC model to experimental results (mirrored five times) performed by Goldscheider [1976]; the results of such comparison are show in the Figure 5.2.

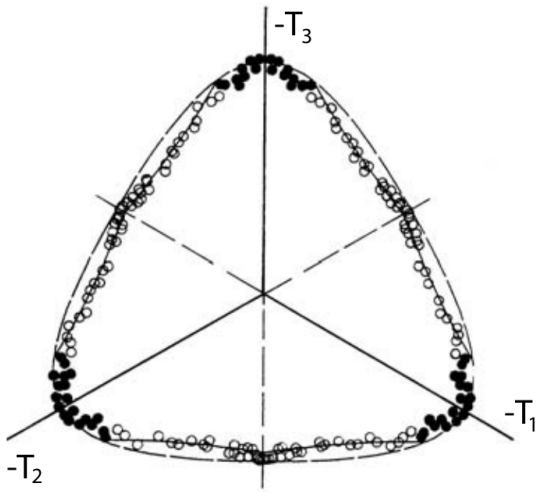

Figure 5.2: Matsuoka-Nakai failure surface incorporated into the hypo-plastic soil model (from Niemunis [2002])

The bounding surface is defined as the surface in stress versus specific volume space that defines all possible soil states. Such surface also is not explicitly defined in hypoplastic soil models. However, in hypoplasticity a similar surface, named the *swept-out-of-memory surface* (SOM) can be derived by replacing $\dot{T}_n = 0$ into Equation 5.3, where T_n is defined as T/p_e^*. Following such procedure, Mašín and Herle [2005] computed the SOM surface for the HC model (see Figure 5.3), and showed that the shape of the bounding surface in constant specific volume plane is controlled by both the critical state friction angle and the ratio $(\lambda^* - \kappa^*)/(\lambda^* + \kappa^*)$. Mašín and Herle [2005] explained that there are slight differences between the SOM surface and the bounding surface, but such differences are negligible when compared with typical error measurement during laboratory testing.

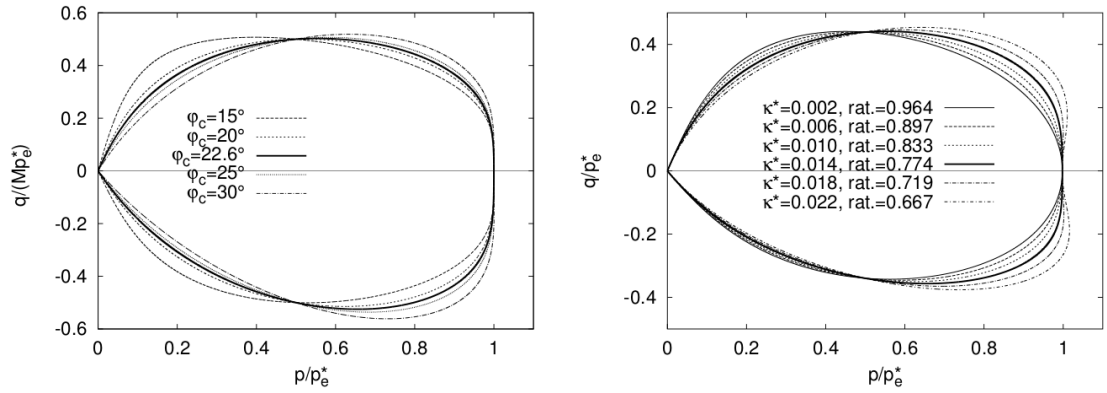

Figure 5.3: Influence of ϕ_c and the ratio $(\lambda^* - \kappa^*)/(\lambda^* + \kappa^*)$ on the SOM surface (from Mašín and Herle [2005])

It should be noted that the SOM surface presented in Figure 5.3 is normalized by equivalent mean normal stress (p_e^*). This normalization technique was originally proposed by Parry [1960].

This increased precision of the HC model is demonstrated in Mašín [2006] and Hájek et al. [2009]. The studies compared triaxial test results of soils reconstituted to overconsolidation ratios that vary from one to ten with model predictions made with the HC, MCC and 3SKH models. It was shown that, using a single set of model parameters, HC model was able to predict the response of all the tests results with a higher accuracy than the one obtained with the MCC and 3SKH models. An example of the higher accuracy provided by the HC model displayed in terms of the measured versus computed triaxial deviatoric stress versus strains and volumetric strain versus shear strains for samples reconstituted at different degrees of overconsolidation is presented in Figure 5.4.

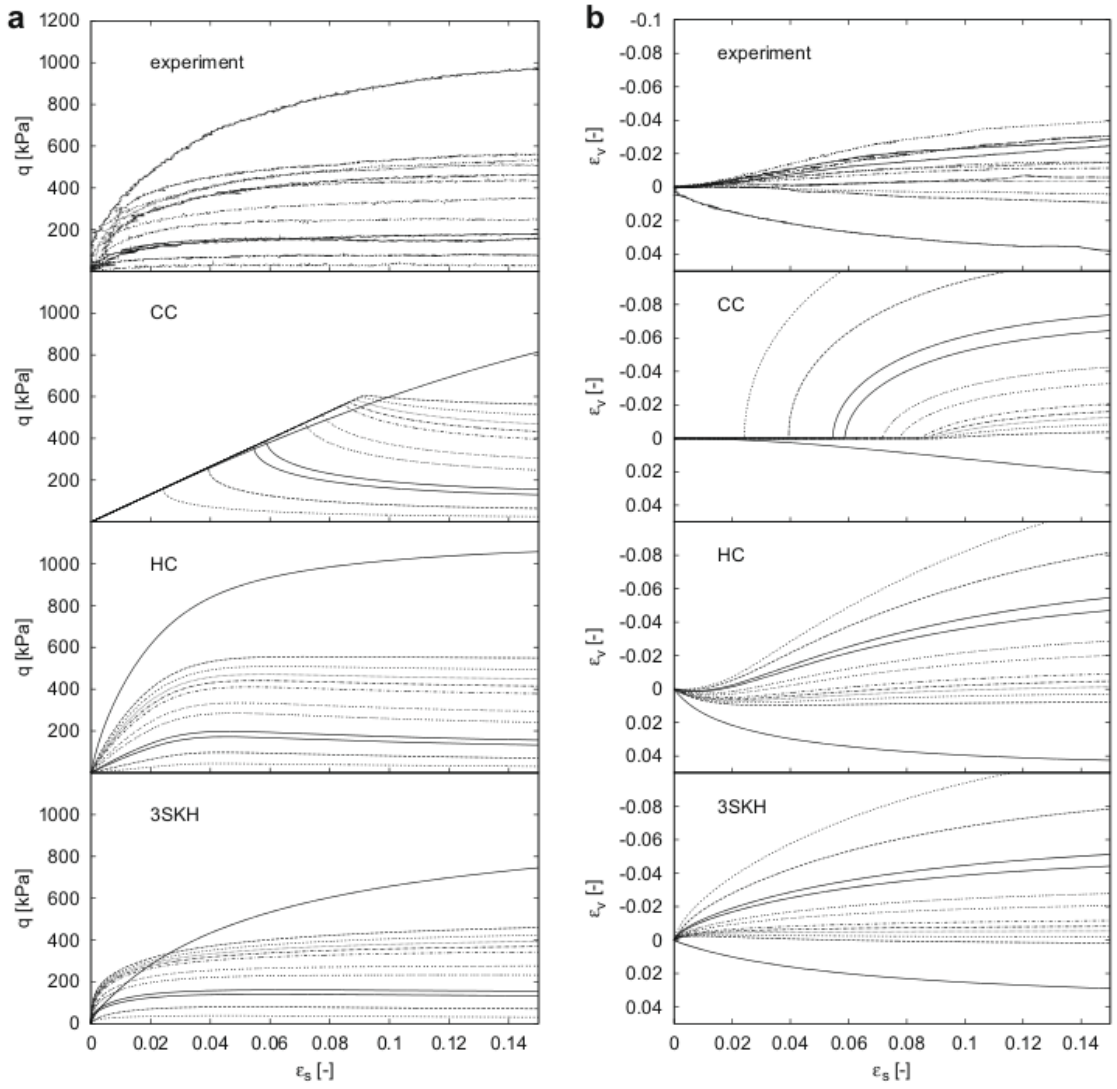

Figure 5.4: Measured versus computed triaxial test results simulated using the MCC (CC), HC and 3SKH models (after Hájek et al. [2009])

5.2.4. Intergranular Strain Concept

Niemunis [2002] and Mašín [2006] indicate that by incorporating the *intergranular strain* concept, the capabilities of the reference model are extended to capture the small strain non-linear soil stiffness. The evolution of the soil stiffness from small to large strains is performed by introducing a new state parameter. The new state parameter, h, is a strain tensor, called the *intergranular strain* tensor. The state parameter h stores recent changes in the stretching tensor. Consequently, the change of the *intergranular strain* tensor is directly related to the change in the stretching tensor (D).

Intergranular strains accumulate upon changes in the stretching tensor until $\|h\|$ (norm of h) reaches a maximum value, defined by the model parameter R (scalar). Consequently, if a state parameter ρ, is defined as $\|h\|/R$, ρ will only vary from zero to one.

Figure 5.5 shows the stress responses in axisymmetric space – only showing h_{11} and h_{22} – introduced by the *intergranular strain* concept upon different directions of the stretching tensor. For instance, in the figure, the condition where after monotonic shearing in the 11 direction (for example, a triaxial compression test), the state parameter ρ reaches a value of one, is represented by having the stretching tensor pointing in the $\overrightarrow{AB}$ direction and the coordinates of the *intergranular strain* tensor equal to the ones of Point "B". At this state, the increased stiffness incorporated by the *intergranular strain concept* vanishes and the stiffness (and stress response) degrades to become equal to the one of the reference model; consequently, in this state any further straining in the same direction would result in a tangential stiffness, M, defined by $L + N$ (stiffness of the reference model when f_s and f_d are equal to one). Conversely, if from this state the direction of stretching is reversed by 180°, the direction of the stretching tensor will point in the $\overrightarrow{BA}$ direction.

In this case, the small-strain tangential stiffness will be fully recovered and will become maximum and equal to the dynamic stiffness $m_R L$. m_R and m_T are model parameters that define the increase in stiffness at small-strain levels in orthogonal strain directions; consequently, if from point "B", the stretching tensor were to point up or down in the figure (perpendicular to $\overrightarrow{AB}$), the tangential stiffness will become equal to $m_T L$.

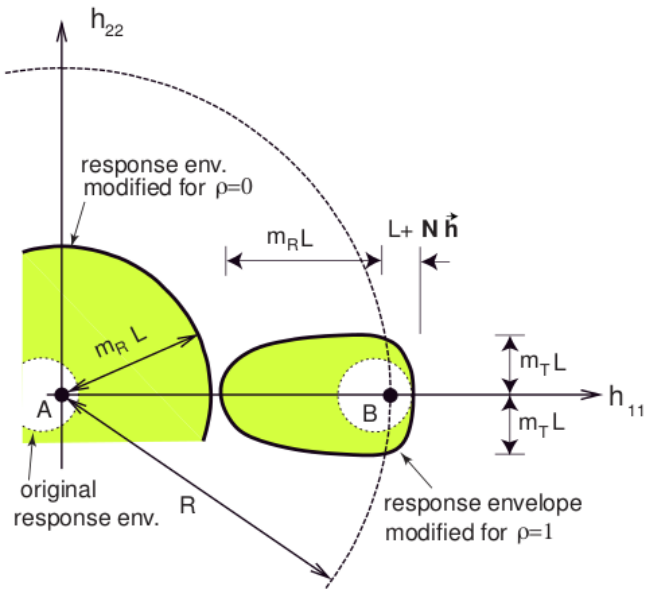

Figure 5.5: Stress response for different values of ρ introduced by the *intergranular strain* concept (after Niemunis [2002])

Because the model parameter m_R defines the maximum shear response after a 180° change in stretching direction, the model parameter m_R is related to the small strain shear stiffness G_o. Mašín [2006] shows that, after some mathematical manipulation on the constitutive tensor L, the relation between G_o and the model parameter m_R, can be expressed as:

$$G_o = \frac{m_R}{r\lambda^*} p' \tag{5.4}$$

Where r, λ^* are the HC reference model parameters and p' is the constant mean normal stress.

The tangential stiffness at intermediate states ($0 < \rho < 1$) will lie between the tangential stiffness of the reference model and the maximum stiffness at small strains. The tangential stiffness tensor, M, at this intermediate state is computed by using non-linear interpolation functions that are controlled by the model parameter χ. The tangential stiffness, M, is computed using Equation 5.5 when $\vec{h} : D > 0$ and using Equation 5.6 when $\vec{h} : D \leqslant 0$.

$$M = [\rho^\chi m_T + (1 - \rho^\chi) m_R] f_s L + \rho^\chi (1 - m_T) f_s L : \vec{h} \otimes \vec{h} + \rho^\chi f_s f_d N \vec{h} \tag{5.5}$$

$$M = [\rho^\chi m_T + (1 - \rho^\chi) m_R] f_s L + \rho^\chi (m_R - m_T) f_s L : \vec{h} \otimes \vec{h} \tag{5.6}$$

In addition, the accumulation of *intergranular strains* with respect to changes in the stretching tensor is also governed by non-linear relations. Specifically, change or rate of *intergranular strains*, $\dot{h}$, is governed by the model parameter β_r, as shown below.

$$\dot{h} = \begin{cases} (I - \vec{h} \otimes \vec{h} \beta_r) : D & \texttt{for } \vec{h} : D > 0 \\ D & \texttt{for } \vec{h} : D \leqslant 0 \end{cases} \tag{5.7}$$

Where $\vec{h}$ is the direction of the *intergranular strain* defined by $h\ \|h\|$, I is the fourth order unity tensor.

Figure 5.6 shows graphically the laws that govern the accumulation of *intergranular strains*. As it can be seen, when the direction of the stretching and *intergranular strain* tensors are opposite ($h : D < 0$), any change in the stretching tensor translates in the direct accumulation of inter-granular strains. However, when the two tensors act in the same direction ($h : D > 0$), the *intergranular strain* only accumulates a fraction of the change in the stretching tensor. And such fraction is controlled by the model parameter β_r.

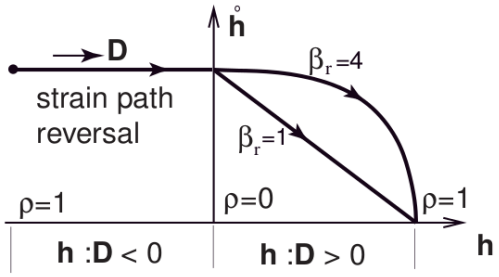

Figure 5.6: Relation between the rate of *intergranular strain* and stretching tensor (after Niemunis [2002])

5.3. HC Model Adapted for Chicago Clays

These following sections describe the process followed to estimate the HC model parameters to predict the soil response of Chicago clays. Some of these parameters are estimated via an optimization routine and others are be defined prior to the optimization process. The HC model is based on ten soil model parameters. As for many models, the model parameters can be divided in two groups: a) parameters with a clear physical meaning whose effect on the soil stiffness or strength can be isolated and their magnitude can be estimated from laboratory or in-situ tests, and b) parameters whose effect cannot be easily isolated and are best identified using fitting procedures attempting to match measured soil data. The latter are good candidates for becoming the optimized parameter in an inverse calibration procedure.

However, availability of data should also be considered when selecting parameters to be used for optimization. For instance, parameters with a clear physical meaning that can be isolated and identified may rely on types of tests that are not available.

Finally, in an attempt to reduce the number of parameters to be optimized, one must consider the sensitivity of each parameter on the overall model response. When a model parameter has a small effect on the overall model response, such model parameters should not be considered as a candidate for optimization (Calvello [2002] and Rechea et al. [2008]).

An important factor to consider when estimating the magnitude of the HC model parameters to predict the response of Chicago clays, and in particular those that developed in-situ at the OMPW excavation, is that the subsurface conditions in the Chicagoland area, in general, consists of multiple layers of glacial tills (Section 4.4). These till layers

were formed under different geological conditions and their plasticity, density and degrees of overconsolidation vary considerably.

The HC model conceptually allows capturing, with a single set of model parameters, the soil behavior at different stress levels, densities or degrees of overconsolidation (Mašín [2006] and Hájek et al. [2009]) . However, the model has not been developed to capture, with the same set of parameters, changes in response caused by variations in soil plasticity (defined by the Atterberg limits).

Consequently, a strategy that extends the validity of the parameters to the different till layers needs to be developed.

5.3.1. Estimation of Reference Model Parameters

The reference model that defines the evolution of soil stiffness at large strains is defined by five soil model parameters: N, λ^*, κ^*, ϕ'_{cv} and r. The definitions of these model parameters are provided in Section 5.2.2.

The model parameters N and λ^*, as shown in Figure 5.1, can be estimated from an isotropically consolidated triaxial test. However, in the HC model and in some other critical state soil mechanics based models, all compression lines with constant deviatoric versus mean normal effective stress ratios (q/p') are assumed parallel to each other in a $ln(p')$ versus $ln(1+e)$ space. Therefore, the model parameter λ^* (slope of the compression line) can be measured from the compression line from any test with constant q/p' ratio; including the consolidation cycles in k_o triaxial tests or oedometer tests, at least for a constant q/p' portion of these tests. If oedometer tests are used, the ratio between

horizontal and vertical stress (k_o) must be measured or estimated to evaluate the mean normal effective stress during compression.

The value of $\ln(1+e)$ at a mean normal effective stress of $1kPa$ on the isotropic compression line (i.e., model parameter N) and the value of $\ln(1+e)$ at $1kPa$ on the k_o compression line do not have the same value. However, if we define the value of $\ln(1+e)$ at $1kPa$ on the k_o compression line as N_o, it can be shown that N is related to N_o by the following expression:

$$N = N_o + \lambda^* [\ln \frac{3}{2k_o + 1} - \ln 1] \tag{5.8}$$

A database of oedometer and k_o triaxial consolidation tests containing test results performed in soil samples collected in various project sites in the Chicago area was compiled and utilized to estimate N and λ^*. A listing of the source of all tests utilized for this purpose is shown in the Table 5.1.

Test ID	Test Type	Water Content, %	Source
BLKDC1	Oedometer	24.0	Kim [2011]
BLKDC2	Oedometer	24.6	Kim [2011]
BLKSC1	Oedometer	25.4	Kim [2011]
BLKSC2	Oedometer	28.3	Kim [2011]
BLKSC3	Oedometer	27.3	Kim [2011]
FB1C2	Oedometer	23.8	Cho [2007]
FB2C1	Oedometer	22.1	Cho [2007]
FB2C2	Oedometer	25.0	Cho [2007]
FB2C3	Oedometer	25.5	Cho [2007]
O1S1C1	Oedometer	25.3	Wang [2011]
O2S2C1	Oedometer	12.3	Wang [2011]
O1S2C1	Oedometer	15.1	Wang [2011]
O2S4C1	Oedometer	15.9	Wang [2011]
O1S3C1	Oedometer	19.2	Wang [2011]
O3S5C1	Oedometer	25.3	Wang [2011]
O2S3TC1	Triaxial k_o	20.1	Wang [2011]
2	Oedometer	40.8	Peck and Reed [1954]
1	Oedometer	45.5	Peck and Reed [1954]
4	Oedometer	27.9	Peck and Reed [1954]
6	Oedometer	14.5	Peck and Reed [1954]
3	Oedometer	33	Peck and Reed [1954]
5	Oedometer	25.8	Peck and Reed [1954]
7	Oedometer	11.1	Peck and Reed [1954]

Table 5.1: List of oedometer and k_o triaxial tests on Chicago clays

The results of the oedometer and k_o triaxial consolidation tests list above, compiled for this study, are shown in Figure 5.7.

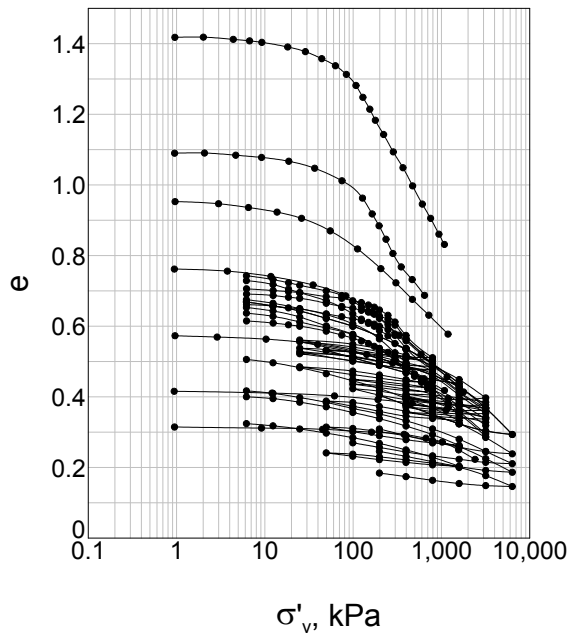

Figure 5.7: Vertical effective stress versus void ratio for Chicago clays tests listed in Table 5.1

If the virgin compression portion of each curve shown in Figure 5.7 is extracted from each of the tests listed above, such curves can be replotted in $\ln(1 + e)$ versus $\ln(p')$ space as shown in Figure 5.8. For the oedometer tests, the effective horizontal stresses were estimated using the correlation of k_o proposed by Finno and Chung [1992] from Chicago clays.

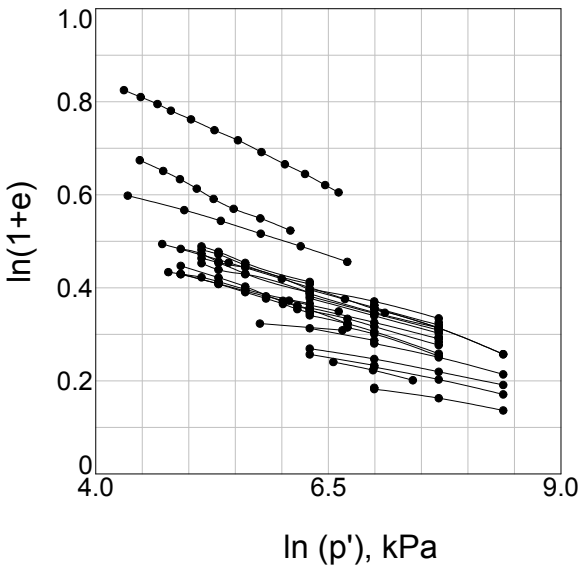

Figure 5.8: Normalized compressibility for Chicago clays tests listed in Table 5.1

As it can be seen in Figure 5.8, a different set of values of N_o and λ^* could be estimated for every test. It is presumed that the variation in N_o and λ^* is caused by differences in composition across the different samples. To overcome the scatter encountered when attempting to estimate the value of N and λ^* for all the tests a normalization that addresses these variations in composition was implemented.

This normalization is described by Coop and Cotecchia [1995] and Baudet [2001]. This normalization is a variation from the work presented by Burland [1990]; which was in turn is based on the method described by Skempton [1970]. Coop and Cotecchia [1995] suggested that the position of the virgin compression line in $\ln(1+e)$ versus $\ln(p')$ space of a reconstituted soil is an intrinsic property of the soil and is linearly related to its Liquid

Limit. Specifically, Coop and Cotecchia showed using Sibari clay data (Figure 5.9.1) that if the specific volume ($v = 1 + e$) in $\ln(1 + e)$ versus $\ln(p')$ space is normalized using:

$$v_n = \exp(\frac{ln(v) - N_o}{\lambda^*}) \tag{5.9}$$

A unique compression line is obtained for all soils, independent of their composition (Figure 5.9.2).

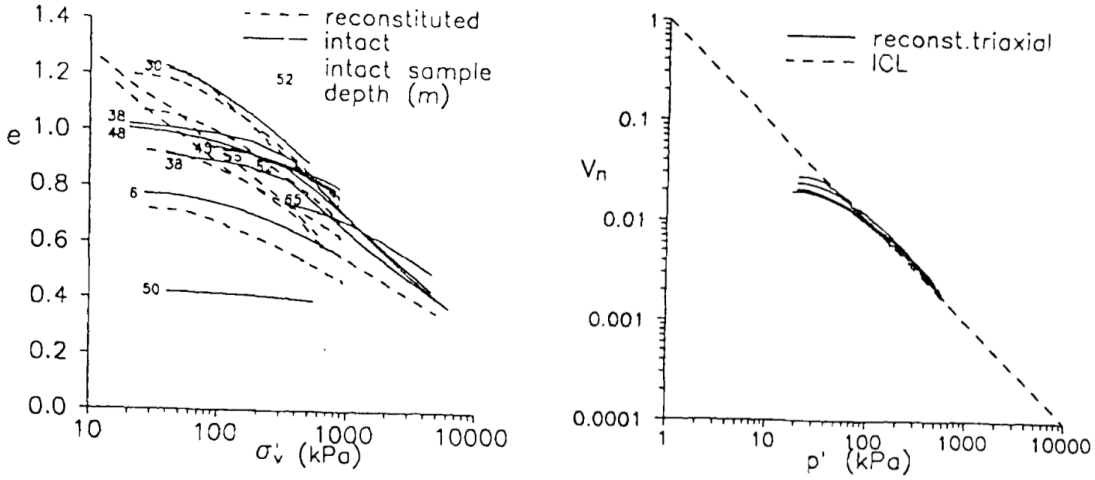

(5.9.1) Vertical Effective Stress versus Void Ratio (5.9.2) v_n versus Mean Normal Stress

Figure 5.9: Sibari consolidation test data (from Baudet [2001])

Additionally, Coop and Cotecchia [1995] demonstrate using Sibari and Bothkennar clay test data (Figure 5.10), the existence of a linear relation between λ^* and N with the void ratio at the Liquid Limit (e_L). Since, as shown in Figure 5.10, a different set of correlations was encountered for Sibari and Bothkennar clay, Baudet [2001] assumed that

the relation between N and e_L and λ and e_L is not universal for all clays, but specific to soils from the same region.

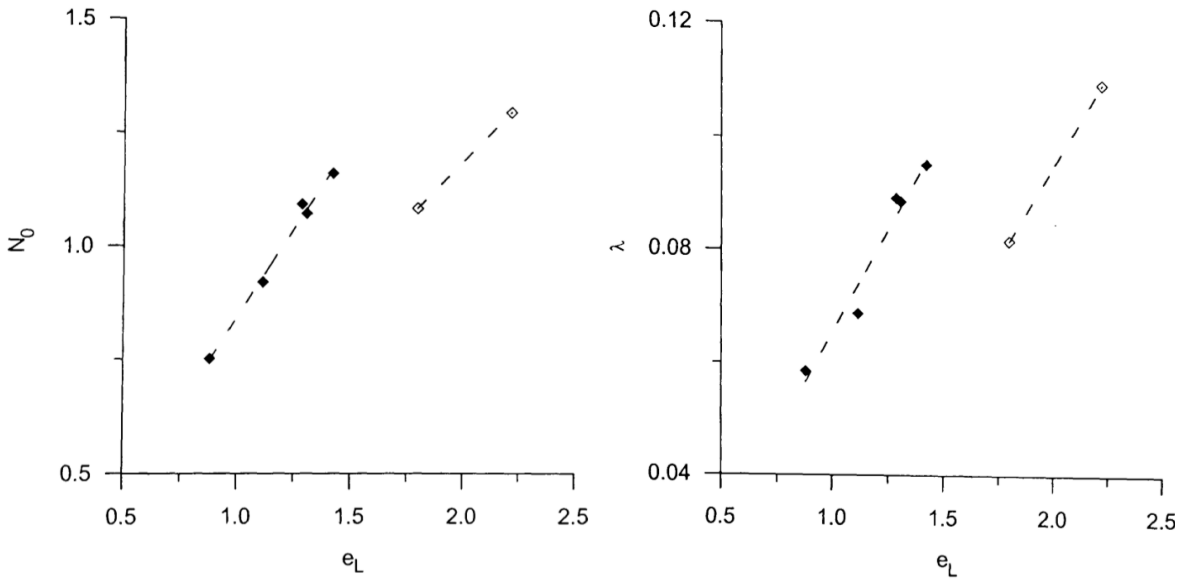

(5.10.1) e_L versus N_o (5.10.2) e_L versus λ^*

Figure 5.10: Relationship between void ratio at Liquid Limit e_L, N_o and λ^* for Sibari (♦) and Bothkennar (◊) clay (from Baudet [2001])

It is important to note that the concept of a unique intrinsic compression line as suggested by Coop and Cotecchia [1995], and explained by Baudet [2001], is applicable to reconstituted samples. In general, when the normalization described above is applied to undisturbed or intact soil specimens a line different from the intrinsic compression line is obtained. This different line is referred to as the "sedimentation line." In general, in intact samples the sedimentation line plots to the right of the instrisic compression line. The offset or separation between these two lines is attributed to difference in structure (fabric and bonding).

Cho [2007] performed a series of oedometer tests on intact and reconstituted compressible Chicago clay samples. For reference, the results from the testing performed by Cho [2007] are shown in Figure 5.11. All tests results, in general, showed no significant difference in the location and in particular in the slope of compression lines (in e versus $log(\sigma' v)$ space) between the reconstituted and intact specimens.

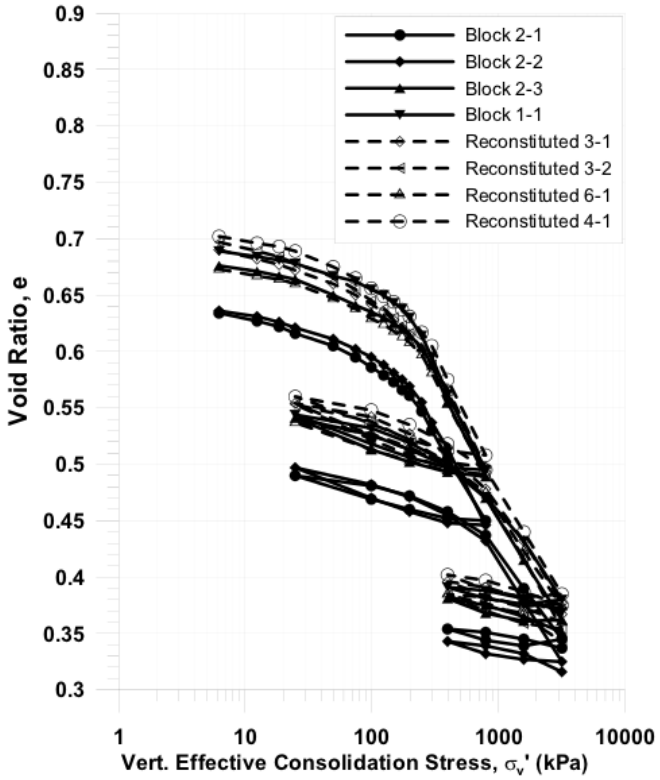

Figure 5.11: Oedometer tests on intact and reconstituted Chicago clays (from Cho [2007])

These test data suggest that the difference in structure due to reconstitution at large strains could be neglected for compressible Chicago clays.

No oedometer data on reconstituted samples were available to evaluate the presence of structure (as defined in this section) for the hard clays from the lower glacial till layers;

however, visual observation does not appear to show the presence of bonding or cementing agents. Based on this visual observation and in absence of conclusive test data, it was assumed that the effects of structure for the hard basal till clays were ignored when describing the compressibility of these soils.

Consequently, the effects of structure at large strains are assumed negligible in this study and the normalization presented by Coop and Cotecchia [1995] is applied to intact or undisturbed Chicago test data assuming no significant difference in the compressibility between intact and reconstituted specimens.

The data points corresponding to the virgin compression line from the test results presented in Figure 5.7 where replotted in $\ln(p') - \ln(v_n)$ space in Figure 5.12.

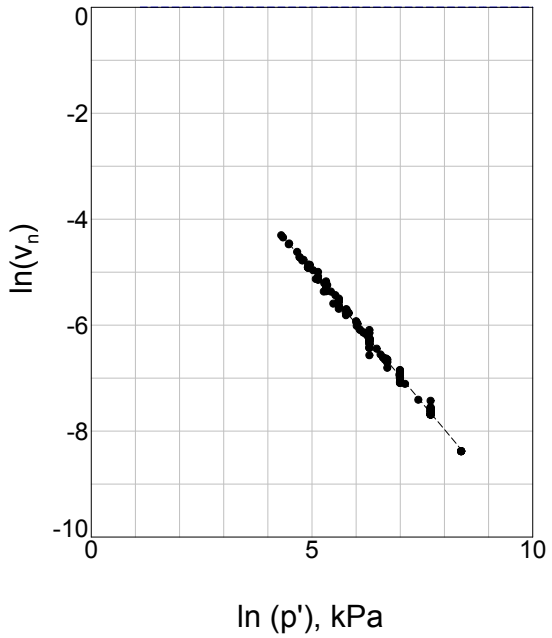

Figure 5.12: Normalized compressibility for Chicago Clays

The Liquid Limit (LL) in Chicago clays as shown by Peck and Reed [1954] is related to the in-situ natural water content (w_n). In this study, the void ratio at the Liquid Limit, e_L, was estimated from the correlation provided by Peck and Reed [1954] and adopting an average specific gravity, G_s, equal to 2.7:

$$LL = 0.82 w_n + 12.0 \tag{5.10}$$

Figure 5.13 shows graphically the relation between e_L and the model parameters N_o and λ^* computed for the Chicago clay specimens in Table 5.1. These empirical relations can be numerically represented using linear regressions:

$$N_o = 1.104 e_L - 0.2099 \tag{5.11}$$

$$\lambda^* = 0.0955 e_L - 0.0229 \tag{5.12}$$

The model parameter κ^* is defined as the slope in $\ln(1 + e)$ versus $\ln(p')$ space of the unload-reload cycles from an isotropic consolidation triaxial test. If the slope during isotropic unloading (or reloading) is assumed equal to the slope under k_o conditions, as suggested by Butterfield [1979], a value of κ^* could be approximated from the oedometer test results presented in Table 5.1. However, because estimating the value of k_o under overconsolidated conditions could be very inaccurate, in particular when the value of k_o approaches 1 (Kulhawy and Mayne [1990]), this procedure was not used.

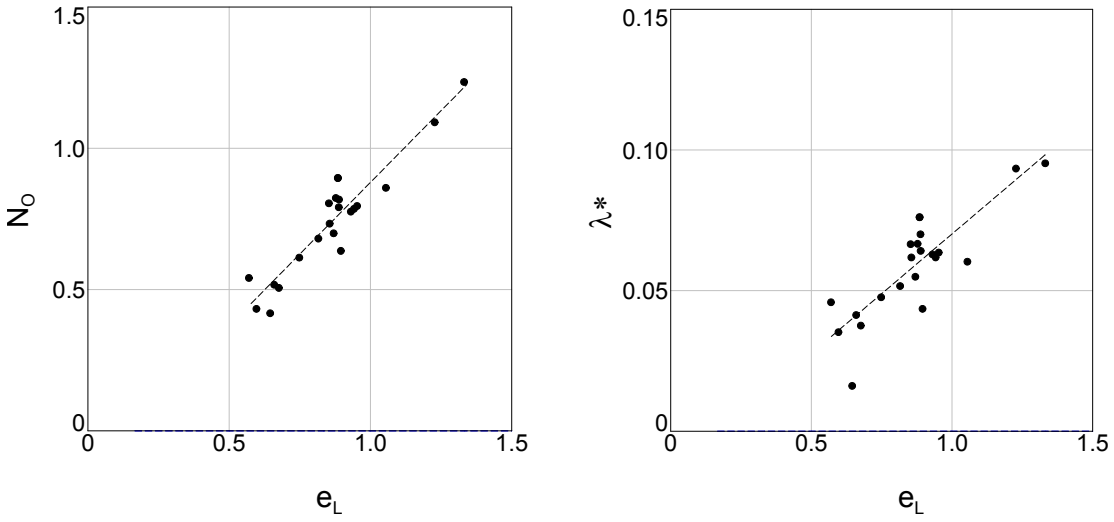

(5.13.1) e_L versus N_o (5.13.2) e_L versus λ^*

Figure 5.13: Relationship between void ratio at Liquid Limit e_L, N_o and λ^* for Chicago clays

Since oedometer test results were not used to estimate κ^*, the only test data that allowed estimating κ^* consisted of the test data on a soft Chicago clay presented by Taylor [1948] and reanalyzed by Butterfield [1979] and one triaxial consolidation test with an unloading cycle on hard glacial tills performed by Wang [2011] (TestID: O2S3TC1 in Table 5.1). The test data reanalyzed by Butterfield showed a ratio of λ^*/κ^* equal to 3.4 and the data presented by Wang showed a ratio approximately equal to 4.0. Instead of adopting a constant value for κ^* for all till layers, a constant ratio λ^*/κ^* equal to 3.5 (derived from the available test data) was used.

It was considered reasonable to set the λ^*/κ^* as a constant, instead of setting constant the value of κ^*, in particular when the application of such parameters will be applied to different glacial till layer of different compositions and plasticity.

This type of simplifying assumptions has been performed by other researchers to reduce the number of parameters used during the optimization process. For example, Calvello [2002] set constant relations between several HS model parameters (i.e., $E_{oed}^{ref} = 0.7E_{50}^{ref}$ and $E_u r^{ref} = 3.0E_{50}^{ref}$) to prevent numerical problems after the model parameter update during the optimization routine.

The critical state friction angle corresponds to the mobilized friction angle (ϕ'_{cv}) at the "ultimate state," where the sample reaches a steady condition where it no longer exhibits changes in volume, shear stress or pore water pressure. The critical state friction angle has a clear physical meaning and can be measured from results of drained or undrained triaxial tests.

Experimental data found in the literature (e.g., Mitchell and Soga [2005] shown in Figure 5.14) shows the strong relation between critical state friction angle with changes in soil composition, reflected in this figure, by the Plasticity Index. Given this empirical evidence, an attempt was made to establish a similar correlation but for Chicago clays.

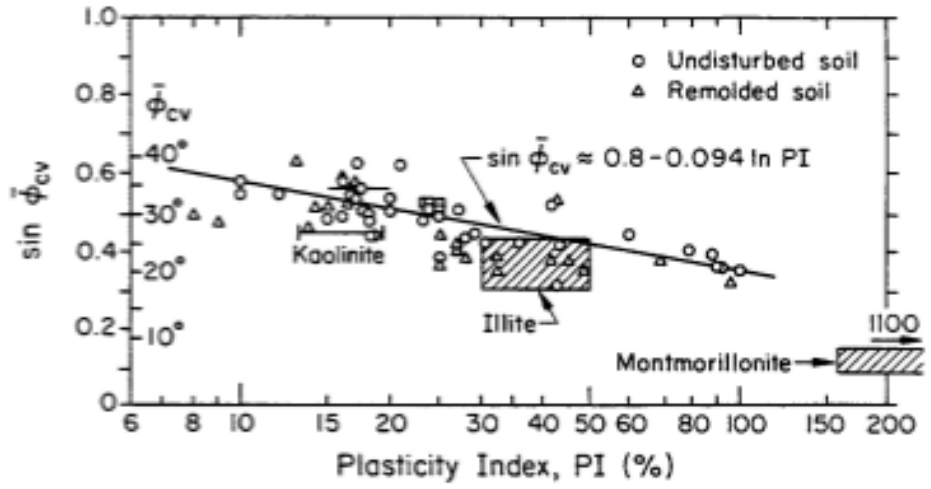

Figure 4-20. $\bar{\phi}_{cv}$ for NC Clays versus PI

Source: Mitchell (22), p. 284.

Figure 5.14: Friction angle versus plasticity index (after Mitchell and Soga [2005]

Finno and Chung [1992] conducted a testing program on a series of undisturbed Chicago soil samples with different composition (Atterberg Limits and gradation) collected from various locations and depths in the Chicago area. The collected samples were reconsolidated using k_o procedures to different pressures in the laboratory environment. This reconsolidation was performed to artificially create soil samples with degrees of overconsolidation ratio of 1, 2 and 4 following the SHANSEP procedures recommended by Ladd and Foott [1974].

The test results performed by Finno and Chung [1992] presented in Figure 5.15 show a remarkable empirical relation between the ratio of the undrained shear strength and the

initial vertical effective stress (s_u/σ'_v) and the natural water content. The trends displayed in Figure 5.15 for the triaxial compression tests are captured in the equation below:

$$\frac{s_u}{\sigma'_v} = 0.46(0.9 - w_n)OCR^{0.9} \tag{5.13}$$

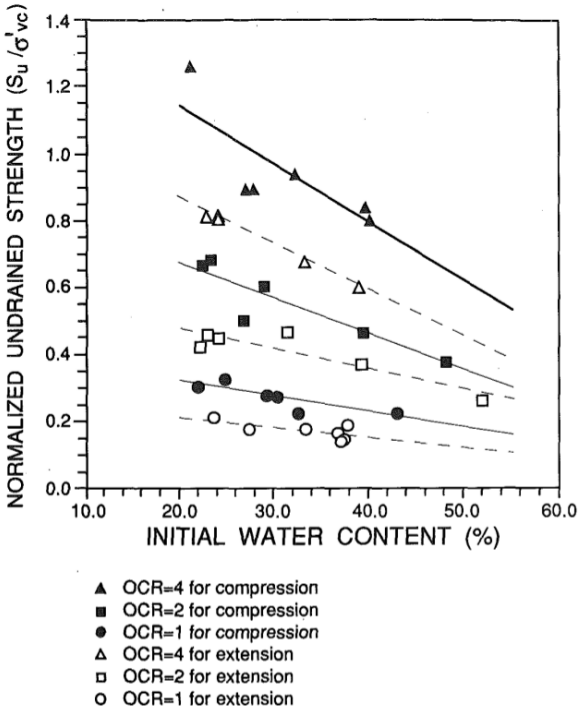

Figure 5.15: Normalized shear strength versus natural water content (after Finno and Chung [1992])

From a theoretical stand point, Wroth and Houlsby [1985] explained that in critical state based models, the ratio between the undrained shear strength and the initial vertical effective stress, for k_o consolidated tests sheared under triaxial compression, depends primarily on the friction angle and that such relationship can be computed as:

$$\frac{s_u}{\sigma'_{v\,NC}} = \frac{sin(\phi'_{cv})}{2a}(\frac{a^2+1}{2})^{\Lambda}; a = \frac{3-\sin(\phi'_{TC})}{2(3-2\sin(\phi'_{TC}))}; \Lambda \approx 0.8 \tag{5.14}$$

If the empirical correlation shown in Equation 5.13 (for $OCR = 1$) is combined with the theoretical Equation 5.14, a semi-empirical relationship between the critical state friction angle and the natural water content can be obtained:

$$\sin(\phi'_{cv}) \approx 0.7385 - 0.9384 w_n \tag{5.15}$$

It should be noted that a large number of additional triaxial tests performed in Chicago clays (e.g., Holman [2005], Cho [2007] and Kim [2011]) could have been used to establish the correlation between the critical state friction angle and the Plasticity Index. Even though these tests were not directly used to derive this correlation, these tests will be used to evaluate its validity as explained in the following chapter, as these laboratory test results are compared to finite element simulations using the model parameters developed in this section.

The model parameter r, as mentioned in Section 5.2.2, is defined as the ratio between the bulk modulus (K_i) and the shear modulus (G_i) for soil starting from an isotropic normally consolidated state. Since intact clays are never encountered in an isotropic condition when in a normally consolidated state, the parameter r cannot be obtained from intact normally or lightly overconsolidated soil specimens; consequently, the model parameter r was selected for optimization. It was assumed, in absence of any further guidance for its selection, that its value will be constant for all till layers. The validity of

this assumption will be evaluated in the following Chapter, when the model predictions are compared to test data.

5.3.2. Estimation of Intergranular Strain Parameters

The addition of the *intergranular strain* concept enhances the reference model, allowing it to predict the non-linear, directional stiffness from very small strain levels. The incorporation of the *intergranular strain* concept introduces five additional model parameters: m_R, m_T, r, β_r and χ. The definition of these parameters was presented in Section 5.2.4. The model parameters β_r and χ control the degradation of the stiffness from maximum shear modulus, G_{VH} or G_{HH}, to the stiffness of the reference model. These parameters are difficult to isolate or estimate from laboratory testing results; therefore, both parameters were selected for optimization.

The model parameter R defines the maximum magnitude of the norm of the *intergranular strain* tensor. To estimate the magnitude of the model parameter R from triaxial test data, ideally, a triaxial test sheared to large strain levels followed by a 180° strain path reversal would be required. In addition, the accurate measurement of R in soft clays would require the use of a triaxial test strain measuring device with a higher accuracy than the ones obtained with the internal LVDTs. Such type of test or measuring capabilities was not available. However, Mašín [2006] explains that the magnitude of the model parameter R does not change significantly for a broad range of clays. In fact, Mašín [2006] reports values of R that only range from $1x10^{-4}$ to $2x10^{-5}$ for six different clays with quite different characteristics. Consequently, the model parameter R was not optimized and set constant with an average value of $5x10^{-5}$.

The parameters m_R and m_T are used to estimate the maximum soil shear modulus, G_{VH} or G_{HH}, at very small strains for perpendicular strain paths. These parameters can be estimated using field shear wave velocity measurements (e.g., cross-hole seismic shear logging, downward shear logging) or measurements of shear wave velocities made in the laboratory environment using bender elements.

In this thesis, these parameters were estimated using the results of cross-hole seismic logging testing performed at the OMPW project site. Figure 5.16 shows the measured horizontal shear wave velocities versus elevation for particles propagating in the horizontal (Vs_{HH}) and vertical direction (Vs_{VH}). This figure shows that there is a small difference between Vs_{HH} and Vs_{VH} at any given elevation, and suggests that the maximum shear modulus is independent of the propagation direction and that the ratio of G_{VH}/G_{HH} is almost equal to one. This agrees with laboratory results presented by Cho [2007] and Kim [2011], which showed that the anisotropy ratio of compressible Chicago clays varies between 1.1 and 1.2. Consequently, considering that the ratio m_R/m_T is equal to G_{VH}/G_{HH}, m_R was assumed to be equal to m_T.

Figure 5.16 shows an increase in the shear wave velocity or initial shear modulus with depth. This trend is anticipated, since the shear wave velocity is proportional to the mean normal effective stress and the mean normal effective stress increases with depth. This relationship between the initial shear modulus and the mean normal effective stress is represented in the HC model as:

$$G_{VH} = \frac{m_R}{r\lambda^*} p' \tag{5.16}$$

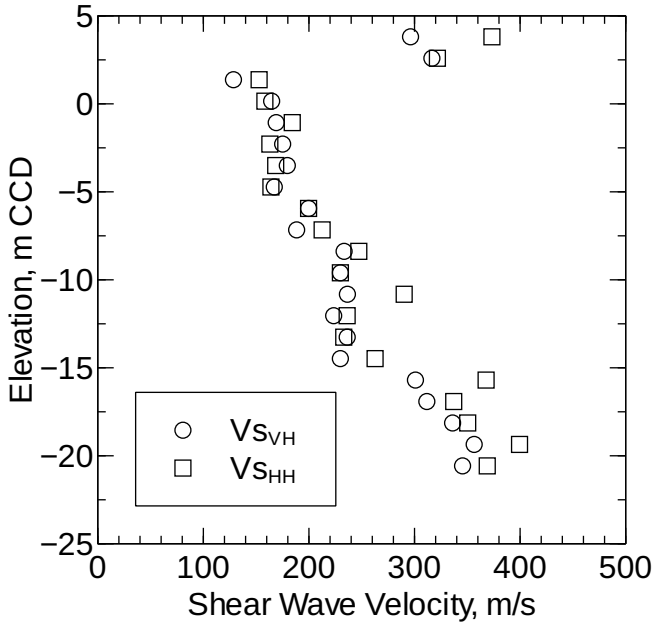

Figure 5.16: Shear Wave Velocity Vs_{HH} and Vs_{VH} measured at the OMPW project site

Numerical manipulation of Equation 5.16 shows that the ratio m_R/r is equal to $G_{VH}\lambda^*/p'$. Given that G_{VH}, λ^*, p' and the natural water content (w_n) can be estimated for each depth where the shear wave velocity was measured, a relation between m_R/r versus w_n can be established and it is shown in Figure 5.17.

Figure 5.17 shows that the relation between the ratio m_R/r and the natural water content, w_n can be approximated as:

$$\frac{m_R}{r} = 190.5 w_n \tag{5.17}$$

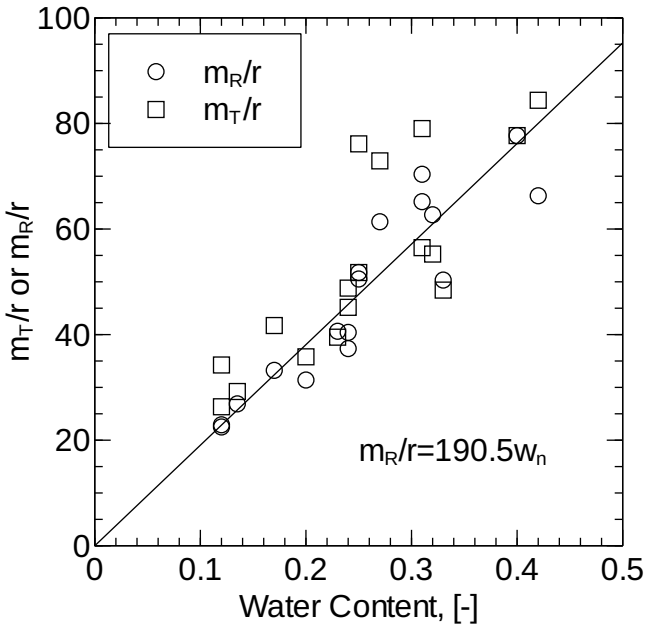

Figure 5.17: Relationship between model parameter m_R/r and void ratio (OMPW data)

Establishing a relationship between m_R/r and the natural water content, in a sense extends the validity of the model parameters to all till layers with varying water content.

5.4. Triaxial Testing Optimization

5.4.1. Finite Element Simulation of Triaxial Testing

The optimized soil model parameters for the HC model to be used to predict the performance of excavations in the Chicago area are estimated using inverse calibration techniques in which triaxial test results performed on soil samples collected in the Chicago area were used as target observations.

Then, the optimized parameters (derived from this optimization cycle) are utilized to calculate the performance of the construction of the OMPW basement structure. The construction performance model predictions are compared to the performance monitoring data to draw conclusions related to the need of performing additional optimization cycles including the initial stages of the performance monitoring data to further refine the magnitude of the constitutive soil model parameters.

This section explains the finite element simulation techniques utilized to model the laboratory tests used as target observations. All results, including the comparison of the observation and predictions of the data used in the first optimization cycle (i.e., triaxial tests) and the observation and prediction of the actual OMPW construction project are presented and discussed in the Chapter 6.

The triaxial tests were modelled using a single four-node quadrilateral finite element (`quad4`) using the commercial computer program Tochnog Professional®. The boundary conditions were changed throughout the simulation to capture the sample recent stress history, from in-situ conditions to the completion of the triaxial tests.

As it is crucial that relevant tests be used for a successful calibration of a material model, the selected tests should be able to capture as close as possible the stress paths that are anticipated in the problem at hand. In this case, the critical stress paths are those observed in a deep excavation. Ng [1999], among others, showed, using field instrumentation and theoretical models that triaxial extension and compression tests can, in general, capture the stress paths in front and behind of the excavated wall, respectively.

Consequently, 21 drained and undrained triaxial compression and extension tests performed on block and Pitcher samples collected at different project sites all across the Chicago area were included in the optimization process. Table 5.2 lists the all the included tests with their test IDs, average sample depth, project site, measured residual stress (σ'_{res}), initial saturation stress (σ'_{sat}), natural water content, overconsolidation ratio (OCR) and horizontal and vertical stress prior to shearing (σ'_{vc} and σ'_{ho}). The reported overconsolidation ratio for each sample used for triaxial testing was estimated from oedometer tests also performed on the soil specimens.

The test IDs that start with B37, FB, LB and O, correspond to samples collected at the Block 37, Ford Center, Lurie and OMPW sites, respectively. The acronyms TC and RTE correspond to triaxial compression and reduced triaxial extension tests, respectively. All the samples from the Lurie and Ford Center were sheared allowing full drainage (i.e., drained triaxial compression and drained reduced triaxial extension tests) and the samples collected at Block 37 and OMPW were sheared in an undrained manner (i.e., undrained triaxial compression and undrained reduced triaxial extension tests). The numeric values included in the test IDs correspond the sample or test number.

TestID	Depth, m [m]	Water Content,% [%]	σ'_{res} [kPa]	σ'_{sat} [kPa]	σ'_{vo} [kPa]	σ'_{ho} [kPa]	OCR [-]	σ'_{vc} [kPa]	σ'_{ho} [kPa]	σ'_{vk} [kPa]	σ'_{hk} [kPa]	Project Site
B37DRTE1	16.29	25	42	42	202.2	105.3	1.1	202.2	131.6	-	-	Block 37
B37DTC1	16.26	24.8	54	54	203.4	105.5	1.1	203.4	132.2	-	-	Block 37
B37RTE1	7.01	27.8	27	27	109.8	62.6	1.2	109.8	65.5	-	-	Block 37
B37RTE2	10.06	21.1	19.9	19.9	138.8	76.5	1.4	138.8	78.8	-	-	Block 37
B37RTE2	10.06	24.8	19.9	19.9	138.8	81.3	1.4	138.8	78.8	-	-	Block 37
B37RTXE4	17.98	22.4	26.1	26.1	201.7	117.9	1.5	201.7	118.6	-	-	Block 37
B37STC1	9.77	23.6	31	31	140.5	77.7	1.3	140.5	93.9	-	-	Block 37
B37TC2	9.45	24.5	29.4	29.4	138.2	74.5	1.2	138.2	83.3	-	-	Block 37
B37TC3	10.21	21.1	20.2	20.2	137.8	76	1.4	137.8	71.2	-	-	Block 37
B37TC4	16.76	22.4	47.3	47.3	200.5	117.2	1.5	200.5	118.6	-	-	Block 37
FB1RTE1	8.23	24.9	38.3	38.3	136.1	86.8	1.7	136.1	78	-	-	Ford Center
FB1TC1	8.38	24.9	37.4	37.4	136.1	86.8	1.7	136.1	75.2	-	-	Ford Center
FB1TC2	8.08	24.9	51.2	51.2	136.1	86.8	1.7	136.1	81.7	-	-	Ford Center
FB2TC2	8.23	24.9	51.2	51.2	136.1	86.8	1.7	136.1	89.1	-	-	Ford Center
LB3RTE1	10.36	29.2	45.9	9.9	133.8	82.4	1.4	133.8	65.9	-	-	Lurie
LB3RTE2	10.52	29.2	47.4	9.7	134.2	82.6	1.4	134.2	65.2	-	-	Lurie
LB3TC2	10.21	29.2	62.1	11.2	134.5	82.8	1.4	134.5	70.9	-	-	Lurie
LB3TC3	10.44	29.2	61.4	20.2	134	82.5	1.4	134	66.7	-	-	Lurie
O1P2TC	24.46	16.9	50	50	269	212.6	3	274.1	196.5	946.7	468.8	OMPW
O2P3TC	25.45	20.9	35	35	279	226.1	2.9	274.3	219	2134.1	1023.4	OMPW
O3P4TC	24.69	17.6	75	75	271	215.0	2.95	270.9	109.6	933.6	372.6	OMPW

Table 5.2: List of triaxial test used for optimization

A detailed description of tests performed on the samples collected at Lurie, Ford and Block 37 are included in Holman [2005], Cho [2007] and Kim [2011], respectively. The test results performed on OMPW samples are partially described in Wang [2011]. As it can be observed, the pool of data includes tests performed on specimens containing a range of void ratio, degrees of overconsolidation and in-situ stress levels that one can expect to encounter for soil in the downtown area of Chicago.

The triaxial testing procedure used for the different tests varied. All samples collected at the Lurie site were saturated using an arbitrarily selected confining stress, which was in general lower than the measured residual stress. Consequently, all tests performed on samples collected at the Lurie site swelled during saturation, prior to consolidation and shearing. After saturation was complete, the samples were reconsolidated monotonically using k_o procedures to a vertical effective stress, σ'_{vc}. The vertical effective stress, σ'_{vc}, was estimated to be equal to the in-situ vertical stress σ'_{vo}. The tests performed on the Ford and Block 37 soil specimens were saturated and consolidated differently. The saturation process was performed using a saturation stress equal to the residual stress, eliminating the swelling cycle applied to the Lurie tests. After the saturation phase was completed, a monotonic k_o consolidation phase to σ'_{vc} was followed.

The OMPW test specimens were also saturated using a stress equal to the residual stress. However, the consolidation phase was not monotonic. The consolidation stresses were first increased using k_o methods to a vertical effective stress (σ'_{vk}) equal to a magnitude similar or higher than the estimated sample pre-consolidation pressure. After the maximum pre-consolidation pressure was reached, an unloading cycle that reduced the vertical stress to in-situ conditions (σ'_{vc}) was applied.

Because the soil samples from the Lurie, Ford, Block 37 and OMPW sites were saturated and consolidated differently prior to shearing, different modelling procedures were used to simulate each test. Different simulation steps tailored to closely represent the stress history from each test, from the in-situ state (prior to sample retrieval) to the triaxial shearing phase, were adopted.

The modelling steps followed to simulate the recent stress history from the soil samples from each site are listed in Tables 5.3, 5.4 and 5.5. Table 5.3 lists the finite element steps followed to model the triaxial tests performed on the Lurie samples. Table 5.4 lists the steps followed to model the triaxial tests performed on the Ford and Block 37 samples. And Table 5.5 displays the finite elements steps followed when modelling the OMPW samples.

Step No	Description	Drainage
0	In-Situ Stresses (σ'_{vo} and σ'_{ho})	Drained
1a	Saturation Stresses (σ'_{sat})	Drained
2	Triaxial Consolidation Stresses (σ'_{vc} and σ'_{hc})	Drained
3	Increase or Decrease Vertical Strain	Drained or Undrained

Table 5.3: Stages for the finite element simulation of triaxial tests used for Lurie samples

Step No	Description	Drainage
0	In-Situ Stresses (σ'_{vo} and σ'_{ho})	Drained
1a	Residual Stresses (σ'_{res})	Drained
1b	Saturation Stresses (σ'_{sat})	Drained
2	Triaxial Consolidation Stresses (σ'_{vc} and σ'_{hc})	Drained
3	Increase or Decrease Vertical Strain	Drained or Undrained

Table 5.4: Stages for the finite element simulation of triaxial tests used for Ford and Block 37 samples

Step No	Description	Drainage
0	In-Situ Stresses (σ'_{vo} and σ'_{ho})	Drained
1a	Residual Stresses (σ'_{res})	Drained
1c	Triaxial Consolidation Stresses (σ'_{vk} and σ'_{hk})	Drained
2	Triaxial Consolidation Stresses (σ'_{vc} and σ'_{hc})	Drained
3	Increase or Decrease Vertical Strain	Drained or Undrained

Table 5.5: Stages for the finite element simulation of triaxial tests used for OMPW samples

The initial step (*Step 0*) in Tables 5.3, 5.4 and 5.5 consisted on initializing the stress boundary conditions to a magnitude equal to the in-situ stress (σ'_{vo} and σ'_{ho}). The horizontal stress (σ'_{ho}) was estimated using the correlation proposed by Chung and Finno [1992], based on overconsolidation ratio and critical state friction angle. In this step, the stresses in the Gauss points of the element were also initialized to have same magnitude as the in-situ stress. In addition to the stresses, the constitutive model state parameters were also initialized. The state parameters that require initialization include the initial void ratio (e_0) and the inter-granular strain tensor h.

The void ratio was computed, following its definition in the HC model, using the expression:

$$e_0 = \exp(N\lambda^* \ln(|OCR_p|) - \lambda^* \ln(|p_0/p_r|)) - 1) \tag{5.18}$$

Where N and λ^* are model parameters defined in Section 5.3, p_r is the reference stress (equal to $1kPa$), p_0 is the estimated in-situ mean normal effective stress, p_e^* is the equivalent pressure at the isotropic normal compression line, as shown in Figure 5.1 and OCR_p is the ratio between p_e^* and p_0. The value of p_e^* is computed from:

$$\ln(p_e^*) = \ln(p_p \frac{3}{1+2k_{NC}}) - \frac{\kappa^*}{\lambda^*} \ln(\frac{p_p}{p_0}) \tag{5.19}$$

where p_p is the mean normal effective stress at the maximum pre-consolidation pressure, κ^* is also a model parameter and k_{NC} is the at-rest pressure coefficient for a soil in a normally consolidated state.

Based on the geologic history at Lurie, Ford, Block 37, OMPW and for most soils in the downtown area of Chicago, the last in-situ geologic loading cycle included the placement of new urban fill at street level. It was assumed that this loading was sufficient to mobilize a vertical strain greater than the model parameter R (defined in Section 5.3.2). Consequently, the inter-granular strain tensor, during *Stage 0*, was initialized with all components equal to zero, with the exception of the vertical direction that was set to be equal to $-R$.

After the completion of *Step 0*, the stresses were increased (or decreased) to the ones corresponding in *Steps 1a*, *1b*, *1c* and *2*, also listed in Table 5.2, using stress control methods. The change in stresses between *Steps 0* and *2* was performed by gradually and simultaneously changing (using linear interpolation) the horizontal and vertical stresses between any two steps. No pore water pressures were allowed to accumulate from *Steps 0* to *2*; hence, the column labeled "Drainage" displayed in Tables 5.3, 5.4 and 5.5 described these steps as "Drained".

In other words, all testing steps prior to shearing were modelled using stress control methods. Consequently, all modelled steps before shear were simulated by imposing the stresses measured during the tests, and not by imposing displacements.

After reaching the end of *Step 2*, the boundary conditions were modified prior to starting the shear phase (i.e., *Step 3*). For numerical stability, the horizontal boundary was changed from a stress control boundary to displacement control. The vertical boundary was set to a constant total stress equal to σ'_{hc}. Pore pressure accumulation was allowed using the penalty formulation only when modelling undrained tests. Vertical positive or negative strains were applied to model triaxial compression or extension tests, respectively. It should be noted that the creep observed in the triaxial testing between the consolidation and the shear phase was not explicitly modelled. This creep cycle cannot be incorporated in the model because the selected HC model does not have facilities to capture time-dependent deformation.

5.4.2. Estimation of Model and State Parameters for Triaxial Tests

Optimization techniques were utilized to estimate the magnitude of the model parameters r, β_r and χ. The procedures used to estimate the remaining seven model parameters were described in detail in Section 5.3; however, for clarity, a summary of the procedures followed during the optimization process is described in this section.

The optimization routine consists of an iterative process. Before each iteration, trial values of r, β_r and χ were assumed to simulate the laboratory tests results using finite elements in an attempt to find the best fit between test results and model predictions. Consequently, before each iteration, the trial values: r_{trial}, $\beta_{r.trial}$ and χ_{trial} are used in conjunction with the known natural water content, w_n, the overconsolidation ratio, OCR, and the in-situ vertical effective stress, σ'_{vo} for each test to compute the remainder of the model parameters following the correlations listed in Table 5.6.

Parameter	Value
e_{LL}	$2.7(0.82w_n + 12)$, assuming $G_s = 2.7$
ϕ'_{cv}, rad	$asin(0.7385 + 0.9384w_n)$
λ^*	$e_{LL}0.0955 - 0.0229$
κ^*	$(e_{LL}0.0955 - 0.0229)/3.5$
k_{NC}	$1 - sin(\phi'_{cv})$
N	$e_{LL}1.104 - 0.2099 + \lambda^*(\log(3/(2k_{NC} + 1)) - \log 1)$, with $p_r = 1kPa$
r	r_{trial}
m_R	$76.0(2.7w_n)r_{trial}$
m_T	$76.0(2.7w_n)r_{trial}$
β_r	$\beta_{r.trial}$
χ	χ_{trial}
R	$5 * 10^{-5}$

Table 5.6: Correlations used to estimate the HC model parameters

And the state parameter e_0, for each test, is defined from the equations provided in Table 5.7.

Parameter	Value
p_0	$\sigma'_{vo}(1+2*(0.53OCR^{0.47}))/3$
p_p	$\sigma'_{vo}(1+2*k_{NC})/3$
p_e^*	$exp(\ln(p_p\frac{3}{1+2k_{NC}})-\frac{\kappa^*}{\lambda^*}\ln(\frac{p_p}{p_0}))$
OCR_p	p_e^*/p_0
e_0	$\exp(N\lambda^*\ln(\lvert OCR_p\rvert)-\lambda^*\ln(\lvert p_0/p_r\rvert))-1)$

Table 5.7: Correlations used to estimate the HC model parameters

It should be noted that most of the model parameters and the state parameters cannot be defined before trial values for r, β_r and χ are adopted.

5.4.3. Evaluation of the Objective Function

In each cycle during the optimization process, after the model and state parameters were evaluation based on the trial values for r, β_r and χ, a finite element simulation of each of the triaxial tests is completed. The results from the finite element simulations are compared to the test data.

Such discrepancy between test data and finite element results are quantified using the objective function shown in Equation 3.5. The objective function is calculated based on the summation residual error measured in each of the test. The residual error for each test is computed using Equation 3.6 using a weighting coefficient equal to one for all observations. In this study, the observations from the test data used to compute the residual error is equal to the deviatoric stresses measured at pre-established strain levels during the shearing portions of the tests.

During the triaxial testing the axial and radial strains were measured using external and internal measuring devices. The internal measuring devices, consisting of LVDTs installed directly on the sample provide reliable readings of strain in the range of 0.03% to 0.5%, while the external measuring device only provide reliable strain measurement higher than 0.5%.

Consequently, since the test data offer reliable information over completely different ranges, for purposes of the optimization process the data collected using internal and external measuring devices were treated as two separate tests. The pre-defined strain levels used to evaluate the deviatoric stresses was established by selecting 30 different points at a constant logarithmic interval over the range of reliable measurements, for the data extracted collected using internal and external strain measuring devices.

5.4.4. Results from the Optimization Process

5.4.4.1. Parametric Evaluation. However, prior to executing the optimization routine using the Leverberg-Marquardt algorithm (LMA), the topology of the objective function was studied. This was accomplished by performing a parametric evaluation of the objective function.

This parametric study was completed by evaluating the objective function using all the laboratory test data presented in Table 5.2 for random values of r, β_r and χ. Therefore, all the tests listed in Table 5.2 were simulated using approximately 50 combinations (trial values) of r, β_r and χ. The random values of r, β_r and χ were selected within a pre-defined domain. The maximum and minimum values in this domain were defined by

the maximum and minimum values reported by Mašín [2011] for different clays. These maximum and minimum values are listed in Table 5.9.

Parameters	Min. Value	Max. Value
r	0.07	0.67
β_r	0.09	0.5
χ	0.7	6.0

Table 5.8: Maximum and minimum reported values for each of the optimized HC model parameters

These values were also used to scale the model parameters using the linear interpolation function defined in Equation 3.1. The magnitude of r, β_r and χ, after applying the scaling function, is defined as r^*, β^* and χ^*, respectively. This magnitude of r^*, β^* and χ^* ranges from zero to one, for all values of r^*, β^* and χ^* within the specified domain. After completing the parametric evaluation of the objective function within the specified domain, the results were linearly interpolated in three-dimensions and equal-error contour plots were generated. These equal-error plots are displayed in three dimensional space in the Figures 5.18, 5.19 and 5.20. For clarity, the contour plots were presented on three different orthogonal planar surfaces defined by $r^* = 0.59$, $\beta^* = 0.21$ and $\chi^* = 0.11$; where $(0.59, 0.21, 0.11)$ is the coordinate in (r^*, β^*, χ^*) space where the minimum error value was encountered.

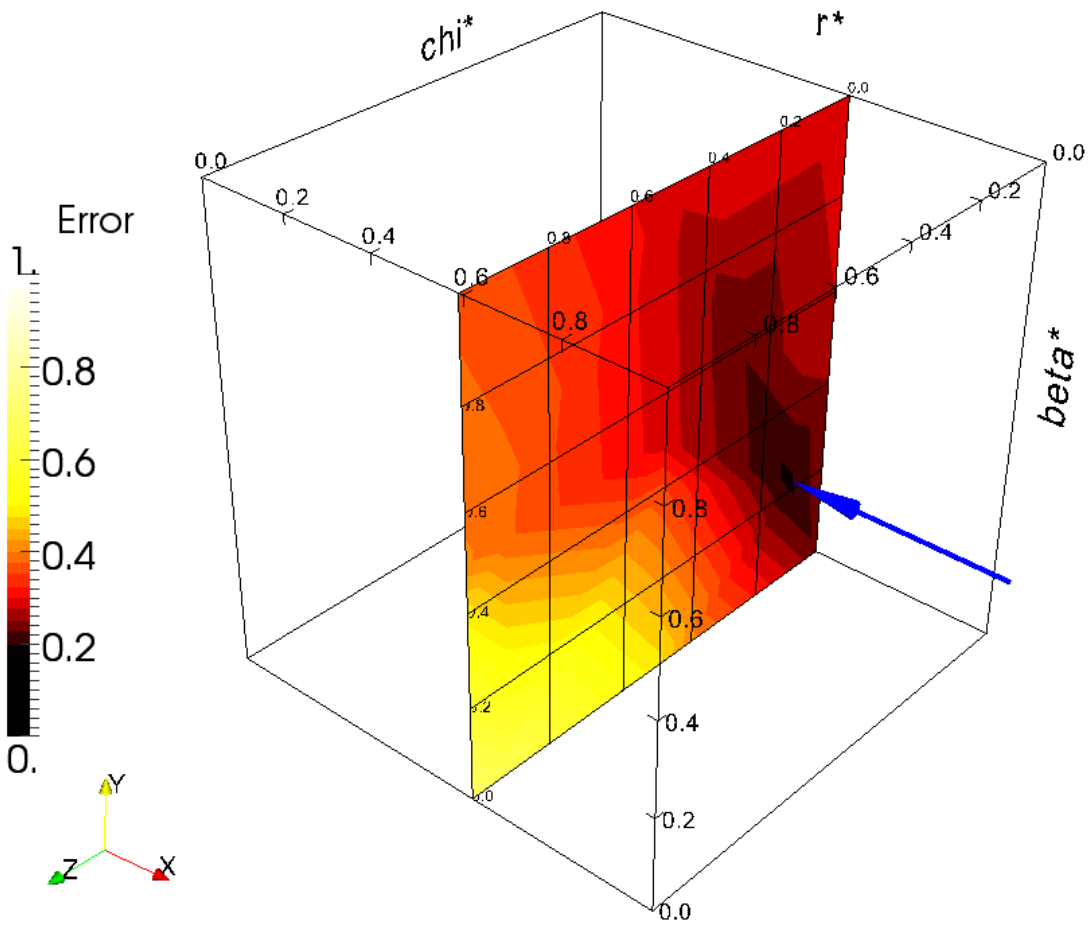

Figure 5.18: Global Error Parametric Evaluation (Surface: $r^* = 0.59$)

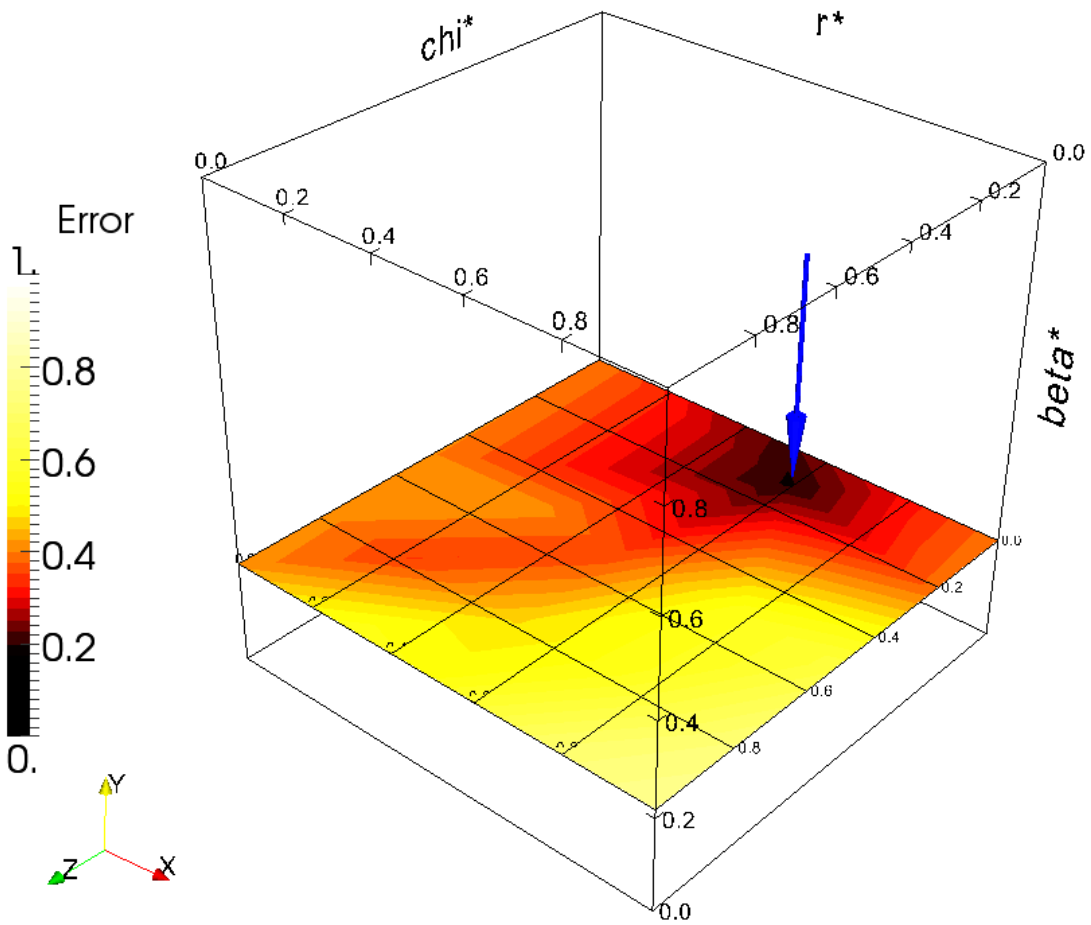

Figure 5.19: Global Error Parametric Evaluation (Surface: $\beta^* = 0.21$)

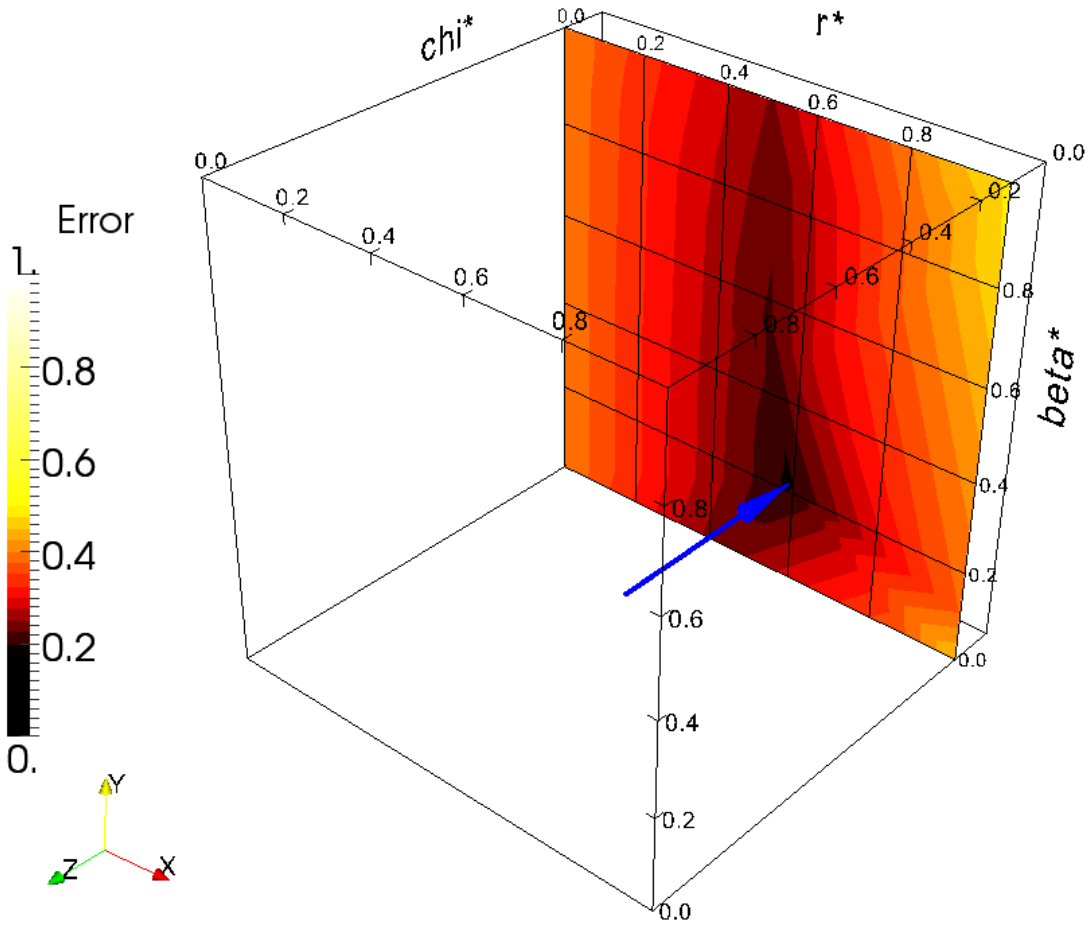

Figure 5.20: Global Error Parametric Evaluation (Surface: $\chi^* = 0.11$)

Figures 5.18, 5.19 and 5.20 show that the topology of the objective function can be described by a series of concentric equal-error surfaces. From this observation, is can be concluded that there is a unique combination of (r^*, β^*, χ^*) that holds the least possible error. Consequently, there is a unique set of parameters r, β_r and χ that provides the best fit to all the triaxial tests used in this first optimization cycle.

In addition, it can also be noted that the magnitude of the model parameter r over the pre-defined range appears to have little effect on the computer error.

5.4.4.2. Optimized Solution. After completing the evaluation of the topology of the objective function using visual inspection, a set of parameters in the vicinity of the solution holding the minimum error was selected as starting point for the automatic error minimization routine discussed in Section 3.1. Such minimization routine arrived to the set of optimized parameters listed in Table 5.9.

Parameters	Scaled Value	Actual Value
r	0.590	0.424
β_r	0.218	0.179
χ	0.109	1.277

Table 5.9: Optimized Parameters after the First Optimization Cycle

The value of the objective function (error), as defined in Equation 3.5, estimated for the set of optimized parameters was 0.194. The location of optimized parameters in (r^*, β^*, χ^*) space is identified in Figures 5.18, 5.19 and 5.20 with an arrow. As expected, the location of the optimized solution is encountered in the area where the parametric evaluations showed the least amount of error.

5.4.5. Observed versus Computed Triaxial Test Results

As explained in Section 3.1.2, the definition of the objective function, $S(b)$ developed for this study, is based on the definition of a residual function, e_i, that is evaluated on a per-tests basis. This residual function, by definition (Equation 3.6) can only adopt values that range from zero to one and express the overall fit between the model prediction and target observations for a given test. The lower the value of e_i, the better the agreement between the test data and the model simulation.

Table 5.10 displays a list of all the laboratory tests utilized in the optimization cycle. The label "e" or "i", shown in parenthesis next to the Test ID, distinguishes whether the data was obtained from the external or internal strain measuring device in the triaxial testing equipment. The error in the prediction of each test, as defined by the residual function, is displayed alongside each of the tests. This table shows that the error, or fit between the finite element prediction and available data, varies from test to test. Figure 5.21 shows a histogram displaying the distribution of error among the simulated laboratory tests. This figure shows that the computed error in approximately 70% of the tests was less than 0.2 and higher for the remainder of the simulations.

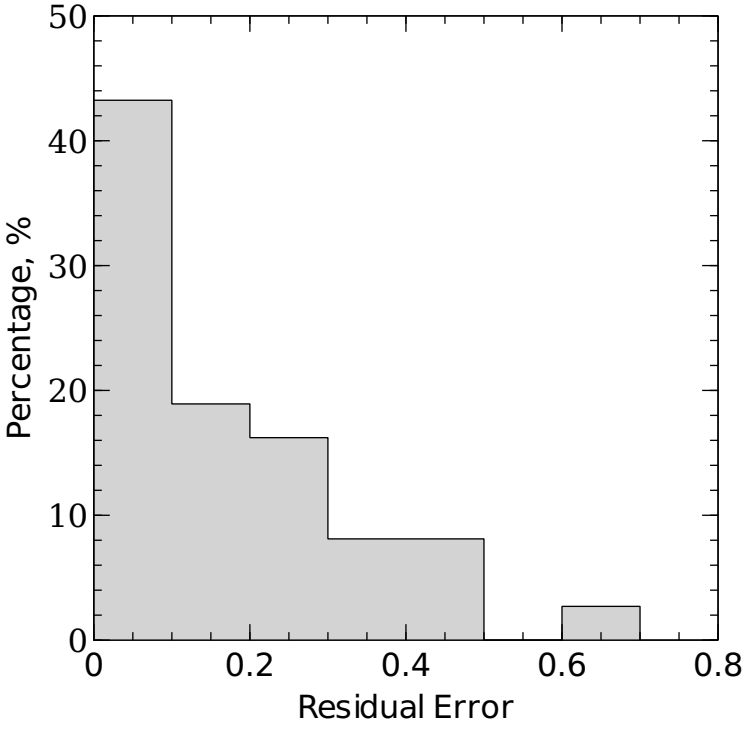

Figure 5.21: Residual error histogram

TestID	Triaxial Test Type	e_i
B37DRTE1(e)	Ck_oU-RTXE	0.282
B37DRTE1(i)	Ck_oU-RTXE	0.49
B37DTC1(e)	Ck_oU-TXC	0.203
B37DTC1(i)	Ck_oU-TXC	0.063
B37RTE1(e)	Ck_oU-RTXE	0.082
B37RTE2(e)	Ck_oU-RTXE	0.104
B37RTE2(i)	Ck_oU-RTXE	0.493
B37RTXE4(e)	Ck_oU-RTXE	0.081
B37RTXE4(i)	Ck_oU-RTXE	0.717
B37STC1(e)	Ck_oU-TXC	0.021
B37STC1(i)	Ck_oU-TXC	0.047
B37TC2(e)	Ck_oU-TXC	0.059
B37TC2(i)	Ck_oU-TXC	0.055
B37TC3(e)	Ck_oU-TXC	0.05
B37TC3(i)	Ck_oU-TXC	0.064
B37TC4(e)	Ck_oU-TXC	0.195
B37TC4(i)	Ck_oU-TXC	0.043
FB1RTE1(e)	Ck_oD-RTXE	0.366
FB1RTE1(i)	Ck_oD-RTXE	0.601
FB1TC1(e)	Ck_oD-TXC	0.089
FB1TC2(e)	Ck_oD-TXC	0.227
FB2TC2(e)	Ck_oD-TXC	0.163
FB2TC2(i)	Ck_oD-TXC	0.249
LB3RTE1(e)	Ck_oD-RTXE	0.097
LB3RTE1(i)	Ck_oD-RTXE	0.362
LB3RTE2(e)	Ck_oD-RTXE	0.409
LB3RTE2(i)	Ck_oD-RTXE	0.255
LB3TC2(e)	Ck_oD-TXC	0.064
LB3TC2(i)	Ck_oD-TXC	0.033
LB3TC3(e)	Ck_oD-TXC	0.046
LB3TC3(i)	Ck_oD-TXC	0.011
O1P2TC(e)	Ck_oU-TXC	0.31
O1P2TC(i)	Ck_oU-TXC	0.237
O2P3TC(e)	Ck_oU-TXC	0.194
O2P3TC(i)	Ck_oU-TXC	0.128
O3P4TC(e)	Ck_oU-TXC	0.179
O3P4TC(i)	Ck_oU-TXC	0.111

Table 5.10: Residual error for each laboratory test

To appreciate how the computed magnitude of the residual is visually reflected on the agreement between the model prediction and the actual test data, a sampling of the test results alongside their model predictions are presented in Figures 5.22 through 5.37. The laboratory test results are displayed toward the left of the figures and the results from the finite element simulations toward the right. The test data collected using internal strain measuring devices are presented in gray color; while the test data collected using external measuring devices are presented in black. Two laboratory tests results alongside their corresponding finite element simulation results were selected from Block 37, Lurie, Ford and OMPW project sites. These two pairs were selected to show one test displaying a "Typical fit" or error, and the other test displaying a "Non-typical fit". The categories: "Typical fit" and "Non-typical fit" are extracted from the distribution of error shown in Figure 5.21. Since most pairs (more than 70%) have an error of less than 0.2, in this study, any pair with an error with less than 0.2 will be said to display a "Typical fit". Pairs with higher error, and worse overall fit, will be called "Non-typical fit".

It should be noted that the complete dataset (i.e., all the utilized laboratory tests results alongside the model prediction) is included in Appendix A.

5.4.5.1. Block 37 results. Typical fit

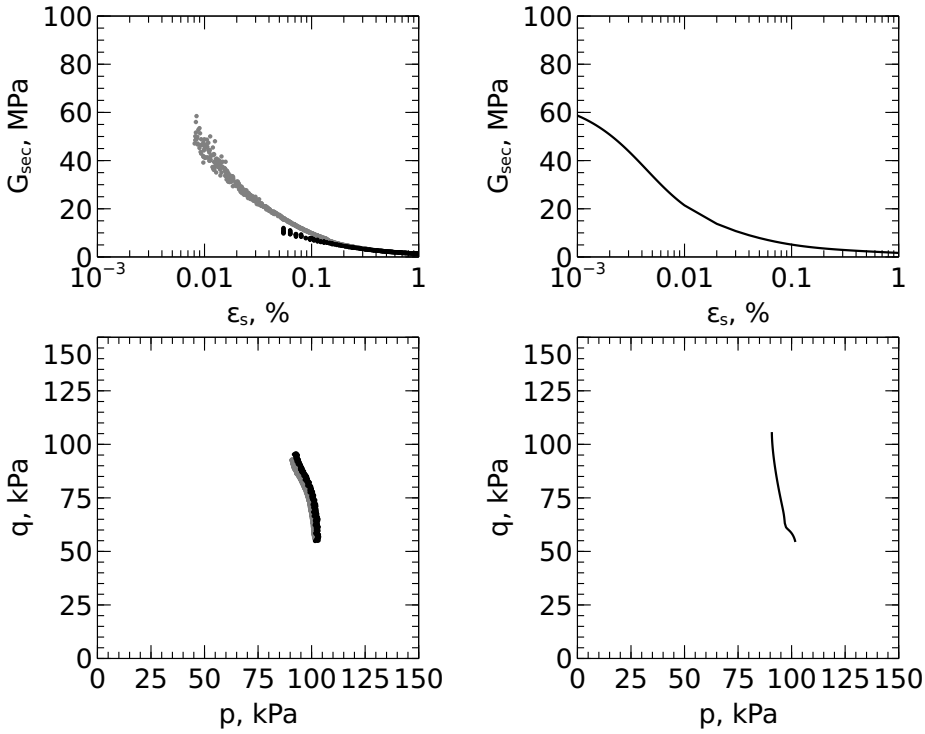

(5.22.1) Data

(5.22.2) Simulation

Figure 5.22: Typical fit, Shear degradation and stress path, TestID: B37TC2

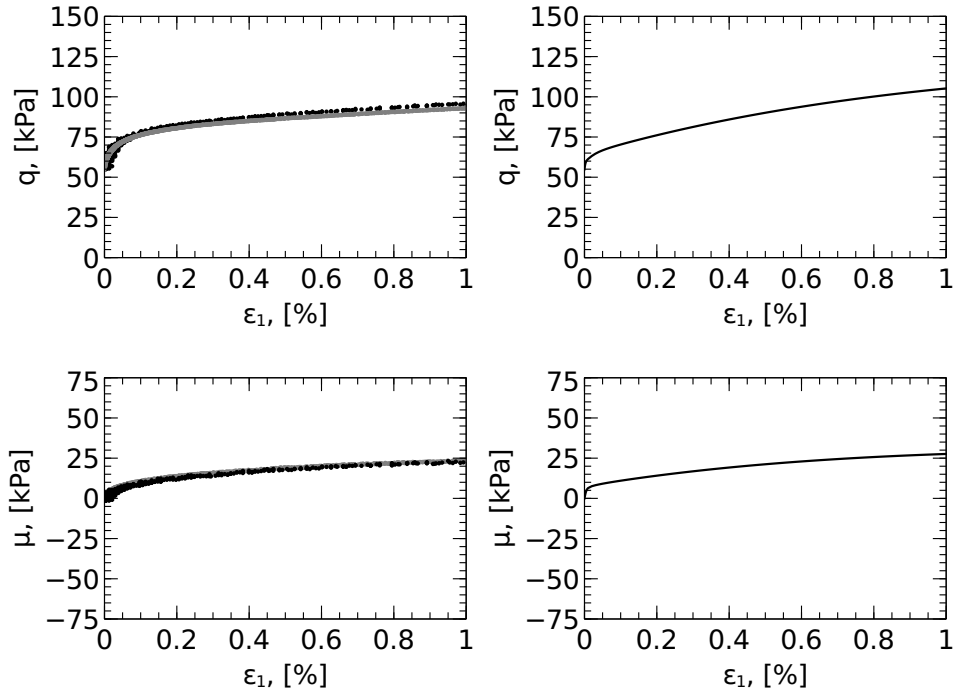

(5.23.1) Data

(5.23.2) Simulation

Figure 5.23: Typical fit, Stress versus strain, TestID: B37TC2

Non-typical fit

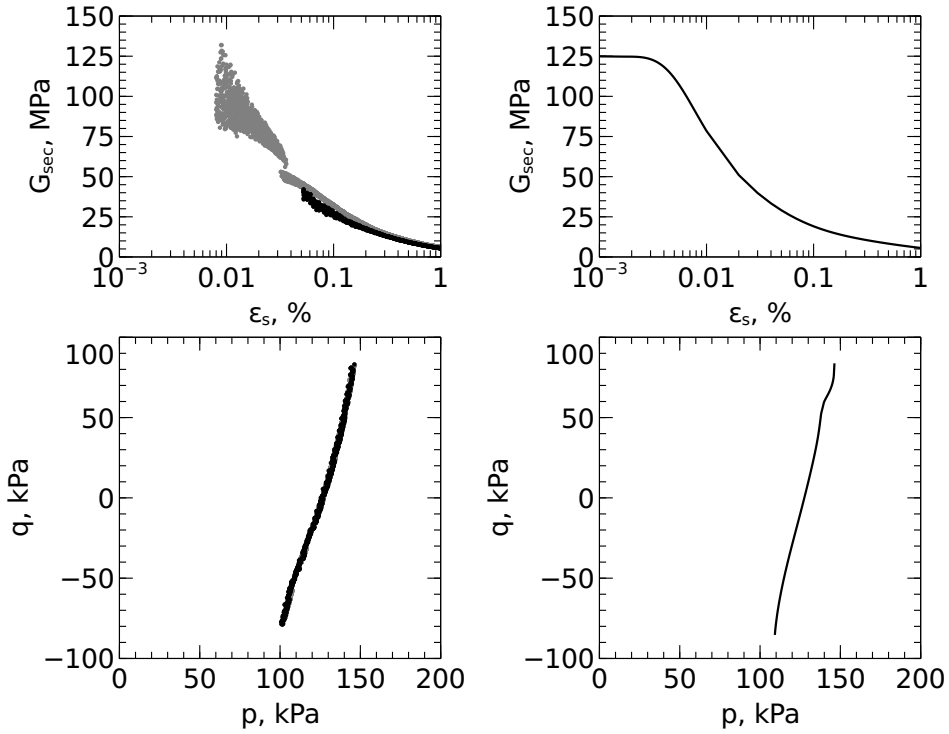

(5.24.1) Data

(5.24.2) Simulation

Figure 5.24: Non-typical fit, Shear degradation and stress path, TestID: B37RTXE4

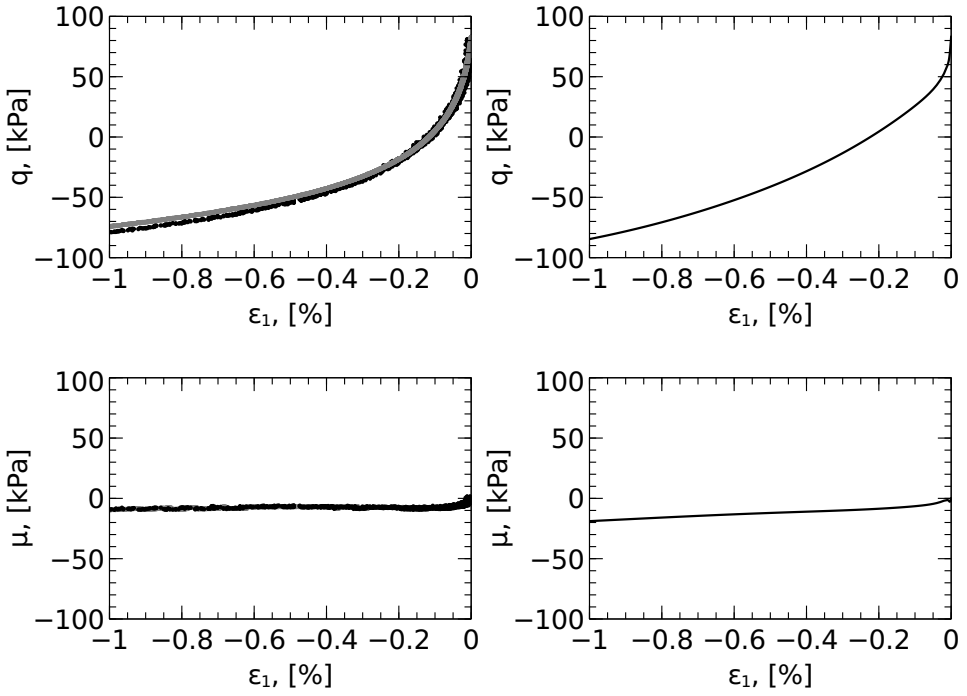

(5.25.1) Data

(5.25.2) Simulation

Figure 5.25: Non-typical fit, Stress versus strain, TestID: B37RTXE4

5.4.5.2. Lurie results. Typical fit

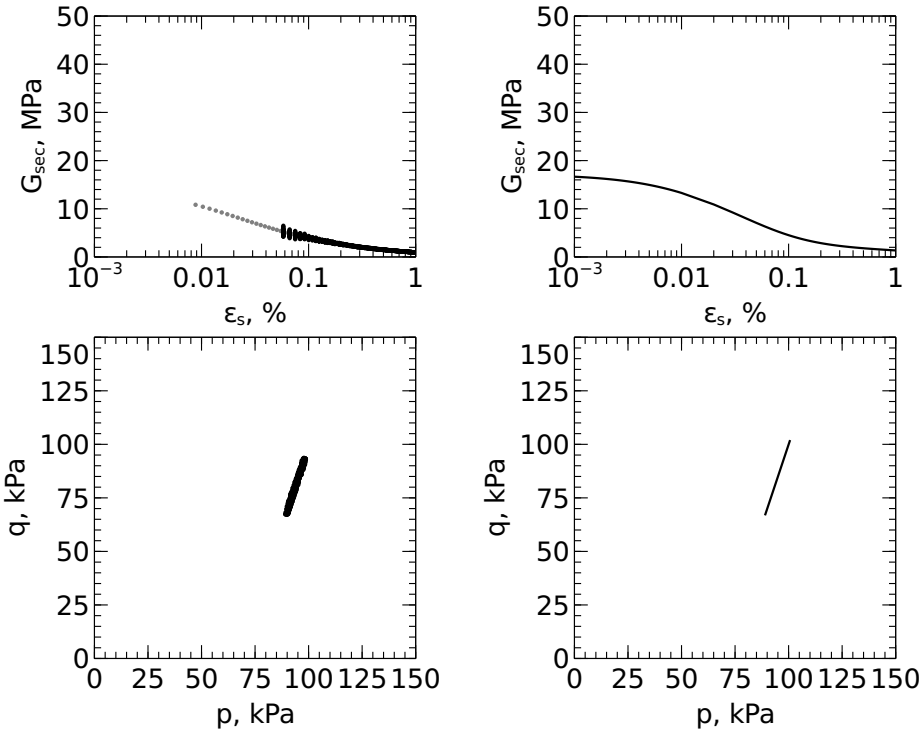

(5.26.1) Data

(5.26.2) Simulation

Figure 5.26: Typical fit, Shear degradation and stress path, TestID: LB3TC3

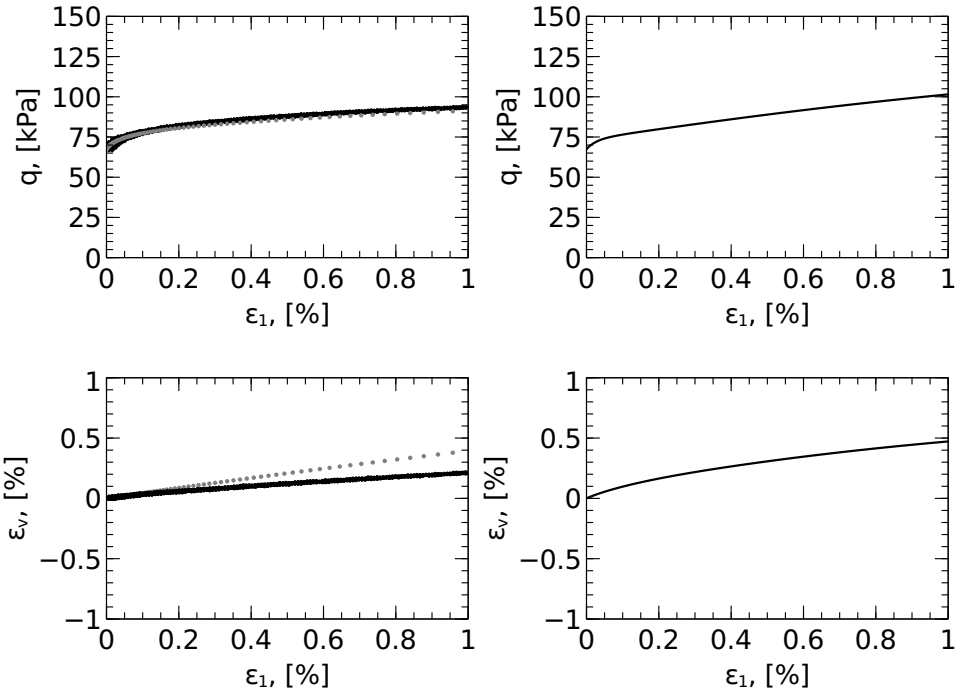

(5.27.1) Data

(5.27.2) Simulation

Figure 5.27: Typical fit, Stress versus strain, TestID: LB3TC3

Non-typical fit

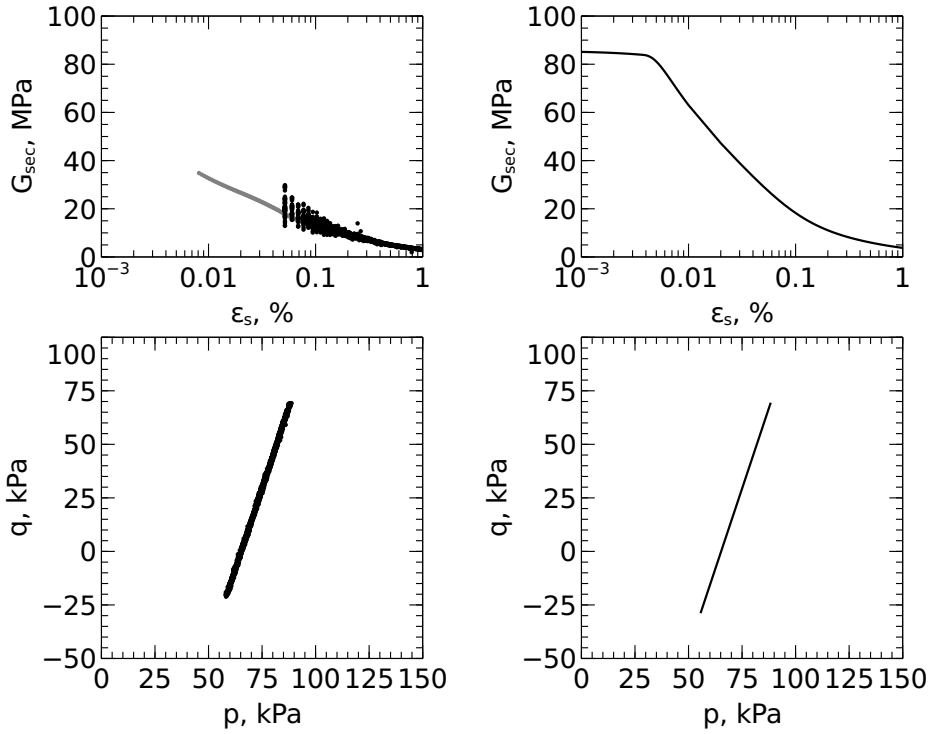

(5.28.1) Data

(5.28.2) Simulation

Figure 5.28: Non-typical fit, Shear degradation and stress path, TestID: LB3RTE2

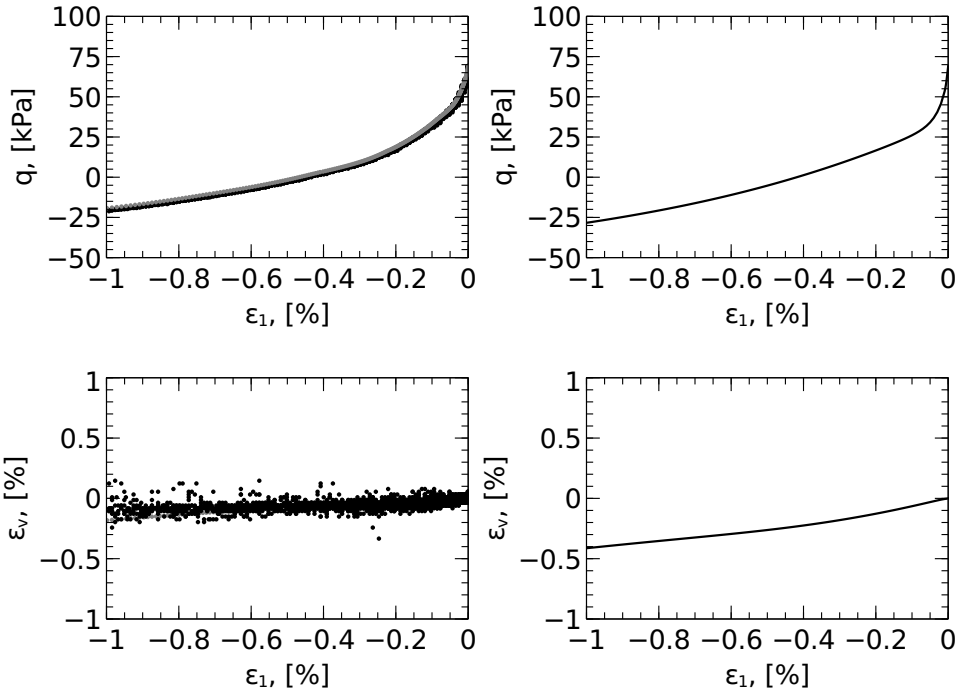

(5.29.1) Data

(5.29.2) Simulation

Figure 5.29: Non-typical fit, Stress versus strain, TestID: LB3RTE2

5.4.5.3. Ford Results results. Typical fit

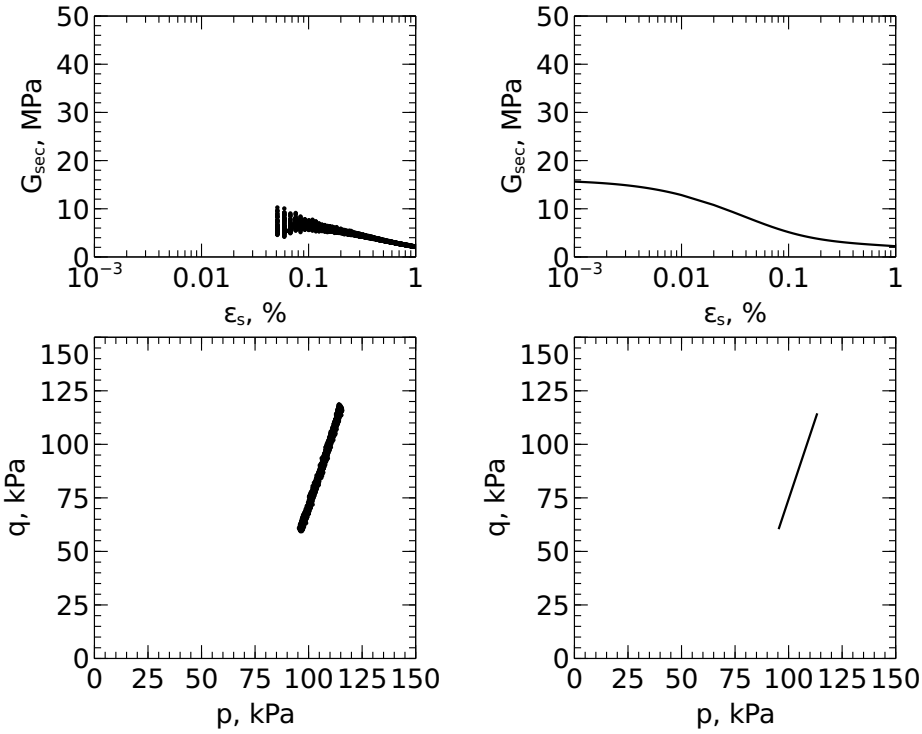

(5.30.1) Data

(5.30.2) Simulation

Figure 5.30: Typical fit, Shear degradation and stress path, TestID: FB1TC1

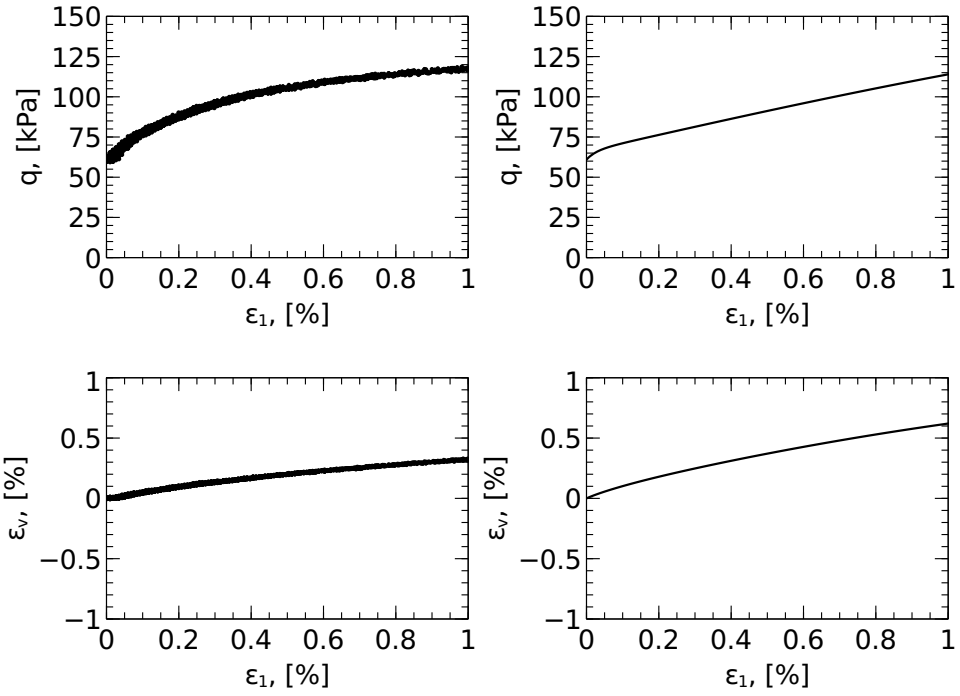

(5.31.1) Data

(5.31.2) Simulation

Figure 5.31: Typical fit, Stress versus strain, TestID: FB1TC1

Non-typical fit

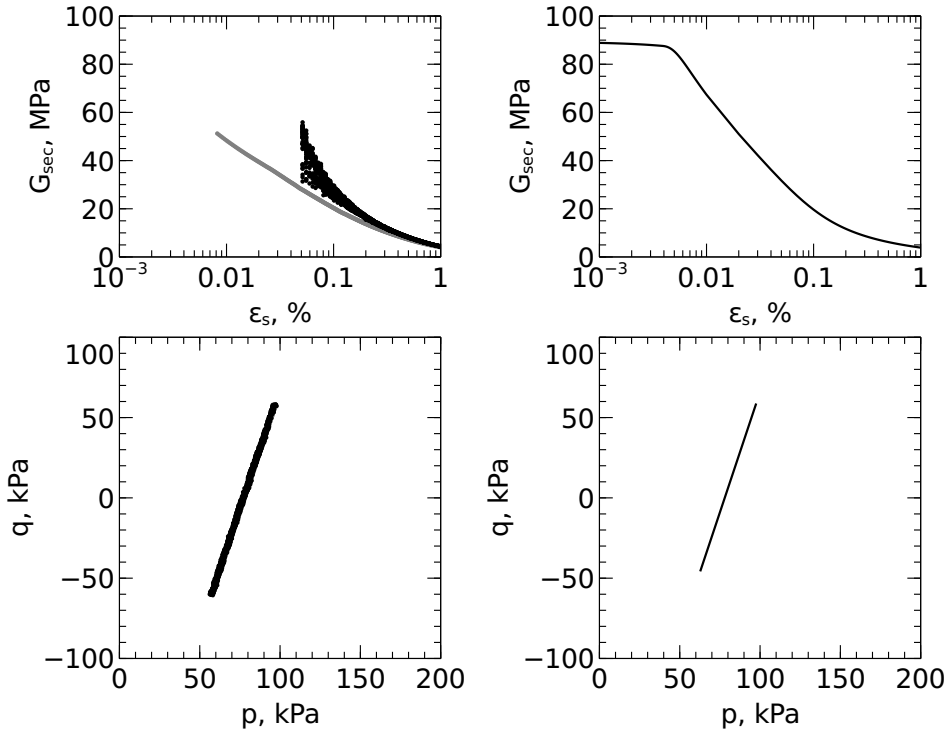

(5.32.1) Data

(5.32.2) Simulation

Figure 5.32: Non-typical fit, Shear degradation and stress path, TestID: FB1RTE1

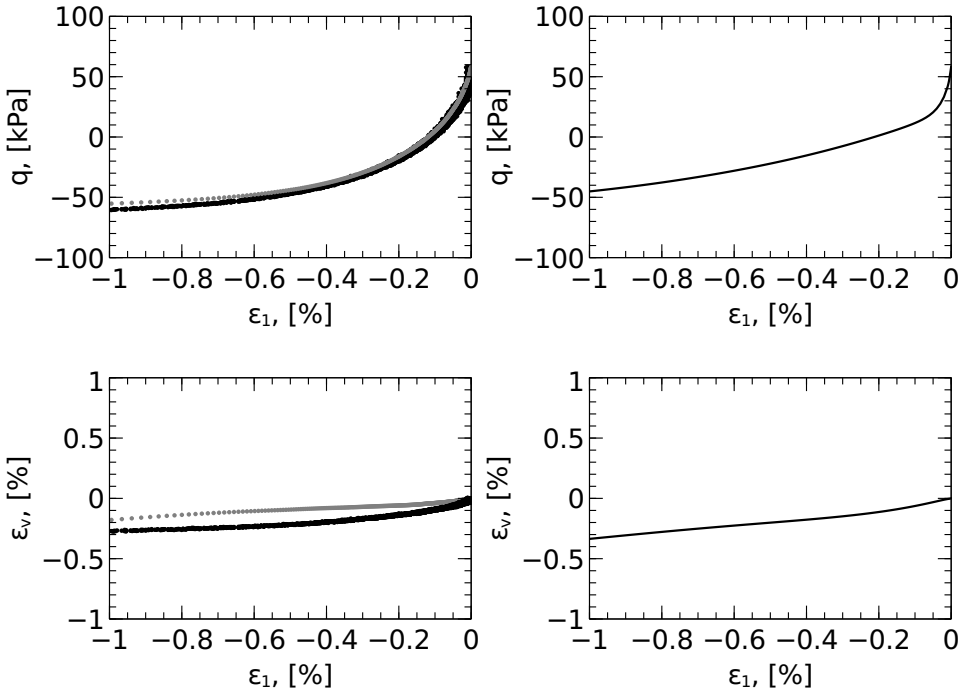

(5.33.1) Data

(5.33.2) Simulation

Figure 5.33: Non-typical fit, Stress versus strain, TestID: FB1RTE1

5.4.5.4. OMPW results. Typical fit

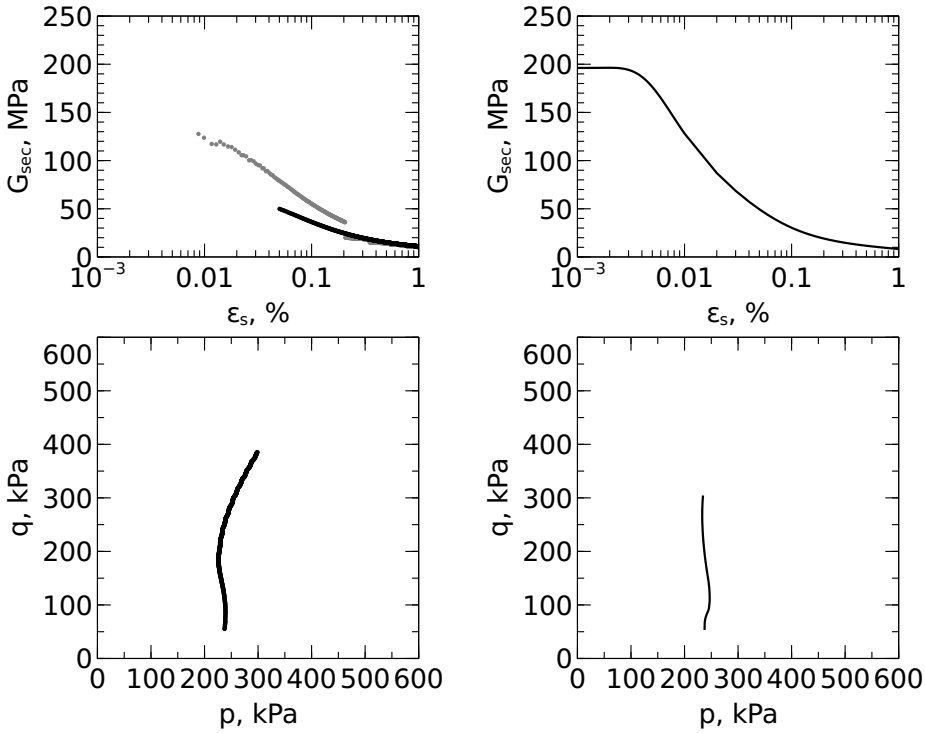

(5.34.1) Data

(5.34.2) Simulation

Figure 5.34: Typical fit, Shear degradation and stress path, TestID: O2P3TC

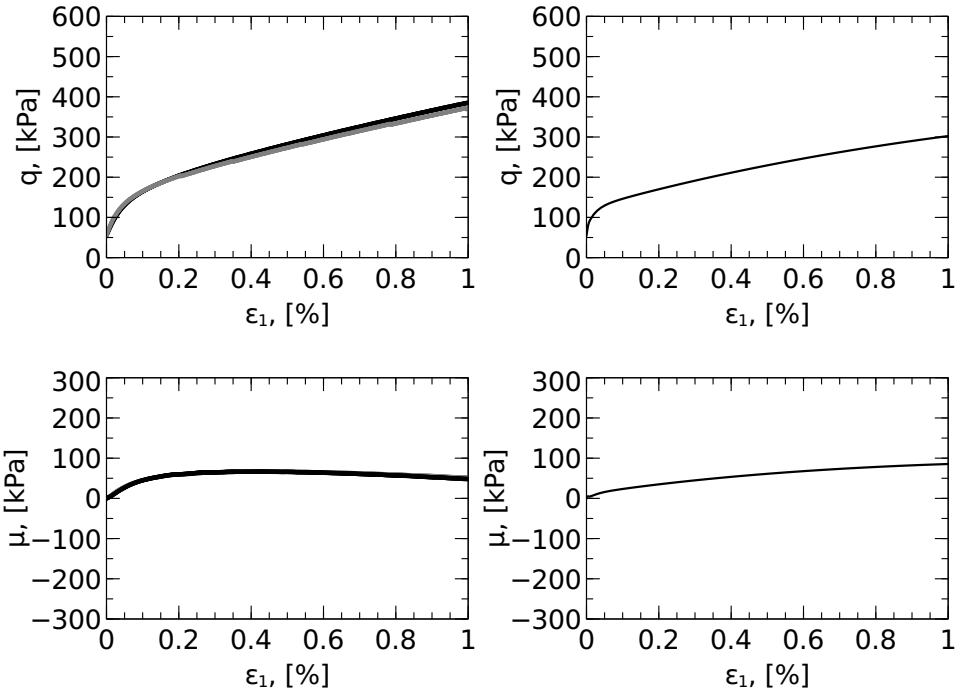

(5.35.1) Data

(5.35.2) Simulation

Figure 5.35: Typical fit, Stress versus strain, TestID: O2P3TC

Non-typical fit

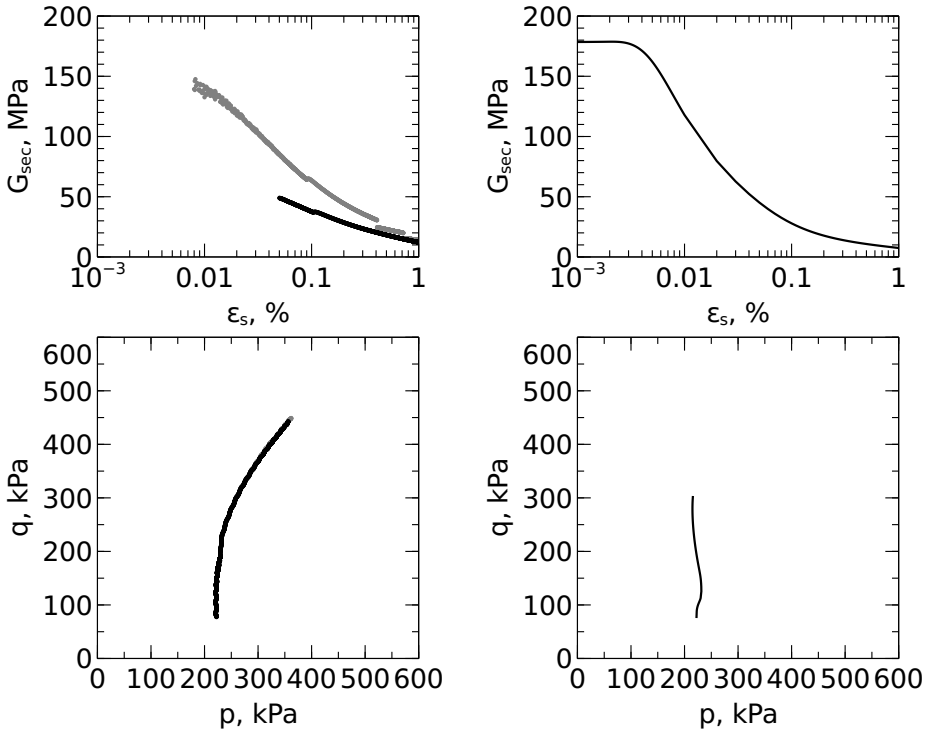

(5.36.1) Data

(5.36.2) Simulation

Figure 5.36: Non-typical fit, Shear degradation and stress path, TestID: O1P2TC

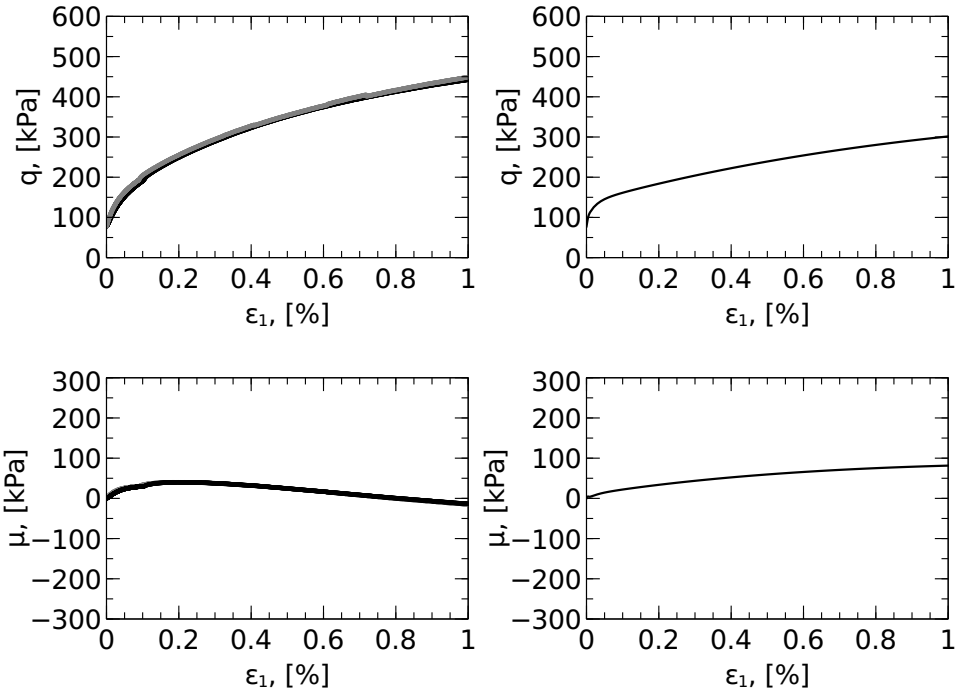

(5.37.1) Data

(5.37.2) Simulation

Figure 5.37: Non-typical fit, Stress versus strain, TestID: O1P2TC

The accuracy of the model prediction presented in Figures 5.22 through 5.37 is reflected by the magnitude of the residual errors displayed in Table 5.10. The geometric mean of the residual errors for all the tests performed on samples collected at the Block 37, Ford Center, Lurie and OMPW sites is equal to 0.11, 0.24, 0.08 and 0.18, respectively. This shows that the highest and lowest accuracy was obtained for the tests performed on samples collected at the Lurie and the Ford Center sites, respectively.

If the calibrated model provided a better accuracy when simulating tests performed on samples from a certain geologic layer, the worse agreement would be observed on samples that have a distinctively high or low degree of overconsolidation or water content. However, the worse agreement was observed in tests performed on samples collected at the Ford Center. The Ford Center soil samples do not have an exceptionally high or low water content and degree of overconsolidation when compared to the rest of the samples. Hence, the calibrated soil model does not seem to favor any geologic layer in particular.

The geometric mean of the residual error for all drained and undrained tests is 0.12 and 0.13, respectively; therefore, the calibrated model does not seem to provide a significantly better accuracy when simulating triaxial tests depending upon the type of drainage during shearing.

Finally, the geometric mean of the residual error for all triaxial compression and extension tests is 0.08 and 0.26, respectively. Consequently, it is clear that a much better accuracy is obtained when simulating triaxial tests sheared in compression.

5.5. Summary

This chapter presented the procedure used to estimate the model parameters of the HC model using laboratory test data to simulate excavations in Chicago glacial tills.

The hypoplastic HC model proposed by Mašín [2006] was selected in this study, because this model was considered suitable for practical applications as it requires a minimum number of parameters, most of which can be obtained from a few standard laboratory tests. This model is based on critical state soil mechanics principles. In addition, the model is provided with the anisotropic Matsuoka-Nakai critical state failure criteria. But most importantly, the HC model is capable of capturing the soil nonlinear anisotropic stiffness from the very small to the high strain levels. The incorporation of recent stress history and small strain stiffness is embedded in the HC model by using the *intergranular strain* concept.

The HC model includes capabilities that allow it to capture changes in stiffness caused by changes in stress levels, density and degree of overconsolidation; however, Chicago clays are composed of till layers. These layers – the focus of this thesis – not only have differences in stress levels, density and degree of overconsolidation, but also have different compositions.

Correlations were established in this study that allows estimating the HC model parameters for the different till layers. These correlations use the natural water content as the dependent variable since this parameter is assumed to reflect the changes in plasticity and composition. Correlations were established to estimate seven of the ten model parameters. The remaining three parameters were computed using optimization procedures.

In general, the model parameters that were not selected for optimization had clear physical meaning and the experimental data needed to estimate their magnitude was available. The parameters that could not be defined based on existing information were selected to be estimated using inverse calibration techniques.

In the optimization procedures used to estimate the three undefined model parameters, finite element simulations were paired with results of sophisticated triaxial test performed on specimens cut from block samples and from Pitcher barrel samples from the OMPW site.

The finite element procedures utilized to model the triaxial tests were presented. The simulation of the triaxial tests was performed attempting to capture recent stress history effects. Hence, all changes in stress from the in-situ conditions (prior to extracting the sample from the subsurface) through all the stress changes during the laboratory tests including the initial saturation stresses, consolidation and shear were explicitly included in the simulation. The creep cycle between the consolidation and shear phases in the triaxial tests was ignored because the HC is not equipped to capture this time dependent response. In addition, to the different finite element stages, the initialization of state parameters, such as density and inter-granular strain were also discussed.

Prior to executing the gradient-based optimization routine, the topology of the objective function was studied. This was accomplished by performing a parametric evaluation of the objective function using values within a predefined range. This study showed that there is a unique set of parameters (r,β_r,χ) that provides the "best-fit" for all the laboratory test data.

After completing the parametric evaluation of the objective function, the gradient-based optimization routine was executed and the optimized model parameters were computed. The definition of the objective function developed for this study is based on the summation of residual errors computed for all of the laboratory test results. The residual error computed for each test was reported. The presented list of residual errors for each test shows that the optimized parameters provide a variable fit for the different tests. In addition to reporting the error from the residual function, the laboratory test data was graphically compared to the finite element simulation in terms of stress versus strain plots, stress paths and shear modulus versus shear strain. These figures, in addition to the reported residual errors, showed that a reasonable agreement was obtained between the test data and model predictions, for most of the cases.

CHAPTER 6

Finite Element Simulation of OMPW

6.1. Finite Element Model

6.1.1. Model Geometry and Boundary Conditions

A fully coupled plane strain finite element model performed with commercial computer program Tochnog Professional® was used to simulate the OMPW excavation along Station No. 2. A structural drawing of the analyzed section is shown in Figure 4.9. A sketch of the finite element model used to represent Section No. 2 is shown below:

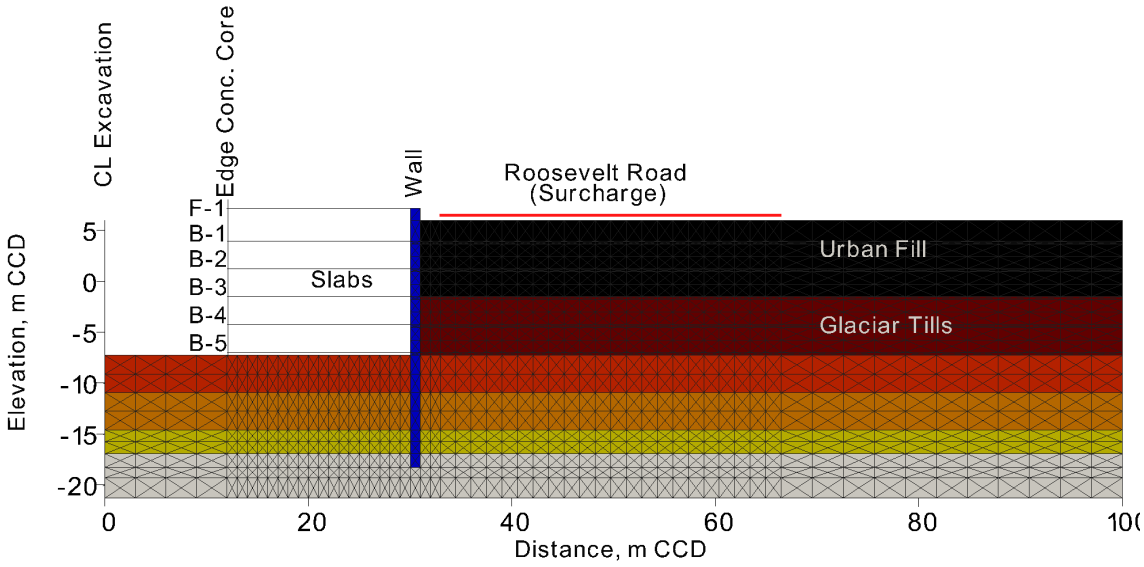

Figure 6.1: OMPW basement excavation finite element model

The finite element mesh was extended from the basement wall toward the South (left in the sketch) to include one half of the whole basement structure. The mesh was extended toward the North (right in the sketch) to the include Roosevelt Road. It Vertically, the finite element mesh was extended to the top of the Valparaiso formation, formed by gravel and boulders laying immediately above the bedrock formation (Elevation -21.3 m, CCD).

The degrees of freedom of the nodes along the vertical boundaries (north and south) were restricted to prevent horizontal movements. The degrees of freedom of the nodes along the bottom of finite element mesh were set to prevent vertical and horizontal movements. Roosevelt Road, including the MSE wall and supporting timber piles were not explicitly modelled. Instead, an equivalent surcharge (equal in magnitude to the vertical pressure applied by the road) was applied over the road footprint. It was considered that any potential gain in modelling accuracy obtained by explicitly incorporating the road and MSE wall in the FE analysis would be hindered by the uncertainty in its soil and material properties. The explicit modelling of the timber piles was not performed because it was considered that because of their limited lateral stiffness, their impact on restraining lateral ground movements would be negligible. In addition, the proper simulation of timber piles would require the use of a three dimensional model, and not the plane strain model used in this study.

Ground water boundaries that prevent flux were imposed on the left and right boundaries of the finite element mesh. The bottom boundary was set to have a hydraulic head equal to the hydraulic head measured at the top of rock formation (equal to -14.5m CCD). A second hydraulic pressure boundary (equal to zero) was imposed to all nodes located at an elevation 0.5m CCD (equal to the elevation of the perched ground water table).

Table 6.1 displays a summary of the different soil layers included in the finite element model. Some basic soil properties and state parameters, such as the unit weight, permeability (k), the overconsolidation ratio (OCR) and at-rest pressure coefficients (k_o and k_{NC}) used to compute the initial conditions are also listed.

Layer	Elev (top) [m]	Elev (bot) [m]	Unit Weight $[kN/m^3]$	k $[m/s]$	OCR	k_{NC}	k_o
Fill	6	−1.52	17.28	0.001			0.43
Blodgett	−1.52	−7.29	18.85	$5E-09$	1.05	0.59	0.6
Deerfield (Upper)	−7.29	−10.95	19.64	$1.6E-09$	1.3	0.44	0.51
Deerfield (Lower)	−10.95	−14.6	19.64	$1.6E-09$	1.3	0.49	0.56
Park Ridge (Upper)	−14.6	−16.95	19.64	$4.1E-10$	4.76	0.45	1.06
Park Ridge (Lower)	−16.95	−19.3	19.64	$4.1E-10$	5.4	0.5	1.16
Tinley	−19.3	−21.3	20.42	$2.5E-10$	3.25	0.4	0.81

Table 6.1: Soil properties for soil layers included in the OMPW finite element model

6.1.2. Constitutive Model Parameters

6.1.2.1. Urban Granular Fill Model Parameters. The superficial fill materials were modelled using a modified version of the Mohr-Coloumb model. In this modified version, the Young's Modulus, E, was set to be dependent (using a power law) on the mean normal stress. The model parameters for this soil model are defined in Table 6.2.

Parameter	Units	Value	Description
E_0^{ref}	-	11610	Reference Stiffness
p_0^{ref}	kPa	100	Reference Stress
α	kPa	0.5	Stress Dependence Coefficient
ν	–	0.33	Primary loading Poisson Ratio
ϕ	degrees	30	Peak friction angle
c	kPa	10	Cohesion Intercept
ψ	degrees	2	Dilatancy angle

Table 6.2: Mohr Coloumb model parameters (with stress dependant stiffness) used for the urban fill

The only difference between the modified version of the model, when compared to the original version, is that the value of E is estimated from the following expression:

$$E = E_0^{ref} * (p/p_0^{ref})^{\alpha} \tag{6.1}$$

Where E_0^{ref} is the Reference Modulus, p_0^{ref} is the Reference Stress and α is the Stress Dependence Coefficient that defines the relationship (power law) between E and the mean normal stress.

The selected stiffness and failure criteria used to model the urban fill are consistent with the model parameters used by Rechea Bernal [2006] and Rechea et al. [2008] to model urban fill in other studies of excavations in the Chicago area. It should be noted that further sophistication in selecting a more advanced soil model would be tarnished by the heterogeneous nature of the urban fill material. It should be recalled that the urban fill material is comprised of a granular fill mixed with construction debris placed in an uncontrolled manner.

6.1.2.2. Glacial Till Layers Model Parameters. The procedure to determine the model parameters of the HC model used for the glacial till layers was extensively discussed in Chapter 5.2.4. A summary table listing the computed magnitude of all the parameters with different values in each layer is presented in the table below:

Layer	ϕ'_{cv}	N	λ^*	κ^*	r	R	β	χ	m_R	m_T
Blodgett	24.2	1.029	0.082	0.023	0.424	$5 * 10^{-5}$	0.179	1.28	28.27	28.27
Deerfield (Up)	34.1	0.635	0.048	0.014	0.424	$5 * 10^{-5}$	0.179	1.28	15.35	15.35
Deerfield (Lo)	30.9	0.759	0.059	0.017	0.424	$5 * 10^{-5}$	0.179	1.28	19.39	19.39
Park Ridge (Up)	33.4	0.66	0.05	0.014	0.424	$5 * 10^{-5}$	0.179	1.28	16.15	16.15
Park Ridge (Lo)	30.3	0.784	0.061	0.017	0.424	$5 * 10^{-5}$	0.179	1.28	20.19	20.19
Tinley	36.7	0.535	0.04	0.011	0.424	$5 * 10^{-5}$	0.179	1.28	12.12	12.12

Table 6.3: HC model parameter for the glacial till layer at OMPW site

In summary, the non-optimized model parameters for each layer were derived following the same procedure described in Section 5.4.2 using, for each layer, the average water content, estimated at-rest pressure coefficients and overconsolidation ratio listed in Table 6.1 as input for the established correlations.

The model parameters r, β and χ have constant values for all layers ($r^* = 0.59$, $\beta^* = 0.21$ and $\chi^* = 0.11$) and they where estimated using the optimization procedures presented in Chapter 5.

The state parameters (void ratio and *intergranular strain* tensor) were estimated in the same way as described in Section 5.4.1. Specifically, the initial void ratio for each geologic layer was estimated using Equation 5.18, based on the overconsolidation ratio profile displayed in Table 6.1. Similarly, for the same reasons described in Section 5.4.1, the *intergranular strain* tensor was initialized with all components equal to zero, with the exception of the vertical direction, where it was set to be equal to $-R$.

6.1.2.3. Structural Slabs. As shown in Figure 6.1, only the portion of the slabs that extend from the wall to the concrete core are included in the plane strain model. The concrete core is assumed to act as an almost rigid support to the concrete slabs. This assumption was explained and justified in Section 4.6.3.

The total anticipated deformation of the modelled slab is caused by the contribution of the elastic compression, creep and shrinkage. Consequently, the total slab strain ϵ can be expressed as:

$$\epsilon = \epsilon_e + \epsilon_c + \epsilon_{sh} \tag{6.2}$$

Where the subscripts e, c and sh are used to represent the elastic, creep and shrinkage strain components, respectively.

The elastic strain ϵ_e occurs immediately after the application of a load. This component can be computed as:

$$\epsilon_e = \sigma_a / E_c \tag{6.3}$$

Where E_c is the concrete elastic modulus and σ_a is equal to the axial stress applied to the slab. ACI [1989] provides an empirical correlation (Equation 6.4) to estimate E_c based on f'_c, which is the concrete compressive strength at 28 days. Both, E_c based on f'_c are expressed in MPa.

$$E_c = 4732\sqrt{f'_c} \tag{6.4}$$

The creep strain is dependent on the stresses applied to the slab. Multiple formulations have been presented in the literature and most of them estimate creep as a ratio of the elastic strain. These formulations include Bažant et al. [1993], ACI [1992], etc. Because of its simplicity and reasonable reported accuracy, the relationships recommended by ACI [1992] were incorporated in this study.

ACI [1992] recommends that in absence of sophisticated creep measurements, the following expressions be utilized to estimate the creep strain:

$$\epsilon_c = v_t \epsilon_e \tag{6.5}$$

Where variable v_t is a time-dependant creep coefficient that can be computed as follows:

$$v_t = 2.35\epsilon_e \gamma_{la} \gamma_\lambda \gamma_h \gamma_T \frac{t_l^{0.6}}{10 + t_l^{0.6}} \tag{6.6}$$

The coefficients γ_{la}, γ_λ, γ_h and γ_T are correction factors for the time of load application, relative humidity, slab thickness and temperature. The variable t_l is the time expressed in days from the application of the load.

The correction values for the conditions at the OMPW project were computed following the ACI [1992] guidelines and their values are listed in Table 6.4.

Variable	Value	Description
γ_{la}	1.00	Loading Age
γ_{λ}	0.73	Ambient Relative Humidity
γ_{h}	0.93	Slab Thickness
γ_{T}	1.00	Temperature Correction

Table 6.4: Creep correction factors

.

If the combined strain caused by elastic compression and creep is denoted by ϵ_{e+c}, it can be shown that that ϵ_{e+c} can be expressed using:

$$\epsilon_{e+c} = \frac{\sigma_a(1 + v_t)}{E_c} \tag{6.7}$$

The finite element modelling strategy used to capture the slab elastic and creep strains includes explicitly modelling the slab as linear elastic elements. This approach would evidently capture the elastic strains in the slab. However, in order to also capture the creep effects, the elastic modulus of the slab could be artificially modified using:

$$E_c(t) = E_c/(v_t + 1) \tag{6.8}$$

It should be noted that $E_c(t)$ (variable with time) can be estimated up-front for each slab (prior to performing the finite element simulation) and can be introduced into the finite element simulation as an input allowing for a straightforward estimate of the combined effect of the elastic and creep components of the slab strain.

It should also be realized that the time-dependency of the slab elastic modulus introduced by $E_c(t)$ – in the finite element model – has no physical meaning. This dependency is adopted simply as an artificial numerical artifact, to capture the correct elastic and creep strains in the finite element model.

On the other hand, shrinkage strain has to be treated and modelled differently from the creep and elastic strains, as its magnitude does not depend on the magnitude of the applied slab stresses. It is assumed in this thesis that any deformation (compression) in the slab due to shrinkage will translate in movement of the wall at the point of contact between the wall and the slab with a magnitude equal to the one of the slab shrinkage. Consequently, if the slab shrinkage can be estimated beforehand, such movement can be directly superimposed (or added) to the computed elastic and creep deformation. This superposition can be accomplished by imposing shrinkage movements to the far end slab nodes (connecting the slab to the concrete core). Consequently, the slab far end nodes are set to have a time-dependent displacement equal in magnitude to the anticipated slab shrinkage.

Similarly to the creep strain, multiple relationships and models have been presented to estimate concrete shrinkage. Probably the most well accepted relationship is also the one proposed by Bažant et al. [1993] and ACI [1992]. In this case the proposal by ACI [1992] was also the one included in this study. ACI [1992] recommends that in absence of sophisticated test information, the following relationship be utilized:

$$(\epsilon_{sh})_t = \gamma_\lambda \gamma_h \gamma_T \frac{t_c}{55 + t_c} 780 * 10^{-6} \tag{6.9}$$

The coefficients γ_{la}, γ_λ, γ_h and γ_T are also correction factors for the time of load application, relative humidity, slab thickness and temperature. The variable t_c is the time expressed in days from the end of concrete curing.

The correction values following the ACI [1992] guidelines and their values are listed below:

Variable	Value	Description
γ_λ	0.58	Ambient Relative Humidity
γ_h	0.88	Slab Thickness
γ_T	1.00	Temperature Correction

Table 6.5: Shrinkage correction factors

The displacement caused by shrinkage can be simply estimated as:

$$\delta_{sh} = (\epsilon_{sh})_t L_s \tag{6.10}$$

Where L_s is the distance from the wall to the concrete core. This displacement (δ_{sh}), variable with time, is directly applied to the far end boundary of the slab.

6.1.2.4. Wall Elements. The retaining wall is composed of secant piles above the maximum excavation depth and tangent piles below. This causes an important variation in the concrete cross sectional area of the wall above and below the cut level. This change in the cross sectional area will consequently create a difference in bending stiffness above and below the cut level.

In the analysis the bending stiffness of the wall above and below the cut level were given different model parameters. The bending stiffness of the secant and tangent portions of the retaining pile wall were analyzed using advanced non-linear concrete and steel

models. These analyses were performed using the commercial computer program SAP 2000®. Specifically, a relation, for both wall sections, between the bending moment and section curvature was derived by enforcing strain compatibility in the wall sections. The Popovic, Thorenfeld & Collins base curve (Collins and Mitchell [1991]) was utilized to represent the concrete stress-stain relationships. The steel was modelled as the "Simple" model (with no strain softening) as described in the SAP2000 material model manual (Computers and Structures [2008]).

The results of these analyses, in terms of a moment versus curvature diagram, are presented in Figure 5.18.

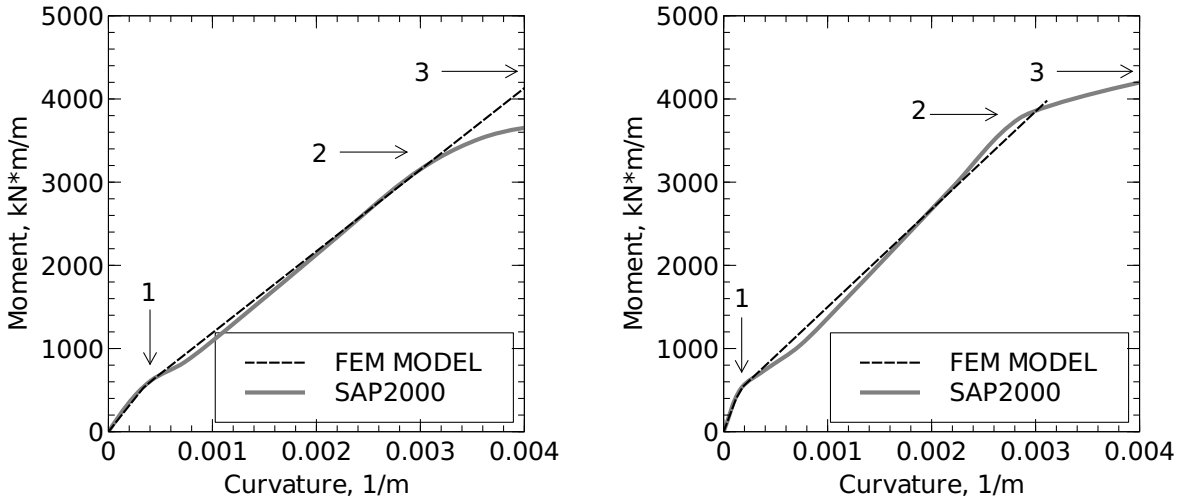

(6.2.1) Tangent Wall

(6.2.2) Secant Wall

Figure 6.2: Moment versus Curvature Diagram for Retaining Wall

Remembering that the slope of a moment versus curvature diagram is equal to the wall bending stiffness (EI); three distinct points that control dramatic changes in bending

stiffness were identified as Point 1, 2 and 3 in Figure 6.2.1 and 6.2.2. Point 1 represents the point at which the initial tensile cracking is observed in the concrete. The second point, Point 2, represents the condition at which the first steel fiber reaches its yield condition in tension. And finally, Point 3 represents the condition where the steel start yielding in compression.

Based on an initial analysis using closed form methods, it was assumed that the maximum anticipated moment in the wall, during the OMPW excavation, will likely exceed the initial cracking bending moment (Point 1), but will not reach the condition where the steel yields in tension (Point 2). This assumption was verified after completing the analysis.

With this in mind, our modelling strategy was focused to capture the changes in stiffness up to Point 2. Therefore, composite members with a simplified bilinear bending stiffness in moment versus curvature space were utilized in the finite element simulation of the excavation. The initial stiffness $(EI)_1$ for our bilinear model was estimated from Figure 5.18 to be approximately equal to $3.333 * 10^6 kNm^2/m$ and $1.571 * 10^6 kNm^2/m$ for the secant and tangent portions of the wall, respectively. The cracking moment, M_{cr} and a second bending stiffness $(EI)_2$ were estimated also for the secant and tangent portions of the wall to be equal to $500 kNm/m$ and $550 kNm/m$, and $1.175 * 10^6 kNm^2/m$ and $0.981 * 10^6 kNm^2/m$, respectively.

Figure 6.3 shows a sketch of the simplified composite member used to represent the wall. This composite member is composed of solid linear elastic elements (`quad4`) and two truss elements (`bar2`), placed in either side of the wall. The truss elements were assigned an elastic-perfectly plastic behavior. The axial stiffness of the truss elements is controlled by the product of the axial stiffness of the truss element $(E_T A_T)$. The maximum allowed

stress (in tension or compression) in the truss element is restricted to f_T. The solid element was assumed to be linear elastic, with a E equal to E_S.

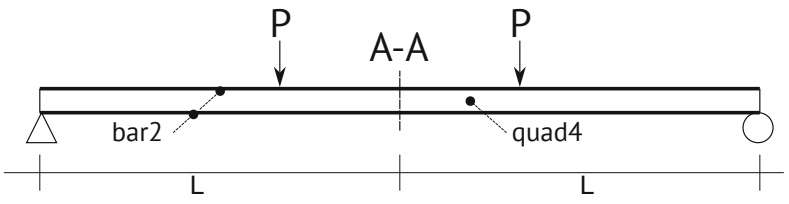

Figure 6.3: Finite Element Analysis Sketch to Verify Composite Member Properties

The modeling strategy consists of identifying the model parameters $E_S I_S$, $E_T A_T$ and f_T that replicate the bilinear target behavior defined by the approximate stiffness $(EI)_1$ and $(EI)_2$ and the cracking moment M_{cr}.

The total moment (M) at any given curvature (Φ) can be separated into the independent contributions of the solid elements (M_S) and truss elements (M_T):

$$M = M_T + M_S \tag{6.11}$$

By definition, the derivative of the moment with respect to the curvature is equal to the bending stiffness. If such derivations are applied to Equation 6.11, one obtains:

$$\frac{\partial M}{\partial \Phi} = \frac{\partial M_S}{\partial \Phi} + \frac{\partial M_T}{\partial \Phi} \tag{6.12}$$

The yield stress (f_T) is selected to enforce the condition that the truss elements yields exactly when the moment M_{cr} is reached. Therefore, it can be shown that for any moment higher than M_{cr}, the second term in Equation 6.12 will vanish resulting in:

$$\frac{\partial M}{\partial \Phi} = \frac{\partial M_S}{\partial \Phi} = (EI)_2 \tag{6.13}$$

Therefore, since $(\partial M_S)/(\partial \Phi)$ is equal to the bending stiffness $(EI)_2$, the model parameter E_S can be estimated as follows:

$$E_S = (EI)_2/(\frac{1}{12}bh^3) \tag{6.14}$$

Where, b and h are the width and depth of the wall, respectively.

In addition, for any condition under pure bending, the curvature can be estimated as:

$$\Phi = \frac{2 * \epsilon_{max}}{h} \tag{6.15}$$

Where ϵ_{max} is the absolute value of the axial maximum strain. And, for any bending moment lower than M_{cr}, M_T can be computed as:

$$M_T = \epsilon_{max} * E_T A_T h \tag{6.16}$$

By combining Equations 6.15 and 6.16, it can be shown that:

$$\frac{\partial M_T}{\partial \Phi} = \frac{h^2 E_T A_T}{2} \tag{6.17}$$

Additionally, by replacing Equations 6.18, 6.13 in Equation 6.12, it can be shown that:

$$E_T A_T = 2\frac{(EI)_1 - (EI)_2}{h^2} \tag{6.18}$$

And then, combining Equations 6.11, 6.15 and 6.16, it can be shown that for a bending moment M equal to M_{cr}:

$$f_T = E_T \frac{M_{cr}}{E_S I_S \frac{2}{h} + E_T A_T h} \tag{6.19}$$

Finally, Equations 6.14, 6.18 and 6.19 can be used to compute the model parameters to be used in the finite element simulation of the excavation, for both the secant and tangent portion of the wall. All computed model parameters for the secant and tangent portions of the wall are listed in Tables 6.6 and 6.7.

Variable	Units	Value	Description
E_T	kNm^2	4315789	Truss Elements Young's Modulus
A_T	m^2/m	1	Truss Elements Cross Sectional Area
f_T	kPa	323.7	Truss Element Yield Stress
E_S	kNm^2	14105263	Solid Element Young's Moduli
I_S	m^4/m	0.0833	Solid Element Moment of Inertia

Table 6.6: Composite beam model parameters for the secant portion of the retaining wall

Variable	Units	Value	Description
E_T	kNm^2	1180593	Truss Elements Young's Modulus
A_T	m^2/m	1	Truss Elements Cross Sectional Area
f_T	kPa	206.6	Truss Element Yield Stress
E_S	kNm^2	11773585	Solid Element Young's Modulus
I_S	m^4/m	0.0833	Solid Element Moment of Inertia

Table 6.7: Composite beam model parameters for the tangent portion of the retaining wall

To further verify the validity of the derived model parameters presented above, a simply supported beam was analyzed using finite element methods. The geometry of the analyzed beam is the one shown in Figure 6.3. A vertical load was applied at the locations identified a P. The curvature and resulting moments were estimated at the center of the beam (Section A-A). The estimated bilinear moment curvature diagram at the center of the beam was extracted from the finite element results and superimposed in Figure 6.2 and labeled "FEM MODEL", further validating this suggested procedure.

6.1.3. Construction Sequence and Simulation Steps

The sequence of construction activities are described in detail in Section 4.6. Table 6.8 shows a summary of the construction activities explicitly incorporated in the finite element simulation of the construction of the basement structure along Station No. 2 of the OMPW project. The table displays four columns, including Step No., Description, Time Start and Time End (expressed in days).

The construction stages described under the "Description" column list the construction activities directly incorporated into the finite element simulation. These activities are simulated (in a finite element sense) through the application of new loads, activation of elements (construction), removal of elements (excavation), or modification of material properties. The Time Start and Time End columns show the finite element integration time. The Construction Day (following the same definition adopted in Section 4.6) is displayed in parenthesis, for reference.

The finite element simulation is started with the initialization of stresses and application of hydraulic and displacement boundary conditions at the beginning of *Step 1*.

Step No.	Description	Time Start, days	Time End, days
1	Initialize Stresses and Boundary Conditions	0 (-10000)*	1 (-9999)*
2	Consolidation	1 (-9999)	6074 (-3926)
3	Reset State Parameters	6074 (-3926)	6075 (-3925)
4	Build MSE Wall	6075 (-3925)	6440 (-3560)
5	Consolidation of Gravity	6440 (-3560)	10090 (90)
6	Installation of Wall	10090 (90)	10305 (305)
7	Consolidation after Wall Installation	10305 (305)	10529 (529)
8	B-1 - Excavation (Fill)	10529 (529)	10536 (536)
9	B-1 - Consolidation	10536 (536)	10549 (549)
10	F-1 Slab Installation	10549 (549)	10579 (579)
11	B-1 - Consolidation	10579 (579)	10641 (641)
12	B-1 - Slab Installation and Curing	10641 (641)	10648 (648)
13	B-1 - Consolidation (...cont)	10648 (648)	10730 (730)
14	B-2 - Excavation (Fill)	10730 (730)	10732 (732)
15	B-2 - Consolidation	10732 (732)	10739 (739)
16	B-2 - Slab Installation and Curing	10739 (739)	10746 (746)
17	B-2 - Consolidation (...cont)	10746 (746)	10780 (780)
18	B-3 - Excavation (Fill)	10780 (780)	10782 (782)
19	B-3 - Excavation (Blodgett)	10782 (782)	10787 (787)
20	B-3 - Consolidation	10787 (787)	10813 (813)
21	B-3 - Slab Install	10813 (813)	10820 (820)
22	B-3 - Consolidation (...cont)	10820 (820)	10858 (858)
23	B-4 - Excavation (Blodgett)	10858 (858)	10876 (876)
24	B-4 - Consolidation	10876 (876)	10884 (884)
25	B-4 - Slab Installation and Curing	10884 (884)	10891 (891)
26	B-4 - Consolidation (...cont)	10891 (891)	10893 (893)
27	B-5 - Excavation (Blodgett)	10893 (893)	10897 (897)
28	B-5 - Consolidation	10897 (897)	11004 (1004)
29	B-5 - Slab Installation and Curing	11004 (1004)	11011 (1011)
30	B-5 - Consolidation (...cont)	11011 (1011)	11026 (1026)
31	Final Inclinometer Reading	11026 (1026)	11123 (1123)
32	Final Strain Gauge Reading	11123 (1123)	11400 (1400)

Note(*) Number in parenthesis is the construction day in relation to that defined in Section 4.6

Table 6.8: Construction steps included in the OMPW finite element simulation

Step 2 is labeled "Consolidation". Multiple "Consolidation" steps are listed in Table 6.8. These steps correspond to stages where the fully coupled finite element integration is continued and the hydraulic boundary conditions are kept constant. This allows for the excess pore water pressures to gradually dissipate. It should be noted that due to the fully coupled nature of the finite element solver, deformations may occur during these steps, as a result of the water pressure dissipation. This initial consolidation step is particularly important to allow the model reach steady-state conditions, considering that non hydrostatic hydraulic boundary conditions were applied in *Step 0*. After a hydraulic steady state condition is reached, in *Step 3*, the HC model state parameters are reset to conform to the values described in section 6.1.2.2 .

Step 4 simulates the construction of Roosevelt Road. This is accomplished by applying a load over the footprint of Roosevelt Road equivalent to the surcharge applied by the elevated road. The load is applied over 365 days that roughly corresponds to the amount of time that took to build the road. After simulating the construction of the road, an additional "Consolidation" step is applied. This step (*Step 5*) lasts for 3650 days (ten years) as this is the amount of time that lapsed between the completion of Roosevelt Road and the beginning of the construction of the perimeter secant pile wall (*Step 6*) at the OMPW project site.

The modelling strategy includes simulating the placement of the perimeter walls as "wished" in place. Hence, the construction of the perimeter wall (*Step 6*) is simulated simply by switching the material model within the wall area from soils to concrete. The `bar2` elements in either side of the wall described in section 6.1.2.4 are also activated. Consolidation step (*Step 7*) follows the construction of the wall, simulating the time that

lapsed, according to the construction records presented in Section 4.6, between the completion of the wall and the beginning of the excavation. Prior to the simulation of the excavation of basement level B-1, all displacements were reset to zero.

Step 8 corresponds to the excavation of level B-1. All excavation steps are simulated by gradually reducing, with time, from the beginning to the very end of the step, the nodal forces within the excavation area to zero. At the end of the step, when all nodal forces are zero, the degrees of freedom of the nodes of the excavated elements are eliminated. In addition, the hydraulic pressure of the nodes in the newly excavated surface (e.g., bottom of level B-1) is used as a new boundary condition and its value is gradually forced to zero. This new hydraulic pressure boundary set to remain equal to zero after the completion of the excavation. *Step 9* includes a consolidation step simulating the time between the completion of the excavation and the installation of the B-1 slab.

Steps 10 and *12* correspond to the installation of slab B-1 and F-1. At the beginning of these steps, `bar2` elements connecting the wall and the concrete core are generated. These slabs are initialized with zero stresses and zero stiffness. The slab stiffness is gradually increased from 0 to 100% of the concrete elastic modulus during this step. After the completion of this step, the E of the slabs are reduced with time as dictated by Equation 6.8. The degrees of freedom (horizontal movement) of the far end node of the slabs (aligned with the concrete core) are also varied with time as dictated by Equation 6.10. After *Step 12*, another consolidation step, simulating the time that lapsed between the placement of the slab and the excavation of the following basement level is applied.

The procedures explained in *Step 8* to *Step 12* are repeated 4 additional times in *Step 13* to *Step 30* to simulate the excavation and slab placement of levels B-2, B-3, B-4 and B-5. Finally, two additional Consolidation steps are applied (*Step 31* and *Step 32*) to simulate the time lapsed from end of construction until the final inclinometer reading was made and last strain gauge data point, included in this thesis, was collected.

6.2. OMPW Computed versus Observed Performance

6.2.1. During Construction Performance

The results from the finite element simulations of the construction alongside the performance monitoring data are shown in Figure 6.4. Specifically, the figure shows the computed horizontal displacement versus elevation alongside the collected inclinometer and optical survey data.

This figure shows a reasonable agreement between the performance data and the finite element simulation, in term of lateral movements. The difference between the observed and computed lateral movement range between almost zero and 3mm, with the largest difference observed during the initial stages of the excavation. The upper 7.7 m of soil at the project site (and in the model) consists of uncontrolled granular fill. Therefore, the disagreement observed during the excavation of the first two basement levels can be partially attributed to the inaccuracy introduced by the model used to represent the uncontrolled fill. The influence of this model becomes less pronounced when the excavation depths extends into the underlying glacial clay, below the urban fill. Consequently, it is expected that the highest discrepancy between observed and computed lateral deflections are observed during the first states of the simulated stages.

A significant disagreement is also observed between the measured and predicted settlements. This disagreement could also be caused by the constitutive model utilized to represent the urban fill. In addition, it should also be recalled, that the optical survey points were located on Roosevelt Road. The Roosevelt Road embankment was not explicitly incorporated in the finite element model. Instead a linear surcharge load was used to

capture the stresses applied by the embankment. Hence, since the embankment was not modeled, the ground surface settlements calculated in the finite element model are estimated at the project site ground surface level. Consequently, the discrepancy between the measured and predicted settlements may be attributed to the deformations that occurred within the embankment, not captured in the model.

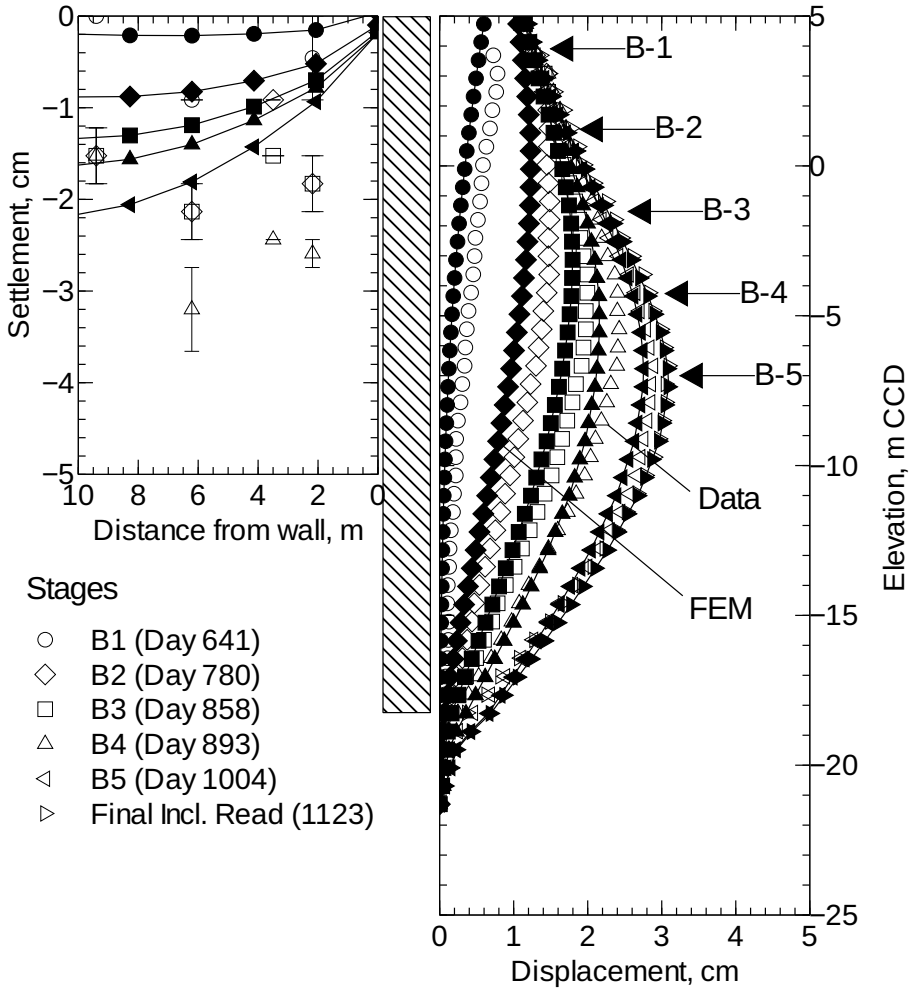

Figure 6.4: Measured versus computed deflection and settlement along ST-2

6.2.2. Post-Construction Performance

Even though the optical survey points and inclinometer data were only collected during construction, strain gauge data were collected for a long period of time after the construction was completed. Hence, to compare the long-term simulated versus predicted performance, the fully coupled finite element analysis of the excavation simulated the additional time after construction completion, when only strain gauge data was collected. The performance after construction completion is presumably controlled by the rate of pore water pressure dissipation and slab creep and shrinkage.

The comparison of long term horizontal movements is presented in Figure 6.5. Figure 6.5 shows the horizontal wall movement versus time at each slab level extracted from the finite element results. These results are displayed in the figure alongside the horizontal movements extracted from the inclinometer and strain gauge data.

This figure shows a good agreement between the observations and model predictions validating the modelling strategy presented in this research of incorporating creep and shrinkage effects into the finite element simulation.

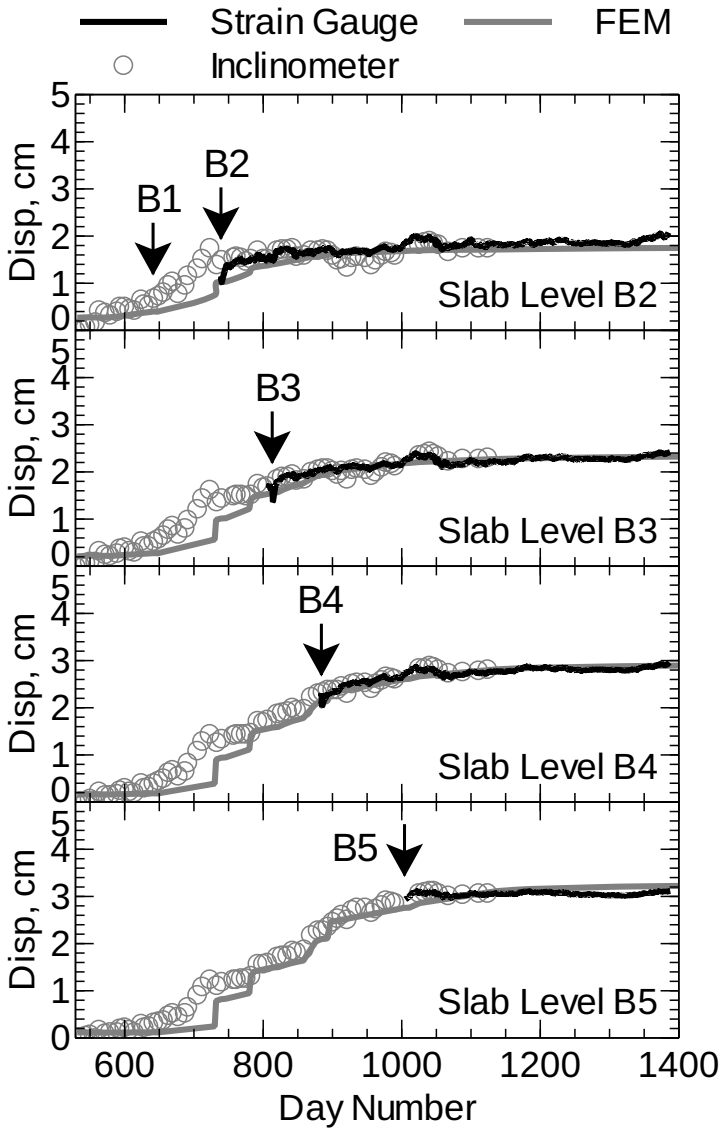

Figure 6.5: Measured versus predicted horizontal ground movements at each slab level along ST-2

6.2.3. Effects of Small Strain nonlinearity

As stated in Chapter 1, one of the objectives of this work was to study the importance of small strain nonlinearity on the prediction of ground movements for deep excavations. In Chapter 3 it was explained that the HC material model is composed by a reference model that is extended to capture stiffness at small strains using the *intergranular strain* concept.

If the *intergranular strain* concept is suppressed or removed from the model, the HC model is no longer able to predict changes in stiffness at small strain levels. For comparison purposes, the simulation of the OMPW basement construction was repeated suppressing the *intergranular strain* extension. The results are shown in Figure 6.6.

Figure 6.6 shows that ignoring the small strain stiffness results in an over-prediction of ground movements. The comparison of Figure 6.6 with Figure 6.4 shows that when the small strain stiffness is suppressed, larger horizontal ground movements are observed, in particular, in the hard glacial till layers next to the toe of the wall.

The small strain stiffness is partly mobilized during ancillary construction activities performed prior to the main excavation, such as the installation of foundations and perimeter walls. These ancillary activities were not explicitly included in the simulation of the OMPW excavation. However, sufficient field data exists that shows that these ancillary activities primarily affect the shallower soft clays and do not significantly affect the underlying hard glacial tills.

Therefore, if it is assumed that the state of stress of the glacial clays has not been significantly disturbed from their condition prior to the beginning of all construction activities,

the comparison of Figure 6.6 with Figure 6.4 would show the importance of incorporating small strain stiffness effects to properly model hard glacial clays.

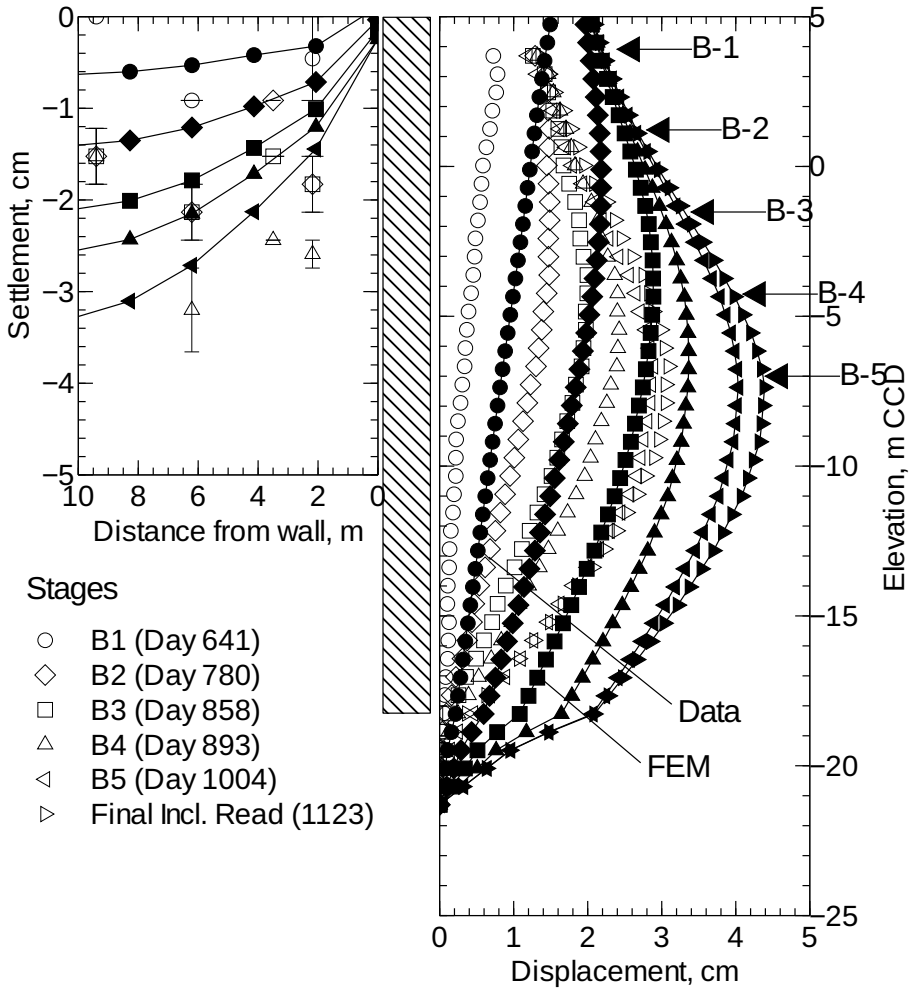

Figure 6.6: Measured versus predicted deflection and settlement along ST-2 ignoring small strain stiffness)

6.2.4. Effects of Slab Creep and Shrinkage

To investigate the benefits of incorporating creep and shrinkage into the finite element simulation of the OMPW excavation, the finite element simulation was repeated ignoring creep and shrinkage effects. In this revised analysis the slabs were assumed to have a linear elastic behavior. The time-dependent behavior of the slabs discussed in Section 6.1.2.3 was not included in the analysis. The small strain nonlinear behavior of the clay layers were incorporated in this simulation.

Figure 6.7 shows the results of this revised analysis. This figure shows that the wall movement can be largely underpredicted if creep and shrinkage effects are ignored.

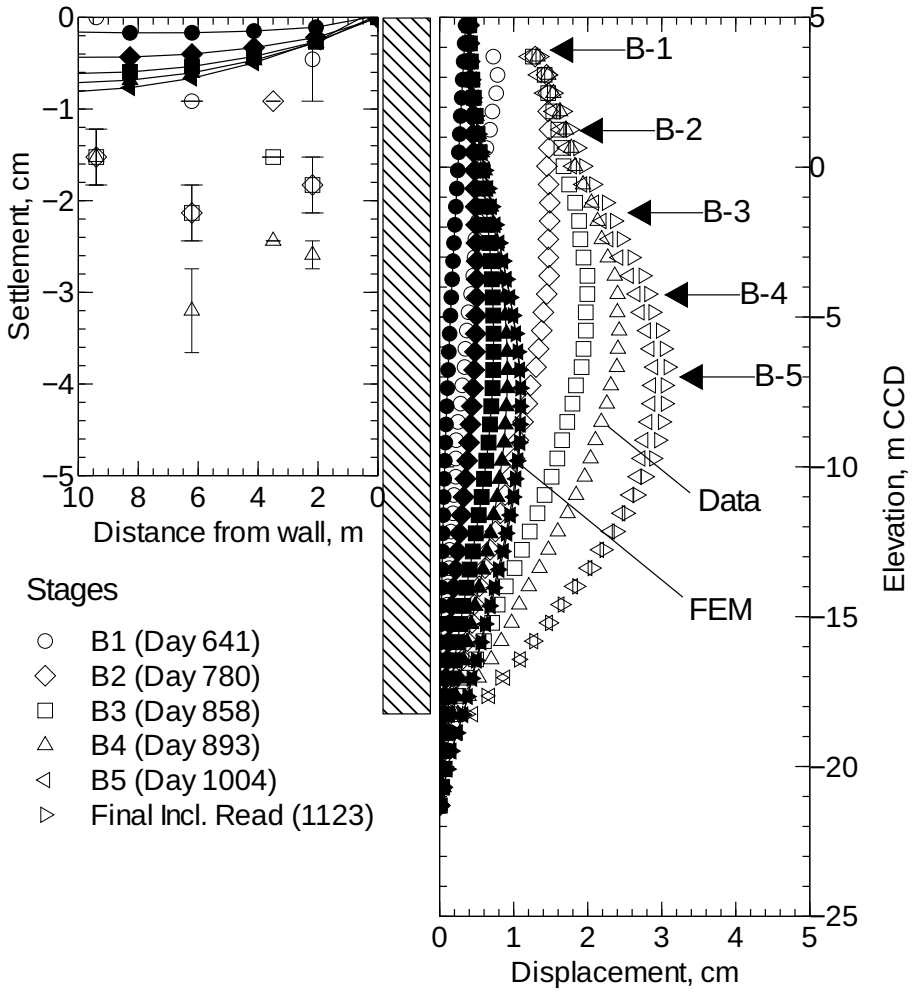

Figure 6.7: Measured versus predicted deflection and settlement along ST-2 ignoring slab creep and shrinkage

6.2.5. Effects of Wall Nonlinear Bending Stiffness

The effects of the nonlinear bending stiffness of the wall elements, discussed in Section 6.1.2.4 were also further studied. For this purpose, the analysis of the OMPW excavation was revised. In this revised analysis the wall elements were assumed to have a linear elastic behavior. Hence, the bending stiffness degradation observed after M_{cr} is exceeded was ignored. In this revised analysis, the soil small strain nonlinearity and slab creep and shrinkage effects were included.

Figure 6.8 shows the result of this revised analysis. This figure shows that there is no significant difference between the computed deflections shown in Figure 6.8 and the ones shown in Figure 6.4. This observation is to some extent surprising considering the maximum computed bending moment in the wall, for the case where the non-linear bending stiffness of the wall was considered, was equal 1763 kNm/m; and this computed bending moment largely exceeds the value of M_{cr} (equal to 550 kNm/m).

However, the historic data presented by Clough et al. [1989] and Long [2001] showed that the system stiffness has little relation with the observed ground movement for cases where the excavations are performed in clays, using stiff retention systems, with a high factor of safety against basal heave. Consequently, the similarity in the computed ground movements considering different wall bending stiffness (linear and non-linear) agrees with the historic test data.

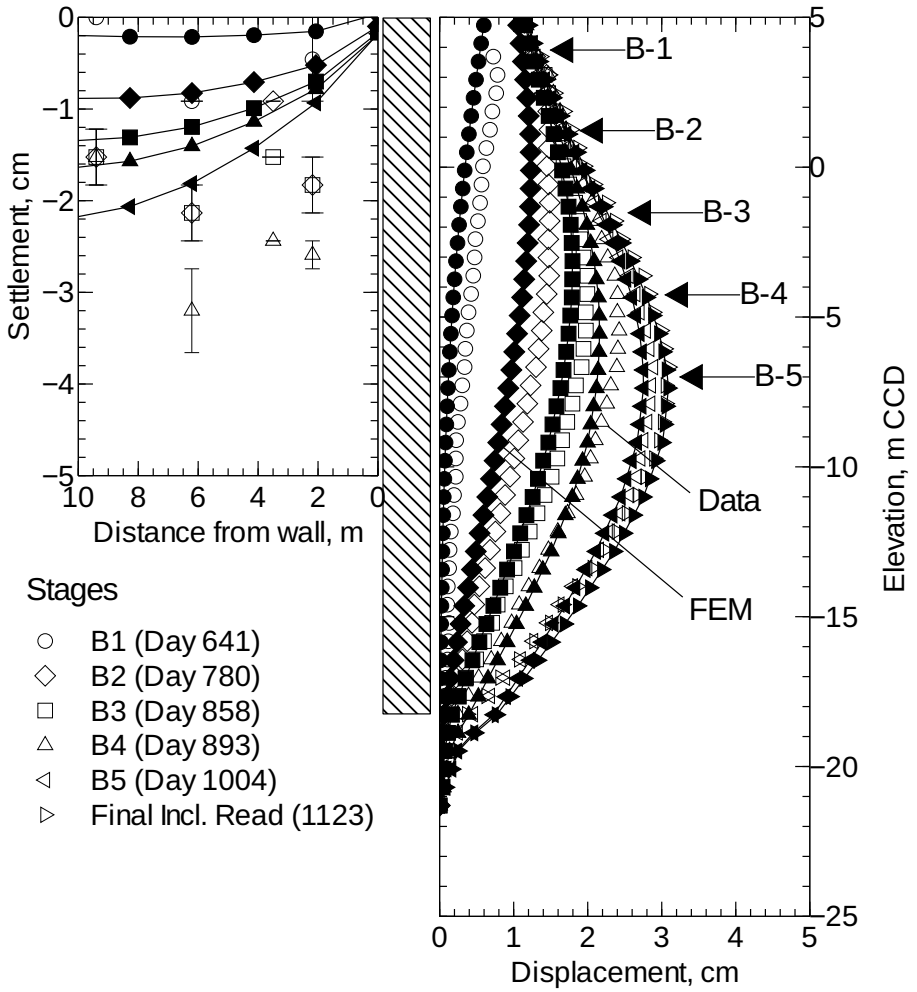

Figure 6.8: Measured versus predicted deflection and settlement along ST-2 ignoring wall nonlinearity

6.3. Summary

The finite element strategy utilized to model the actual basement construction at the OMPW project was discussed in this chapter. A fully coupled plane strain analysis was used to simulate one of the sections (Section No. 2) at the OMPW site. A detailed description of all the construction steps explicitly included in the finite element simulation was listed.

Additional aspects considered necessary for the proper simulation of the basement construction, affecting the structural elements of the basement structure were also presented. Specifically, a simple strategy that allows capturing the nonlinear bending stiffness of the retaining walls was developed for this study and presented in this section. In addition, the slabs response to load and time (i.e., elastic, creep and shrinkage strains) were included in the finite element model based on the guidelines provided by ACI [1992].

The computed optimized model parameters obtained in Chapter 5 were utilized to perform the finite element simulation of the construction of the OMPW basement structure. The results from the finite element simulation were compared to the performance monitoring data; this comparison showed an overall reasonable agreement between field observations and computed performance. However, the finite element simulations showed a significantly better agreement with performance data when comparing horizontal ground movements than when comparing the vertical ones.

The effects of small strain stiffness on the computed ground movements at OMPW were studied by suppressing the *integranular strain* extension of the HC model. This revised analysis showed that the small strain stiffness is needed for the proper prediction of displacements in overconsolidated clays till layers. It was also shown that ignoring creep

and shrinkage effects results in a large underestimation of displacements. Finally, it was also determined that the bending stiffness of the wall elements is not very critical in determining wall movements when the factor against basal heave is large, in agreement with prior observations made by Clough et al. [1989] and Long [2001].

But more importantly, this thesis provides evidence that if sample disturbance is minimized and if an adequate constitutive soil model that properly captures recent stress history effects and changes in stiffness from the very small to the large strain levels, multiple laboratory and field conditions can be modelled with a single set of parameters. This research emphasizes the importance of incorporating small strain nonlinearity when modelling excavation support systems, and not only for cases where small ground movements are expected, as it could be presumed, but also in cases where large movements occur, such as the OMPW site.

CHAPTER 7

Summary and Conclusions

The main objective of this thesis was to enhance the capability to predict both, field performance of excavations in Chicago and laboratory test data, using FE methods using a single set of model parameters. The methodology used to estimate the soil model parameters was based on optimization techniques.

Multiple successful attempts exist in the literature that includes the estimation of model parameters using optimization techniques for predicting laboratory or field performance, but not both. The inability to match both, field performance and laboratory test data, with a single set of model parameters is often attributed to disturbance existing in the samples used for soil testing. Another possible cause for the discrepancy is the selection of an inadequate constitutive model to represent the complex behavior of soils.

This thesis attempted to overcome these potential problems by utilizing, primarily, high quality test data performed on specimens cut from block samples to eliminate or reduce the disturbance effects. In addition, an advanced constitutive hypoplastic soil model developed by Mašín [2006] (HC model) was used to represent the soil behavior. The HC model is defined by ten model parameters and it is capable of capturing changes in stiffness from the very small to very large strain levels. In addition, it is formulated to be consistent with the principles of critical state soil mechanics using density as an state variable to capture changes in soil response at different overconsolidation ratios (OCR). It is also provided with an anisotropic failure law that allow is to properly represent

failure when the soil is sheared under different stress paths. The stratigraphy in Chicago consists of a series of glacial till layers with varying degrees of OCR. These layers also have variable compositions, reflected in observed changes in their Atterberg limits. For Chicago clays, as shown by Peck and Reed [1954], these changes in plasticity are directly related to changes in the natural water content of the different till layers. Consequently, for the proper selection of the model parameters, the variability of composition and OCR between the glacial till layers must be taken into account.

The first step to estimate the constitutive model parameters for the HC model included developing correlations that allow estimating seven of the ten model parameters. These correlations used the OCR and the natural water content as the dependent variables. The natural water content was selected as this parameter is assumed to reflect the changes in plasticity and composition. The remaining three parameters were computed using optimization procedures.

The three remaining model parameters were optimized using the results from triaxial test results as target observations. The triaxial tests used in the optimization process included drained and undrained triaxial compression and extension tests performed on samples collected at different project sites across the Chicago area. In the optimization process, all the triaxial tests were simulated using finite element methods and the three HC model parameters were estimated to provide the best possible fit between simulated results and test data, in terms of deviatoric stress versus axial strain. The result from this optimization process showed that a reasonable agreement between test data an model prediction was obtained. The calibrated HC model did not appear to favor any particular till layer or type of drainage during shearing (i.e., drained or undrained tests). However,

evaluation of the results showed that a better agreement between the test data and the finite element simulations was obtained for the samples sheared in compression.

The finite element simulation of each of the triaxial test results included modelling explicitly the recent stress history of the soil samples from the in-situ conditions through the initial saturation stresses, consolidation and shear. The optimization routine used in this study was the Levenberg-Marquardt gradient based algorithm. After defining the seven soil model parameters using correlations to the OCR and the natural water content of the Chicago glacial tills and the remaining three parameters with optimization routines, the calibrated soil model was tested against the field performance data collected in an excavation performed in the Chicago area. Section No. 2 along the north retaining wall of the excavation at the OMPW project site was used for this purpose.

The OMPW excavation consisted of a five basement level excavation. The excavation at OMPW was performed using top-down construction methods. The perimeter retaining walls consisted of secant pile walls. The lateral support for the walls was provided by reinforced concrete slabs. The performance monitoring instrumentation available at the OMPW project site included optical survey points, inclinometers and strain gauges installed in the floor slabs. A detailed description of the soil, groundwater conditions, construction activities and performance monitoring information at OMPW was presented in this thesis. The observed performance at OMPW agrees with the performance data presented in the literature for similar structures and soil conditions in terms of maximum normalized ground movements. Specifically, the computed normalized ground movements ranged from 0.6% to 0.9%H, if the ancillary movements are considered, and ranged from

$0.2\%H$ to $0.3\%H$, if no ancillary movement are considered (i.e., movements strictly associated with the main excavation of the basement structure). Section No. 2 of the OMPW excavation was modeled using finite element methods to test the validity of the HC model parameters calibrated using laboratory test data. Special attention was given to the structural elements (i.e., retaining walls and floor slabs) in the finite element simulation. Strategies that allow capturing the nonlinear bending stiffness of the retaining walls and time-dependent deformations of the supporting concrete slabs (i.e., elastic, creep and shrinkage) were explicitly incorporated in the finite element modelling strategy.

The results from the finite element simulation were compared to the performance monitoring data; this comparison showed an overall reasonable agreement between field observations and computed performance. The finite element simulations showed good agreement with performance data when comparing horizontal ground movements close to the wall. However, the computed settlements behind the wall did not agree well with those observed, primarily as a result of the presence of a thick, surficial urban fill stratum and a MSE wall.

The effects of small strain stiffness on the computed ground movements at OMPW were studied by suppressing the intergranular strain extension of the HC model. If the intergranular strain extension is suppressed from the HC model, the small strain stiffness effects are no longer represented by the model. This revised analysis showed that the small strain stiffness is needed for the proper prediction of displacements in the deep overconsolidated clays till layers at the site. It was also shown that ignoring creep and shrinkage effects results in a large underestimation of displacements. Finally, it was also determined that the bending stiffness of the wall elements, at the OMPW site, is not

very critical in determining wall movements.. This observation agrees with the test data presented by Clough et al. [1989] and Long [2001] for sites with a large the factor against basal heave.

This thesis showed that if sample disturbance is minimized and if an adequate constitutive soil model that properly captures recent stress history effects and changes in stiffness from the very small to the large strain levels is employed; then multiple laboratory and field conditions can be modelled with a single set of parameters.

Finally, and possibly the most important practical contribution of this thesis, is that a reasonable prediction of both, laboratory and field data, can be achieved by using the correlations developed in this thesis. Such correlations only use the natural water content and OCR as dependent variables, allowing one to estimate the model parameters of an advanced soil model (HC model) that can later on be used to simulate excavation in Chicago clays. In other words, this thesis developed a methodology that an engineering practitioner can use to estimate the model parameters of an advanced soil model, by only knowing the natural water content and OCR. Such a calibrated model could be utilized to obtained finite element predictions of excavations in Chicago clays with a similar accuracy to the one shown in this thesis.

Bibliography

ACI. Building code requirements for reinforced concrete. Technical Report ACI 318-89, American Concrete Institute, Detroit, Mich., 1989.

ACI. Prediction of creep, shrinkage, and temperature effects in concrete structures. Technical Report ACI 209R-92, American Concrete Institute, 1992.

J. H. Atkinson, D. Richardson, and S. E. Stallebrass. Effect of recent stress history on the stiffness of overconsolidated soil. *Géotechnique*, 40:531–540, 1990.

B. Baudet. *Modeling effects of structure in soft natural clays*. PhD thesis, City University, London, 2001.

Z. Bažant, Y. Xi, S. Baweja, and I. Carol. Preliminary guidelines and recommendations for characterizing creep and shrinkage in structural design codes. pages 805–829, Barcelona, Spain, 1993.

L. Bjerrum and O. Eide. Stability of strutted excavations in clay. *Geotechnique*, 6:32–48, 1956.

S. J. Boone. Ground-movement-related building damage. *Journal of Geotechnical and Geoenvironmental Engineering*, 122(11):886–896, 1996.

J. H. Bretz. Geology of the chicago region: Part 1 - general. Technical Report Bulletin 65, Illinois State Geological Survey, 1939.

J. Burland. On the compressibility and shear strength of natural clays. *Géotechnique*, 40 (3):329–378, 1990.

J. B. Burland. "Small is beautiful"- the stiffness of soils at small strains. *Canadian Geotechnical Journal*, 26:499–516, 1989.

R. Butterfield. A natural compression law for soils (an advance on e–log p prime). 1979.

M. Calvello. *Inverse Analysis of a Supported Excavation through Chicago Glacial Clays*. PhD thesis, Northwestern University, Evanston, IL, 2002.

M. Calvello and R. J. Finno. Selecting parameters to optimize in model calibration by inverse analysis. *Computers and Geotechnics*, 31(5):410–424, 2004.

W. Cho. *Recent Stress History Effects on Compressible Chicago Glacial Clay*. PhD thesis, Northwestern University, 2007.

W. Cho, T. Holman, Y. Jung, and R. Finno. Effects of swelling during saturation in triaxial tests in clays. *Geotechnical Testing Journal*, 30(5):378–386, 2007.

C. Chung and R. Finno. Influence of depositional processes on the geotechnical parameters of chicago glacial clays. *Engineering Geology*, 32(4):225–242, 1992.

A. Cividini, L. Jurina, and G. Gioda. Some aspects of 'characterization' problems in geomechanics. *International Journal of Rock Mechanics and Mining Sciences & Geomechanics Abstracts*, 18(6):487–503, 1981.

C. R. I. Clayton, D. W. Hight, and R. J. Hopper. Progressive destructuring of bothkennar clay. implications for sampling and reconsolidation procedures. *Géotechnique*, 42(2): 219–239, 1992.

G. W. Clough and T. D. O'Rourke. Construction induced movements of insitu walls. In *Design and Performance of Earth Retaining Structures*, Geotechnical Special Publication, pages 439–470. New York, NY, 1990.

G. W. Clough, E. M. Smith, and B. P. Sweeney. Movement control of excavation support systems by iterative design. pages 869–884, 1989.

A. Collin. *Recherches expérimentales sur les glissements spontanés des terrains argileux: accompagnées de considérations sur quelques principes de la mécanique terrestre*. 1846.

M. Collins and D. Mitchell. *Prestressed Concrete Structures*. 1991.

Computers and I. Structures. SAP 2000, 2008.

M. Coop and F. Cotecchia. The compression of sediments at the archeological site of sibari. volume 1, pages 55–62, Copenhagen, 1995.

P. Dziadziuszko, Y. Ichikawa, and Z. Sikora. Inverse analysis procedure for identifying material parameters of hypoplastic constitutive model for soils. *Journal of the Society of Materials Science, Japan*, 49(9Appendix):212–220, 2000.

R. Finno and X. Tu. Selected topics in numerical simulation of supported excavations. In *Numerical Modeling of Construction Processes in Geotechnical Engineering for Urban Environment*, pages 3–9, London, 2006.

R. Finno, F. Voss, E. Rossow, and J. Blackburn. Evaluating damage potential in buildings affected by excavations. *Journal of Geotechnical & Geoenvironmental Engineering*, 131 (10), 2005.

R. J. Finno and M. Calvello. Supported excavations: Observational method and inverse modeling. *Journal of Geotechnical and Geoenvironmental Engineering*, 131(7):826–836, 2005.

R. J. Finno and C. Chung. Stress-Strain-Strength responses of compressible chicago glacial clays. *Journal of Geotechnical Engineering*, 118(10):1607–1625, 1992.

Geokon. Installation manual, models 4911A/4911, VW rebar strain meters, 2010.

G. Gioda and G. Maier. Direct search solution of an inverse problem in elastoplasticity: Identification of cohesion, friction angle and in situ stress by pressure tunnel tests. *International Journal for Numerical Methods in Engineering*, 15(12):1823–1848, 1980.

D. E. Goldberg. *Genetic Algorithms in Search, Optimization, and Machine Learning*. 1 edition, 1989.

M. Goldscheider. Grenzbedingung und fliessregel von sand. Technical report, 1976.

V. Hájek, D. Mašín, and J. Boháč. Capability of constitutive models to simulate soils with different OCR using a single set of parameters. *Computers and Geotechnics*, 36 (4):655–664, 2009.

B. Hardin and W. Black. Vibration modulus of normally consolidated clay. *Journal of Soil Mechanics and Foundations*, 94(SM2):353–369, 1968.

Y. Hashash and A. Whittle. Soil modeling and prediction of deep excavation behaviour. 1993.

D. Hight. Sampling effects on soft clay: : An update on ladd and lambe (1963). In *ASCE Geotechnical Special Publication No. 119*, pages 86–121, Cambridge, 2001.

M. C. Hill. *Methods and guidelines for effective model calibration : with application to UCODE, a computer code for universal inverse modeling, and MODFLOWP, a computer code for inverse modeling with MODFLOW / by Mary C. Hill.* Water-resources investigations report ; 98-4005. Denver, Colo. :, 1998.

T. Holman. *Small Strain Behavior of Compressible Chicago Glacial Clays.* PhD thesis, Northwestern University, Evanston, IL, 2005.

G. Houlsby and C. P. Wroth. The variation of the shear modulus of a clay with pressure and overconsolidation ratio. *Soils and Foundations*, 31(3):138–143, 1991.

R. J. Jardine. Nonlinear stiffness parameters from undrained pressuremeter tests. *Canadian Geotechnical Journal*, 29:436–447, 1992.

T. Kim. *Incrementally nonlinear responses of soft Chicago glacial clays.* PhD thesis, Northwestern University, Evanston, IL, 2011.

T. Kim and R. J. Finno. Anisotropy evolution and irrecoverable deformation in triaxial stress probes. *Journal of Geotechnical and Geoenvironmental Engineering*, 2011.

D. Kolymbas. *Introduction to hypoplasticity.* Rotterdam ;;Brookfiled, 2000.

D. Kolymbas. An outline of hypoplasticity. *Archive of Applied Mechanics*, 61:143–151, 1991.

F. Kulhawy and P. Mayne. Manual for estimating soil properties for foundation design. Technical report, Electric Power Research Institute, 1990.

C. C. Ladd and R. Foott. New design procedure for stability of soft clays. *Journal of the Geotechnical Engineering Division*, 100(Gt7):763–786, 1974.

A. Ledesma, A. Gens, and E. Alonso. Identification of parameters of nonlinear geotechnical models. In *Computer Methods and Advances in Geomechanics*, pages 1005–1011. 1991.

S. Levasseur, Y. Malécot, M. Boulon, and E. Flavigny. Soil parameter identification using a genetic algorithm. *International Journal for Numerical and Analytical Methods in Geomechanics*, 32(2):189–213, 2008.

K. Levenberg. A method for the solution of certain non-linear problems in least squares. *The Quarterly Journal of Applied Mathematics*, II(2):164–168, 1944.

M. Long. Database for retaining wall and ground movements due to deep excavations. *Journal of Geotechnical and Geoenvironmental Engineering*, 127(3):203–224, 2001.

R. G. Lukas and B. L. de Bussy. Pressuremeter and laboratory test correlations for clays. *Journal of the Geotechnical Engineering Division*, 102(9):945–962, 1976.

D. Marquardt. An algorithm for Least-Squares estimation of nonlinear parameters. *SIAM Journal on Applied Mathematics*, 11(2):431–441, 1963.

H. Matsuoka and T. Nakai. Stress-Deformation and strength characteristics of soil under three different principal stresses. *Proc. of JSCE*, (232):59–70, 1974.

D. Mašín. A hypoplastic constitutive model for clays. *International Journal for Numerical and Analytical Methods in Geomechanics*, 29(4):311–336, 2005.

D. Mašín. *Hypoplastic models for fine-grained soils*. PhD thesis, Charles University, Prague, 2006.

D. Mašín. Hypoplasticity for practical applications. part4. determination of material parameters, 2011.

D. Mašín and I. Herle. State boundary surface of a hypoplastic model for clays. *Computers and Geotechnics*, 32(6):400–410, 2005.

G. Mesri. "New design procedure for stability of soft clays." discussion. *Journal of the Geotechnical Engineering Division*, pages 409–412, 1975.

G. Mesri, T. Feng, S. Ali, and T. M. Hayat. Permeability characteristics of soft clays. In *Proceedings*, volume 1, pages 187–192, New Delhi, India, 1994.

J. K. Mitchell and K. Soga. *Fundamentals of Soil Behavior*. 3 edition, 2005.

MWRD. Metropolitan water reclamation district of greater chicago, 2011.

C. Ng. Stress paths in relation to deep excavations. *ASCE J. of Geotechnical and Geoenvironmental Engineering*, 125(5):357–363, 1999.

A. Niemunis. *Extended hypoplastic models for soils*. PhD thesis, Ruhr-University Bochum, 2002.

G. Otto. *An interpretation of the glacial stratigraphy of the city of Chicago*. PhD thesis, The University of Chicago, Chicago, IL, 1942.

R. H. G. Parry. Triaxial compression and extension tests on remoulded saturated clay. *Géotechnique*, 42:166–180, 1960.

R. B. Peck. Advantages and limitations of the observational method in applied soil mechanics. *Géotechnique*, 19(2):171–187, 1969a.

R. B. Peck. Deep excavations and tunneling in soft ground. In *Seventh International Conference on Soil Mechanics and Foundation Engineering*, volume 4, pages 225–290, Mexico City, 1969b.

R. B. Peck and W. Reed. Engineering properties of chicago subsoils. Technical report, 1954.

PLAXIS. Material model manual. Technical report, Delft, Netherland, 2010.

E. P. Poeter and M. C. Hill. UCODE, a computer code for universal inverse modeling. *Computers & Geosciences*, 25(4):457–462, 1999.

S. Rampello, G. M. B. Viggiani, and A. Amorosi. Small-strain stiffness of reconstituted clay compressed along constant triaxial effective stress ratio paths. *Géotechnique*, 47: 475–489, 1997.

C. Rechea, S. Levasseur, and R. Finno. Inverse analysis techniques for parameter identification in simulation of excavation support systems. *Computers and Geotechnics*, 35 (3):331–345, 2008.

C. Rechea Bernal. *Inverse analysis of excavations in urban environments*. PhD thesis, Northwestern University, Evanston, IL, 2006.

J. Renders. Algorithmes génétiques et réseaux de neurones. *Hermes*, 1994.

K. Roscoe and J. B. Burland. On the generalized stress-strain behaviour of wet clay. *Engineering Plasticity*, pages 535–609, 1968.

W. Schriever. *Landslides in Clays, 1846, Translated by W.R. Schriever With the Assistance of J.P. Carriere, R.F. Legget, and D.H. Macdonald. With a Memoir on Alexandre Collin, by A.W. Skempton*. 1956.

A. Skempton. The consolidation of clays by gravitational compaction. *Q. J Geological Soc.*, 125:373–411, 1970.

M. Son and E. J. Cording. Responses of buildings with different structural types to Excavation-Induced ground settlements. *Journal of Geotechnical and Geoenvironmental Engineering*, 137:323, 2011.

S. E. Stallebrass. *Modelling the efects of recent stress history on the behaviour of overconsolidated soils*. PhD thesis, The City University, 1990.

S. E. Stallebrass and R. N. Taylor. The development and evaluation of a constitutive model for the prediction of ground movements in overconsolidated clay. *Géotechnique*, 47:235–253, 1997.

T. Svoboda and D. Mašín. 3D simulations of a NATM tunnel in stiff clays with soil parameters optimised using monitoring data from exploratory adit. Rome, Italy, 2011.

T. Svoboda and D. Mašín. Impact of a constitutive model on inverse analysis of a NATM tunnel in stiff clays. Technical report, Charles University, Czech Republic, 2008.

D. W. Taylor. *Fundamentals of soil mechanics*. 1ST edition, 1948.

K. Terzaghi, R. B. Peck, and G. Mesri. *Soil mechanics in engineering practice*. 1996.

G. Viggiani and J. Atkinson. Stiffness of fine-grained soil at very small strains. *Géotechnique*, 45(2):249–265, 1995.

J. Wang. Laboratory testing on chicago hard clays. Internal report, Nortwestern University, 2011.

C. Wroth and G. Houlsby. Soil mechanics - property characterization and analysis procedures. In *Proceedings of the 11th International Conference on Soil Mechanics and Foundation Engineering*, volume 1, pages 1–55, San Francsico, CA, 1985.

APPENDIX A

Triaxial Test Data versus Finite Element Simulations

A.0.1. Optimized Simulations

Stress-Strain Data

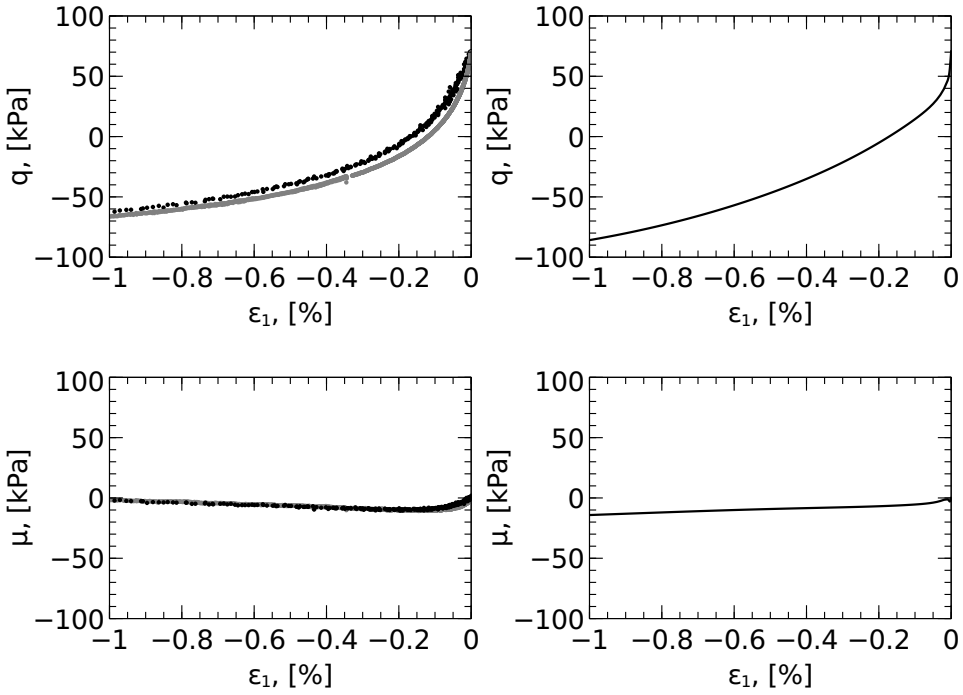

(A.1.1) Data

(A.1.2) Simulation

Figure A.1: Stress versus strain, TestID: B37DRTE1

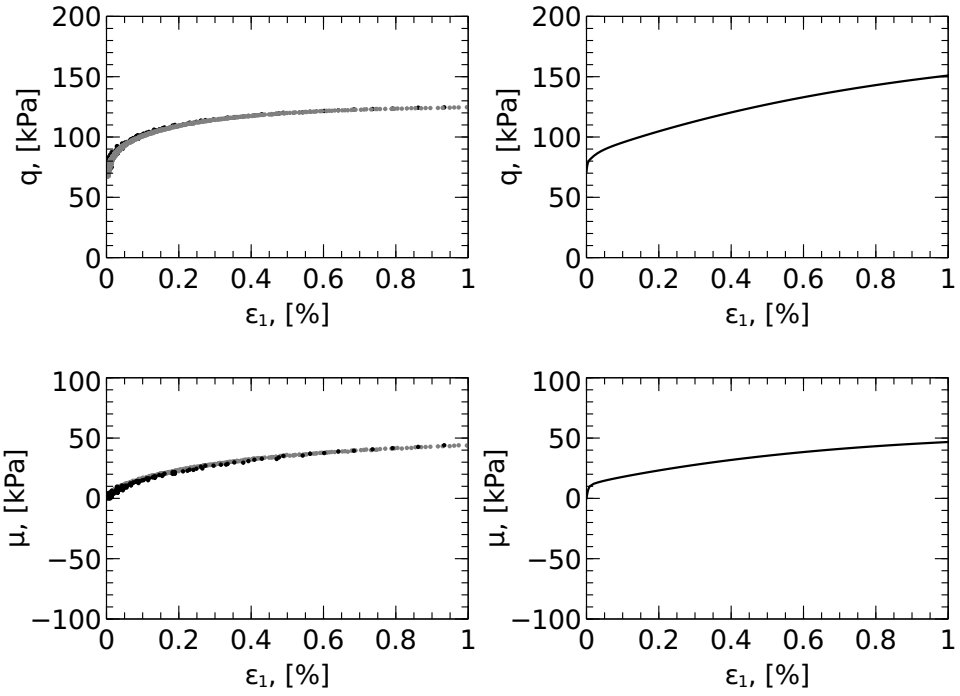

(A.2.1) Data

(A.2.2) Simulation

Figure A.2: Shear degradation and stress path, Stress versus strain, TestID: B37DTC1

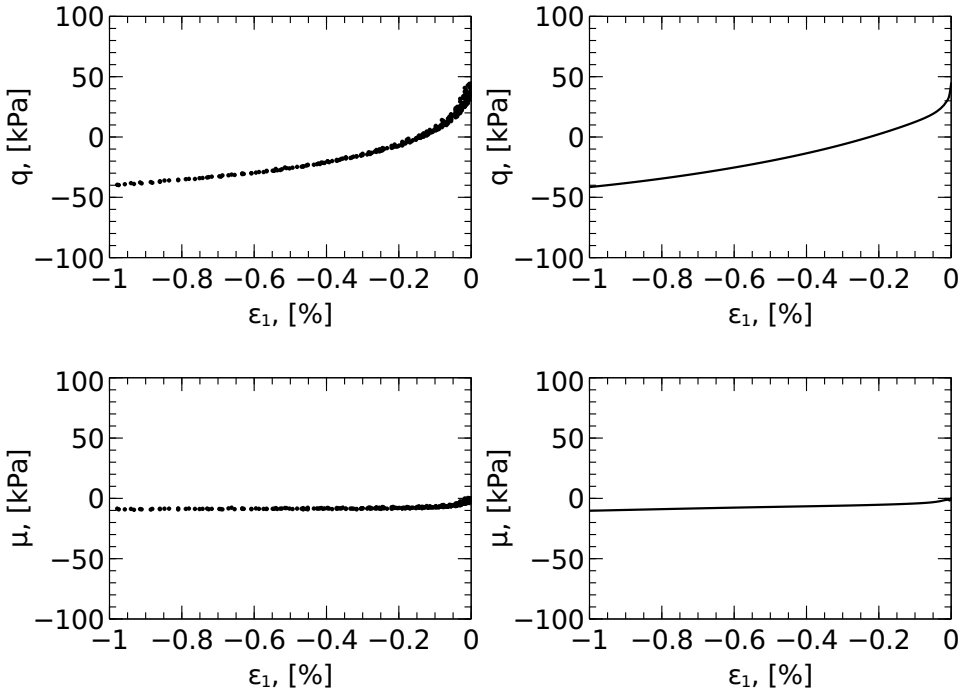

(A.3.1) Data

(A.3.2) Simulation

Figure A.3: Stress versus strain, TestID: B37RTE1

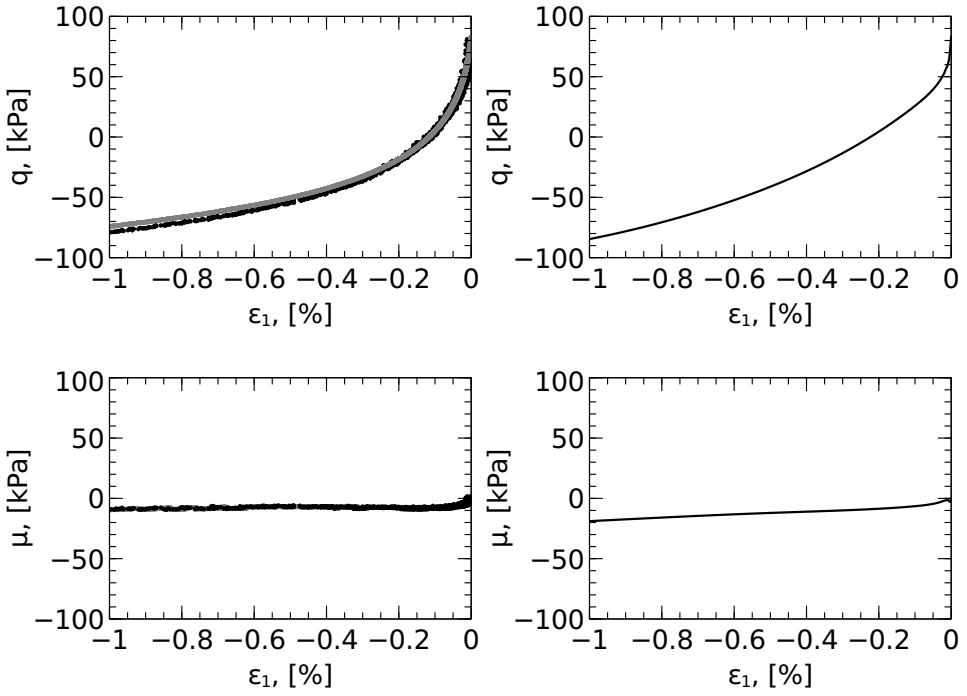

(A.4.1) Data

(A.4.2) Simulation

Figure A.4: Stress versus strain, TestID: B37RTXE4

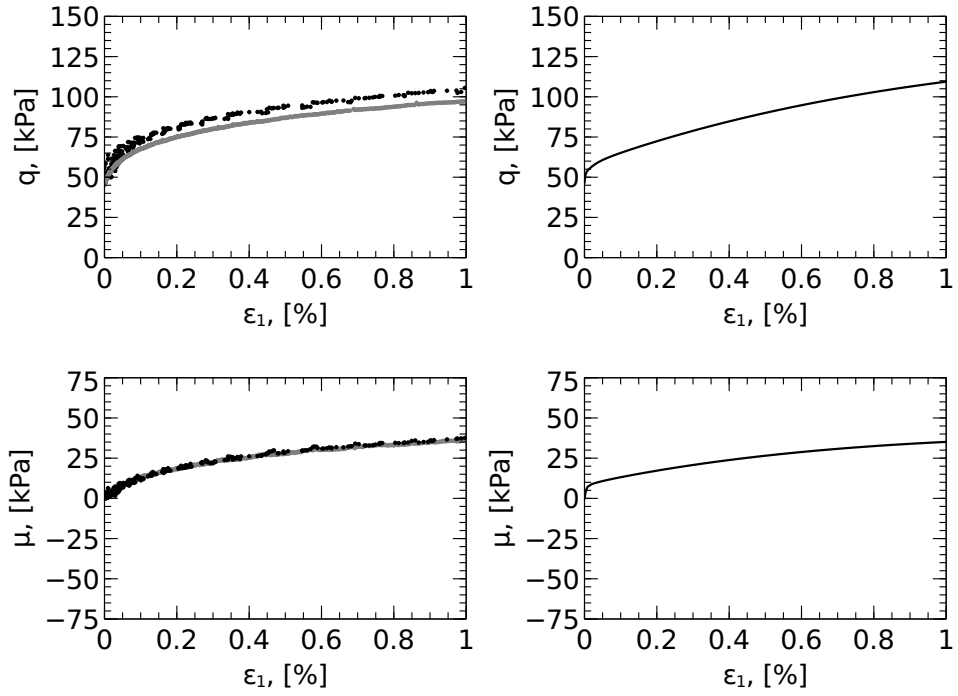

(A.5.1) Data

(A.5.2) Simulation

Figure A.5: Stress versus strain, TestID: B37STC1

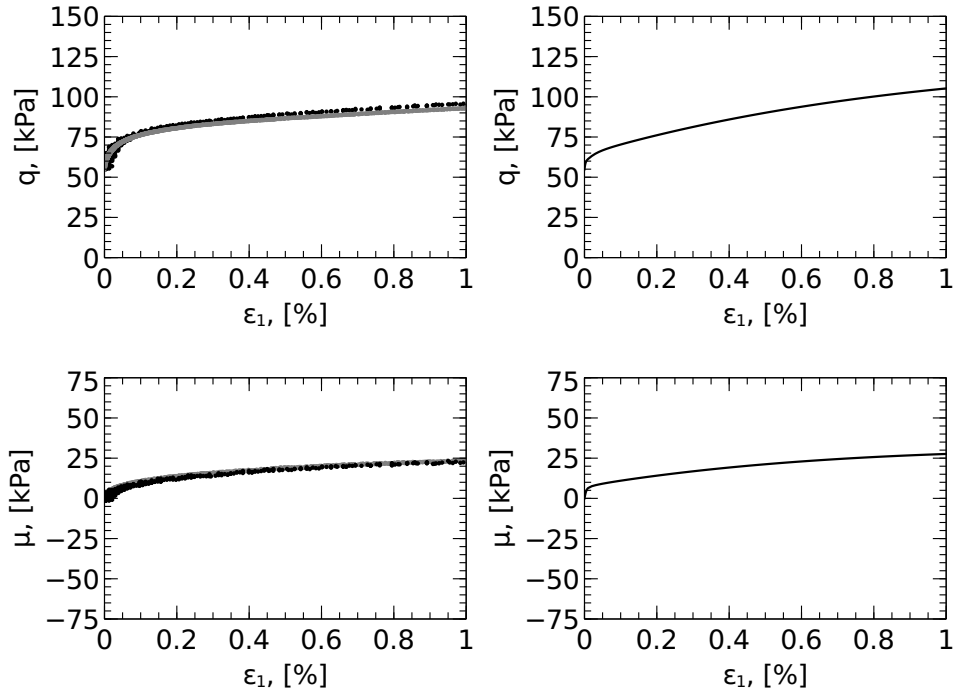

(A.6.1) Data

(A.6.2) Simulation

Figure A.6: Stress versus strain, TestID: B37TC2

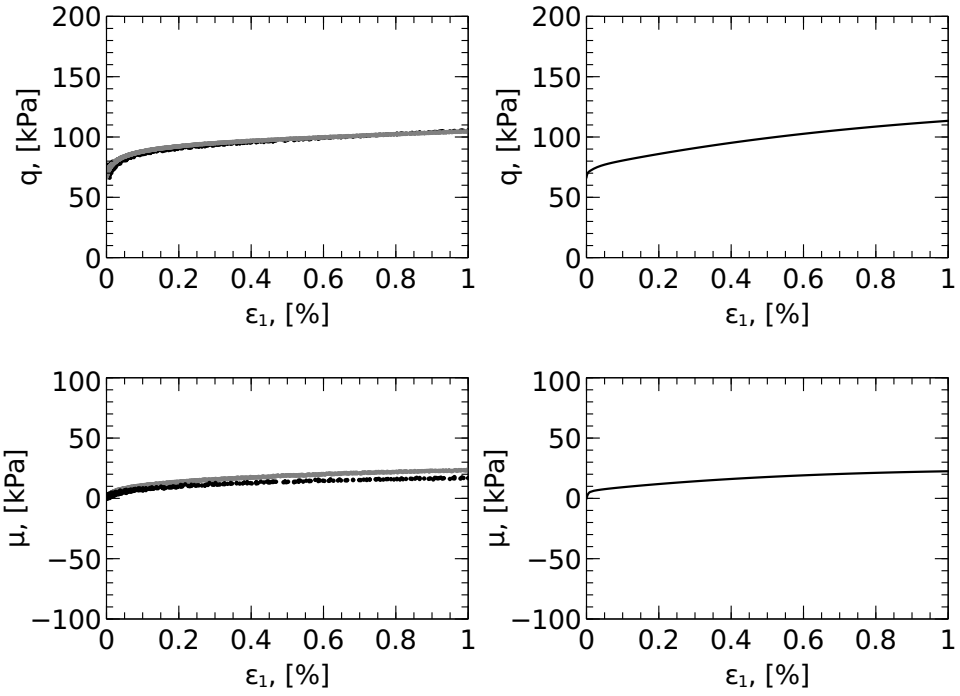

(A.7.1) Data

(A.7.2) Simulation

Figure A.7: Stress versus strain, TestID: B37TC3

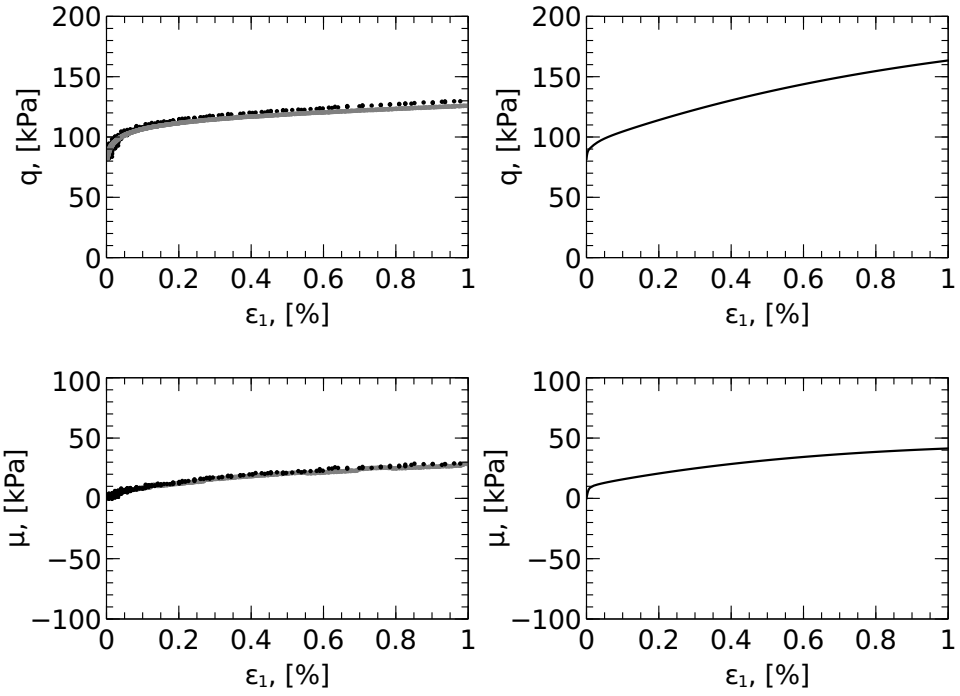

(A.8.1) Data

(A.8.2) Simulation

Figure A.8: Stress versus strain, TestID: B37TC4

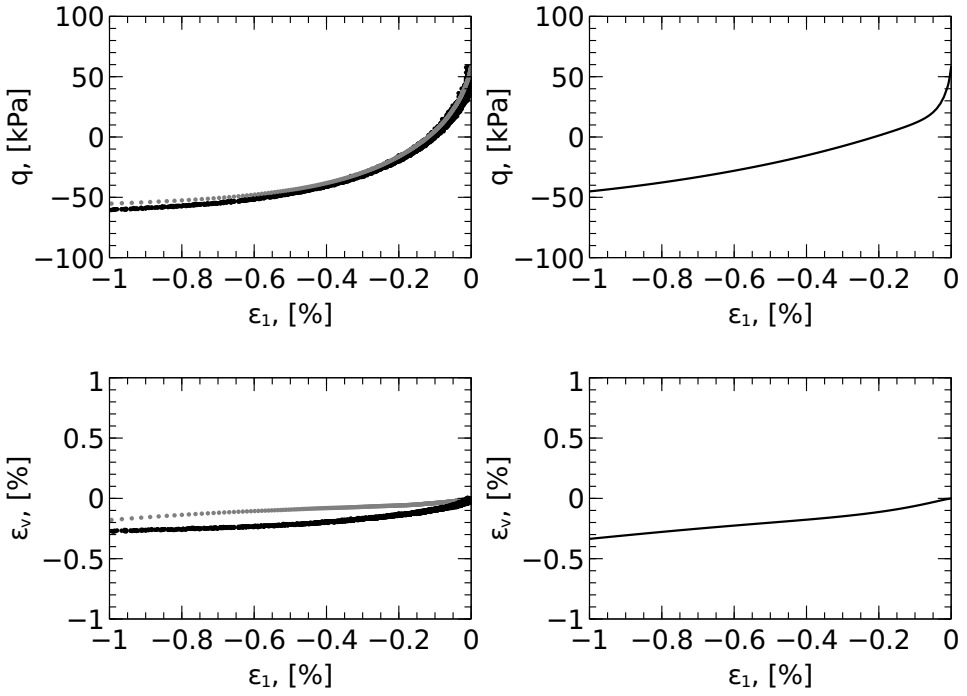

(A.9.1) Data

(A.9.2) Simulation

Figure A.9: Stress versus strain, TestID: FB1RTE1

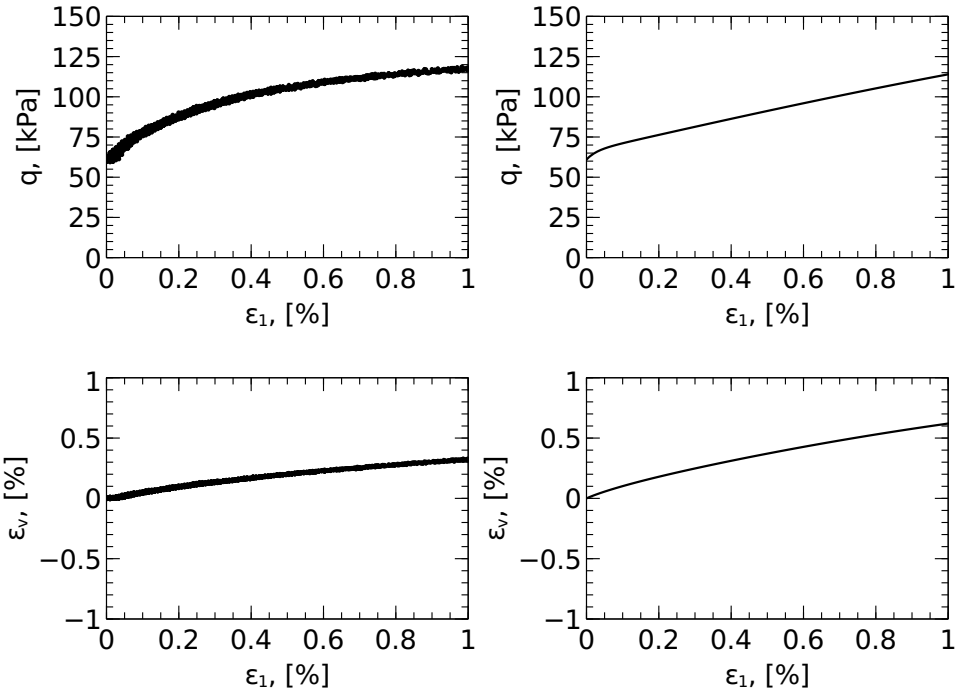

(A.10.1) Data

(A.10.2) Simulation

Figure A.10: Stress versus strain, TestID: FB1TC1

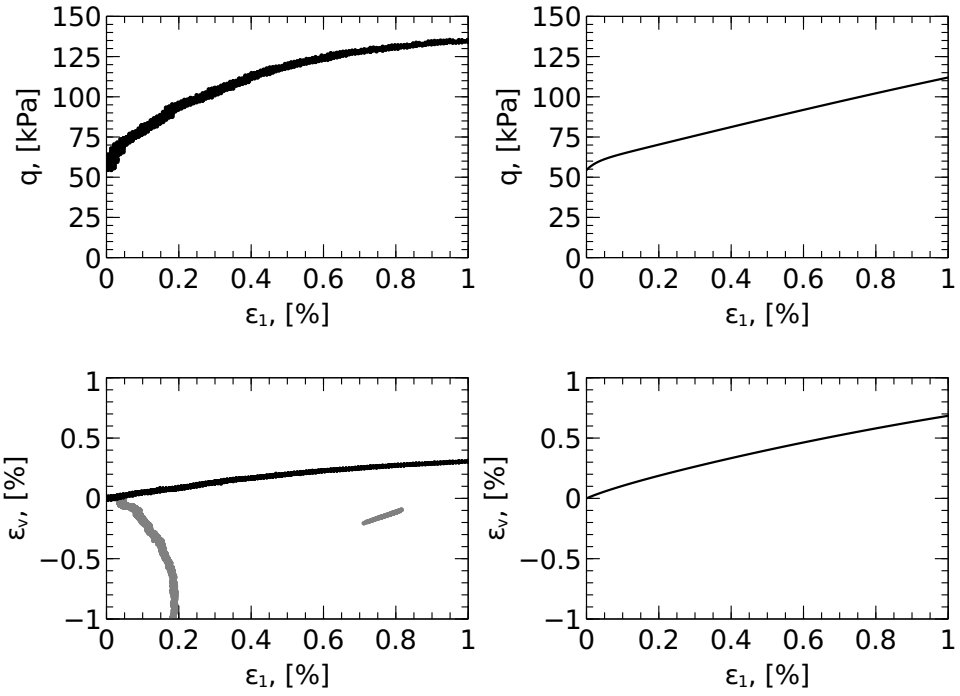

(A.11.1) Data

(A.11.2) Simulation

Figure A.11: Stress versus strain, TestID: FB1TC2

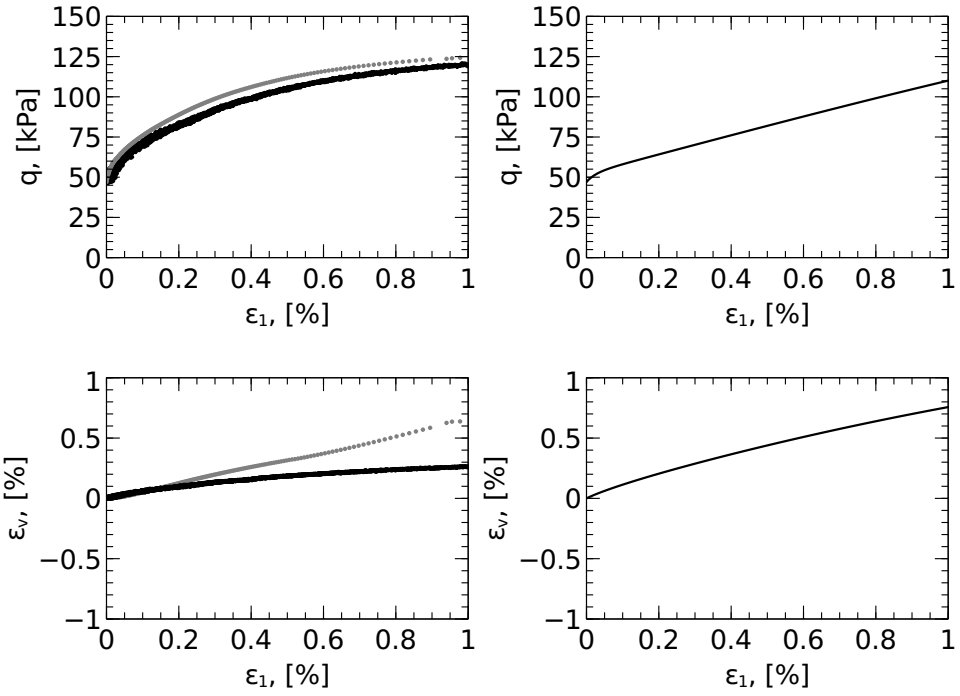

(A.12.1) Data

(A.12.2) Simulation

Figure A.12: Stress versus strain, TestID: FB2TC2

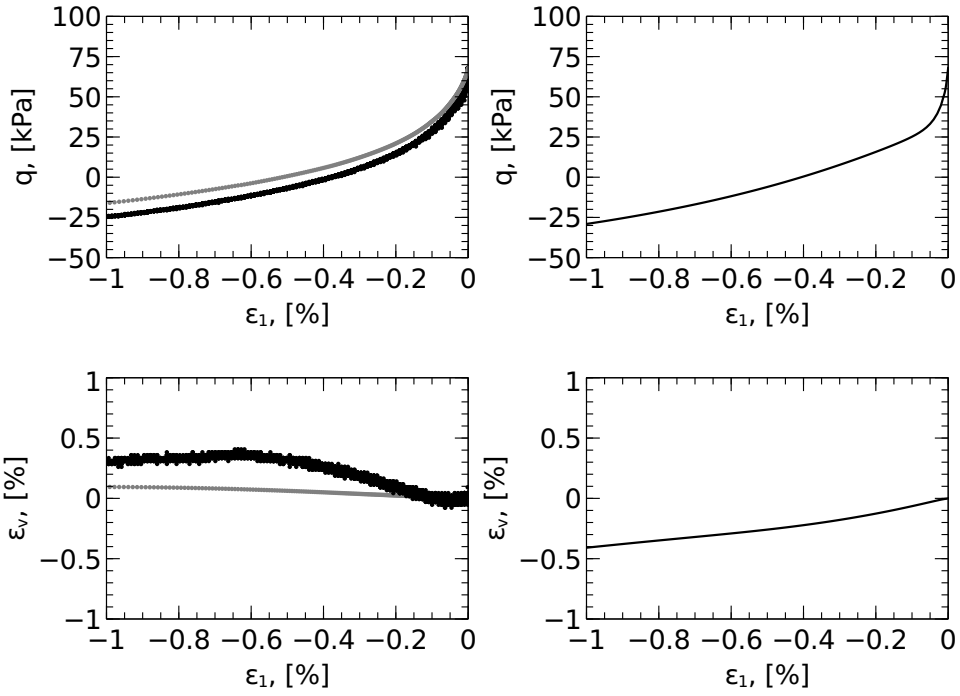

(A.13.1) Data

(A.13.2) Simulation

Figure A.13: Stress versus strain, TestID: LB3RTE1

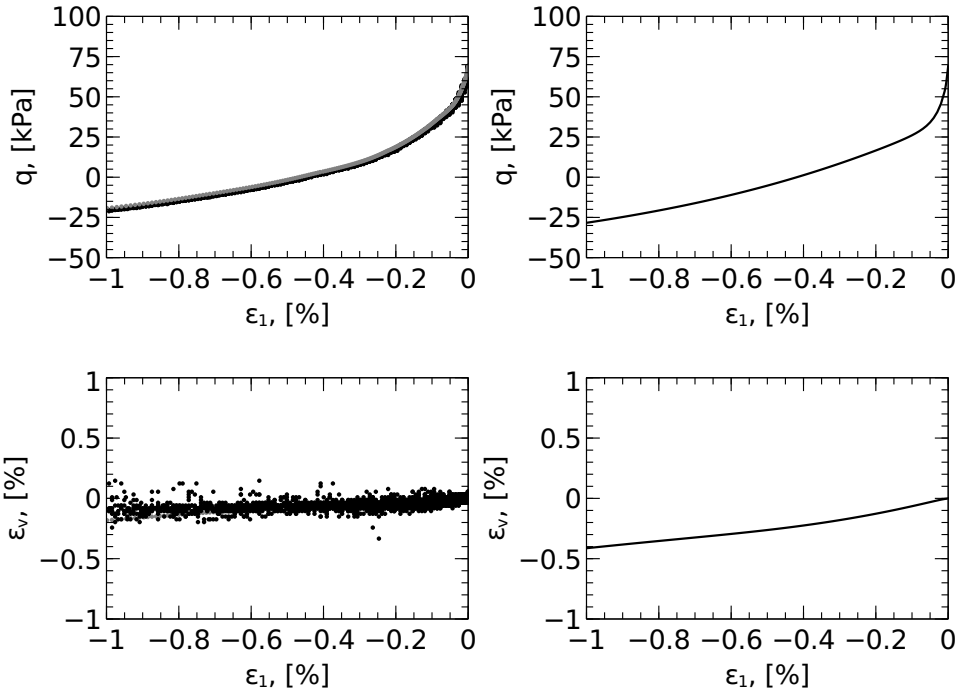

(A.14.1) Data

(A.14.2) Simulation

Figure A.14: Stress versus strain, TestID: LB3RTE2

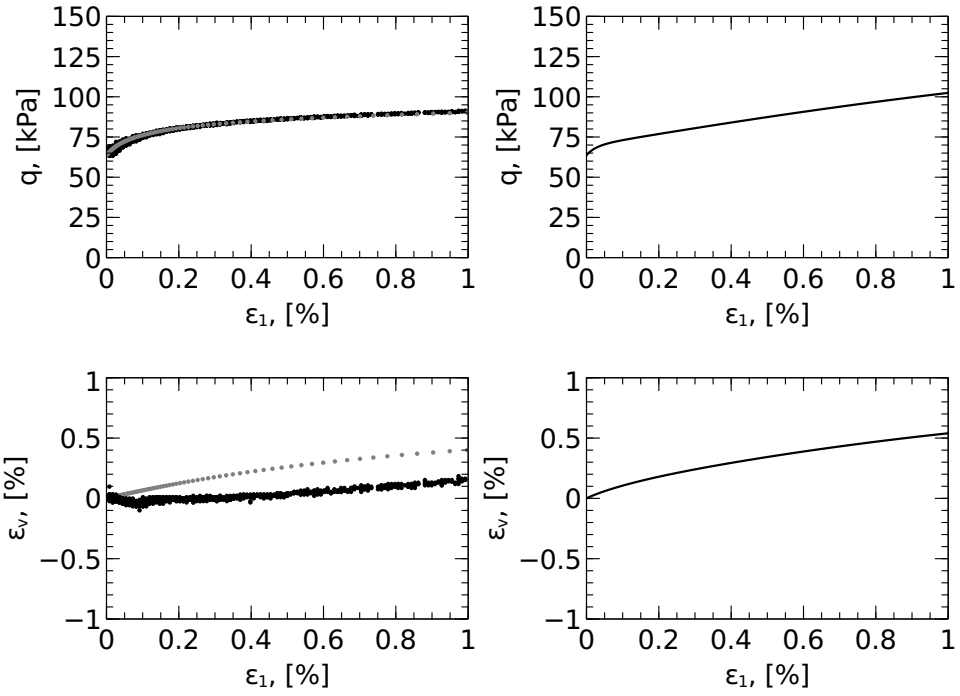

(A.15.1) Data

(A.15.2) Simulation

Figure A.15: Stress versus strain, TestID: LB3TC2

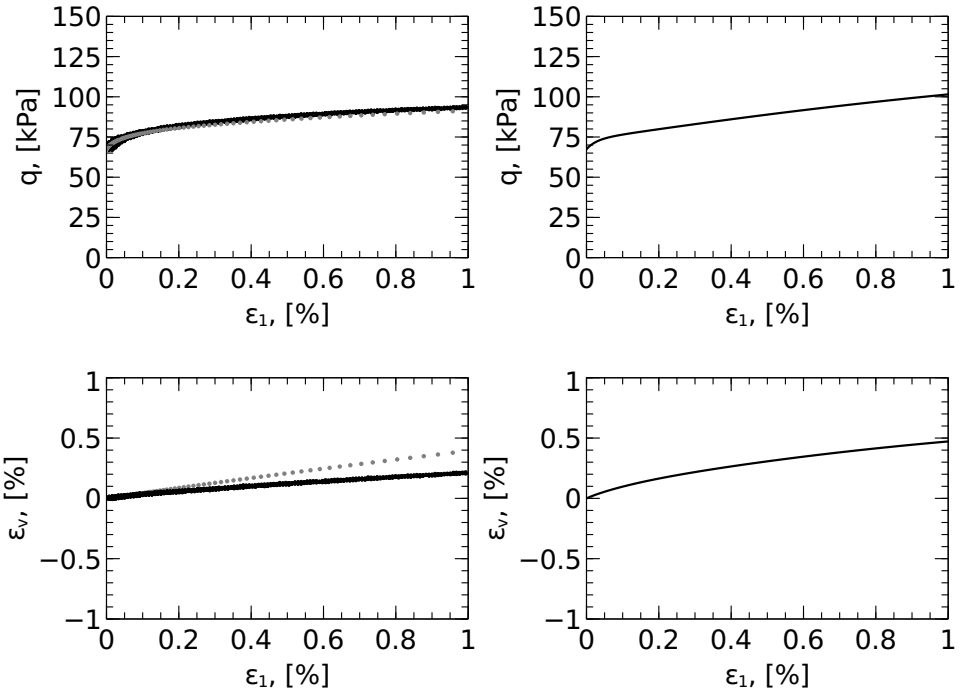

(A.16.1) Data

(A.16.2) Simulation

Figure A.16: Stress versus strain, TestID: LB3TC3

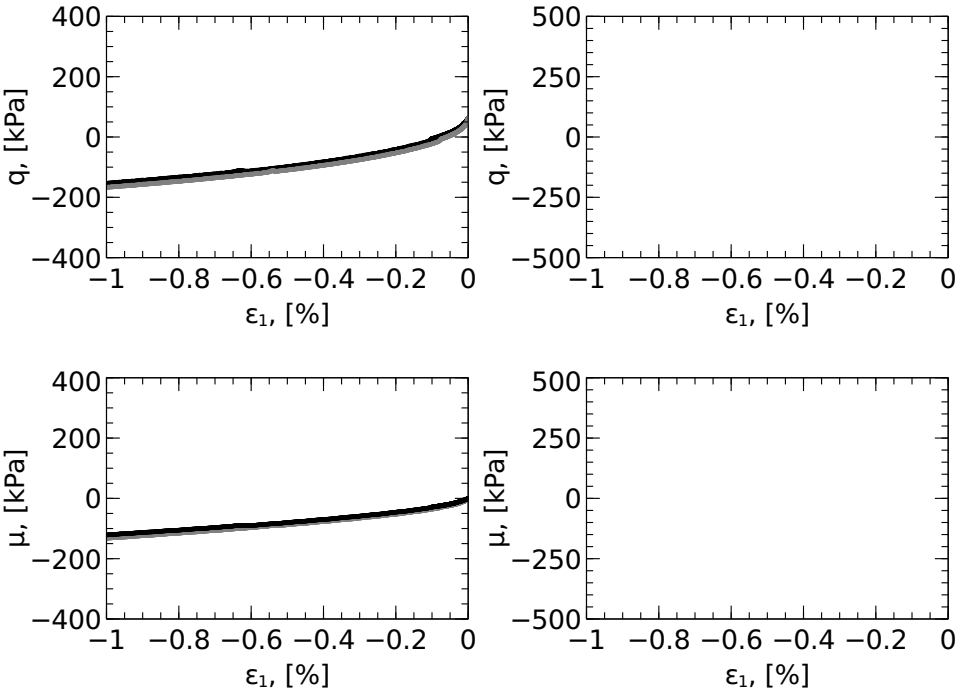

(A.17.1) Data (A.17.2) Simulation

Figure A.17: Stress versus strain, TestID: O1P1RTE

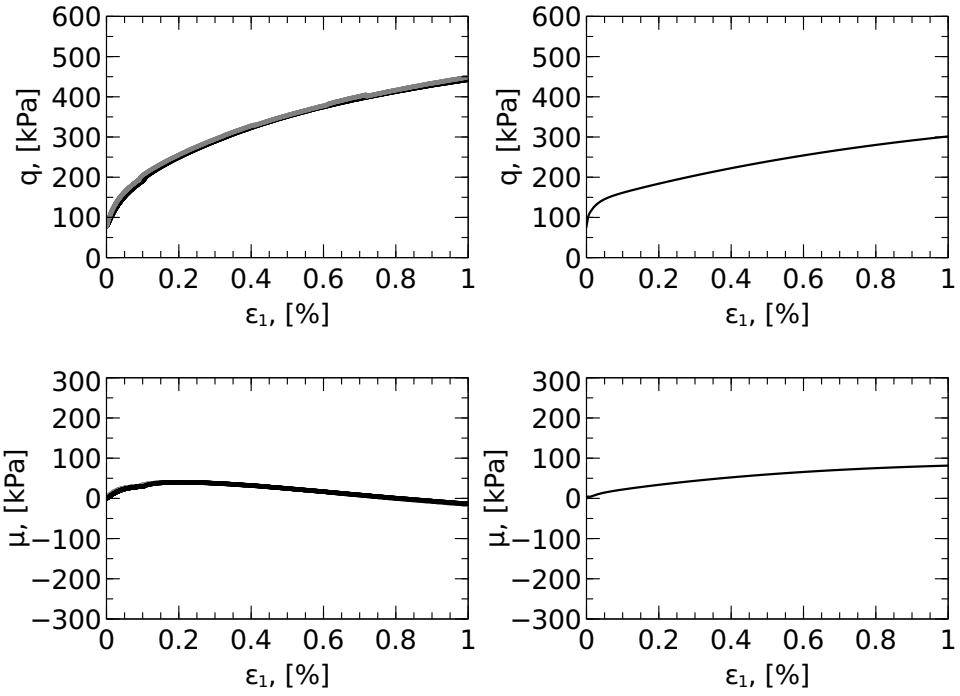

(A.18.1) Data

(A.18.2) Simulation

Figure A.18: Stress versus strain, TestID: O1P2TC

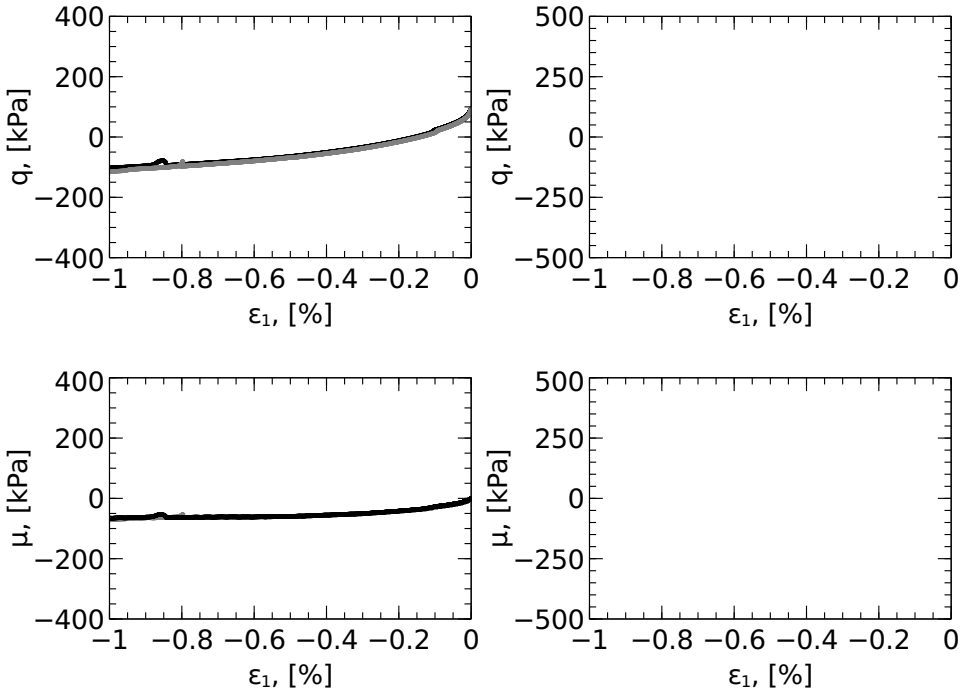

(A.19.1) Data (A.19.2) Simulation

Figure A.19: Stress versus strain, TestID: O2P1RTE

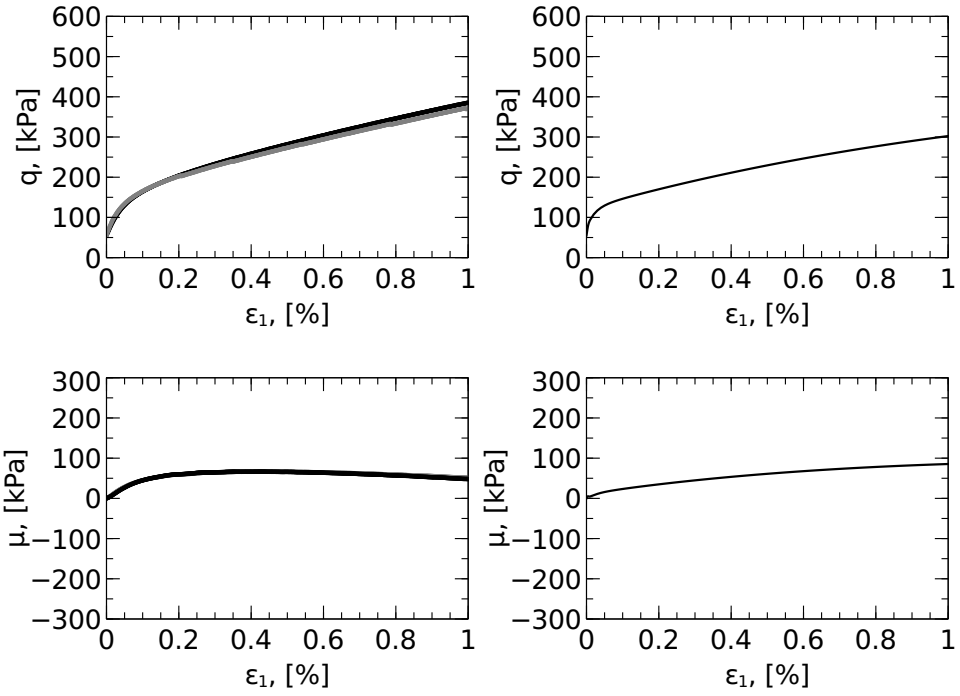

(A.20.1) Data

(A.20.2) Simulation

Figure A.20: Stress versus strain, TestID: O2P3TC

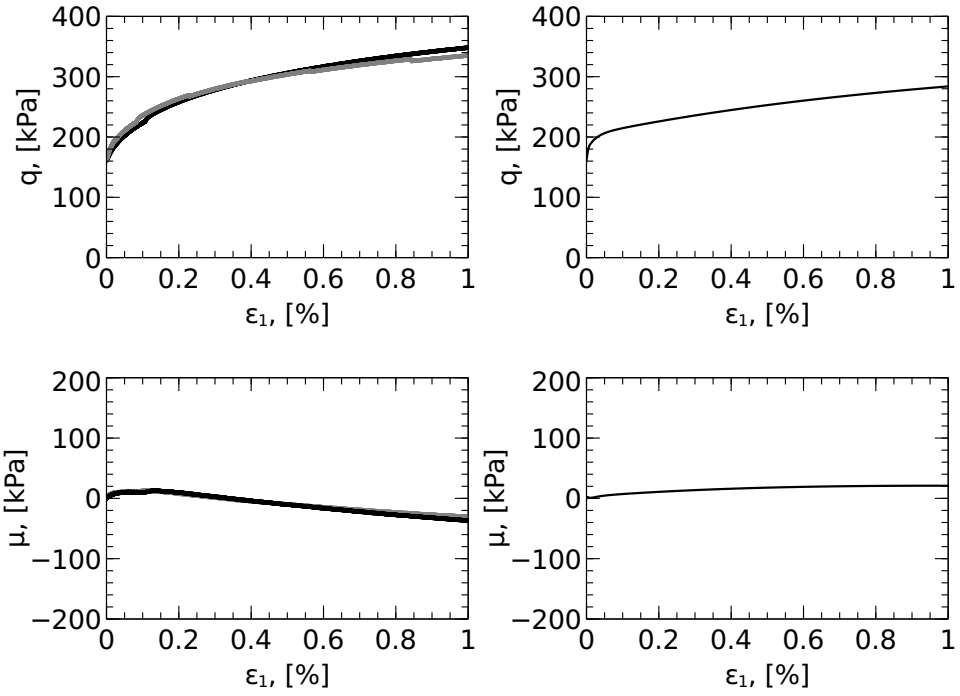

(A.21.1) Data

(A.21.2) Simulation

Figure A.21: Stress versus strain, TestID: O3P4TC

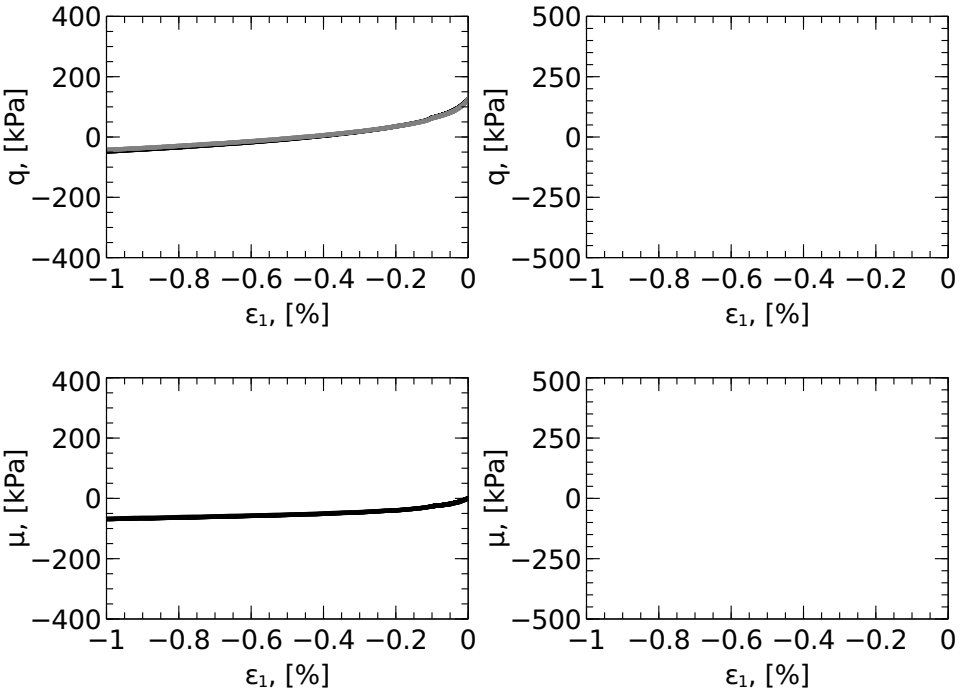

(A.22.1) Data (A.22.2) Simulation

Figure A.22: Stress versus strain, TestID: O3P5RTE

Stiffness degradation and stress paths

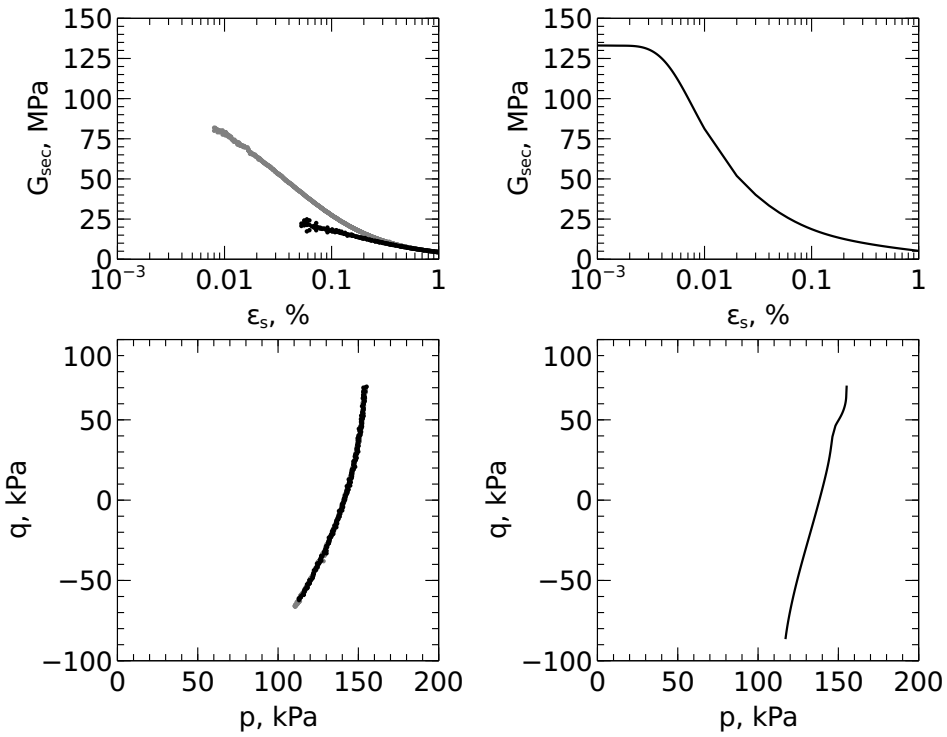

(A.23.1) Data

(A.23.2) Simulation

Figure A.23: Shear degradation and stress path, TestID: B37DRTE1

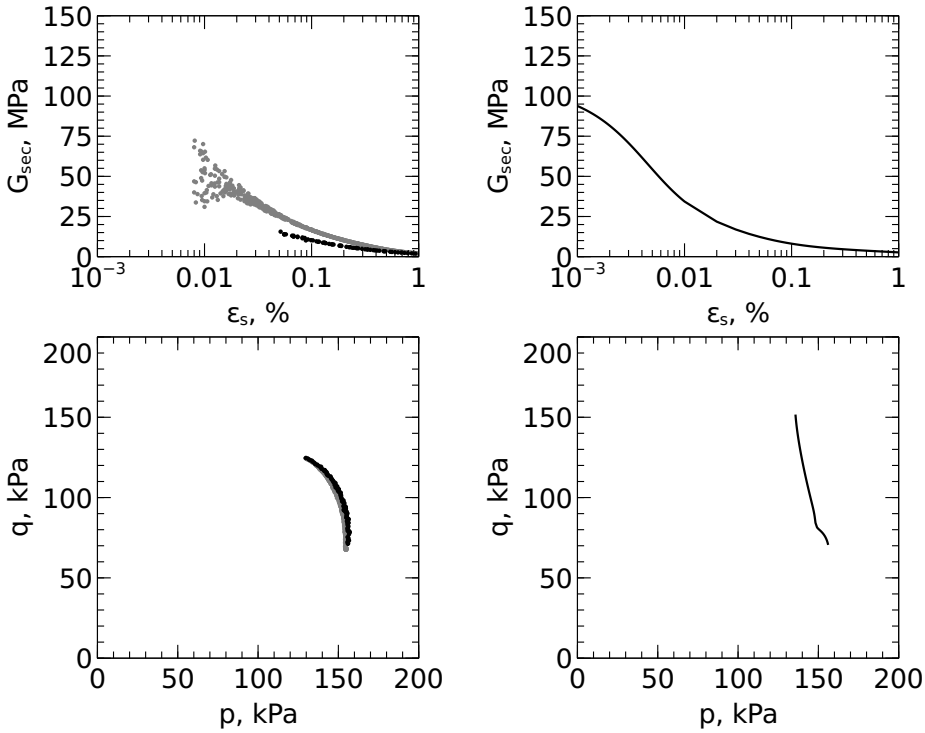

(A.24.1) Data

(A.24.2) Simulation

Figure A.24: Shear degradation and stress path, TestID: B37DTC1

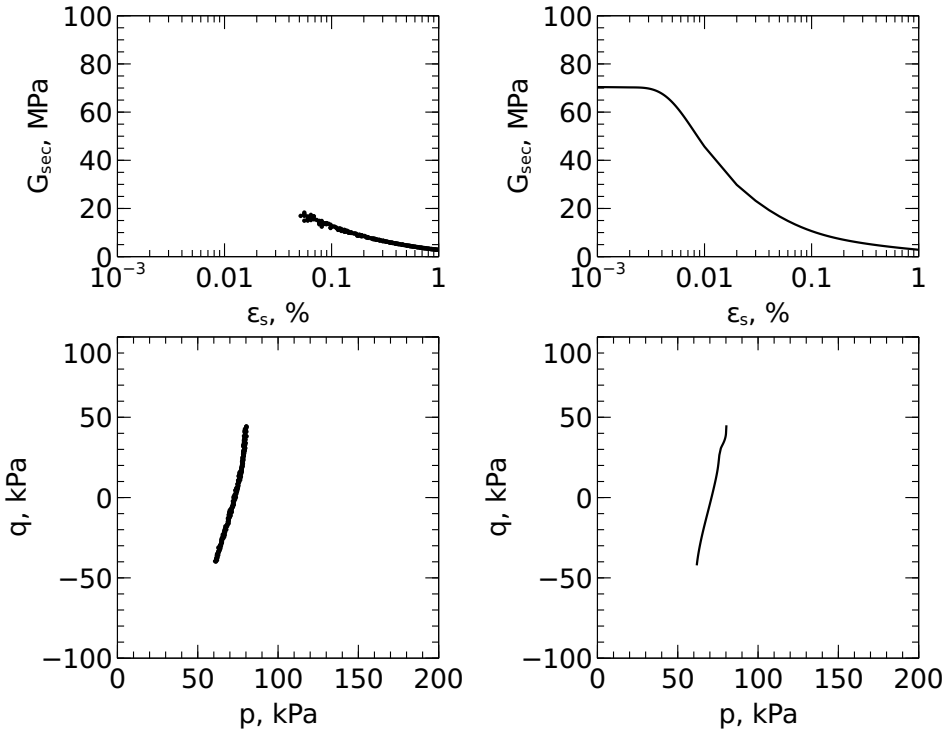

(A.25.1) Data

(A.25.2) Simulation

Figure A.25: Shear degradation and stress path, TestID: B37RTE1

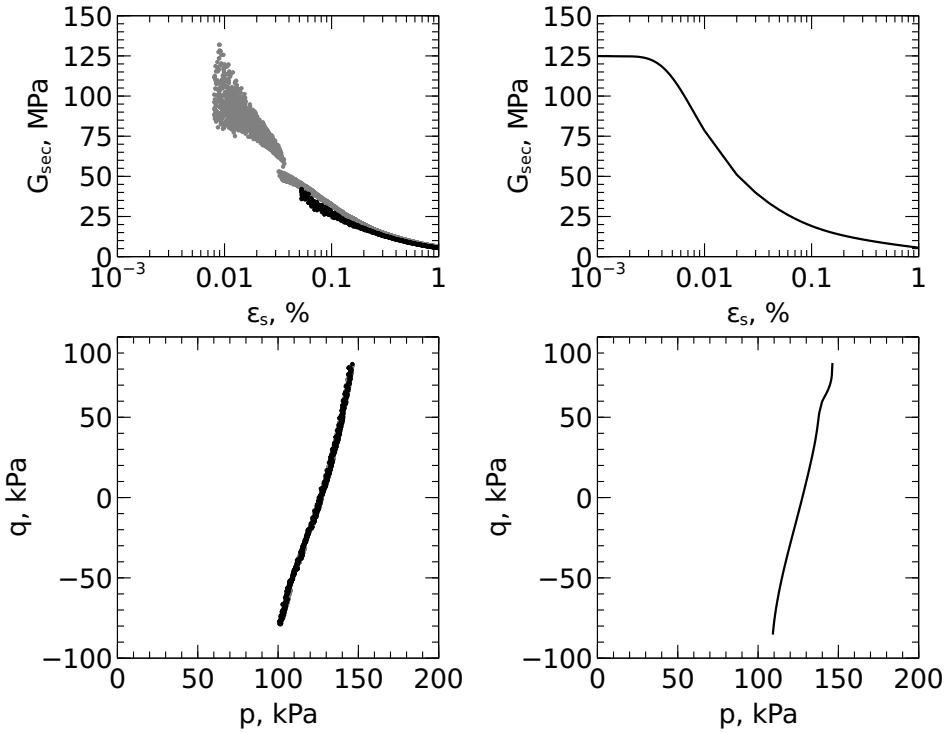

(A.26.1) Data

(A.26.2) Simulation

Figure A.26: Shear degradation and stress path, TestID: B37RTXE4

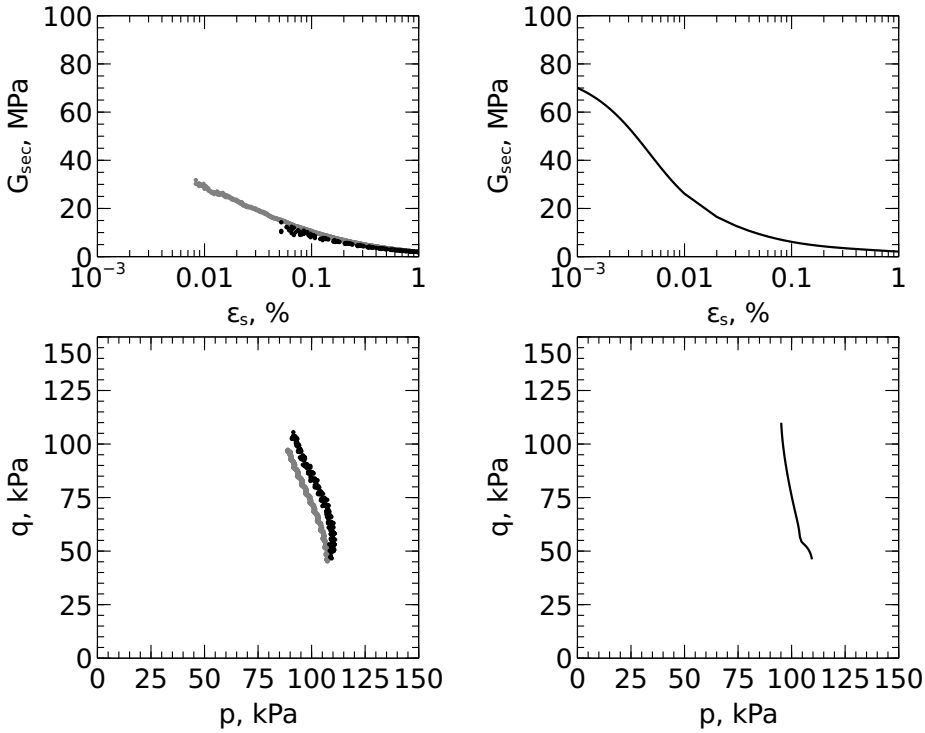

(A.27.1) Data

(A.27.2) Simulation

Figure A.27: Shear degradation and stress path, TestID: B37STC1

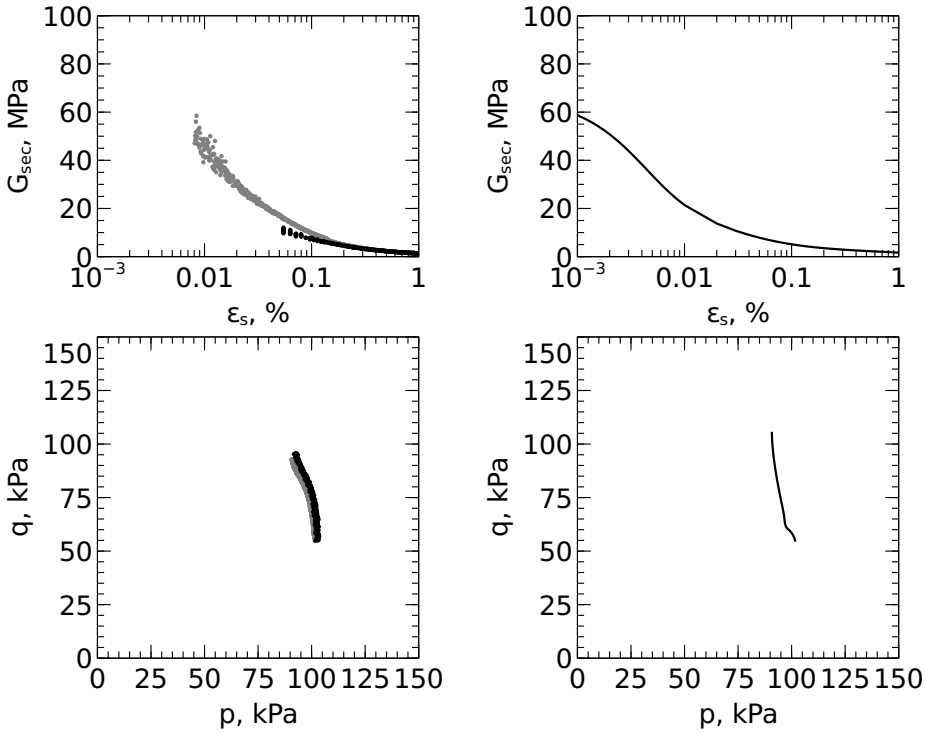

(A.28.1) Data

(A.28.2) Simulation

Figure A.28: Shear degradation and stress path, TestID: B37TC2

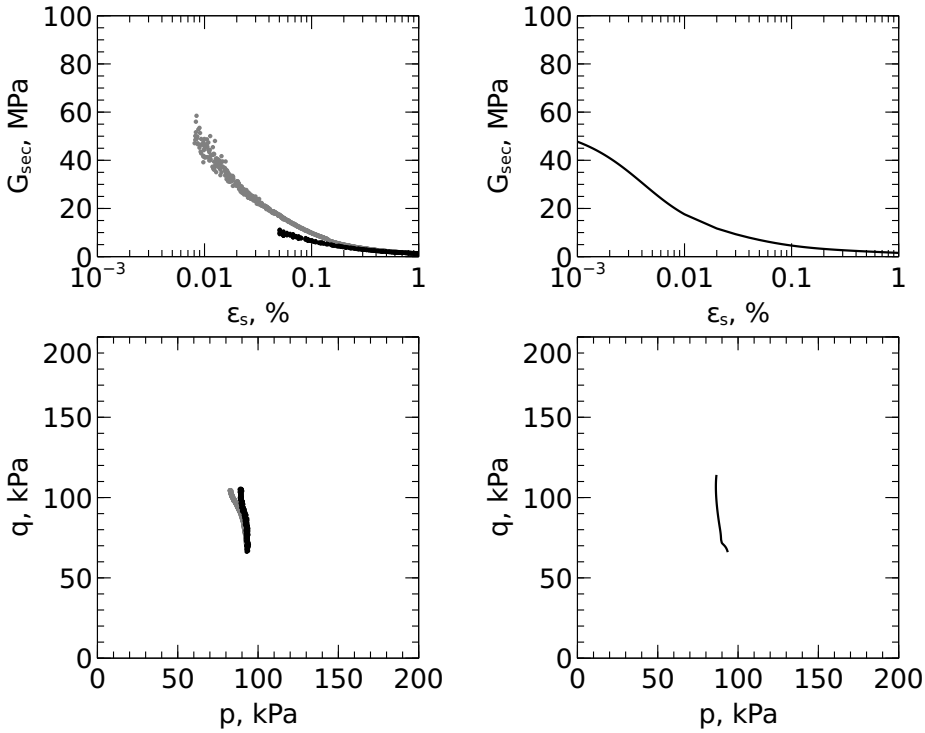

(A.29.1) Data

(A.29.2) Simulation

Figure A.29: Shear degradation and stress path, TestID: B37TC3

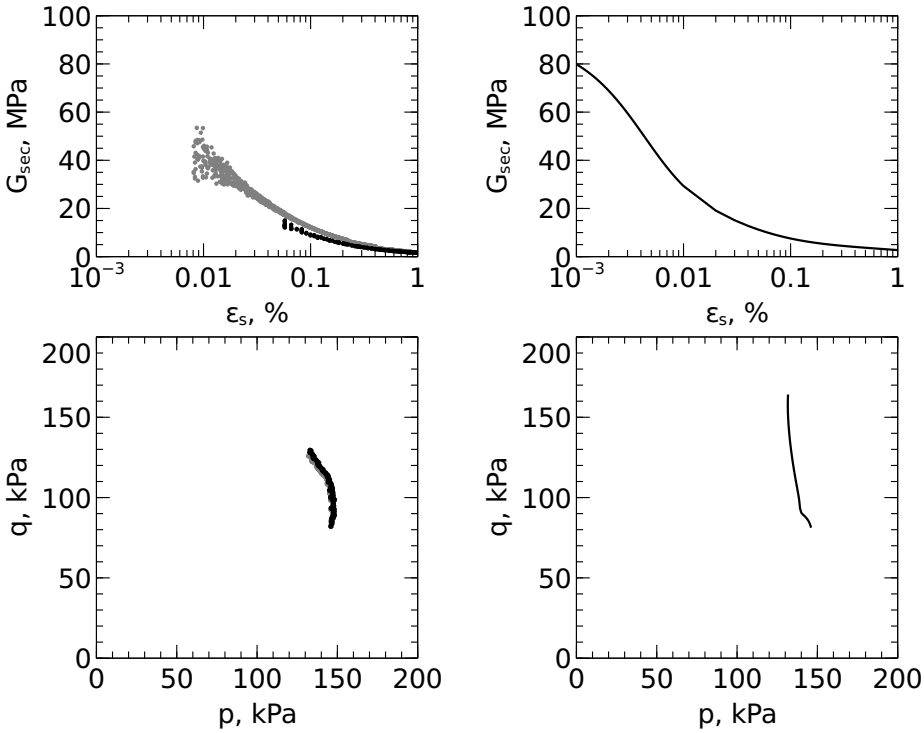

(A.30.1) Data

(A.30.2) Simulation

Figure A.30: Shear degradation and stress path, TestID: B37TC4

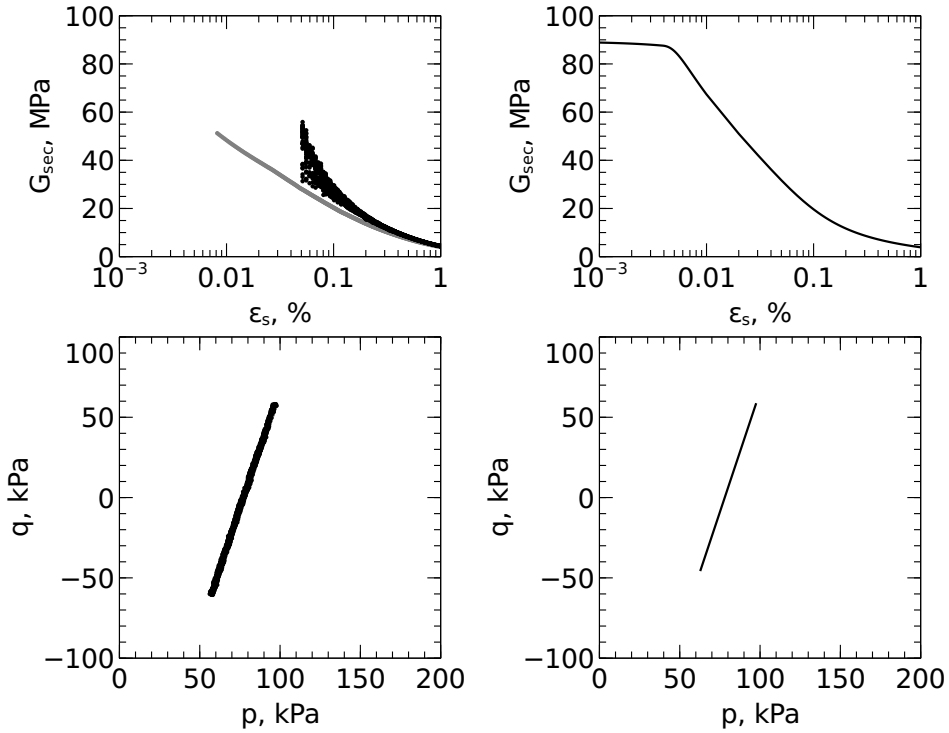

(A.31.1) Data

(A.31.2) Simulation

Figure A.31: Shear degradation and stress path, TestID: FB1RTE1

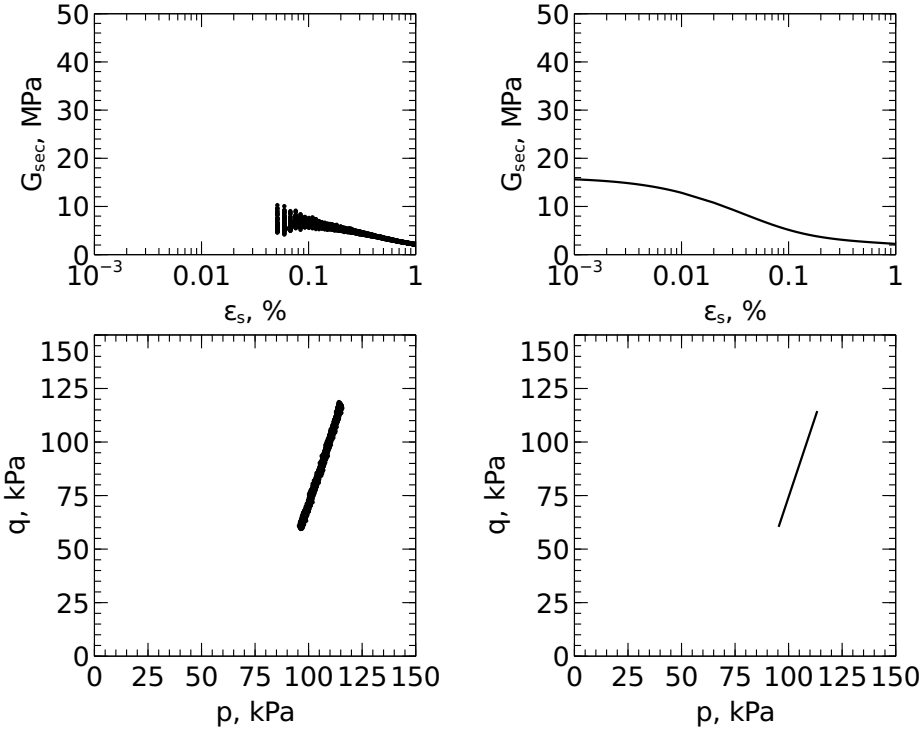

(A.32.1) Data

(A.32.2) Simulation

Figure A.32: Shear degradation and stress path, TestID: FB1TC1

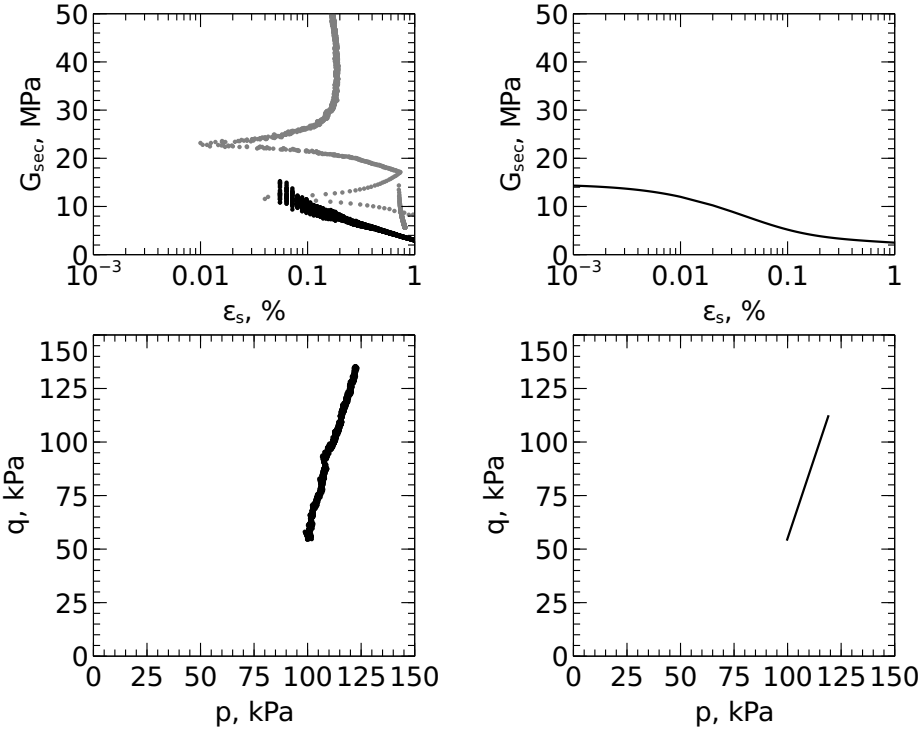

(A.33.1) Data

(A.33.2) Simulation

Figure A.33: Shear degradation and stress path, TestID: FB1TC2

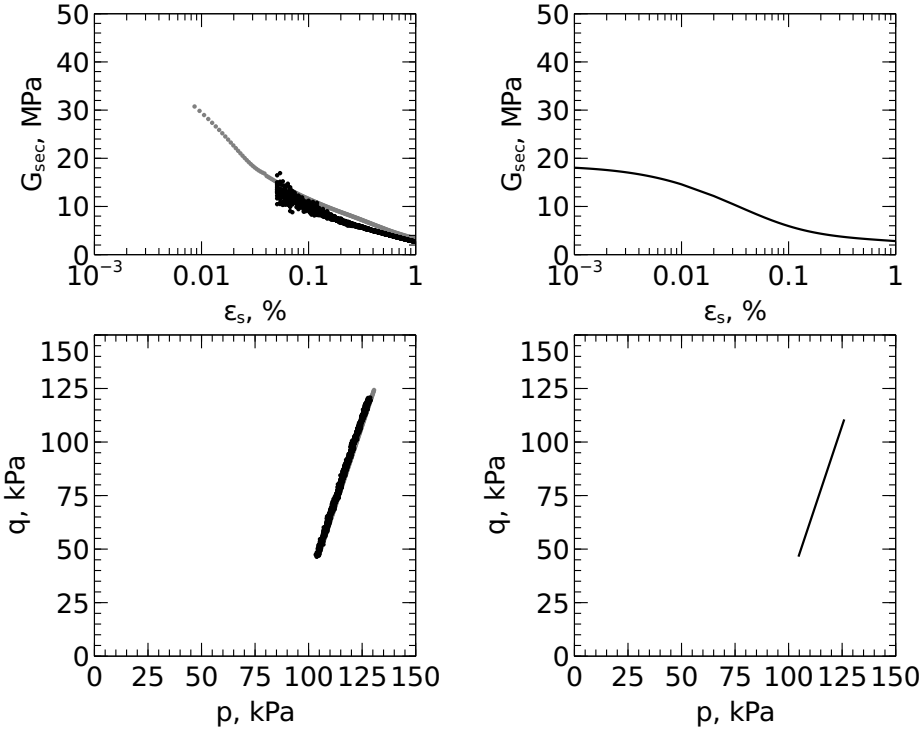

(A.34.1) Data

(A.34.2) Simulation

Figure A.34: Shear degradation and stress path, TestID: FB2TC2

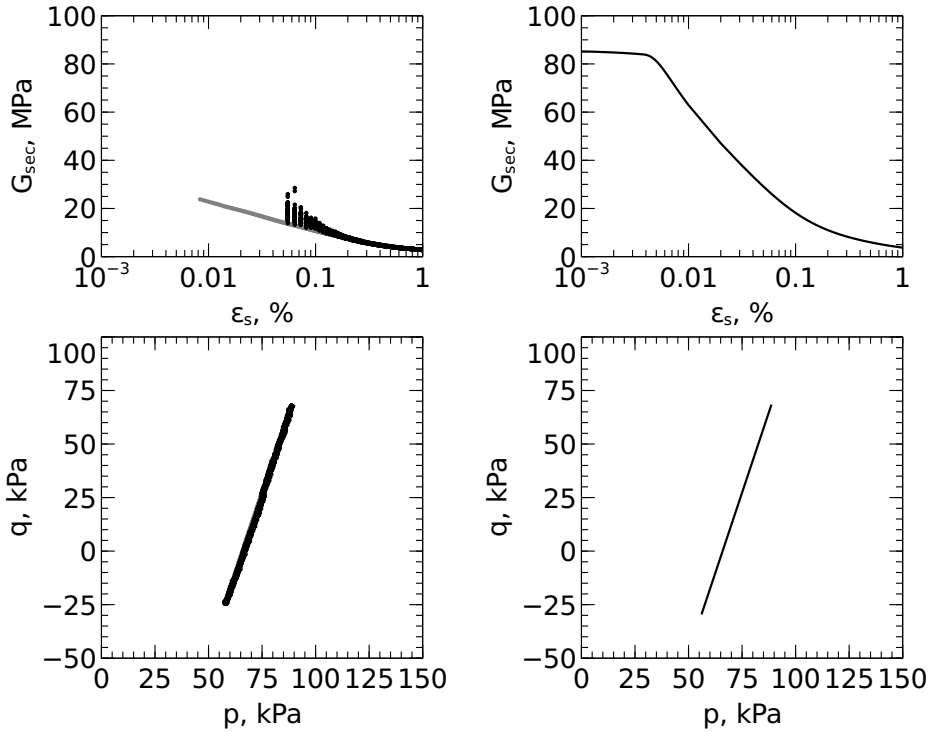

(A.35.1) Data

(A.35.2) Simulation

Figure A.35: Shear degradation and stress path, TestID: LB3RTE1

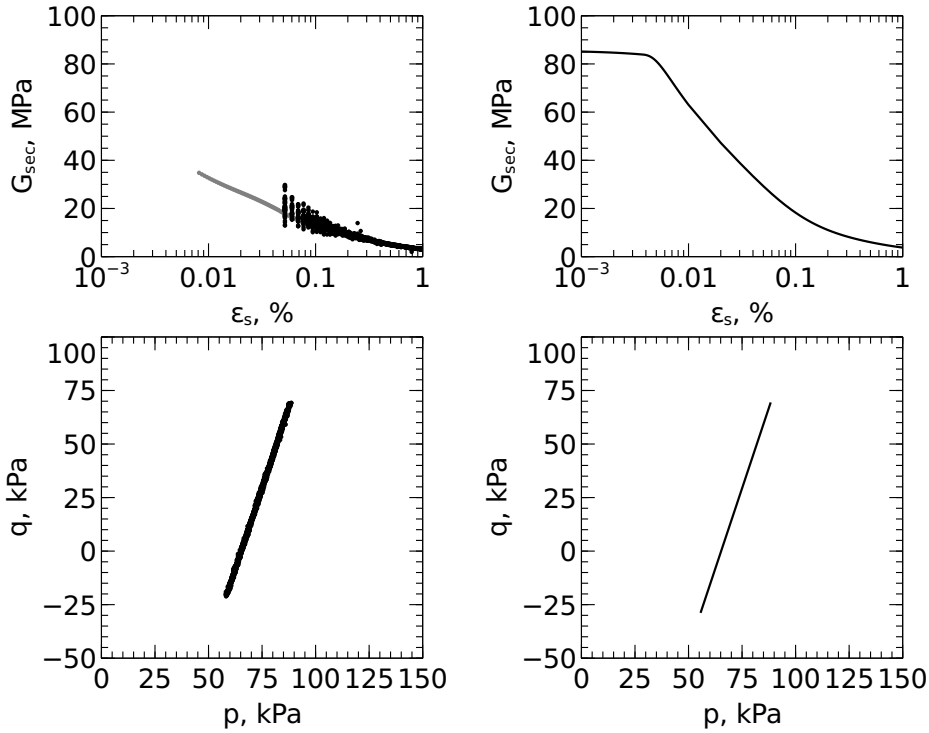

(A.36.1) Data

(A.36.2) Simulation

Figure A.36: Shear degradation and stress path, TestID: LB3RTE2

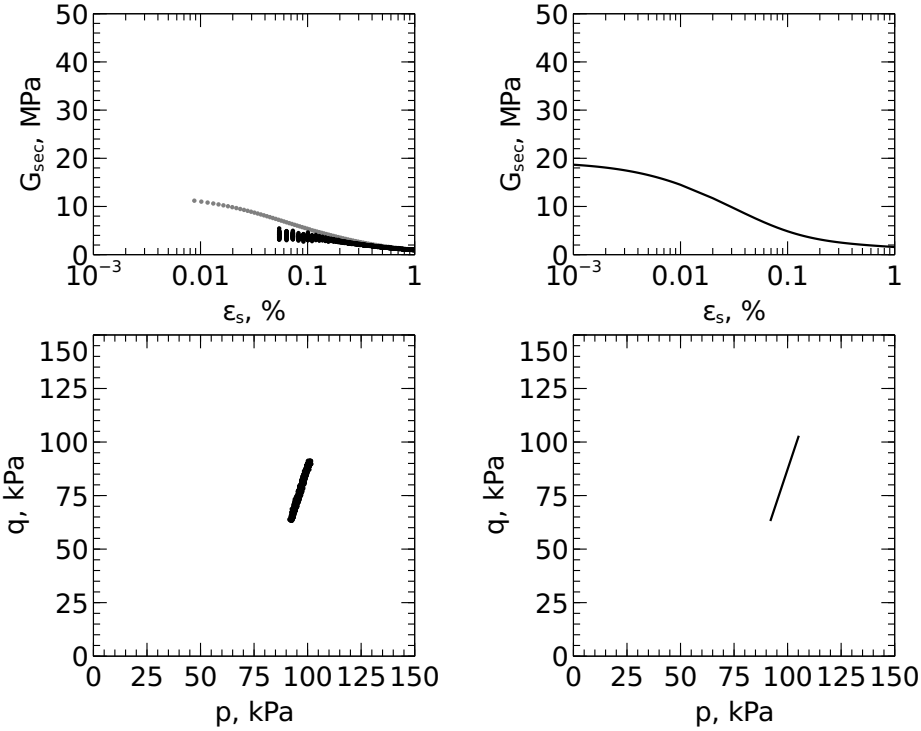

(A.37.1) Data

(A.37.2) Simulation

Figure A.37: Shear degradation and stress path, TestID: LB3TC2

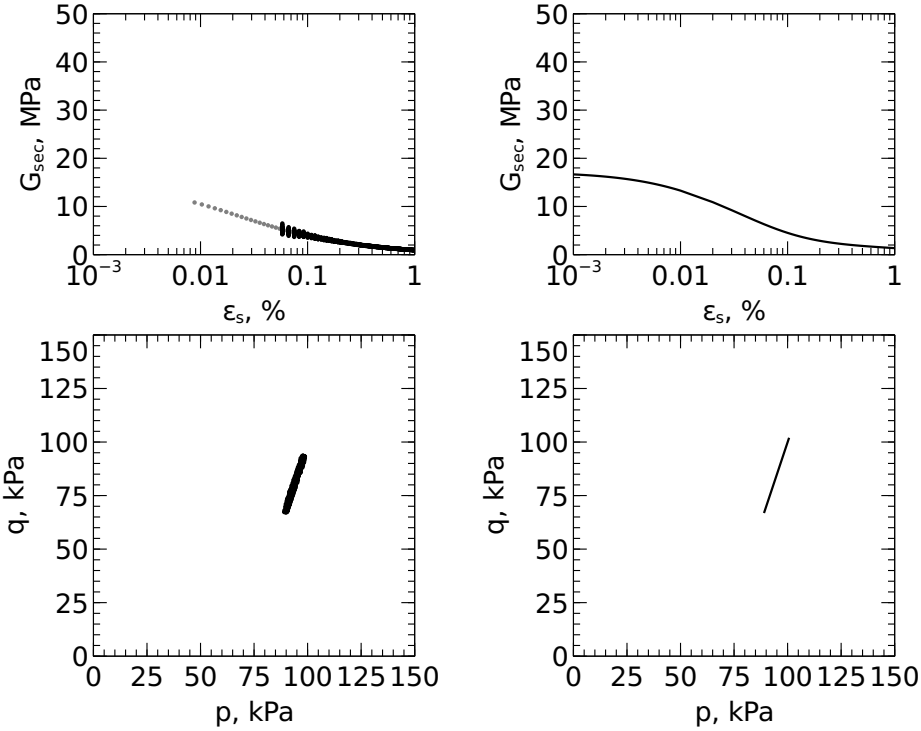

(A.38.1) Data

(A.38.2) Simulation

Figure A.38: Shear degradation and stress path, TestID: LB3TC3

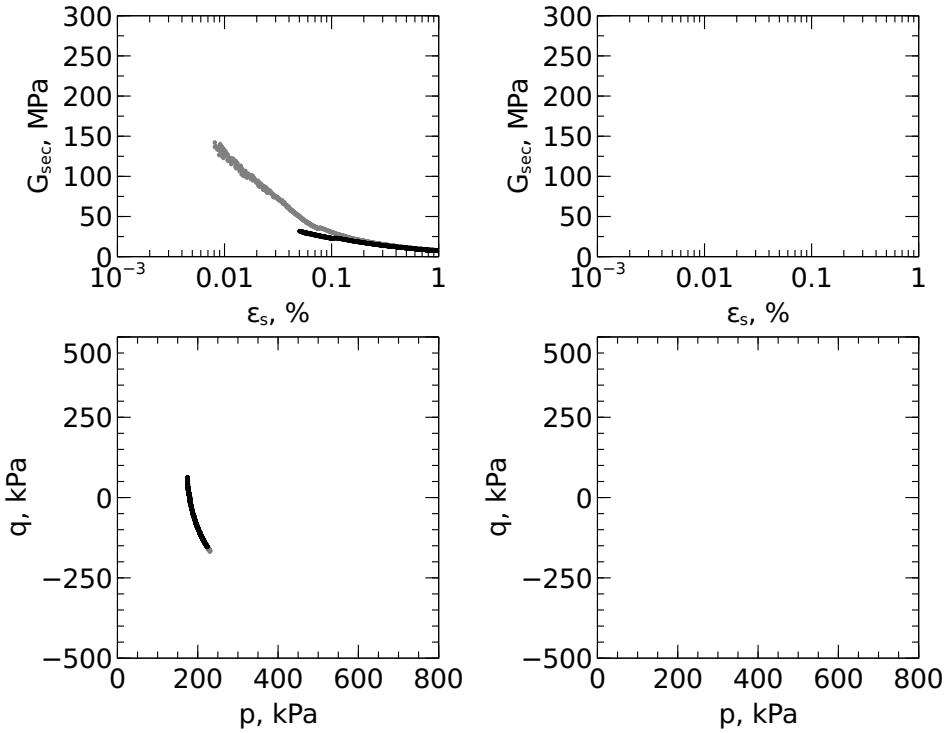

(A.39.1) Data

(A.39.2) Simulation

Figure A.39: Shear degradation and stress path, TestID: O1P1RTE

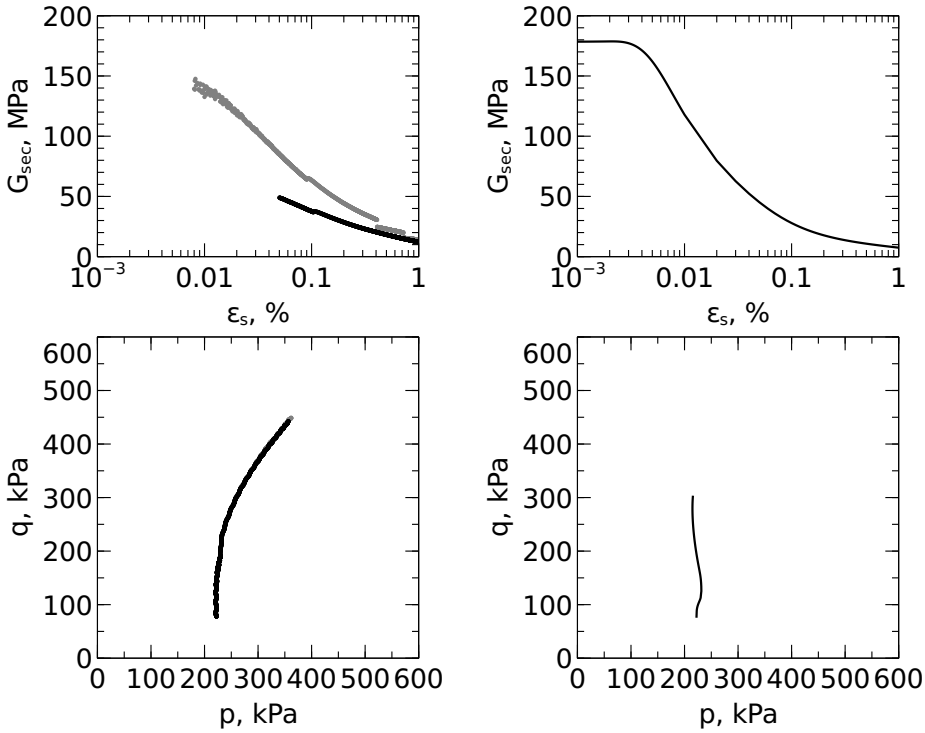

(A.40.1) Data

(A.40.2) Simulation

Figure A.40: Shear degradation and stress path, TestID: O1P2TC

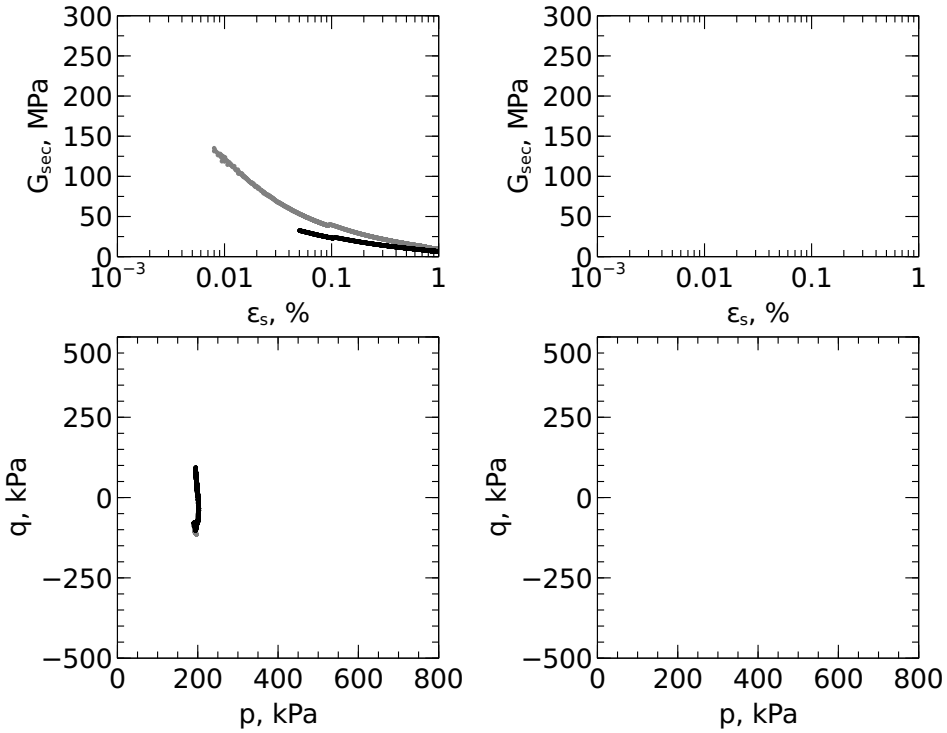

(A.41.1) Data

(A.41.2) Simulation

Figure A.41: Shear degradation and stress path, TestID: O2P1RTE

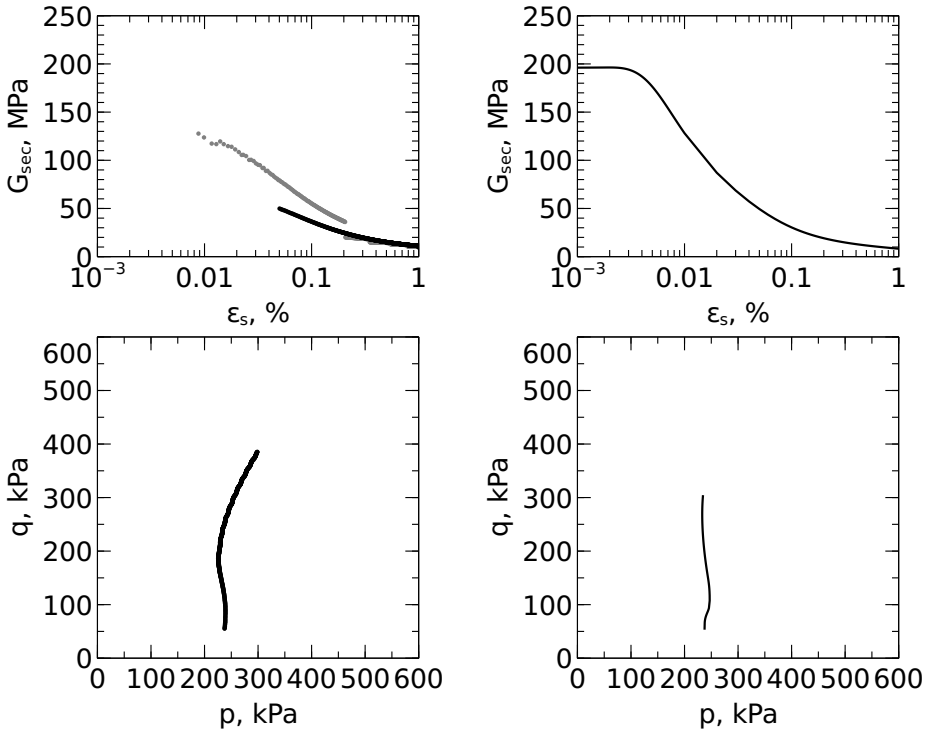

(A.42.1) Data

(A.42.2) Simulation

Figure A.42: Shear degradation and stress path, TestID: O2P3TC

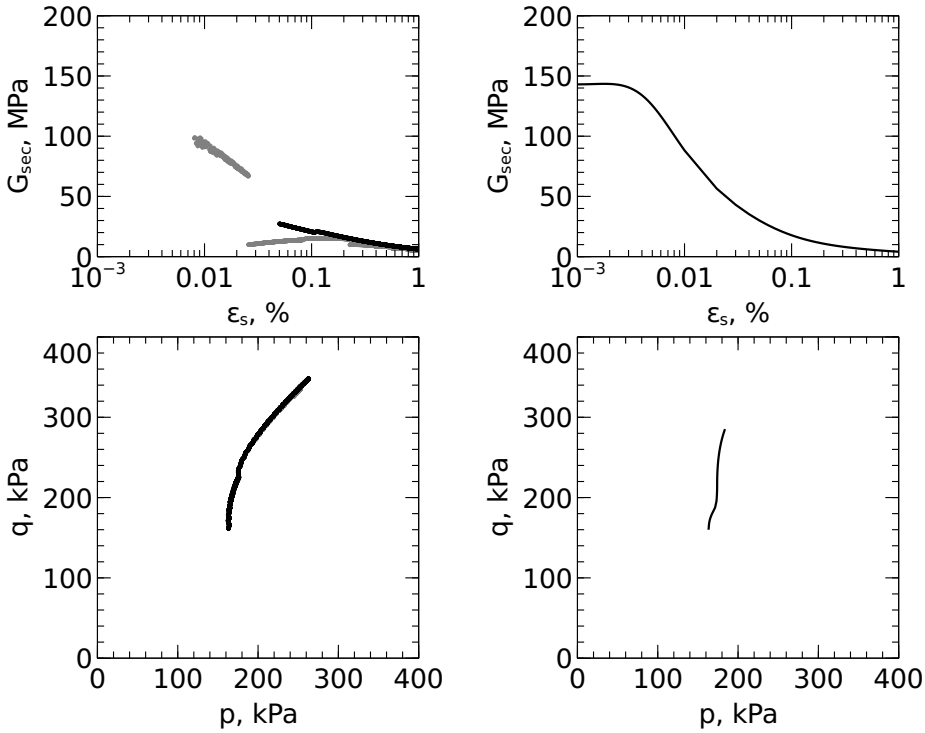

(A.43.1) Data

(A.43.2) Simulation

Figure A.43: Shear degradation and stress path, TestID: O3P4TC

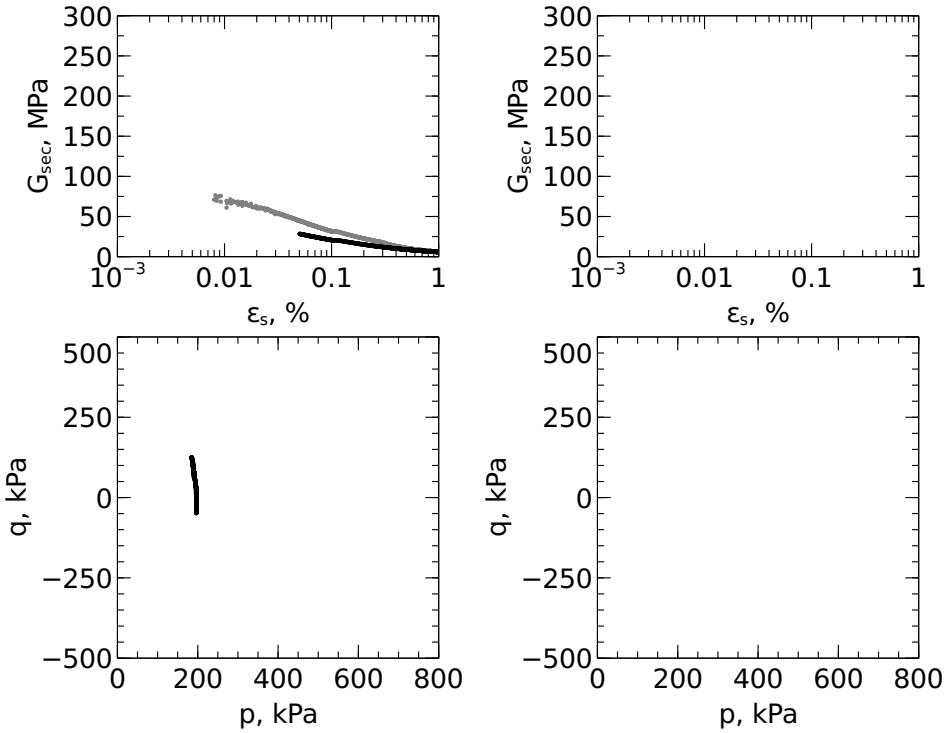

(A.44.1) Data

(A.44.2) Simulation

Figure A.44: Shear degradation and stress path, TestID: O3P5RTE

Analysis of Top-Down Construction at the Block 37 Project in Chicago, Illinois

Kristi Sue Kern

6/6/2011

Abstract

The Block 37 Project in Chicago, Illinois presented a good case study to evaluate the performance of an excavation support system during top-down construction. Top-down construction is an increasingly popular form of construction being employed by contractors in urban environments because of its apparent ability to minimize adjacent ground movements. The ground movements observed during the Block 37 excavation were evaluated and compared to previous case studies herein. A finite element simulation was produced to recreate the excavation activities to more closely see the effect of specific construction activities on adjacent ground movements. The creep and shrinkage of the lateral support elements were calculated as a possible explanation for the discrepancy between the observed movements and the calculated movements from the finite element simulation.

Acknowledgements

First, and most importantly, I would like to thank Professor Richard J. Finno, my academic advisor, for his guidance throughout my research. I would also like to thank Professor Charles H. Dowding for being a part of my defense committee and for providing feedback and recommendations to my research. I would also like to thank the National Science Foundation (NSF Grant # 0928184) and the Infrastructure Technology Institute for providing financial support for this research.

Secondly, I would like to thank my fellow students; especially Linlong Mu, Taesik Kim and Fernando Sarabia who worked on research related to my project and often provided data and direction that was very much appreciated. I would also like to thank my other fellow students, Hilde Knai, Aaron Gallant, Ali Patrone, Luis Arboleda, Carlos Vega-Posada and David Zapata-Medina, who worked alongside me to juggle class work and research.

Last but not least, I would like to thank my family and friends who put up with me during many stressful times. I could not have done this without all of your support.

Table of Contents

Chapter 1: Introduction 1-1

1.1 Purpose 1-2

1.2 Organization of Thesis 1-2

Chapter 2: Site Description 2-1

2.1 Project Overview 2-1

2.1.1 Site Location 2-1

2.1.2 Soil Geology and Stratigraphy 2-2

2.1.3 Excavation Support System 2-4

2.1.4 Construction Sequence 2-7

2.2 Instrumentation 2-8

2.2.1 Inclinometers 2-8

2.2.2 Settlement Points 2-9

2.3 Summary 2-10

Chapter 3: Observed Deformations during Construction of Excavation Support System 3-1

3.1 Inclinometer Data 3-1

3.1.1 Cross Section A 3-4

3.1.2 Cross Section B 3-6

3.1.3 Cross Section C 3-8

3.2 Inclinometer Data Analysis 3-10

3.3 Settlement Data 3-15

3.4 Settlement Point Data Analysis 3-16

3.5 Summary and Conclusions 3-23

Chapter 4: Finite Element Model 4-1

4.1 Input parameters 4-3

4.1.1 Structural Elements 4-3

4.1.2 Soil Elements 4-7

4.2 Installation of Slurry Wall 4-10

4.3 Potholing 4-11

4.4 Excavation and Floor Slab Installation 4-15

4.5 Summary 4-16

Chapter 5: Comparison of Computed and Observed Performance 5-1

5.1 Baseline Simulation 5-1

5.2 Creep and Shrinkage 5-4

5.2.1 Creep 5-5

5.2.2 Shrinkage 5-5

5.2.3 Correction Factors 5-6

5.3 Bending Moments 5-9

5.4 Undrained Simulation 5-10

5.5 Lateral Support Lengths 5-11

5.6 Summary and Conclusions 5-12

Chapter 6: Conclusions and Recommendations for Future Work 6-1

Chapter 7: References.....7-1

Figures

Figure 2-1: Block 37 Site Location....2-1

Figure 2-2: Soil Stratigraphy....2-2

Figure 2-3: Structural Slurry Wall Location....2-5

Figure 2-4: Slurry Wall Cross Section....2-6

Figure 2-5: Inclinometer Locations....2-9

Figure 2-6: Settlement Point Locations....2-10

Figure 3-1: Lateral Movements during Slurry Wall Installation....3-4

Figure 3-2: Cross Section A Lateral Movements (after Slurry Wall Installation)....3-5

Figure 3-3: Cross Section B Lateral Movements (after Slurry Wall Installation)....3-7

Figure 3-4: Cross Section C Lateral Movements (after Slurry Wall Installation)....3-9

Figure 3-5: Typical Profiles of Movement for Braced and Tied-Back Walls (Clough & O'Rourke, 1989) ..

....3-10

Figure 3-6: INC-61A without Cantilever Movements....3-12

Figure 3-7: Design Curves to Obtain Maximum Lateral Wall Movement for Soft to Medium Clays

(Clough, 1989)....3-13

Figure 3-8: Maximum Lateral Wall Movement vs. System Stiffness (Finno &Wang, 2006)....3-15

Figure 3-9: Settlement at End of Construction for 3 Cross Sections....3-16

Figure 3-10: Inclinometer and Settlement Point Comparison at Cross Section A and Z....3-17

Figure 3-11: Predicted Settlement Profile (Hseih and Ou, 1998)....3-18

Figure 3-12: Cantilever Area and Deep Inward Area for INC-61A....3-19

Figure 3-13: Relationship between the Cantilever Area and Deep Inward Area for INC-61A....3-19

Figure 3-14: Predicted and Actual Normalized Settlement Profiles....3-20

Figure 3-15: Spandrel Profile and Cross Section Z with Assumed Maximum Settlement....3-21

Figure 3-16: Settlement Profile Parallel to Excavation (Roboski, 2004)....3-22

Figure 3-17: Proposed Settlement Profile and Measured Settlement Points. 3-23

Figure 4-1: Finite Element Model Mesh (PLAXIS, 2010) 4-1

Figure 4-2: Anchor Span Lengths for Cross Section A 4-6

Figure 4-3: Cross Section Showing Slab Lengths at A.....4-6

Figure 4-4: Inclinometer Movements Due to Slurry Wall Installation 4-11

Figure 4-5: Lateral Movements Due to Potholing in Inclinometers Adjacent to Slurry Wall 4-12

Figure 4-6: Webcam Photo during Potholing (Hill, 2006) 4-13

Figure 4-7: Potholing dimensions.....4-13

Figure 4-8: Lateral Movements Due to Potholing in Inclinometers Adjacent to Slurry Wall and PLAXIS Results.....4-14

Figure 4-9: PLAXIS Model After Final Construction Stage 4-15

Figure 5-1: Cantilever Movements from Cross Section A Baseline PLAXIS Simulation and Recorded Movements.....5-2

Figure 5-2: Deep Inward Movements from Cross Section A Baseline PLAXIS Simulation and Recorded Movements.....5-3

Figure 5-3: Cross Section A Baseline PLAXIS Simulation and INC-61A with Creep and Shrinkage 5-8

Figure 5-4: Bending Moments in Cross Section A PLAXIS Simulation.....5-9

Figure 5-5: Cross Section A PLAXIS with and without Consolidation 5-10

Figure 5-6: Cross Section A PLAXIS with varying Slab Lengths.....5-12

Tables

Table 2-1: Dates of Major Construction Activities....2-7

Table 3-1: Installation Summary of Inclinometers....3-3

Table 4-1: Finite Element Model Calculation Steps....4-2

Table 4-2: Slurry Wall Material Parameters (Solid Element)....4-4

Table 4-3: Slurry Wall Material Parameters (Plate Element)....4-4

Table 4-4: Floor Slab Material Parameters (Anchor Element)....4-5

Table 4-5: Floor Slab Lengths (Anchor Element)....4-7

Table 4-6: MC Material Parameters for Sand Fill, Tinley and Valparaiso....4-8

Table 4-7: Hardening Soil Material Parameters for Blodgett, Deerfield and Park Ridge....4-10

Table 5-1: Summary of Finite Element Simulations....5-1

Table 5-2: Creep Strains....5-7

Table 5-3: Shrinkage Strains....5-7

Chapter 1: Introduction

Urban excavation is becoming increasingly more challenging because of more stringent restrictions on resulting ground deformation. These restrictions are needed to minimize the impact to surrounding structures and may be prescribed in terms of total settlement, differential settlement and/or wall movements. These restrictions can be as small as a maximum movement of 0.5 to 1.5 inches. Furthermore, developers and owners are turning to top-down construction to take the excavation process off the critical path of construction. Top-down construction consists of installation of a vertical retaining wall prior to excavation. Then lateral support in the form of a permanent floor slab is constructed near the ground surface to restrain the wall laterally. Spaces are left open through the lateral supports so excavation can commence below these supports. The soil is then excavated below the cast-in-place floor slab. The benefits of top-down construction consist of a faster overall construction time because construction proceeds upwards and the excavation extends downward simultaneously. Also, the lateral supports consist of the permanent floor slabs, which can save both time and money.

Another benefit of top-down construction is the relative stiffness of the system. Often the top-down construction process results in a stiffer system as compared to conventional bottom-up excavation support systems. Top-down construction eliminates the need for a temporary excavation support system and thus eliminates the additional movements that result from removing the temporary system and installing the permanent system. Consequently, the ground movements surrounding the excavation should be less than conventional excavation processes, everything else being equal.

Performance monitoring is also an important component of the construction of excavation support systems. A contractor is often compelled to monitor the lateral wall movements and adjacent settlements to prove that the movements are within the restrictions imposed by the regulatory body. The contractor may also use the performance monitoring data to spot possible problems with the construction process

and to improve upon the system. If wall movements are greater than the maximum allowable movements, the contractor may have to install additional lateral supports.

The Block 37 Development, located in Chicago, Illinois is an example of top-down construction in an urban setting. A reinforced concrete slurry wall formed the perimeter wall at the site. The lateral support system consisted of 4 concrete floor slabs installed during excavation as part of the permanent structure. Inclinometers and settlement points were monitored throughout construction to record the lateral wall movement and adjacent ground settlement near the excavation. This thesis summarizes the construction activities and associated ground deformations and presents the results of finite element simulations of the process.

1.1 Purpose

The purpose of these analyses is to evaluate the performance of the slurry wall along the northern edge of the Block 37 excavation based on available construction documents and performance monitoring data. Specifically, the inclinometer movements and settlements recorded during excavation are analyzed with respect to the excavation progress. Finite element simulations of the construction process are created to compare the calculated lateral movements with the performance monitoring data. Creep and shrinkage of the concrete lateral support elements (basement floor slabs) are evaluated to show the potential significance of these time-dependent movements. Conclusions are presented and recommendations for future work are provided.

1.2 Organization of Thesis

Four chapters follow this introduction. Chapter 2 presents a general description of the site, the excavation support system and the stratigraphy. Chapter 3 summarizes the performance monitoring data collected during excavation. The inclinometer and settlement data are presented in relation to key construction activities. Chapter 4 summarizes the finite element analyses. The input parameters required for the analyses and their basis of selection are presented. Details of the finite element simulations are

summarized. Chapter 5 compares the performance monitoring data and results of the finite element analyses. Computed results are compared with lateral movements, and surface settlements. The possible effects of creep of the lateral supports on the observed movements are discussed. Chapter 6 presents conclusions and suggestions for future work.

Chapter 2: Site Description

The Block 37 project is a top-down construction project completed in an urban environment. This chapter will provide an overview of the project. Also included is a description of the monitoring data collected throughout construction.

2.1 Project Overview

The excavation for the Block 37 project commenced in 2007 and was completed in 2008. This section provides a description of the site location, soil geology and stratigraphy. The excavation support system and the construction sequence are also described in this section.

2.1.1 Site Location

The Block 37 Development is located in Chicago, Illinois. As shown in Figure 2-1, the site is located in the downtown area of Chicago and is bordered on the north by Randolph Street, east by State Street, south by Washington Street and west by Dearborn Street.

Figure 2-1: Block 37 Site Location

The site had been developed prior to construction and consisted of a variety of commercial spaces. Because existing structures were present on the site, excavation and removal of existing foundations (potholing) were required prior to construction. The excavation support system employed for the Block 37 development was a structural slurry wall constructed around the perimeter of the site, supported horizontally by reinforced-concrete floor slabs. For the floor slabs to provide support during the excavation, a top-down construction approach was used. The focus of this study is the performance of the section along the northern portion of the site, adjacent to Randolph Street.

2.1.2 Soil Geology and Stratigraphy

Chicago soils have been studied for many years and the knowledge of the basic stratigraphy is widely available. Figure 2-2 shows the basic stratigraphy at the site.

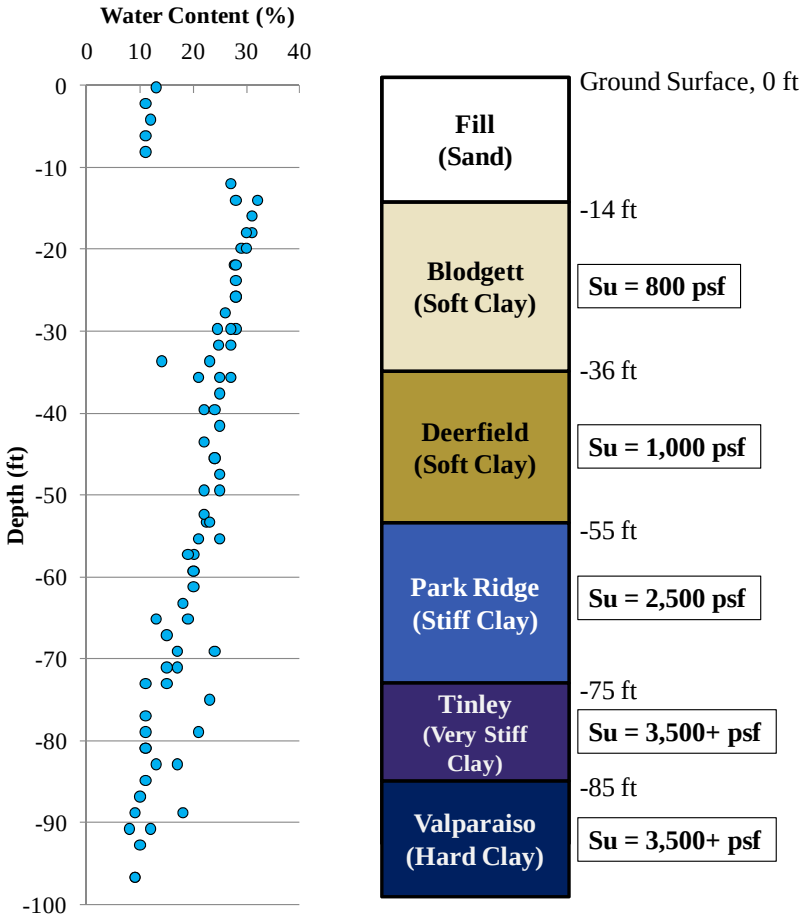

Figure 2-2: Soil Stratigraphy

There are 6 soil layers underlying the project site. The top layer is an urban fill material consisting of a sandy soil and construction debris. The fill layer is present from the ground surface to approximately 14 ft below ground surface. Underlying the fill material are several layers of glacially deposited clays. The first two layers are soft to medium stiff clays which are very similar mineralogically, but exhibit different geotechnical characteristics due to the type of glacial deposition. The first layer is the Blodgett Stratum, which underlies the fill material. This clay was deposited in a supra-glacial environment, which include glaciolucustrine clays and melt-out and flow tills (Finno & Chung, 1992). Because of this complicated depositional environment, the Blodgett generally has variable geotechnical characteristics, including water content, strength and stiffness. Underlying the Blodgett clay is a medium stiff clay, called the Deerfield stratum, present from 37 to 55 ft below ground surface. The Deerfield layer exhibits much more uniform geotechnical characteristics than the Blodgett stratum which can be attributed to the depositional environment. The Deerfield was deposited as a basal melt-out till or a waterlain paratill (Finno & Chung, 1992).

Underlying the soft to medium stiff clay layers lie three stiffer clay layers. These layers were deposited before the softer clay layers. Because these layers are older, they are also stiffer since more time was allowed for the clay to age. More importantly, glaciers were present over the lower two very stiff to hard clay layers resulting in the clays being overconsolidated. The stiff Park Ridge clay is located approximately 55 to 74 ft below ground surface. A deposit locally known as “hardpan” is found beneath the Park Ridge Strata. The upper portion of the hardpan at this site is a very stiff clay layer called Tinley clay. This Tinley clay layer exists between 74 and 84 ft below ground surface. The Valparaiso layer underlies the Tinley layer and is also part of the hardpan. The Valparaiso layer is a hard clay.

A clay crust layer is often present on top of the Blodgett stratum. At this site, the crust is relatively thin (2 to 8 ft thick), and in some cases is not present at all. Because of the irregularity of this clay crust, it was not shown in Figure 2-2 and was omitted from the analyses performed herein because of the lack of continuity of the layer.

2.1.3 Excavation Support System

The Block 37 development employed a top-down construction technique. The main purpose of the top-down construction is to build up as well as excavate down concurrently. This approach takes the excavation off the critical path of a project, and results in longer excavation times than conventional bottom-up construction. Usually, some sort of perimeter support is installed prior to any additional construction and then lateral supports are added as excavation progresses. Typical excavation progresses at a slower rate because of limited access; however, the construction up from ground level occurs at the same time, and overall a faster construction time is usually achieved. The Block 37 development deviated from a typical top-down construction system because the ground surface lateral support was not installed prior to any significant excavation; rather the first lateral support was placed after 20 ft of excavation. The contractor made the decision to delay placement of the ground surface slab on the basis of construction expediency. The impact of this decision on the resulting ground movements will be apparent in Chapter 3.

A 3 ft thick structural slurry wall was constructed around the perimeter of the site as shown in Figure 2-3. A cross section of the slurry wall and the locations of each basement slab along the north wall adjacent to Randolph Street are shown in Figure 2-4. After installation of the slurry wall the existing foundations were removed. This process was not well-documented at this site. After the potholing activities, the excavation progressed in stages to the four basement floors (B1, B2, B3 and B4). Because the "ground" slab was placed after slab B1, the slurry wall was cantilevered with an unsupported length of about 20 ft before any lateral support was placed. The total depth of the slurry wall was 70 ft. Note that the elevations shown in Figure 2-4 refers to the Chicago City Datum (CCD).

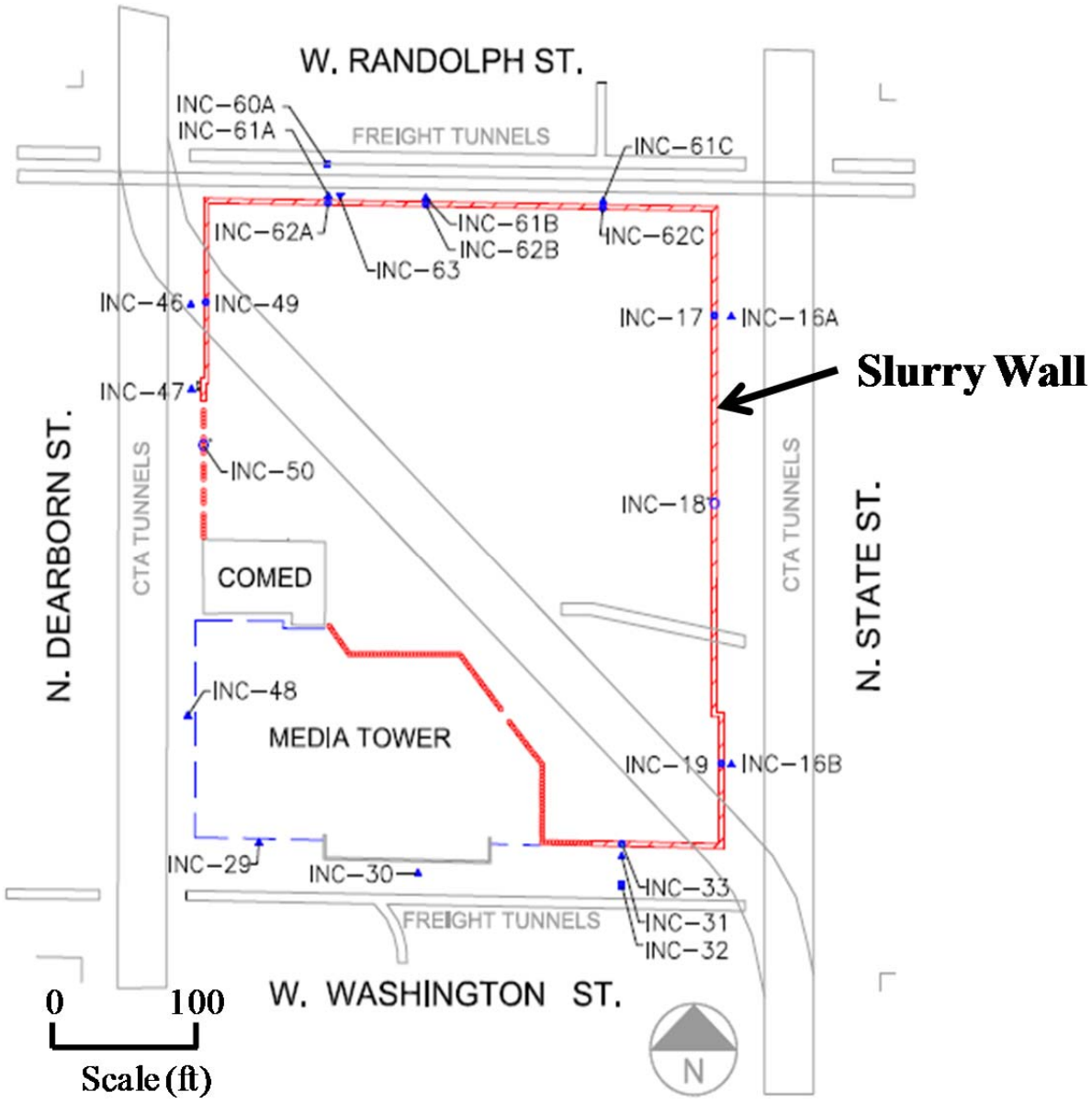

Figure 2-3: Structural Slurry Wall Location

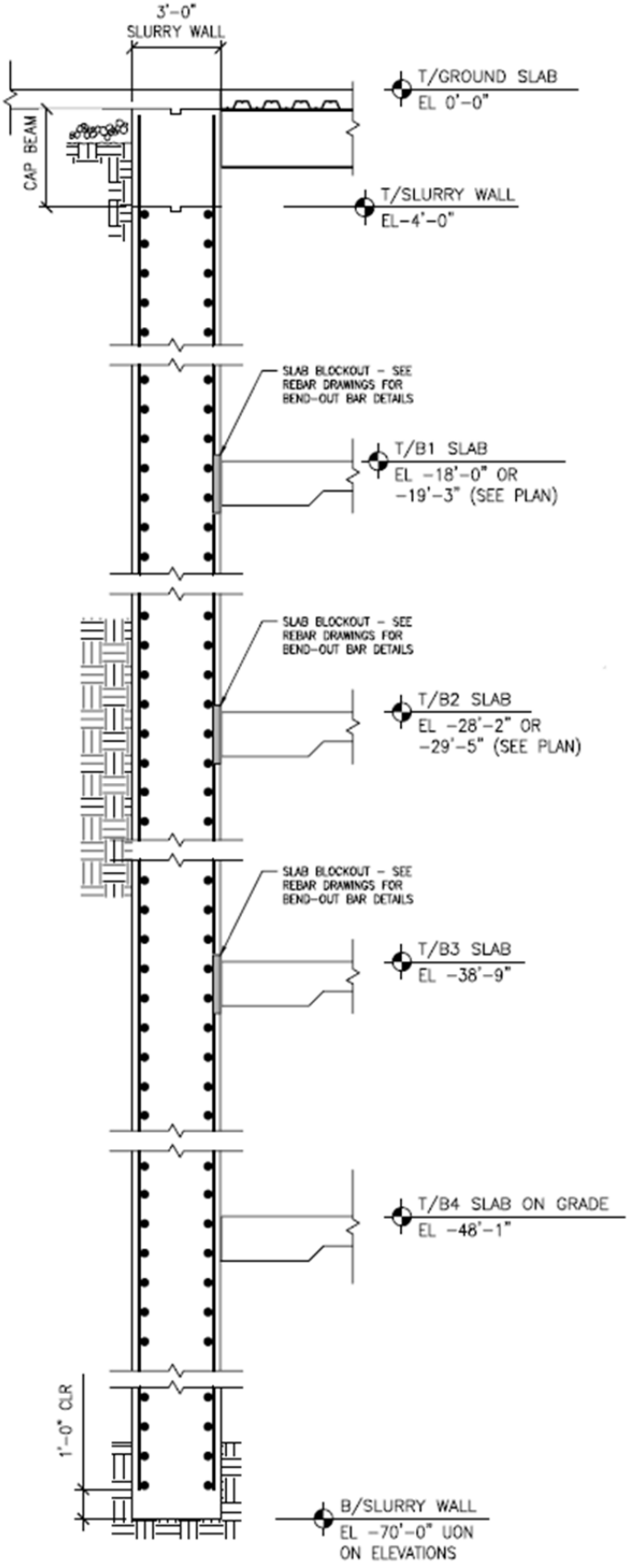

Figure 2-4: Slurry Wall Cross Section

2.1.4 Construction Sequence

Construction for the Block 37 development commenced in January 2007. A table of the major construction activities and the dates when they occurred are summarized below in Table 2-1. These dates were deduced from construction records obtained from the Contractor.

Table 2-1: Dates of Major Construction Activities

Construction Activity	Dates
Slurry Wall	01/07-02/07
Potholing	03/07-05/07
Excavation Begins	06/07-07/07
B1 Slab Installed	08/07-10/07
B2 Slab Installed	11/07-12/07
B3 Slab Installed	02/08-05/08
B4 Slab Installed	06/08

The slurry wall was installed early in 2007. After the installation of the slurry wall, the potholing activities were performed. Potholing consisted of removal and excavation of existing foundations present on-site and then refilling the excavated areas. The dates of the potholing activities in the above table are approximate because specific documents regarding the potholing activities were not available.

The excavation for Block 37 started in the summer of 2007 and continued until the summer of 2008. The floor slabs were installed incrementally from the first basement slab (B1) on down to the fourth (B4) during the year of construction. The floor slabs provided the main lateral support for the excavation support system; therefore, installation of each floor slab was required before additional excavation could commence. Weekly progress was summarized on drawings for mining and concrete activities and these dates in Table 2-1 are judged accurate to within one to two weeks. The potholing activities were

estimated based on the installation date of the slurry wall and the excavation start date. Also, note that the installation of the ground floor slab is not summarized in the construction activities. The Contractor did not install the ground floor slab prior to excavation. Thus, the lateral support at the top of the slurry wall was not present. This omission resulted in significant cantilever movements, as will be shown in Chapter 3.

2.2 Instrumentation

Instrumentation was installed throughout the site to monitor the performance of the excavation support system and general construction activities. The instrumentation of interest to this study are the inclinometers and settlement points on the north side of the excavation.

2.2.1 Inclinometers

The inclinometers located along Randolph Street are shown in Figure 2-5. There are three cross sections (A, B, and C) along which inclinometers were installed. The lateral ground movements recorded at these inclinometer locations are analyzed in Chapter 3. Inclinometers were installed both in and within 5 ft of the slurry wall at each of the three cross sections. An additional inclinometer (INC-60A) was installed approximately 25 ft from the slurry wall at Cross Section A.

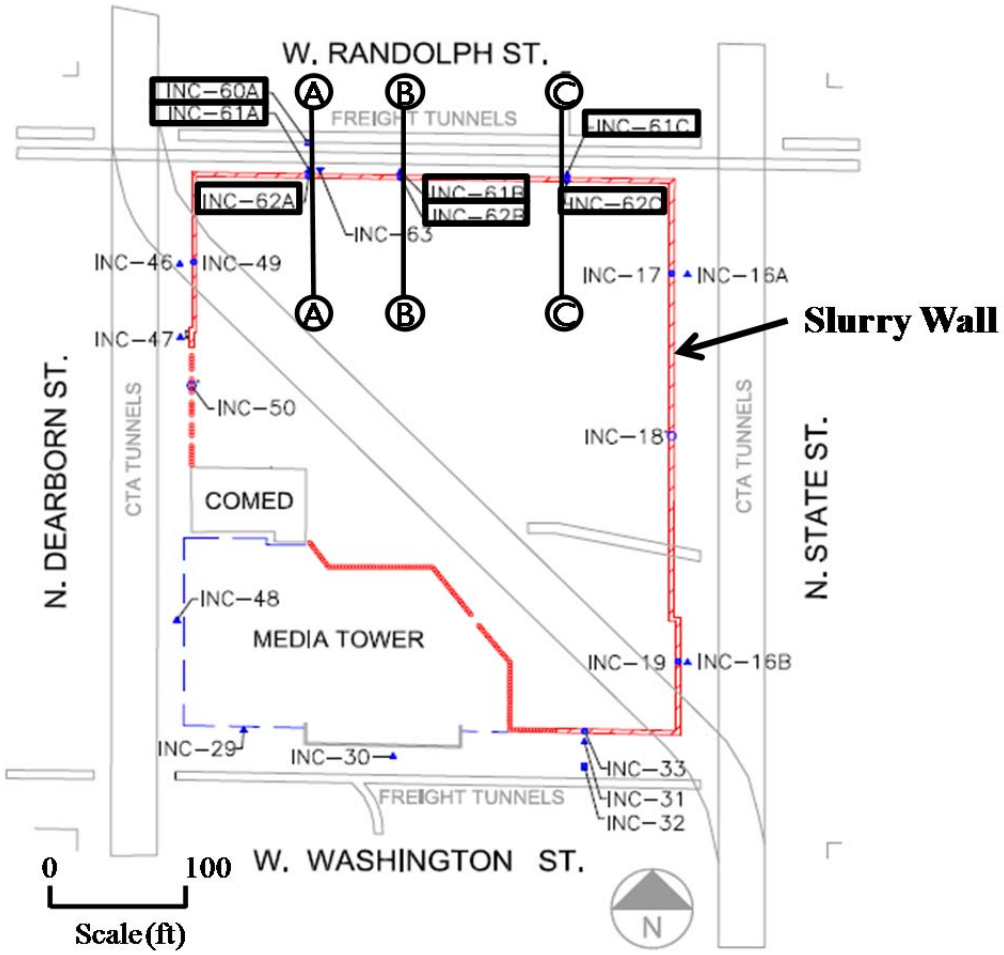

Figure 2-5: Inclinometer Locations

2.2.2 Settlement Points

The location of the settlement points are shown below in Figure 2-6. The settlement points of interest are located approximately 40 to 80 ft east of the Northwest corner of the slurry wall, along Randolph Street. Three cross sections of settlement points (X, Y and Z) are analyzed in further detail in subsequent sections. The further the distance from the corner of the slurry wall, the less the settlement will be affected by the corner at the western side of the site. Therefore, cross section Z should relate more closely to the 2D analysis than cross section X. Note that the location of Cross Section Z is approximately the same as the location of Cross Section A from the inclinometers. The fact that these two are aligned in the same location will be useful for subsequent analyses.

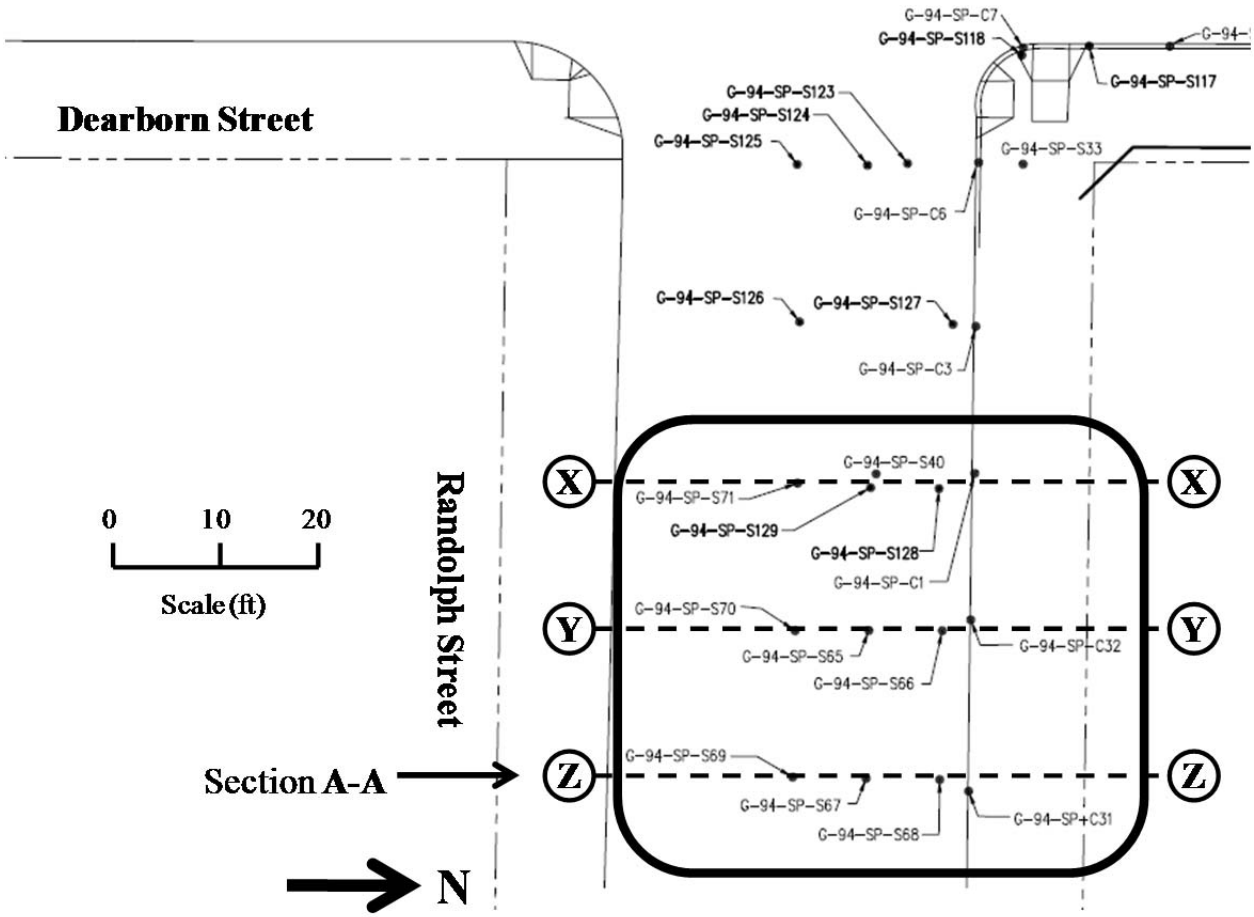

Figure 2-6: Settlement Point Locations

2.3 Summary

The Block 37 project is located in downtown Chicago, Illinois. The site is located in an urban area with the usual existing infrastructure. The soil stratigraphy consists of a surficial fill, and 5 layers of clays ranging from soft to hard. The excavation support system is a structural slurry wall with reinforced concrete floor slabs as lateral supports. The construction occurred in 2007 and 2008. Inclinometers and settlement points were used to monitor ground movements along the north end of the excavation during construction.

Chapter 3: Observed Deformations during Construction of Excavation Support System

Inclinometers and settlement points were installed at the site to monitor horizontal wall movements and settlements adjacent to the excavation. The settlement points and some inclinometers were installed prior to construction and were monitored during and after construction. Inclinometers located in the slurry wall were installed when the slurry wall was installed. This chapter summarizes these movements and evaluates this response in light of expected performance based on published data.

3.1 Inclinometer Data

Inclinometers were installed throughout the site to measure lateral deformations of the soil and slurry wall. The inclinometers of interest to this thesis are shown in Figure 2-5. An inclinometer is basically a plastic pipe placed in a borehole with the outside of the borehole backfilled with weak grout. The pipe and grout are assumed to move with the surrounding soil. The inside of these pipes have 4 grooves along the length, 90 degrees apart. To take readings, an inclinometer sensor is placed in the grooves to the bottom of the pipe and lifted in 2 ft increments to measure the tilt in the casing. The sensor reads the angle of the pipe, which is used to obtain a profile of the alignment of the pipe. The inclinometer sensor typically is placed in the grooves perpendicular to the excavation and a biaxial sensor is used to obtain movements both parallel and perpendicular to the excavation.

The inclinometer movements of interest for this study are perpendicular to the excavation. The inclinometer movements parallel to the excavation did not appear to show any significant trend in movements. Movements in the parallel axis would usually start to move in one direction and then the opposite direction. The magnitude of the movements were much smaller (typically less than 0.5 inches) than the movements in the perpendicular direction (typically 1.5 to 2.5 inches). Furthermore, the parallel movements are based on the “B-Axis” of the inclinometer, which is an order of magnitude less accurate than the “A-Axis” of the inclinometer, which was used to measure movements perpendicular to the wall

in this case. Because the movements parallel to the wall were small and erratic, they were judged to be insignificant and were omitted from these analyses.

A summary of the installation of the inclinometers is provided in Table 3-1. The notation for each inclinometer in the table describes the location. A, B or C describes its location along the wall. The inclinometers noted by “61” were placed in the ground within several ft of the slurry wall location prior to its installation. The inclinometers noted by “62” were placed in the slurry wall. The “60” inclinometer was located about 25 ft behind the wall.

Two inclinometers (INC-62A and INC-61B) were damaged during construction and were eventually replaced. Another inclinometer (INC-62B) was reinstalled after being damaged, but was missing data from the bottom portion of the inclinometer, apparently because it was filled with debris. Inclinometers were reinstalled within several feet of the original location of the inclinometer. The slurry wall inclinometers were installed during the construction of the slurry wall and reinstalled inclinometers were installed adjacent to the slurry wall, because installation through the hardened concrete was not feasible. Therefore, the reinstalled inclinometers represented movements adjacent to the slurry wall and not actual slurry wall movements. Also, another inclinometer (INC-61C) had a portion of the bottom filled with debris and therefore does not have data for the lower portion of the inclinometer.

Table 3-1: Installation Summary of Inclinometers

Inclinometer ID	Installation Date	Installed Depth (ft)	Last Collection Date	Notes
INC-60A	1/10/2007	88	11/3/2008	
INC-61A	12/6/2006	88	11/3/2008	
INC-62A (Wall)	2/21/2007	56	11/3/2008	No data (9/17/2007 – 10/26/2007); Reinstalled adjacent to wall (10/26/2007)
INC-61B	12/6/2006	88	11/3/2008	No data (3/21/2007 – 10/26/2007); Reinstalled (10/26/2007)
INC-62B (Wall)	3/29/2007	68	11/3/2008	Bottom 12 ft filled (9/28/2007 – 10/15/2007); Reinstalled (10/26/2007)
INC-61C	12/6/2006	88	8/5/2008	Bottom 40 ft filled (3/20/2008)
INC-62C (Wall)	2/21/2007	66	7/22/2008	

As a result of these occurrences, several adjustments were made to the inclinometer data to attempt to obtain a "continuous" record of lateral deformation at each of the three sections. Adjustments were made for missing data, unrealistic results, toe movements and other reasons explained later in further detail. To more easily visualize the data, only significant construction dates were plotted for each inclinometer. Each cross section was also adjusted to have the same start date, corresponding to right after slurry wall installation, to more easily compare the lateral movements that developed during construction. For inclinometers that were installed prior to slurry wall installation, the data was zeroed when compared to the other inclinometers in the cross section.

The lateral movements adjacent to the wall that occurred as a result of slurry wall installation are summarized in Figure 3-1. These movements reflect the effect of installation of the slurry wall on the surrounding ground movements. One can see that the majority of the lateral movements occurred in the soft clay layers (Blodgett and Deerfield) and are relatively small, less than 0.15 inches. Almost zero movement was observed below 40 ft in depth. According to Clough & O'Rourke (1989) past performance data suggests that a settlement of approximately 0.5 inches adjacent to the slurry wall would be expected due to the installation of the 70 ft deep slurry wall. If it is assumed that the settlement was

approximately equal to the lateral wall movement, then approximately 0.5 inches of lateral movement would be expected. This expected performance indicates that the slurry wall construction process was excellent at minimizing movements in the adjacent soil.

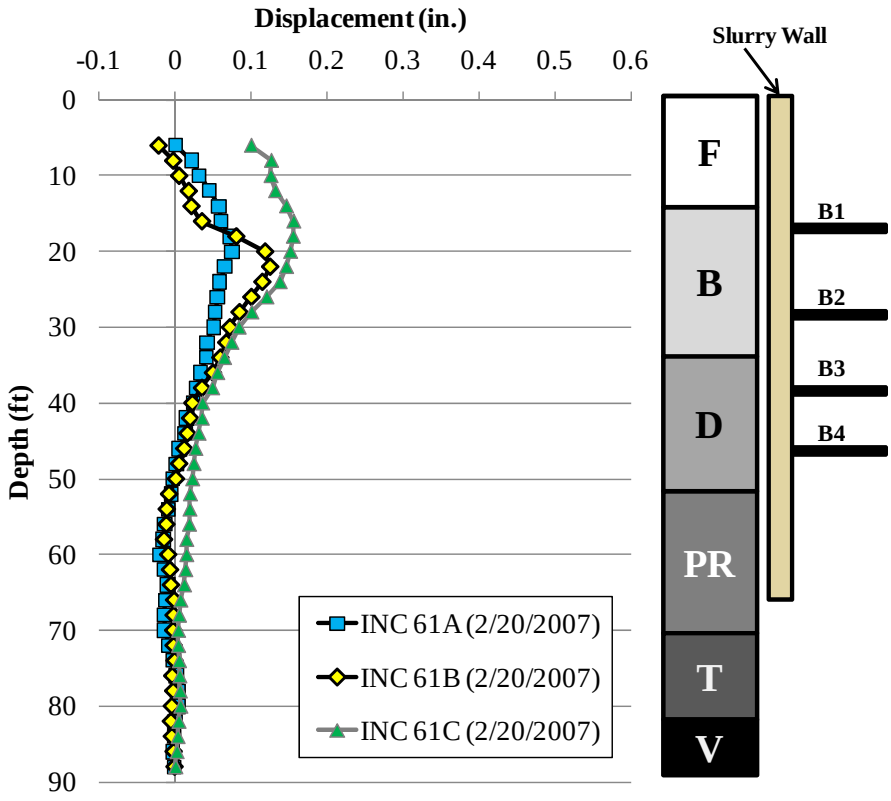

Figure 3-1: Lateral Movements during Slurry Wall Installation

3.1.1 Cross Section A

Cross section A shown in Figure 3-2, contained three inclinometers (INC-60A, INC-61A and INC-62A). INC-60A was located approximately 25 ft behind the slurry wall. INC-61A was located adjacent to the slurry wall, approximately 2 ft away, and INC-62A was located within the slurry wall. Cross Section A was located approximately 80 ft east of the northwest corner of the slurry wall. The start date for each inclinometer was adjusted to be approximately 2/20/2007, so the movements could be compared more easily.

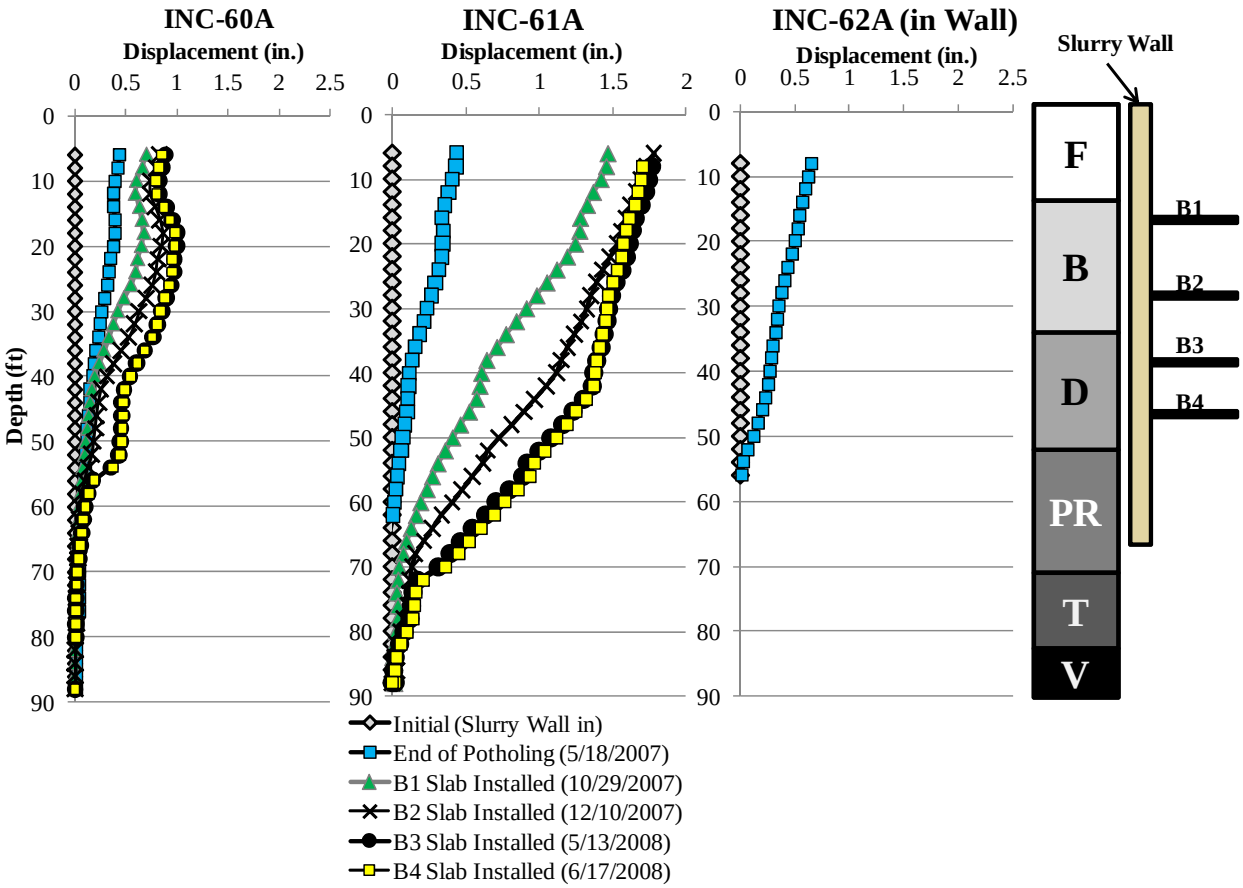

Figure 3-2: Cross Section A Lateral Movements (after Slurry Wall Installation)

Adjustments were not made to INC-60A. The initial reading for this inclinometer occurred on 1/10/2007, slightly before the start dates of the other inclinometers, but this reading was the closest to 2/20/2007. This inclinometer was located approximately 25 ft behind the slurry wall; therefore, smaller movements were recorded at this inclinometer than at the other two in the same cross section.

INC-61A was adjusted to modify the start date and also some data were deleted that did not appear accurate. First, the start date of 2/20/2007 was used as the initial reading even though 12/6/2006 was the first reading at the inclinometer. All subsequent movements were adjusted to account for this alternative start date. The maximum lateral movement in the inclinometer prior to zeroing was approximately 0.1 inches as shown in Figure 3-1. Movements progressed into the excavation until 2/16/2008 when excavation was progressing from B2 to B3 and then the inclinometer showed movements that started to

move in the opposite direction. After 2/16/2008, excavation was progressing from B2 to B4 and the B3 and B4 slabs were installed, all of which would not cause backward movements. It was assumed that the movements after 2/16/2008 were a result of errors during inclinometer readings and were not included in the analysis. Therefore, readings after this date were supplemented with data from the reinstalled inclinometer for INC-62A. INC-62A was reinstalled adjacent to the slurry wall, not in the slurry wall as previously located. INC-62A (Replaced) had a location similar to INC-61A. The data for INC-62A (Replaced) was included in the INC-61A movements to complete the recordings.

Inclinometer INC-62A had reliable readings until 9/7/2007. After this date, data were unable to be obtained from the inclinometer. The inclinometer was then reinstalled on 10/26/2007, adjacent to the slurry wall, not in the slurry wall as previously located. Because the inclinometer was no longer located within the slurry wall, the movements were not included in the INC-62A (in Wall) lateral movements.

3.1.2 Cross Section B

Cross section B contained two inclinometers (INC-61B and INC-62B) as shown in Figure 3-3. INC-61B was located adjacent to the slurry wall, approximately 2 ft from the slurry wall and INC-62B was located within the slurry wall. Cross Section B was located approximately 145 ft east of the northwest corner of the slurry wall, near the center of the wall along Randolph Street. The start date for each inclinometer was adjusted to be approximately 3/29/2007, so the movements could be compared more easily. The maximum lateral movement in the inclinometer prior to zeroing was approximately 0.1 inches, as shown in Figure 3-1. The lateral movements at this section are shown in Figure 3-3.

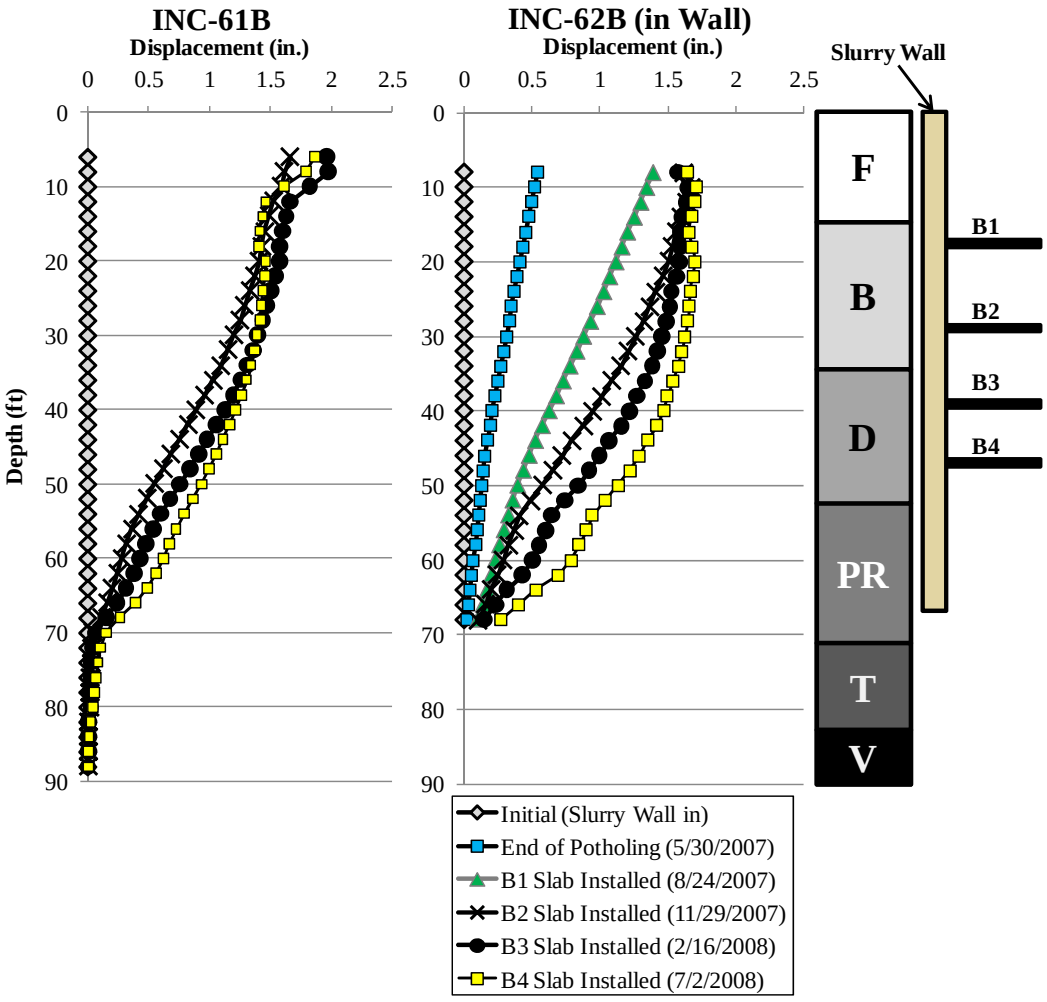

Figure 3-3: Cross Section B Lateral Movements (after Slurry Wall Installation)

Several adjustments were made on INC-61B. First, the start date was adjusted to start on 3/27/2007; the first reading was taken on 12/6/2006. Second, almost seven months (3/27/2007 to 10/26/2007) was missing for INC-61B so adjustments were made to account for this missing data. The total movement which occurred from 3/29/2007 to 10/26/2007 in INC-62B was used to estimate movements in INC-61B between 3/27/2007 and 10/26/2007. Because so much information was missing from INC-61B and the inclinometer had to be reinstalled, some major construction activities such as potholing and B1 Slab installation were not captured by INC-61B. The movements below the slurry wall were also estimated, but based on INC-61A movements. These two inclinometers from two different cross sections were

approximately 65 ft apart. This assumption may not be strictly valid as each cross section had some differences associated with the slab location and construction sequence. However, only the toe movements were taken from this inclinometer and it appeared that the toe movements were fairly consistent for all inclinometers located close to the wall.

Because INC-62B was located in the slurry wall, adjustments were made to account for toe movements of the slurry wall. Each increment of movement at the toe was adjusted based on movements in INC-61B. Because INC-62B and INC-61B are less than 5 ft from each other and the depth of the correction was 70 ft where the wall would move with the adjacent soil because of relative stiffness of the soil mass is much greater than that of the slurry wall at this depth, it was assumed with some confidence that these two inclinometers would have similar movements. INC-61B movements showed that the toe moved approximately 0.3 inches by the end of construction.

Cross Section B was omitted from future analyses because of the missing data and the assumption needed to compile the trend shown in Figure 3-3. The inclinometer installed adjacent to the wall (INC-61B) was missing significant construction events (i.e., potholing and B1 Slab installation) and the inclinometer within the wall (INC-62B) did not capture movements near or below the toe of the slurry wall. Therefore, the cross section was determined to have insufficient data for subsequent analyses.

3.1.3 Cross Section C

Cross section C contained two inclinometers (INC-61C and INC-62C) as shown in Figure 3-4. INC-61C was located adjacent to the slurry wall, approximately 2 ft from the slurry wall and INC-62C was located within the slurry wall. Cross Section C was located approximately 75 ft west of the northeast corner of the slurry wall. The start date for each inclinometer was adjusted to be approximately 2/21/2007, so the movements could be compared more easily. The maximum lateral movement due to slurry wall installation in INC-61C was approximately 0.15 inches as shown in Figure 3-1.

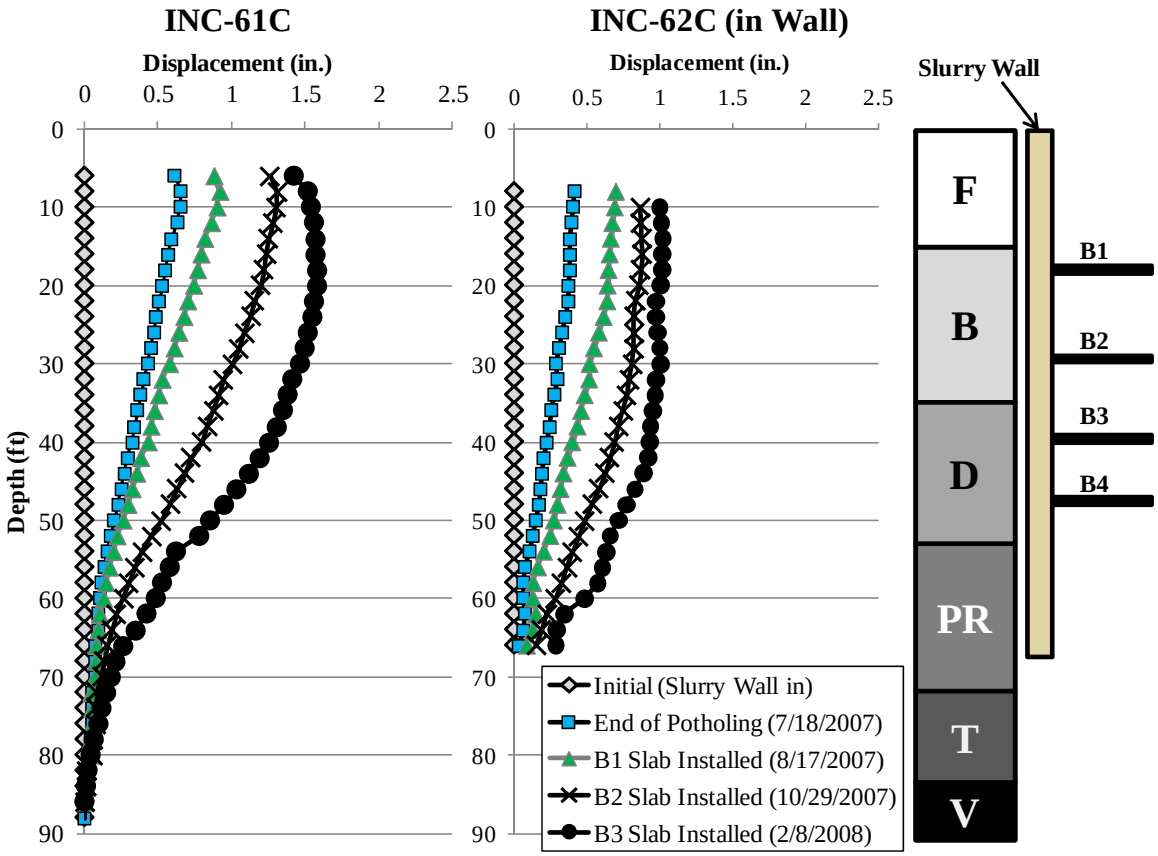

Figure 3-4: Cross Section C Lateral Movements (after Slurry Wall Installation)

Several adjustments were made to INC-61C to account for different start dates and unrealistic data. First, the start date of 2/20/2007 was selected instead of the first reading, which occurred on 12/6/2006. Additionally, after the reading on 3/20/2007, the bottom 40 ft of the inclinometer was filled; therefore, only data up until this date was presented.

INC-62C was adjusted to account for toe movements and for unrealistic movements. First, the toe movements were adjusted to match those movements recorded in INC-61C. It was assumed that since INC-61C and INC-62C were less than 5 ft apart, the movements should be similar. The adjacent inclinometer (INC-61C) was approximately 30 feet deeper than the bottom of the wall and was used to estimate toe movements of INC-62C. The inclinometer was also adjusted for unrealistic data after 3/15/2008. The movements appeared to start decreasing and moving into the wall, which does not appear

realistic, therefore, only data up until 3/15/2008 were presented for INC-62C. Consequently, movements are not presented for B4 Slab Installation and for the last reading.

Like Cross Section B, Cross Section C was omitted from future analyses because of missing data. Both inclinometers in this cross section were missing significant construction events (i.e., B4 Slab installation). Therefore, the cross section was determined to have insufficient data for subsequent analyses.

3.2 Inclinometer Data Analysis

Cross Sections B and C did not provide data throughout the entire duration of construction Therefore, only Cross Section A will be considered in this analysis and subsequent finite element analyses, presented in Chapter 5.

The inclinometer profile for Cross Section A shows that there were significant cantilever movements in the slurry wall. Expected lateral movement patterns (Clough & O'Rourke, 1989) for a deep excavation are shown in Figure 3-5, which indicate that typical movements consist of both cantilever and deep inward movements. The wall experiences cantilever movements (a) until some type of lateral support is in place (b) and then deep inward movements are expected after this point.

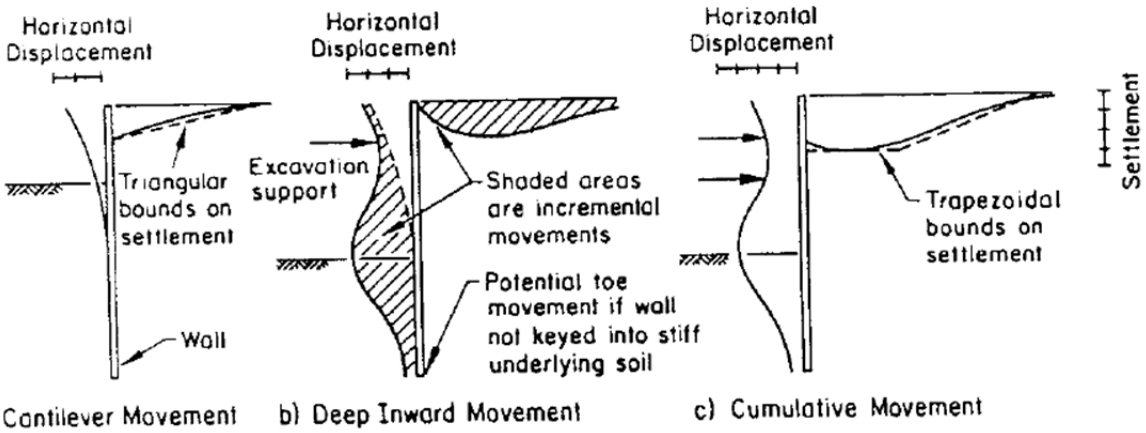

Figure 3-5: Typical Profiles of Movement for Braced and Tied-Back Walls (Clough & O'Rourke, 1989)

One factor affecting the amount of cantilever movement is the depth at which the excavation support is placed. For the Block 37 excavation, the first lateral support was placed after approximately 20 ft of excavation. Therefore, significant cantilever movements were experienced by the slurry wall because both potholing and excavation to the B1 slab were performed with no lateral brace in place. The potholing activities consisted of excavation and removal of existing foundations prior to the construction of any lateral support. The potholing activities induced approximately 0.5 inches of movement near the top of the slurry wall at this section, as shown in Figure 3-2.

The second cause of cantilever movements was the omission of the ground slab prior to excavation. Usually in top-down construction, a slab is installed to provide lateral support at the ground surface, thereby minimizing cantilever wall movements. However, the ground slab was omitted at Block 37 and the B1 slab was the first to be placed, located 20 ft below ground surface. The omission of the ground slab prior to excavation resulted in significant cantilever movements; as much as 1.5 inches at Section A. If the ground slab had been installed prior to excavation activities, then the cantilever movements would have undoubtedly been smaller.

To see more easily the deep inward movements, the cantilever movements (lateral movements up until B1 Slab Installation) were removed from the inclinometer movements in INC-61A and are shown in Figure 3-6. The movements show approximately 1 inch of deep inward movement near the base of the excavation at a depth of 48 ft. As shown in Figure 3-5, the maximum deep inward movements normally occur near the base of the excavation, depending on the stiffness of the soils near and below the bottom of the cut.

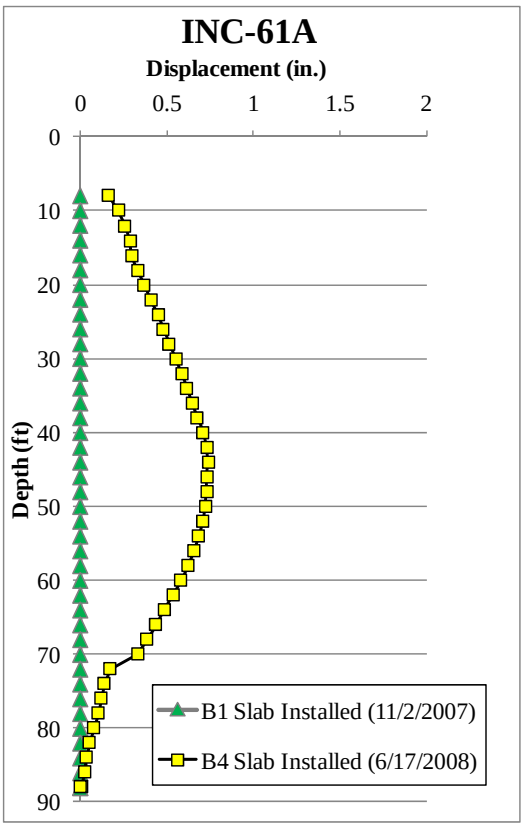

Figure 3-6: INC-61A without Cantilever Movements

The maximum lateral wall movement can be estimated based on a method developed by Clough & O'Rourke (1989) as summarized in Figure 3-7. First, the factor of safety against basal heave is calculated using:

$$FS = \frac{N_c S_{ub}}{H\left(\gamma - \frac{S_{uu}\sqrt{2}}{B}\right)} \qquad 3\text{-}1$$

where N_c is the bearing capacity factor, S_{ub} is the undrained shear strength of the soil below the excavation, H is the height of the excavation, γ is the unit weight of the soil, S_{uu} is the undrained shear strength of the soil from the ground surface to the excavation depth, and B is the width of the excavation. The factor of safety against basal heave was calculated for two different scenarios: when the excavation progressed to the B1 slab elevation at 20 ft below ground surface (B1) and at the B4 slab elevation at the end of construction, 48 ft below ground surface (B4). The bearing capacity factor, N_c, is equal to 5.14 for

both scenarios. The undrained shear strength of the soil above the excavation was approximately 800 psf for both scenarios. The undrained shear strength of the soil below the excavation for the B1 scenario and B4 scenario was approximately 1000 psf and 3000 psf, respectively. The height of the excavation, H, was 20 ft and 48 ft, as previously mentioned. The width of the excavation was approximately 300 ft and the unit weight of the soil was taken as 120 pcf for both scenarios. The factor of safety against basal heave was calculated to be 2.2 for B1 scenario and 2.8 for B4 scenario.

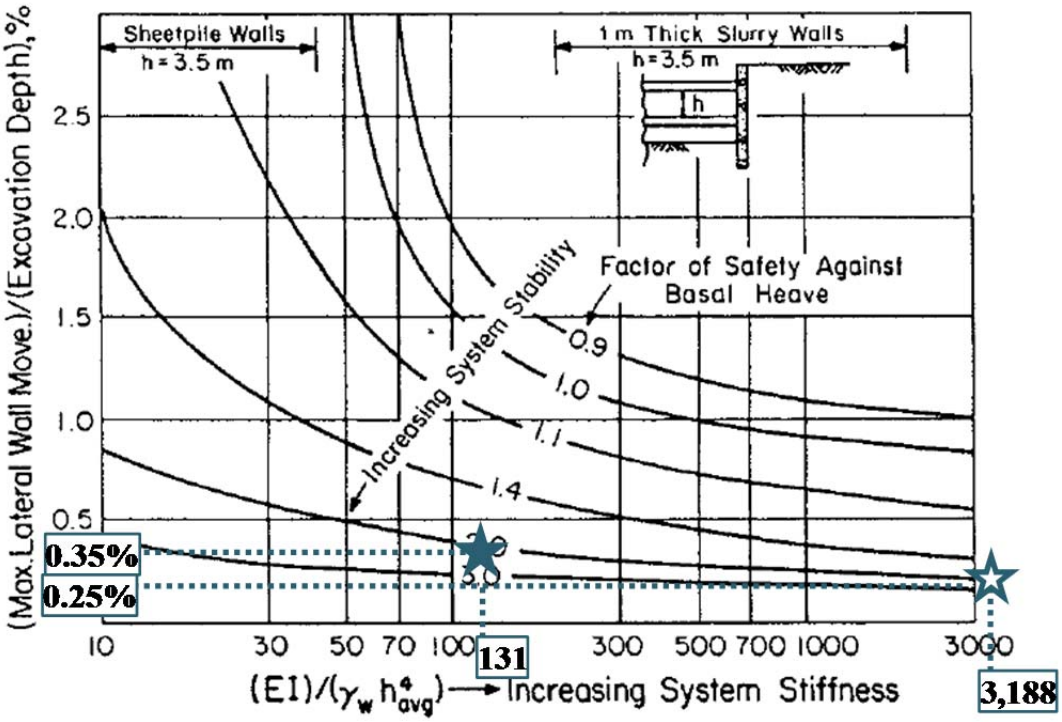

Figure 3-7: Design Curves to Obtain Maximum Lateral Wall Movement for Soft to Medium Clays (Clough, 1989)

Next, the system stiffness was calculated using the following equation,

$$\frac{EI}{\gamma_w h_{avg}^4} \qquad \textbf{3-2}$$

where E is the Young's modulus of the slurry wall, I is the moment of inertia of the slurry wall, γ_w is the unit weight of water and h_{avg} is the average spacing between lateral supports. The Young's modulus was equal to 580,000,000 psf, corresponding to a concrete mix with a compressive strength of 5,000 psi. The

moment of inertia per foot width of wall was 2.25 lb-ft^2/ft with a height of 3 ft. The unit weight of water was 62.4 pcf and the average spacing between supports was approximately 9 ft for the B4 scenario and 20 ft for the B1 scenario. These values resulted in a system stiffness of 131 for the B1 scenario and 3,188 for the B4 scenario.

The two scenarios are plotted in Figure 3-7; the B1 scenario is demarked by a solid star and the B4 scenario is demarked by an empty star. One can see that the expected maximum lateral wall movements are estimated to be 0.35% of the excavation depth for B1 scenario. This would correspond to approximately 0.8 inches of cantilever wall movement would be expected for this system. According to Figure 3-2, this estimated value is less than the actual movements recorded by the inclinometers. The inclinometers indicate that approximately 1.5 inches of cantilever movement was recorded. The B4 scenario resulted in an estimated lateral deformation of approximately 0.25%. This would correspond to approximately 1.4 inches of lateral deformation. According to the inclinometer profile presented previously, this is very close to the actual movements, which is 1.5 inches, excluding movements due to potholing.

Another method to analyze the maximum lateral wall movements during the cantilever stage was developed by Finno and Wang (2006). Figure 3-8 shows a plot of the maximum cantilever wall movement as a percentage of the excavation depth vs. the wall stiffness. The symbols in the figure represent field observations reported in the literature. The values in the cross-hatched area of the figure were based on finite element simulations for walls and soils of different stiffnesses. The maximum wall movement for the cantilever case should vary from 1.9 to 3.1 inches based on the finite element simulations. The observed cantilever movement, approximately 1.5 inches, was lower than these estimated values, although within the range of the reported field performance data.

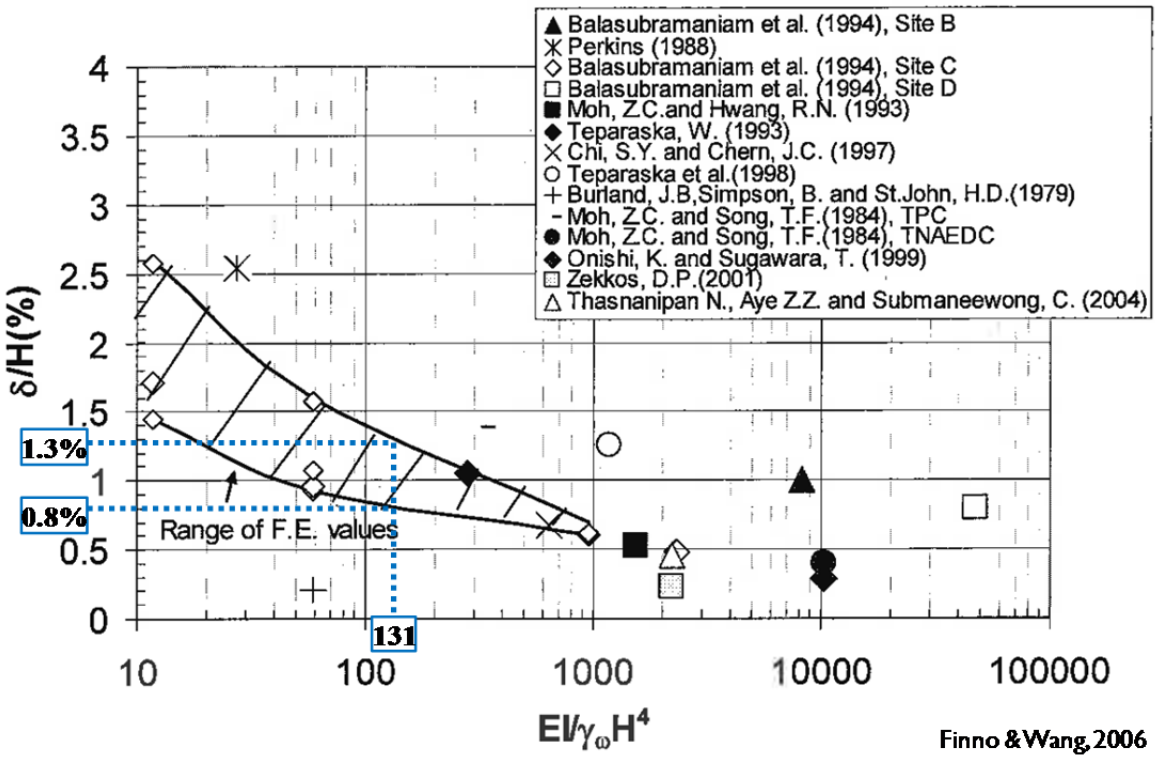

Figure 3-8: Maximum Lateral Wall Movement vs. System Stiffness (Finno &Wang, 2006)

3.3 Settlement Data

Settlement point data was collected for the Block 37 development from September 18, 2006 until October 31, 2008. Three cross sections were analyzed, as shown in Figure 2-6. Cross Section X is located approximately 40 feet east of the northwest corner of the slurry wall. Cross Section Y is located approximately 60 feet east and Cross Section Z is located approximately 80 feet east of the northwest corner of the slurry wall. The final settlements at each cross section are shown in Figure 3-9.

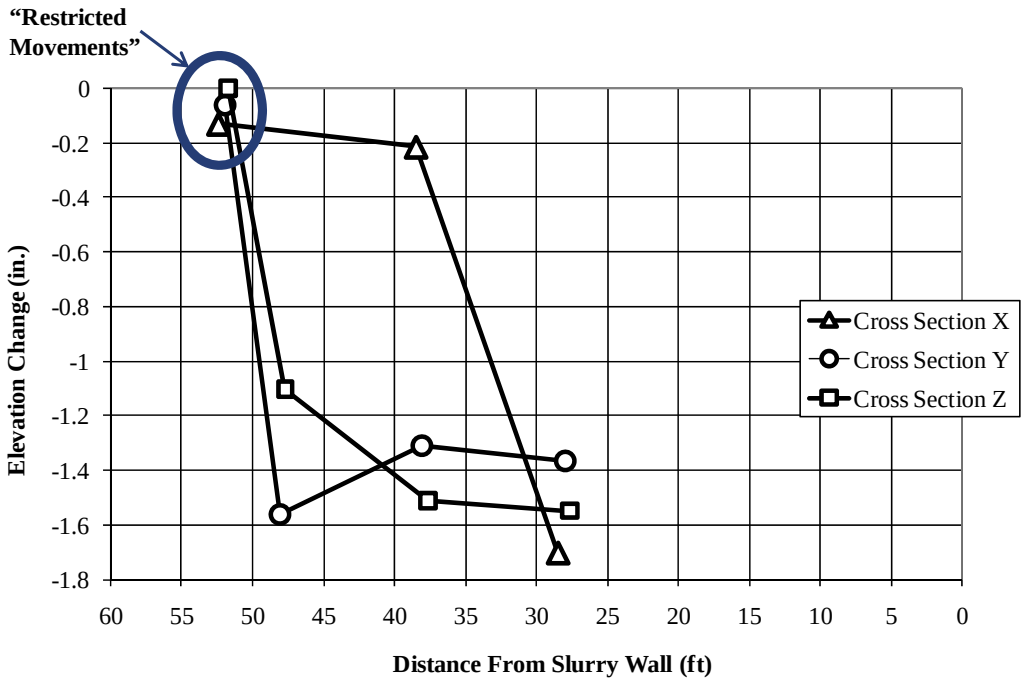

Figure 3-9: Settlement at End of Construction for 3 Cross Sections

The settlement point profiles show the change in vertical movement from an initial value; therefore, the starting position of the profile is at 0.0 in. All three profiles show approximately 1.3 to 1.7 inches of movement near the excavation and almost negligible movements (less than 0.2 inches) approximately 50 ft behind the wall. The settlement points approximately 50 ft behind the wall were located on the sidewalk along the northern side of Randolph Street. The negligible movements at this location are indicative of a vault located below the sidewalk that is structurally connected to the adjacent building, thus restricting settlements. Therefore, these points will be omitted from subsequent analyses.

3.4 Settlement Point Data Analysis

Cross Section A from the inclinometer movements and Cross Section Z from the settlement points are located within approximately 10 ft of each other, and these are presented together in Figure 3-10. Cross Section Z was broken up into the same time periods as the inclinometer data to see how the settlements develop as construction proceeds. The inclinometers from Cross Section A, located adjacent to the slurry wall and approximately 25 ft behind the slurry wall and the settlement points from Cross Section Z are

shown below in Figure 3-10. One can see that as the slurry wall moves into the excavation, more settlements are measured behind the slurry wall, as one would expect.

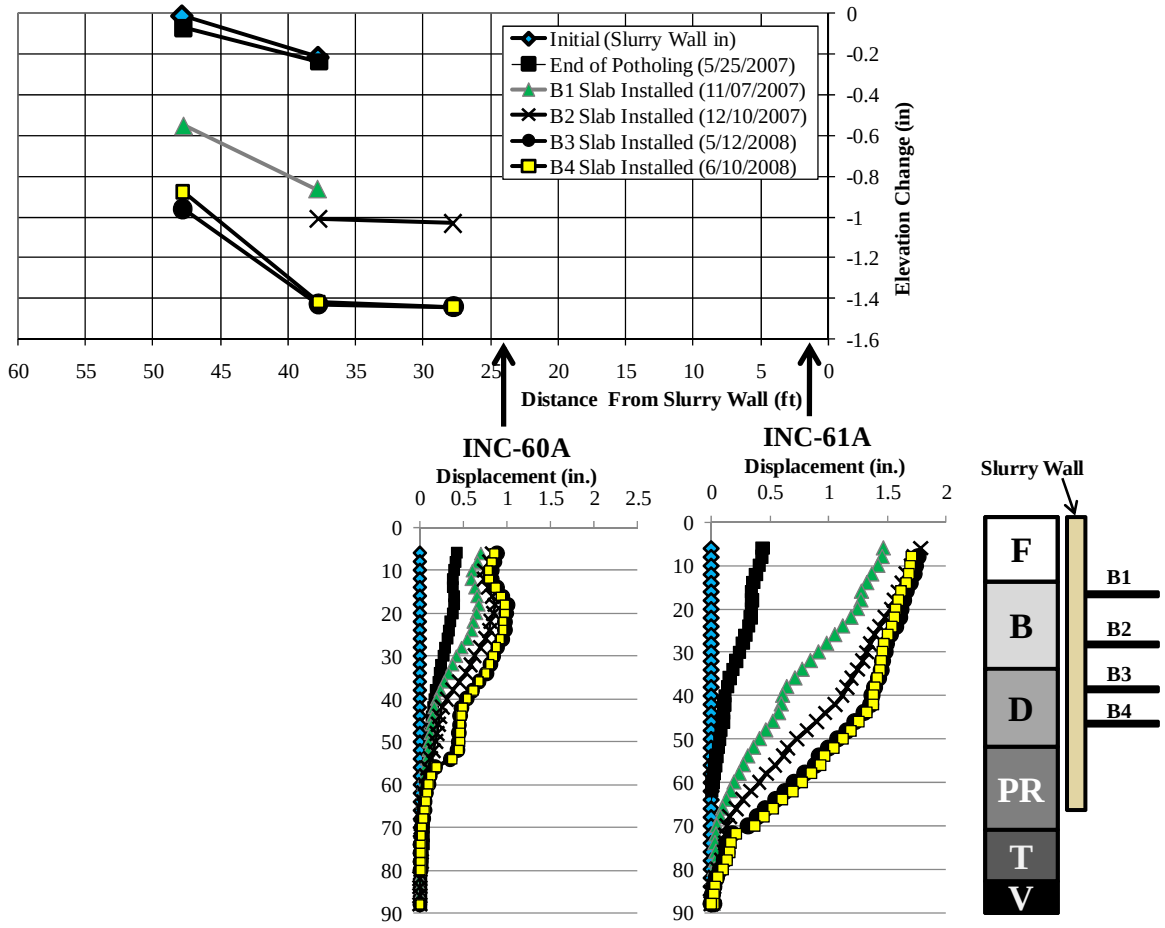

Figure 3-10: Inclinometer and Settlement Point Comparison at Cross Section A and Z

The above figure illustrates the relation between the horizontal movements and the settlements behind the slurry wall. The potholing and excavation to the B1 slab elevation caused about 1.5 inches of horizontal movements near the surface, or about 75% of the total recorded throughout construction. The maximum settlement behind the wall for this same time period was about 0.9 inches. The settlements increased during the B2 and B3 slab installation and then the settlements were very small, less than 0.1 inches. This little settlement is expected because little lateral wall movement was observed after the B3 slab

installation. The maximum settlement (1.5 inches) was approximately 75% of the maximum lateral ground movement at this section.

Predicted normalized settlement profiles adjacent to excavations are shown in Figure 3-11. Hsieh and Ou (1998) proposed two settlement profiles for spandrel and concave movements. A settlement envelope proposed by Clough and O'Rourke (1989) is also shown, which represents concave movements. The spandrel type settlement profile develops when an excavation experiences significant cantilever movements in comparison to deep inward movements.

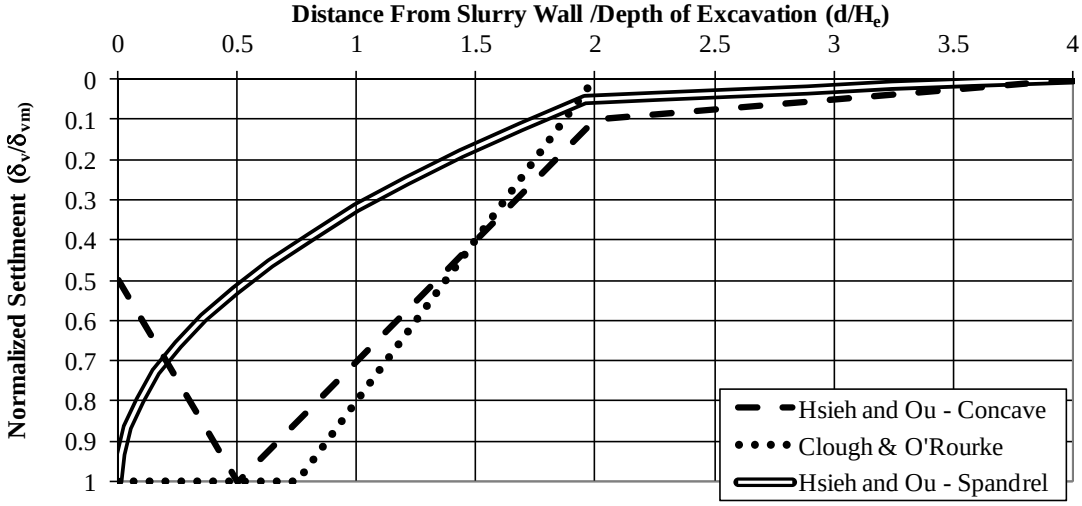

Figure 3-11: Predicted Settlement Profile (Hseih and Ou, 1998)

The data from INC-61A is used to compute the area of cantilever movement and the area of deep inward movement as shown in Figure 3-12. The area of the cantilever movement (A_c) was calculated to be approximately 4.4 ft^2 (0.41 m^2) and the area of the deep inward movement (A_s) was calculated to be 2.8 ft^2 (0.26 m^2). These values can then be plotted in Figure 3-13 to determine which type of settlement profile is expected (Hsieh and Ou, 1998).

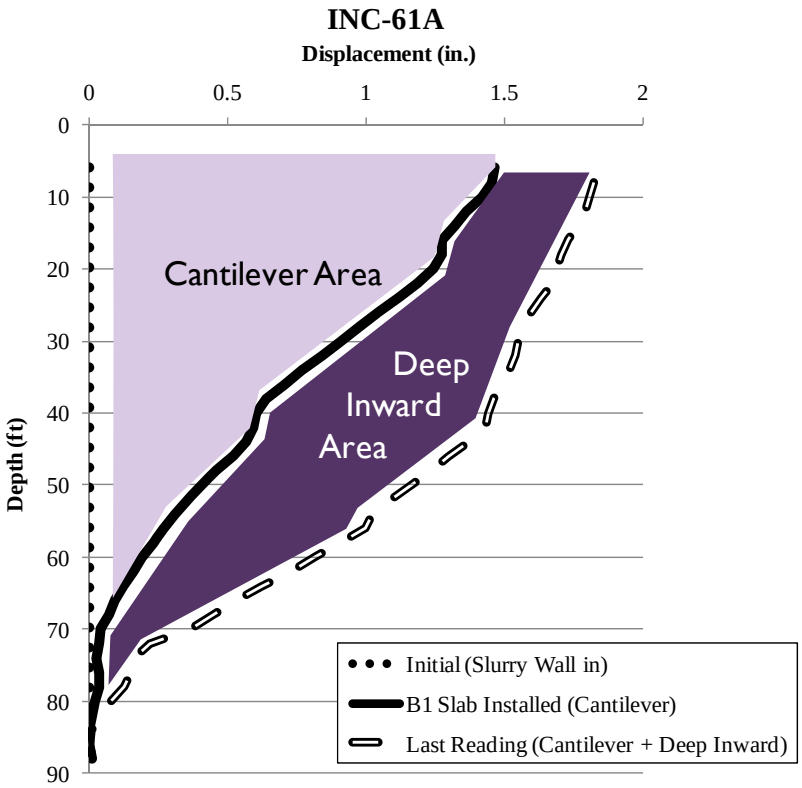

Figure 3-12: Cantilever Area and Deep Inward Area for INC-61A

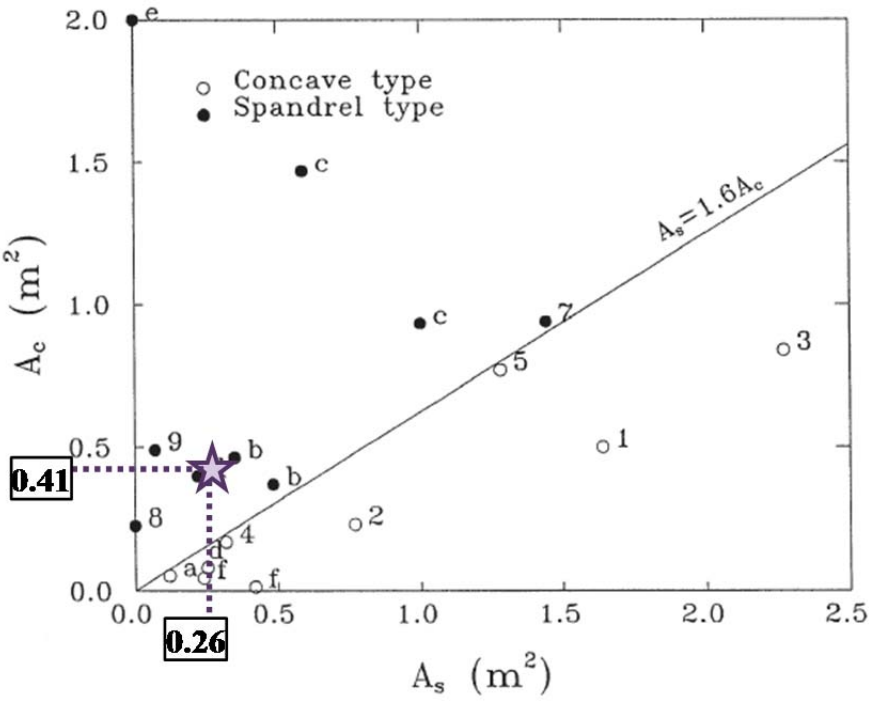

Figure 3-13: Relationship between the Cantilever Area and Deep Inward Area for INC-61A

According to Hsieh and Ou (1998), one would expect a spandrel type settlement profile. Figure 3-14 shows the predicted profiles along with the settlement point readings for Cross Section Z, assuming the maximum settlement was recorded. In other words, it is assumed that the 1.5 inches of settlement measured at approximately 25 ft behind the slurry wall was the maximum surface settlement behind the slurry wall. The maximum settlement may have occurred in a location that was not measured, which is likely if a spandrel profile is present. Cross Section Z was selected because it is located closest to the middle of the slurry wall, which is closest to a plane strain condition. With this assumption of maximum settlement, the data appears to fit the concave profile and the Clough & O'Rourke (1989) envelope fairly well.

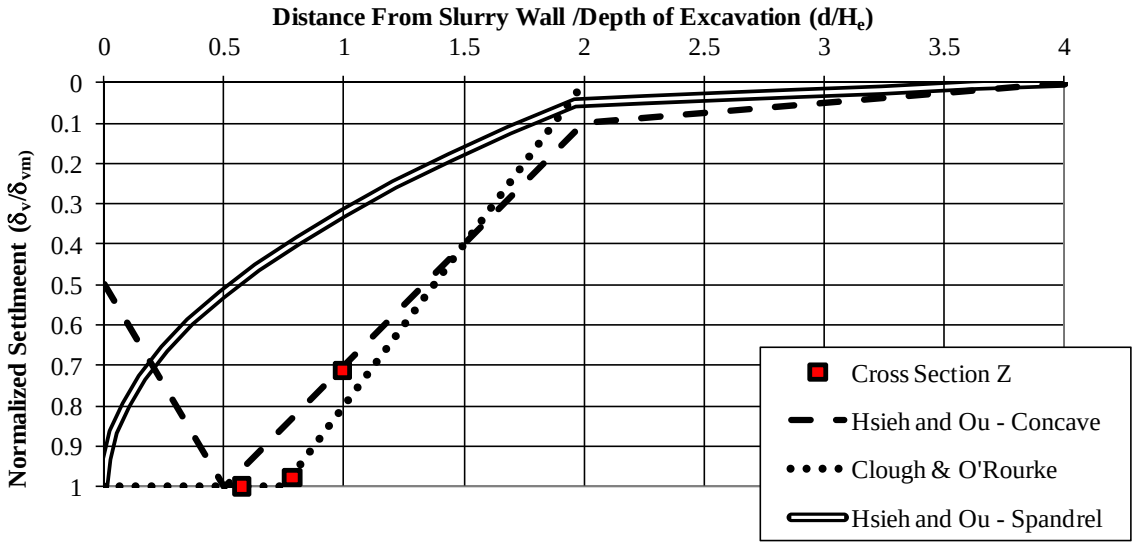

Figure 3-14: Predicted and Actual Normalized Settlement Profiles

Another way to analyze the settlement point data is to assume a settlement profile and adjust the settlement points by selecting a maximum settlement that would fit the profile best. Therefore, if one were to assume the spandrel type profile, which according to the observed cantilever and deep inward movement, should be the profile expected for the site, one can then plot the settlement points to fit the spandrel profile.

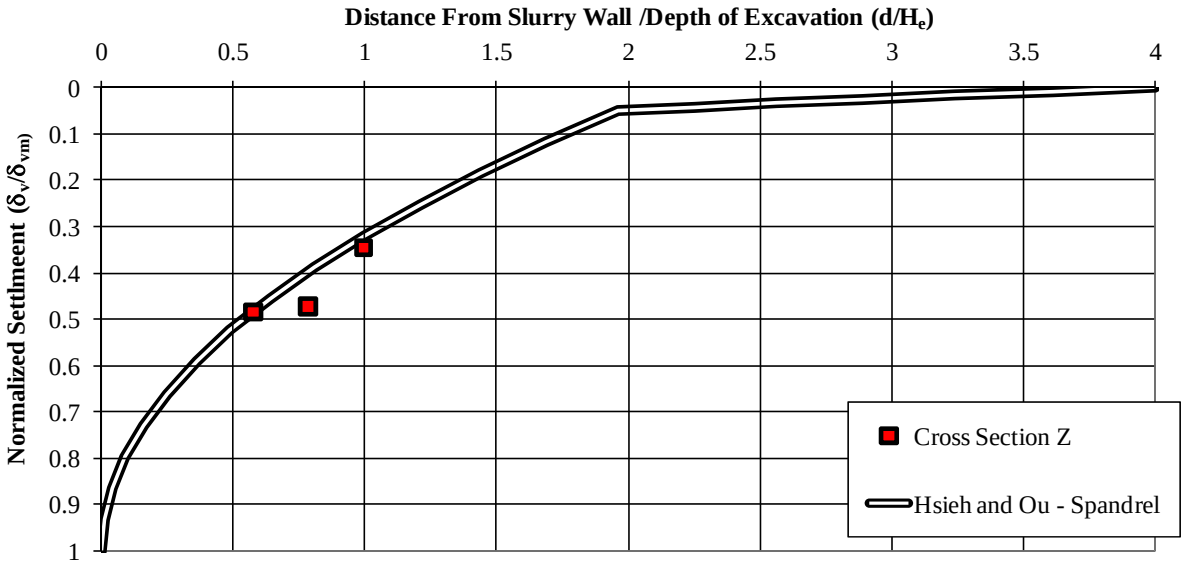

Figure 3-15: Spandrel Profile and Cross Section Z with Assumed Maximum Settlement

Figure 3-15 shows the Hsieh and Ou (1998) spandrel profile at Cross Section Z assuming the settlement at 25 ft fit the profile. For this assumption, a maximum settlement of 3.2 inches is expected to occur adjacent to the wall. With this assumption, the data can be used to fit the spandrel profile as well.

It was shown that the settlement data may fit either settlement profile based on which assumption is used. Because of the large cantilever movements as compared to the deep inward movements, it seems more realistic for a spandrel type settlement profile to be present. Therefore, the assumption that the maximum settlement was not recorded is more valid than the assumption that the maximum settlement was recorded.

Roboski (2004) presented a settlement profile parallel to the excavation as shown in Figure 3-16. The profile was developed to account for corner effects on ground movements. One would expect settlements and lateral movements to be less near the corner of an excavation because of the increase in stiffness the corner provides.

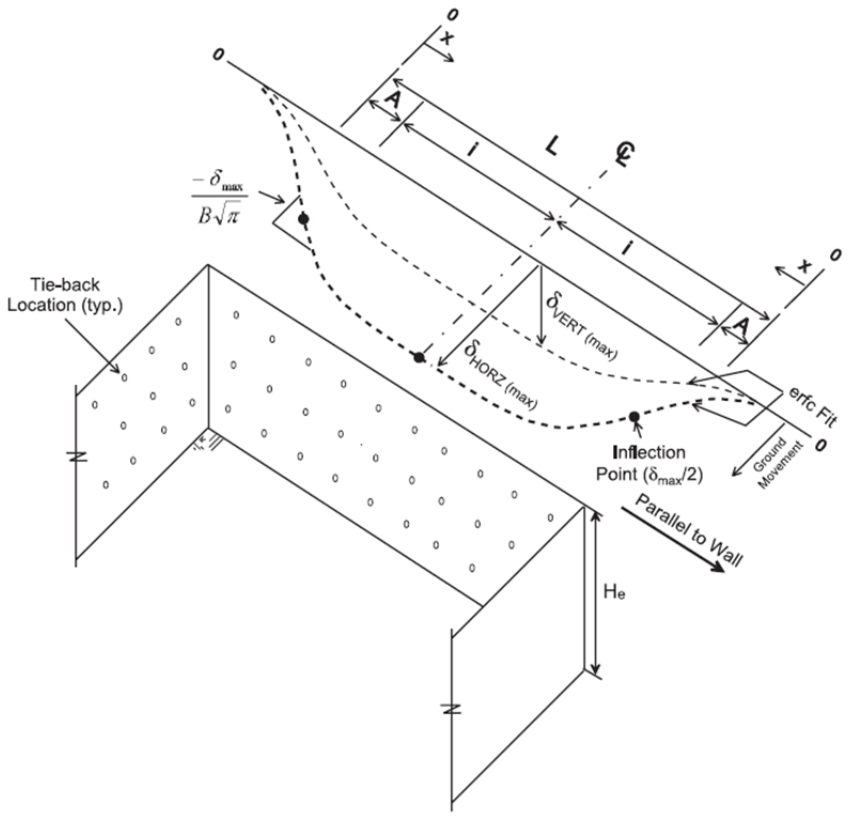

Figure 3-16: Settlement Profile Parallel to Excavation (Roboski, 2004)

The following equation is used to calculate the settlements along the wall:

$$\boldsymbol{\delta(x) = \delta_{max}\left[1 - \frac{1}{2}erfc\left(\frac{2.8\left\{x+L\left[0.015+0.035\ln\left(H_e/L\right)\right]\right\}}{0.5L+L\left[0.015+0.035\ln\left(H_e/L\right)\right]}\right)\right]} \quad \textbf{3-3}$$

where δ_{max} is the maximum settlement at the midpoint (L/2), x is the distance from the corner, H_e is the depth of the excavation and L is the length of the excavation. A settlement profile was calculated for a distance of 27 ft behind the slurry wall, where the first set of data points was measured in the three cross sections. As previously noted, Cross Section X, Y and Z were located approximately 40 ft, 60 ft and 80 ft east of the corner of the slurry wall, respectively. The maximum settlement at this location was assumed to be approximately 1.55 inches, based on the maximum settlement observed at 80 ft east of the corner of the slurry wall. The depth of the excavation was 48 ft and the length of the excavation was 300 ft. The

calculated settlement profile using equation 3-3 and the three measured settlement points were plotted below in Figure 3-17.

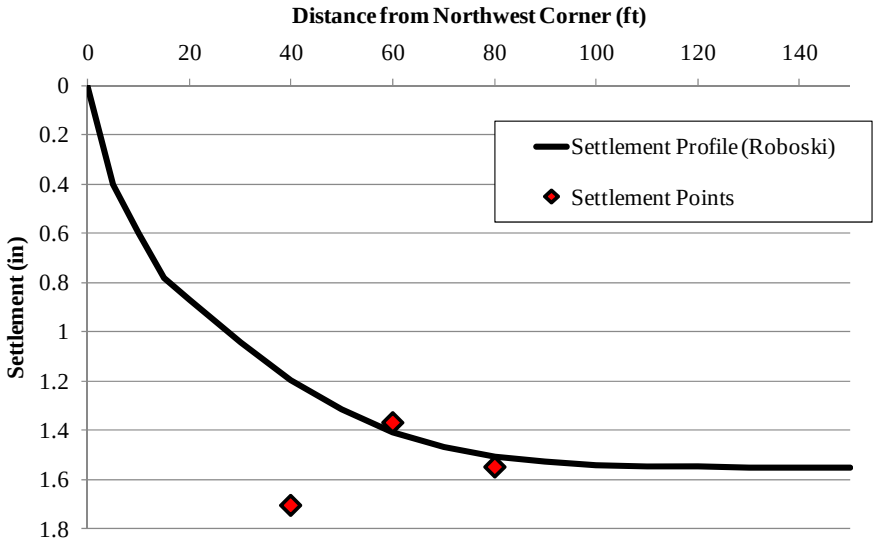

Figure 3-17: Proposed Settlement Profile and Measured Settlement Points.

One can see that two of the settlement points appear to agree fairly well with the predicted profile and one appears to be an outlier. However, three points are not enough to conclude a trend. More settlement points located at other distances from the corner would be helpful in determining if the proposed profile fit the field data. Also, a profile cut at additional distances behind the wall, would also help to draw a conclusion regarding the proposed profile.

3.5 Summary and Conclusions

Chapter 3 presented the performance monitoring data available from the Block 37 project. Inclinometer data were presented and analyzed. Some inclinometers required adjustment to present the data more clearly. It was concluded that several inclinometers did not provide enough useful data and were not included in subsequent analyses. Specifically cross sections B and C were missing a significant amount of data and therefore, only Cross Section A will be used to provide a basis of comparison for the results of the finite element analyses.

Settlement point data was also provided in this chapter. Settlement data was compared to several predicted profiles. It was shown that the cantilever movements were large compared to the deep inward movements, which would signify that the spandrel profile is expected to control. If a spandrel profile was present, the maximum settlement is expected to occur near the slurry wall. Since settlements were only recorded 25 ft behind the slurry wall and further, it is likely the maximum settlement behind the wall was not recorded.

The observed movements in the inclinometers and settlement points were consistent with that expected based on past performance data and the construction sequence at the site. The inclinometer movements were consistent with the predicted values based on procedures found in Clough & O'Rourke (1989) and Finno & Wang (2006). Clough & O'Rourke's (1989) calculations were less than the observed cantilever and total movements, while Finno & Wang's (2006) predictions were greater than observed cantilever movements.

Settlement profiles could be interpreted to be consistent with predicted profiles presented by Clough & O'Rourke (1989), Hsieh & Ou (1998) and Roboski (2004), depending on assumptions regarding maximum settlement. However, based on the amount of cantilever movement in relation to deep inward movement, it was concluded that the spandrel type profile proposed by Hsieh and Ou (1998) should be expected at the Block 37 site. The available settlement data was limited; therefore, only broad conclusions were drawn from these data. It is recommended that more settlement data be evaluated before any specific conclusions may be drawn.

Chapter 4: Finite Element Model

A finite element model was created to simulate the construction events that occurred during the excavation of the Block 37 development. The software employed for the finite element analysis was 2D PLAXIS v10. Since the size of the excavation was so large, only one half of the excavation in the north-south direction was modeled. The input parameters used to simulate the construction were chosen based on site specific data and results of existing analyses performed on Chicago Clay, and are summarized in the subsequent sections. Installation of the slurry wall, potholing of existing foundations and excavation and floor slab installation of four basement levels were modeled in the simulation.

The finite element mesh is shown in Figure 4-1. The total width of the excavation was 200 ft, but the width of the modeled excavation was 100 ft since only half was modeled. The width behind the slurry wall was 200 ft which was approximately two widths of the modeled excavation. The total depth of the model was 100 ft which was approximately two depths of the modeled excavation.

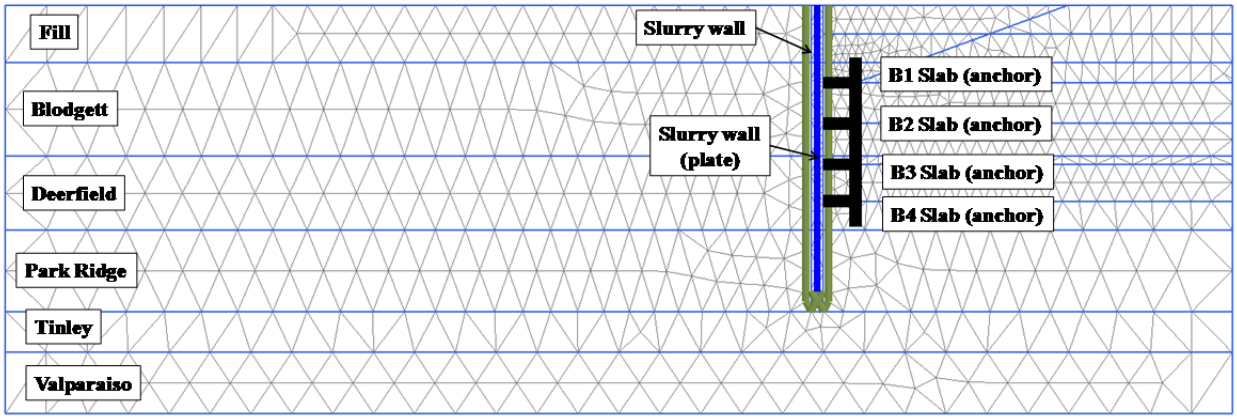

Figure 4-1: Finite Element Model Mesh (PLAXIS, 2010)

The calculation steps modeled in PLAXIS are summarized in Table 4-1. The table shows each construction stage, type of calculation (plastic or consolidation) and the number of days for each stage. The plastic calculation indicates an undrained analysis, while a consolidation stage indicates a partially drained analysis. The number of days is only relevant to the consolidation stages since the amount of

partial drainage is time dependent, while a plastic calculation phase is independent of time. The input parameters to the model, as well as further details regarding the calculation phases are summarized in subsequent sections.

Table 4-1: Finite Element Model Calculation Steps

Step	Construction Stage		Calculation	Time (days)
1	Slurry Wall Installation		Plastic	
2	Potholing (to 7 ft)		Plastic	
3	Potholing (to 14ft)		Plastic	
4	Potholing (to 19 ft)		Plastic	
5	Refilling		Plastic	
6	Slurry Wall Installation & Potholing duration		Consolidation	114
7	Excavate to B1	B1-1 (to 7 ft)	Plastic	
8			Consolidation	29
9		B1-2 (to 14 ft)	Plastic	
10			Consolidation	29
11		B1-3 (to 21 ft)	Plastic	
12			Consolidation	28
13	Install B1 Slab		Plastic	
14			Consolidation	8
15	Excavate to B2		Plastic	
16			Consolidation	35
17	Install B2 Slab		Plastic	
18			Consolidation	49
19	Excavate to B3		Plastic	
20			Consolidation	102
21	Install B3 Slab		Plastic	
22			Consolidation	9
23	Excavate to B4		Plastic	
24			Consolidation	30
25	Install B4 Slab		Plastic	
26			Consolidation	142

4.1 Input parameters

The input parameters for the constitutive models used in the finite element simulation were based on existing laboratory and field test results, field performance data, and construction documents provided by the contractor. Construction documents were used to establish length of time required for each construction stage. Three material models were used to simulate the various materials: Linear Elastic, Mohr-Coulomb (MC) and Hardening Soil (HS). Structural and soil elements and material parameters used in the PLAXIS model are summarized in further detail. Many of the soil parameters were obtained from Calvello (2002) who simulated the Chicago and State Subway excavation located approximately 1 mile north of the site. Calvello (2002) modeled the Blodgett, Deerfield, Park Ridge, and Tinley soil layers using the Hardening Soil (HS) model in PLAXIS.

Field performance data, specifically inclinometer readings between potholing and the end of the cantilever stage were used to calibrate the model. Because of the relatively unknown extent of potholing, various dimensions were modeled to achieve a best fit simulation for potholing.

4.1.1 Structural Elements

The slurry wall and floor slabs were modeled as Linear Elastic materials. Both the floor slabs and the slurry wall consist of reinforced concrete. Concrete exhibits linear elastic behavior at small movements and since small movements were expected, the structural elements were assumed to function in the linear elastic zone. As will be seen in Chapter 5, this was true for most of the excavation. The linear elastic material model is the simplest material model provided by PLAXIS and is based on Hooke's law for isotropic linear elastic behavior. Two parameters are required as input to the Linear Elastic Model: Young's modulus, E, and Poisson's ratio, ν. It is also possible to specify a stiffness, E, that varies linearly with depth.

PLAXIS can model structural elements as a solid element, a plate element or an anchor element. The slurry wall was modeled as a solid element with a plate element centered in the slurry wall soil element.

This plate element, with a negligible stiffness, was included to allow the bending moments in the slurry wall to be calculated accurately. The floor slabs were modeled using fixed-end anchor elements. The material input parameters for the slurry wall are summarized in Table 4-2 and Table 4-3. The material input parameters for the floor slabs are summarized in Table 4-4.

Table 4-2: Slurry Wall Material Parameters (Solid Element)

Type	Non-porous
γ_{dry} (pcf)	150
γ_{wet} (pcf)	150
ν	0.2
E_{ref} (psf)	5.80E+08
E_{incr} (psf)	0
e_{init}	0.5
R_{inter}	1.0

The dry unit weight, γ_d, and wet unit weight, γ_{wet}, were set equal to the typical unit weight of concrete, 150 pcf. Poisson's ratio,ν, initial void ratio, e_{init}, and stiffness, E_{ref}, were chosen from the study conducted by Morgan (2006). The stiffness of the slurry wall was calculated from the design compressive strength of 5000 psi. The incremental increase in stiffness, E_{incr}, was 0, indicating no increase in stiffness with depth. The interface, R_{inter}, was equal to 1.0, indicating an interface at which no relative slip was allowed between the soil and concrete until the shear stresses at the interface equal the shear strength of the adjacent soil.

Table 4-3: Slurry Wall Material Parameters (Plate Element)

EA (lb/ft)	3.00
EI (lb-ft^2/ft)	2.25
d (ft)	3.0

The modulus of elasticity of the slurry wall plate was selected to be 1.0 psf, a negligible value. The width of the slurry wall was 3.0 ft. When the stiffness was multiplied by the area of the slurry wall (3.0 ft^2/ft),

the axial stiffness, EA, was determined to be 3.0 lb/ft. Likewise, the bending stiffness, EI, was calculated from the geometry of the slurry wall to be 2.25 lb-ft^2/ft. PLAXIS output provide moments in the slurry wall, but in this case their values are based on the negligible stiffness. This value must be multiplied by the actual stiffness of the slurry wall to obtain realistic values. This approach was used because the actual slurry wall was modeled using solid elements, from which one can only approximate the bending moments in solid elements. The addition of the plate element enabled an accurate calculation of the bending moments in the slurry wall.

Table 4-4: Floor Slab Material Parameters (Anchor Element)

B1	EA (lb/ft)	5.80E+08
	$L_{spacing}$ (ft)	1
B2	EA (lb/ft)	5.80E+08
	$L_{spacing}$ (ft)	1
B3	EA (lb/ft)	5.80E+08
	$L_{spacing}$ (ft)	1
B4	EA (lb/ft)	3.87E+08
	$L_{spacing}$ (ft)	1

The use of fixed-end anchor supports used to model the floor slabs requires one to specify an axial stiffness, out-of-plane spacing and length of anchor support. The floor slab axial stiffness, EA, was calculated from the stiffness of 5000 psi concrete and the thickness of the floor slab. The B1, B2 and B3 slabs were 12 inches thick and the B4 slab was 8 inches thick; therefore, B4 had a lower axial stiffness than the upper floor slabs. The horizontal spacing, $L_{spacing}$, was set equal to 1, corresponding to a continuous slab. The fixed-end support was fixed at one end (i.e., slurry wall) and the length of the anchor was input manually. The length of the anchors varied as shown below in Figure 4-2 and Figure 4-3.

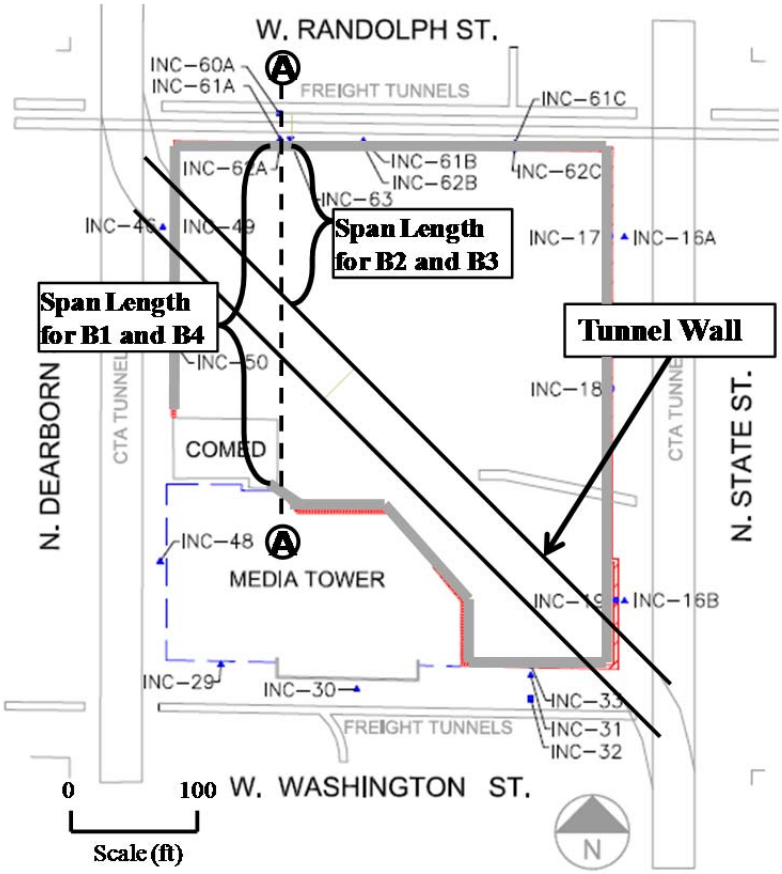

Figure 4-2: Anchor Span Lengths for Cross Section A

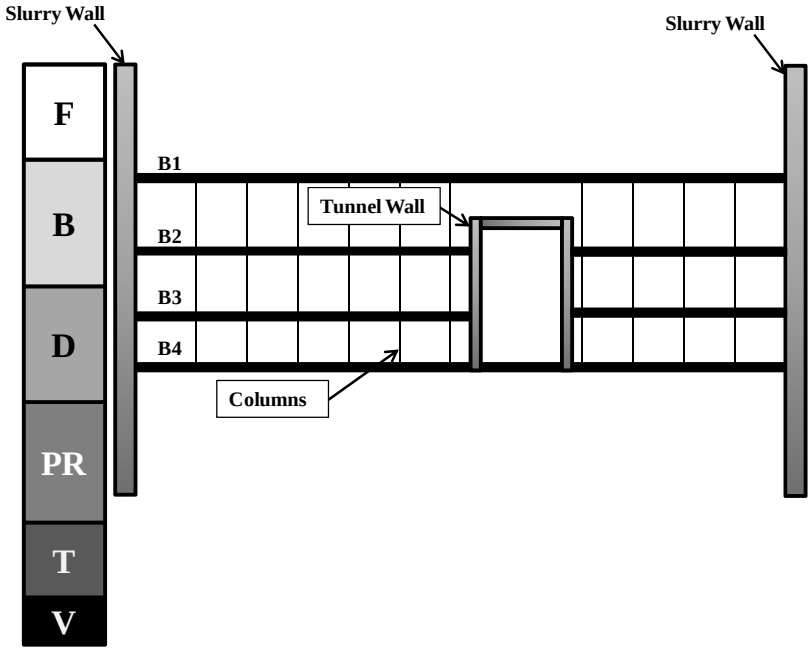

Figure 4-3: Cross Section Showing Slab Lengths at A

As shown in Figure 4-2, a set of parallel structural walls went through the middle of the site to allow construction of a tunnel to make a connection between the subways under State and Dearborn Streets. The tunnel was located between slab B1 and slab B4, thereby impacting the floor slab span lengths for B2 and B3, as shown in Figure 4-3. Table 4-5 summarizes the anchor lengths used in the PLAXIS model for each floor slab. Floor slabs B2 and B3 abutted a tunnel wall that was more flexible than the slurry wall cast against the ground, as was the case for floor slabs B1 and B4. The tunnel wall was a concrete wall approximately 2 ft thick and the slurry wall on the southern side of the site was the same as the slurry wall on the northern portion of the site (Figure 2-4). Since the B2 and B3 floor slabs abutted a much less stiff wall than B1 and B4, the anchor lengths for B2 and B3 were the total span length and the anchor lengths for B1 and B4 were half the span length. The longer span lengths for B2 and B3 imply that these supports are more flexible than those at the B1 and B4 levels.

Table 4-5: Floor Slab Lengths (Anchor Element)

	Floor Slab	Length (ft)
Cross Section A	B1	100
	B2	80
	B3	80
	B4	100

4.1.2 Soil Elements

The six soil layers summarized in Section 2.1.2 were modeled in PLAXIS using solid elements. Two different constitutive models, Mohr-Coulomb (MC) and Hardening Soil (HS), were used to model the different soil layers. The MC material model available in PLAXIS simulates the stress-strain responses as elastic perfectly-plastic. The model has a yield surface equal to the MC failure surface. The material behaves linear elastically inside the yield surface and the soil will accumulate irreversible strains only when the soil fails. The MC model was used to simulate three soil layers: the fill material, the Tinley stiff

clay and the Valparaiso hard clay. The input parameters for the MC materials are summarized in Table 4-6.

Table 4-6: MC Material Parameters for Sand Fill, Tinley and Valparaiso

	Mohr-Coulomb Materials		
	Sand Fill	**Tinley**	**Valparaiso**
Material Type	**Drained**	**Undrained**	**Undrained**
γ_{dry} (pcf)	120	125	130
γ_{wet} (pcf)	120	125	130
ν	0.33	0.1	0.1
E_{ref} (psf)	3.68E+05	3.0E+06	6.0E+06
c_{ref} (psf)	400	1000	1000
φ (°)	35	45	45
ψ (°)	5	0	3
E_{incr} (psf)	30000	0	0
c_{incr} (psf)	0	0	0
y_{ref} (ft)	0	0	0
e_{init}	1	0.5	0.5
T-Strength (psf)	0	0	0
R_{inter}	0.67	0.5	0.5
k_x (ft/day)	50	.0005	.0005
k_y (ft/day)	50	.0003	.0003
K_0	0.5	0.458	0.426

The majority of the input parameters for the MC materials were chosen from Morgan (2006), with the exceptions noted in the following. The stiffness, E_{ref}, for the sand fill was selected based on inverse analysis performed by Calvello (2002). The other stiffness values were selected based on pressuremeter tests provided in a report by STS Consultants (STS Project No 25337-H, August 2004). Hydraulic conductivity, k, values were selected from analyses performed by Calvello (2002).

The material type was chosen as either drained or undrained for the above materials. Drained behavior indicates no build up of excess pore pressures while undrained behavior allows for full development of

excess pore pressures. The sand fill was a free draining material, while the Tinley and Valparaiso were clays with low permeabilities.

The HS model, in contrast to the MC model, has yield surfaces that are not the same as the failure surface. Shear hardening yield surfaces and a volumetric hardening cap yield surface are included in the HS model. A stiffness modulus, E_{50}^{ref}, is defined corresponding to the reference confining pressure, p^{ref} according to the following equation:

$$E_{50} = E_{50}^{ref} \left(\frac{c \cot \phi + \sigma'_3}{c \cot \phi + p^{ref}} \right)^{m} \qquad \textbf{4-1}$$

where E_{50} is the secant stiffness at 50% of the failure stress in a drained triaxial compression test. According to the equation, the stiffness changes as the minor principal stress changes and hence the stiffness can increase with depth, as a function of a power m. The stiffness for one-dimensional compression is represented by E_{oed}^{ref}. The unload/reloading is characterized by E_{ur}^{ref} and ν_{ur}. Both E_{ur} and E_{oed} have the same form as E_{50} in Equation 4-1. Failure is characterized according to MC failure criteria, cohesion (c), friction angle (ϕ), and dilatancy (ψ). The HS model was used to simulate the Blodgett, Deerfield and Park Ridge strata. The input parameters for the HS materials are summarized in Table 4-7.

Table 4-7: Hardening Soil Material Parameters for Blodgett, Deerfield and Park Ridge

	Hardening-Soil Materials		
	Blodgett	**Deerfield**	**Park Ridge**
γ_{dry} (pcf)	115	120	125
γ_{wet} (pcf)	115	120	125
$E_{50,ref}$ (psf)	18,700	22,460	51,110
$E_{oed,ref}$ (psf)	13,090	15,720	35,780
$E_{ur,ref}$ (psf)	56,100	67,380	153,340
c_{ref} (psf)	1	1	1
φ (°)	23.4	25.6	32.8
ψ (°)	0	0	0
ν_{ur}	0.2	0.2	0.2
P_{ref} (psf)	100	100	100
m	0.8	0.85	0.85
$K_{0(nc)}$	0.603	0.568	0.458
c_{incr} (psf)	0	0	0
R_f	0.9	0.9	0.9
T-Strength (psf)	0	0	0
R_{inter}	1	1	0.5
d-inter	0	0	0
e_{init}	1	1	1
k_x (ft/day)	.0005	.0005	.0005
k_y (ft/day)	.0003	.0003	.0003

The majority of the input parameters for the HS materials were chosen from Morgan (2006), with the exception of the stiffness parameters. All three HS materials were clays and therefore, the material type was chosen as undrained. The stiffness, E_{50}^{ref}, E_{oed}^{ref}, and E_{ur}^{ref} were selected based on inverse analysis performed by Mu et al. (2011), as described in Chapter 5.

4.2 Installation of Slurry Wall

The slurry wall was installed prior to any potholing or excavating. Based on construction records and inclinometer movements adjacent to the slurry wall (Figure 4-4), the slurry wall was installed with little impact on the surrounding soil. The movements shown are the final movements of the inclinometers

adjacent to the slurry wall during slurry wall installation. One can see that significant movements in the soil adjacent to the slurry wall did not occur as the wall was placed, and thus the slurry wall installation process was very good at minimizing movements in adjacent soil. The majority of the movements during slurry wall installation were experienced in the softer clays (Blodgett and Deerfield) and very little movements were recorded below a depth of 40 ft. Because of these observations, the PLAXIS simulation modeled the installation of the slurry wall as a simple material replacement. That is, the material was instantly changed from the existing soil (i.e., fill, Blodgett, Deerfield, etc.) to a linear elastic material and the unit weight was changed for that of soil to that of concrete. This step resulted in negligible computed movements.

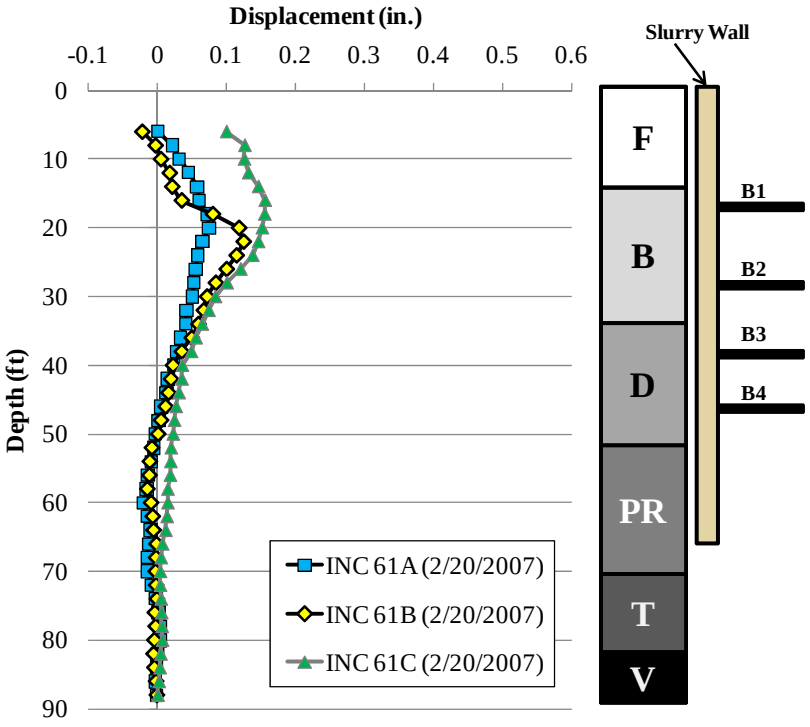

Figure 4-4: Inclinometer Movements Due to Slurry Wall Installation

4.3 Potholing

The potholing activities at Block 37 were not recorded with any consistency during construction. Thus the extent of potholing as well as the times when potholing occurred was not documented. The

inclinometers showed that significant movement occurred prior to excavation, which indicated the potholing was significant enough to cause movements of the slurry wall and soil adjacent to the wall. The inclinometers in the soil behind the wall indicated a fairly consistent deformation pattern due to potholing as shown in Figure 4-5.

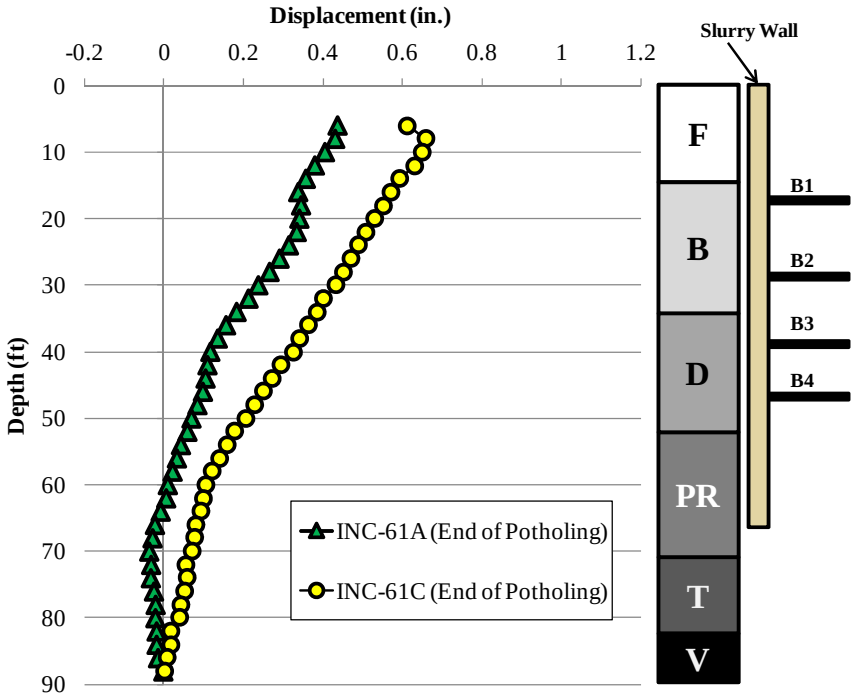

Figure 4-5: Lateral Movements Due to Potholing in Inclinometers Adjacent to Slurry Wall

These movements as well as a photo from the potholing activities (Figure 4-6) were used to create a PLAXIS simulation of potholing. According to Figure 4-6 the potholing was done adjacent to the slurry wall; however, the depth and width of the potholing could not be determined from the photo. Several dimensions were simulated to come up with the "best" guess simulation, which had an excavated depth of 19 feet and the geometry as shown in Figure 4-7. The "pothole" was refilled to grade and the computed movements at this stage were compared against the observed values in Figure 4-8. The pothole excavation was made in steps, to 7 ft, 14 ft and 19ft. Thereafter, the potholing was refilled after excavation.

Figure 4-6: Webcam Photo during Potholing (Hill, 2006)

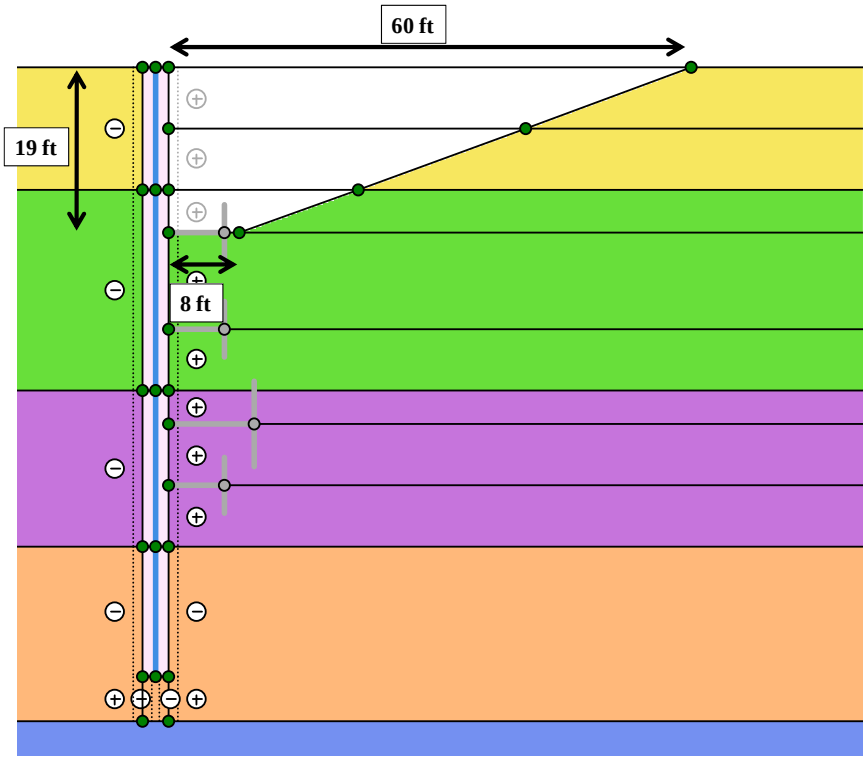

Figure 4-7: Potholing dimensions

Both the slurry wall installation and the potholing were modeled in an undrained condition (plastic calculation); however, a consolidation phase was added after these activities to account for the time required to complete these activities. The slurry wall installation, in PLAXIS, did not have an impact on the adjacent soil movements except for consolidation of soil below the toe of the slurry wall due to the increase in unit weight from soil to concrete. The potholing construction was done over a relatively short time period that the assumption of undrained conditions is judged to be reasonable. The consolidation phase after the potholing was added to the model to reduce excess pore pressures that developed during the undrained construction stages (i.e., slurry wall installation and potholing).

The computed wall displacements from the PLAXIS simulation are compared in Figure 4-8 to the slurry wall movements due to potholing. One can see the agreement was good, especially at Section A, the section with the most complete data set, as described in Chapter 3. Because little information was available about potholing activities, this simulation was judged sufficient for the analysis.

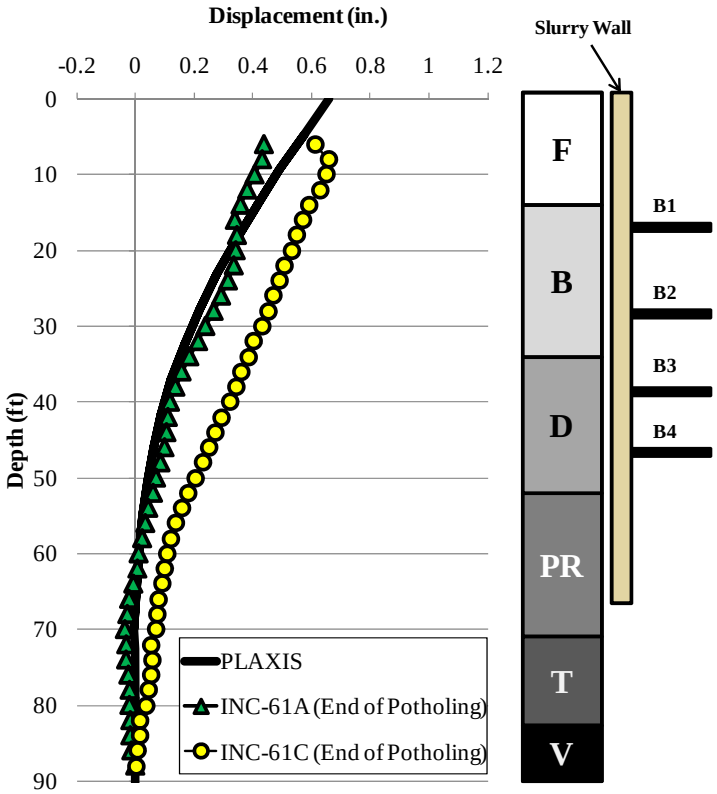

Figure 4-8: Lateral Movements Due to Potholing in Inclinometers Adjacent to Slurry Wall and PLAXIS Results

4.4 Excavation and Floor Slab Installation

The excavation of the site was modeled using the construction sequence provided by the geotechnical engineer for the project. The site was excavated from the ground surface to 48 ft below ground surface following the sequence provided in Table 4-1. Figure 4-9 shows the PLAXIS model after the final construction stage. The excavation progressed to each basement elevation (B1 through B4) and each floor slab was installed subsequently. Each excavation step was modeled as "Staged Construction" using a plastic calculation in PLAXIS and followed by a consolidation phase, which accounted for the time it took to complete each construction step. Table 4-1 summarizes the number of days each stage of construction was consolidated before advancing to the next stage.

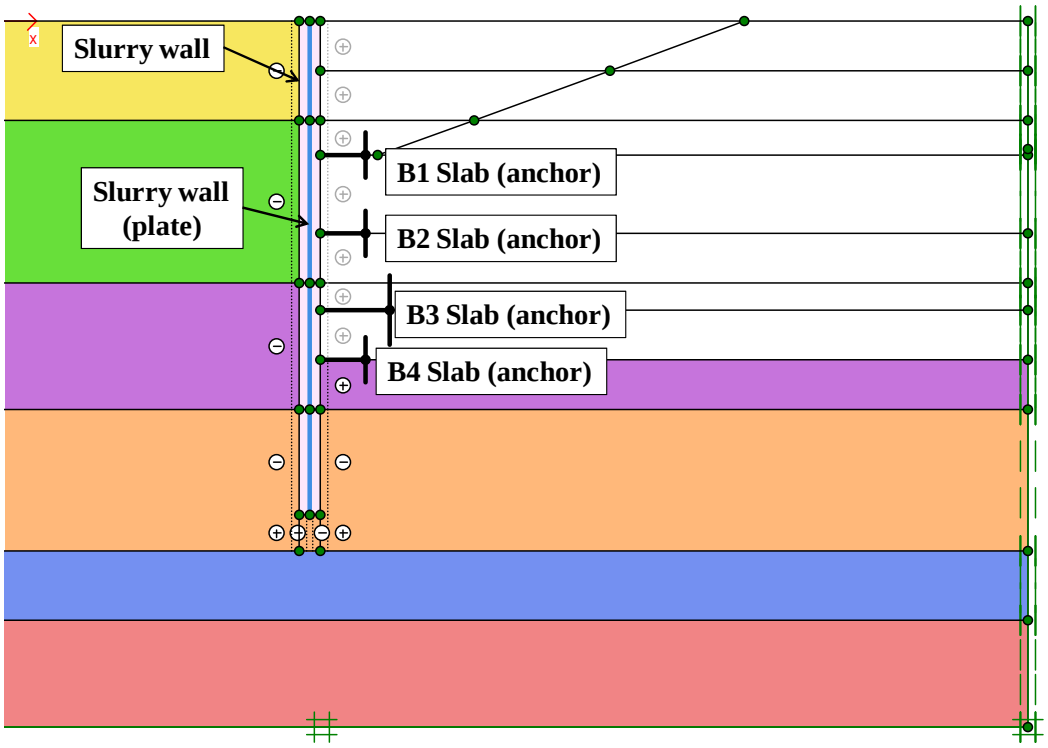

Figure 4-9: PLAXIS Model After Final Construction Stage

The excavation to the B1 slab elevation was done in three steps. The total depth to the B1 elevation was 19 ft. The first portion of the B1 construction stage was excavated to a depth of 7 ft. The second portion was excavated to a depth of 14ft and the third portion was excavated to the B1 elevation of 19 ft. Each

subsequent excavation was to each of the 3 other basement slabs. The time of the consolidation stages, which correspond to how long it took to excavate to each basement slab and the time it took to install each basement slab are summarized in Table 4-1. The results of the analyses are shown in Chapter 5.

4.5 Summary

This chapter presented the finite element model used in the analysis of the Block 37 excavation. The model was created for Cross Section A because it had the most useful performance monitoring data available to compare to in the subsequent chapter. The geometry of the model and mesh were presented, along with the input parameters for each geometric element. Soil elements were modeled using the HS and MC material models. The slurry wall and floor slabs were modeled using solid elements, plate elements and anchor elements and the behavior of each was modeled as linear elastic. The calculation steps were summarized for slurry wall installation, potholing, excavation and basement slab installation. Each construction stage was modeled based on available documentation provided by the Engineer, with the exception of the potholing. The potholing was modeled based on a photo during construction and measured lateral movements.

Chapter 5: Comparison of Computed and Observed Performance

The results of the finite element simulations are presented herein. Each finite element simulation was compared to the relevant performance monitoring data. Additional analyses were also performed on the output data to explain any discrepancies. The simulations that were performed for Cross Section A and the purposes of each are summarized in Table 5-1. The creep and shrinkage of the floor slabs was calculated to see if the discrepancies between the baseline simulation and the recorded movements could be explained by creep and shrinkage. The bending moments from the baseline simulation were compared to the cracking moment to determine if the cracking moment was exceeded.

Table 5-1: Summary of Finite Element Simulations

Simulation/Analysis	Summary	Purpose
Baseline	All input parameters are those discussed in Chapter 4	To compare to recorded lateral movements and settlements
Undrained Simulation	All input parameters are the same as baseline, except consolidation phases were omitted	To analyze the effect of drainage (consolidation) on the analysis
Lateral Support Lengths	All input parameters are the same as baseline, except the lateral support lengths are varied	To analyze the effect of the anchor lengths

5.1 Baseline Simulation

The baseline PLAXIS simulation modeled Cross Section A with all the input parameters presented in Chapter 4 and the results are summarized in Figure 5-1 and Figure 5-2. Two vertical cross sections were cut at the same location as the inclinometers (INC-60A and INC-61A) and the PLAXIS results were compared to the recorded lateral movements. A horizontal cross section was also cut along the ground surface to compare the PLAXIS-computed settlements with the recorded settlements.

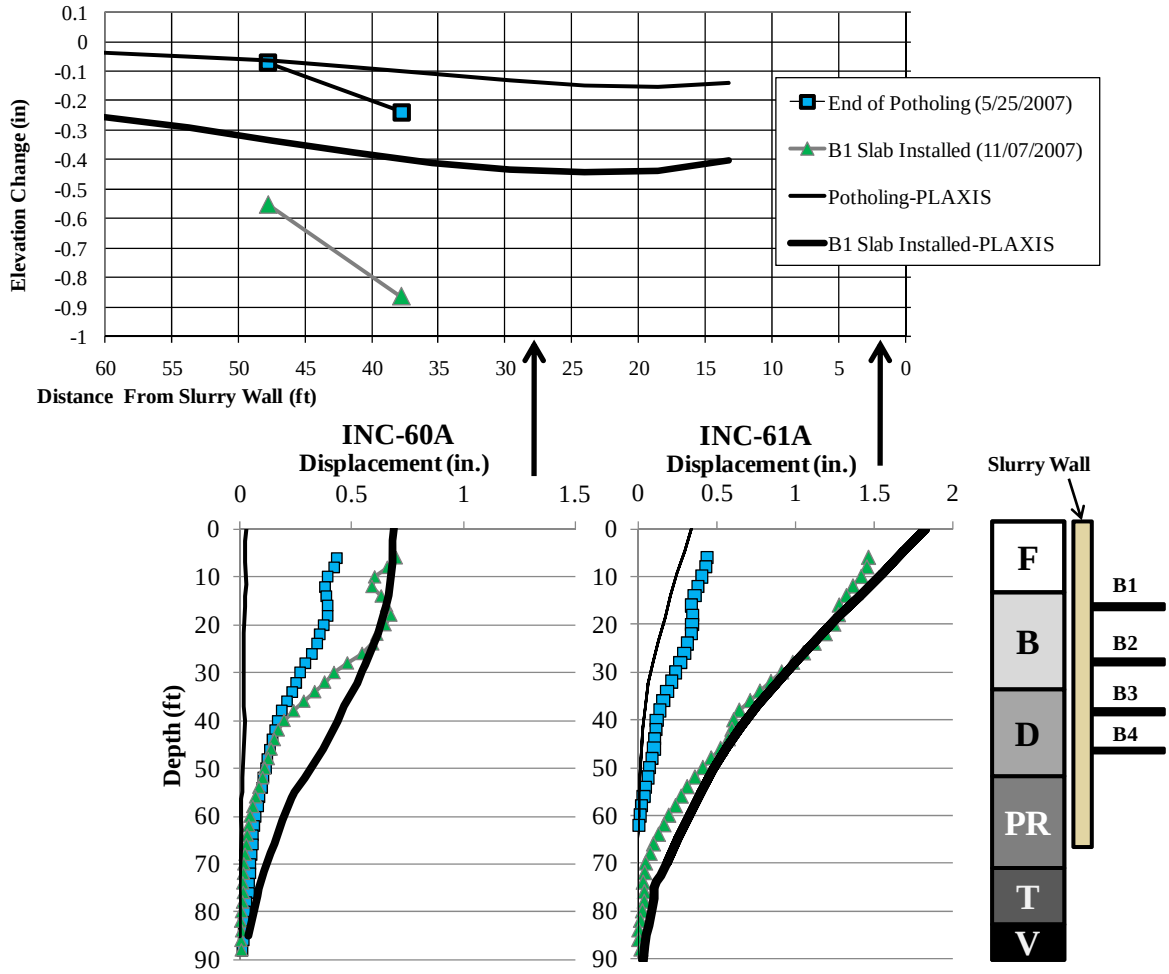

Figure 5-1: Cantilever Movements from Cross Section A Baseline PLAXIS Simulation and Recorded Movements

Figure 5-1 shows the cantilever movements, which include potholing, excavation to and installation of the B1 slab. The PLAXIS-computed lateral movements are very similar to the recorded movements at the end of the cantilever movements. This is to be expected since the movements at this stage were used by Mu et al. (2011) to optimize the stiffness parameters (E_{50}^{ref}) of the Blodgett, Deerfield and Park Ridge Strata. Additionally, the PLAXIS-computed movements agree with the INC-61A movements better than the INC-60A movements. The recorded settlements are greater than the PLAXIS-computed settlements at this cantilever stage. Based on work by Finno & Calvello (2005), HS parameters, based on inverse

analysis for the magnitudes of movements at the end of the cantilever stage of this excavation are good predictors of response for subsequent stages of excavation.

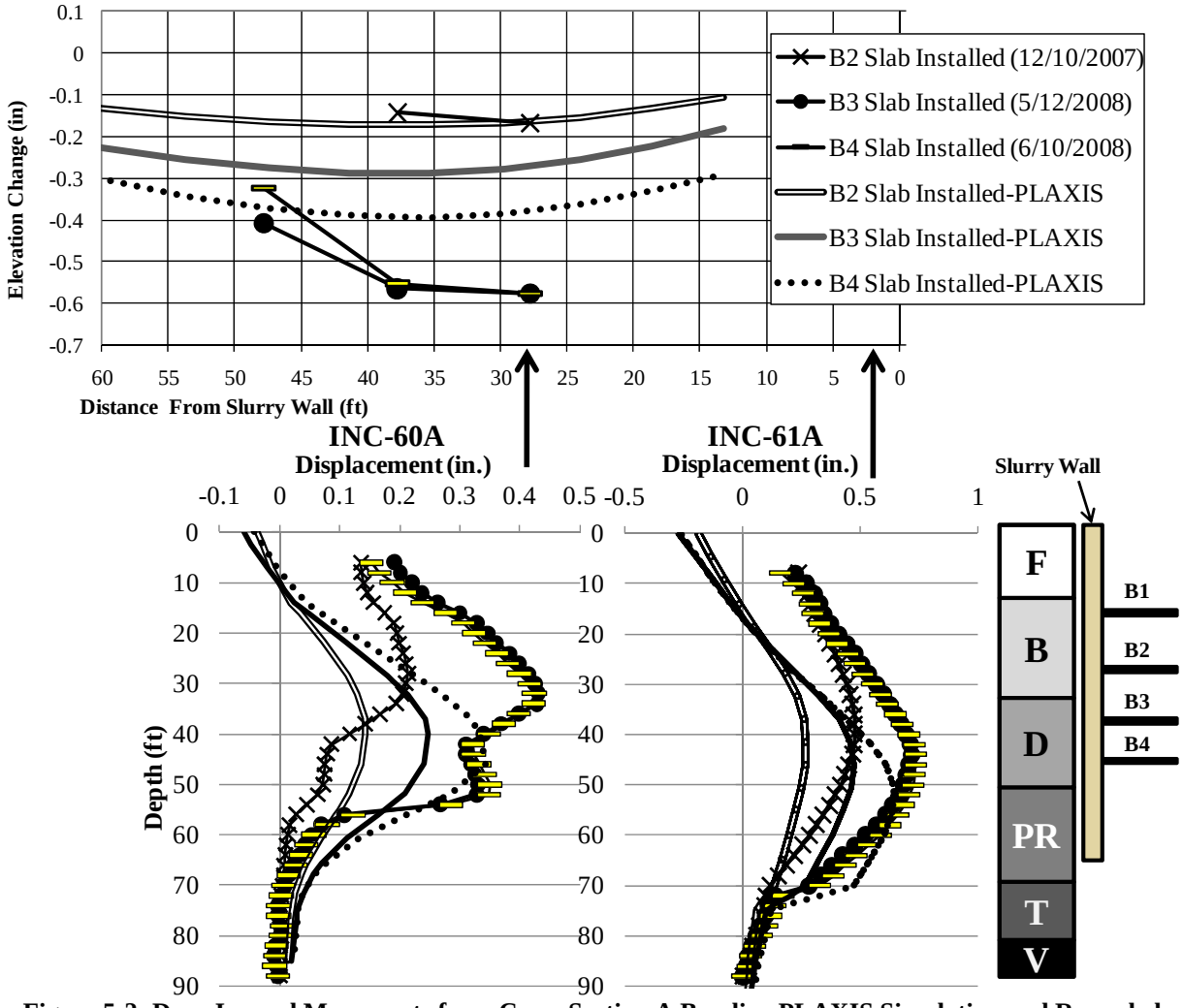

Figure 5-2: Deep Inward Movements from Cross Section A Baseline PLAXIS Simulation and Recorded Movements

Figure 5-2 shows the deep inward movements. The results indicate that the deep inward movements computed by PLAXIS are overall less than the observed movements recorded in the inclinometers, especially near the ground surface. Likewise, the PLAXIS-computed settlements for Cross Section A are also less than the recorded settlement at Cross Section Z, as shown in Figure 5-2. In each construction stage, with the exception of B2, the computed settlements are less than the recorded settlements. One

may expect this, because as previously discussed; the settlements adjacent to excavations are dependent upon the maximum lateral wall movement. Since the computed lateral wall movements were less than the recorded movements, one would also expect the computed settlements to be less than the recorded settlements. Furthermore, because small-strain non-linearity is not included in the HS or MC models, one would expect the computed settlements to be less than the observed values. The shape of the settlement profile calculated in PLAXIS, though subtle, appears to show a concave profile rather than the expected spandrel profile. Again, this discrepancy may be due to the fact that the settlements in general were lower than the recorded settlements and the material models do not calculate the settlements accurately.

One may note that as the excavation progresses in the PLAXIS model and the first lateral support is placed (B1 Slab Installed), the lateral movements are virtually zero at the lateral support after this construction stage. In other words, once the lateral support is in place, the lateral movements are restricted within PLAXIS. Conversely, one can see that the recorded movements show additional movements after the lateral supports are placed. Given that parameters were optimized based on field data to this point, one explanation as to why the PLAXIS movements are less than the observed movements is that the creep and shrinkage of the basement floor slabs were not taken into account with the PLAXIS simulation and that these movements may have been significant enough to impact the excavation support system and the surrounding soil movements.

5.2 Creep and Shrinkage

The finite element simulations that were created do not take into account time-dependent processes in the concrete, such as creep and shrinkage. Shrinkage is the volume change concrete experiences regardless of load. Concrete during curing decreases in moisture content and undergoes some shrinkage. Creep movements occur under a sustained load and are time dependent. The floor slabs supporting the slurry wall were expected to carry significant loads and therefore may undergo creep strains. PLAXIS does not have a model to represent time-dependent material properties. However, to evaluate the possibility that

these effects are indeed important, a method recommended by the American Concrete Institute (ACI) was utilized to estimate the magnitude of the movements. Creep and shrinkage movements were calculated for each concrete basement slab for each cross section.

5.2.1 Creep

The creep strains, *cs*, were calculated by:

$$cs = v_t \varepsilon_i \quad \text{5-1}$$

where v_t is the creep coefficient and ε_i is the instantaneous strain. The instantaneous strain was calculated using:

$$\varepsilon_i = \frac{\sigma}{E_{ci}} \quad \text{5-2}$$

where σ is the applied constant stress and E_{ci} is the initial modulus of elasticity. The applied constant stress was taken from the results of the finite element simulations. The initial modulus of elasticity was the same as the input parameters in the PLAXIS simulations. The creep coefficient, v_t, was calculated using:

$$v_t = \frac{t^{0.60}}{10+t^{0.60}} v_u \quad \text{5-3}$$

where t is the time in days after loading and v_u is the ultimate creep coefficient defined as the ratio of creep strain to instantaneous strain. ACI recommended that in the absence of specific creep data for local aggregates, the average value of v_u be taken as:

$$v_u = 2.35\gamma_c \quad \text{5-4}$$

where γ_c is the product of applicable correction factors. Table 4-1 was used to calculate, t, by summing the number of days after the installation of the applicable slab until the end of construction.

5.2.2 Shrinkage

The shrinkage strains were calculated using the following equation:

$$(\epsilon_{sh})_t = \frac{t}{35+t}(\epsilon_{sh})_u \quad \textbf{5-5}$$

where *t* is the time in days after loading and $(\epsilon_{sh})_t$ is the ultimate shrinkage strain. ACI recommended that in the absence of shrinkage data for local aggregates and conditions, the average value of the ultimate shrinkage strain $(\epsilon_{sh})_t$ be taken as:

$$(\epsilon_{sh})_u = 780\gamma_{sh} \times 10^{-6} \quad \textbf{5-6}$$

where γ_{sh} is the product of all applicable correction factors, summarized in the section following. The time, *t*, was calculated the same as for the creep calculations.

5.2.3 Correction Factors

Corrections were made for relative humidity and volume to surface ratio of the slabs. The relative humidity at the site varied between an annual average of 62% in the afternoon to 80% in the morning (City Rating). An overall average of 71% was used in the analysis for the correction for relative humidity, using the following equations:

$$\textbf{Creep: } \gamma_\lambda = 1.27 - 0.0067\lambda \quad \textbf{5-7}$$

$$\textbf{Shrinkage: } \gamma_\lambda = 1.40 - 0.0102\lambda \quad \textbf{5-8}$$

where λ is the relative humidity. The creep and shrinkage relative humidity correction factors were 0.7943 and 0.6758, respectively.

The correction factors for the volume to surface ratio (*v/s*) was applied for a ratio other than the default value of 1.5. The following equations were used to correct for the different *v/s* ratios.

$$\textbf{Creep: } \gamma_{vs} = 2/3\left[1 + 1.13e^{-0.54v/s}\right] \quad \textbf{5-9}$$

$$\textbf{Shrinkage: } \gamma_{vs} = 1.2e^{-0.12v/s} \quad \textbf{5-10}$$

The v/s for the 12 inch thick slabs (B1, B2 and B3) was 6, while the v/s for the 8 inch thick slab (B4) was 8. The 8 inch thick slab was cast on grade; therefore, only one side was used in the calculation of the surface area. The resulting creep correction factors for the 12 inch and 8 inch thick slabs were 0.696 and

0.677, respectively. The shrinkage correction factors for the 12 inch and 8 inch thick slabs were 0.584 and 0.459, respectively. A summary of the correction factors, strains and length changes for creep and shrinkage are shown in Table 5-2 and Table 5-3, respectively.

Table 5-2: Creep Strains

Cross Section – Slab	Product of Creep Correction Factors	Length (ft) of Slab	Time (days) after loading	Applied Constant Stress (psf)	Creep Strain	Length Change (in.)
A-B1	0.553	100	373	25,160	4.38×10^{-5}	0.053
A-B2	0.553	80	330	34,500	5.91×10^{-5}	0.057
A-B3	0.553	80	179	32,200	5.00×10^{-5}	0.048
A-B4	0.537	90	142	4,990	1.08×10^{-5}	0.012

The strains and length changes induced by creep were relatively insignificant when compared to total wall movements. In other words, the length change due to creep was less than 3% of the total wall movements. These movements would likely not produce any visible difference in wall movements. However, the shrinkage of the concrete produced strains that were more significant.

Table 5-3: Shrinkage Strains

Cross Section – Slab	Product of Shrinkage Correction Factors	Length (ft) of Slab	Time (days) after loading	Shrinkage Strain	Length Change (in.)
A-B1	0.395	100	373	2.82×10^{-4}	0.338
A-B2	0.395	80	330	2.79×10^{-4}	0.267
A-B3	0.395	80	179	2.58×10^{-4}	0.248
A-B4	0.311	90	142	1.94×10^{-4}	0.210

The shrinkage strains and change in length due to shrinkage were quite significant when compared to total wall movements. The movements were more than 15% of the wall movements. Therefore, these calculations suggest that wall movements could be attributed to more than the simple removal of soil. The shrinkage of the floor slab may also play a significant role in the behavior of the excavation support system.

To illustrate the creep and shrinkage movements, the increments presented in Table 5-2 and Table 5-3 were added to the final movements calculated by PLAXIS. Figure 5-3 shows the final PLAXIS-computed movements with the creep and shrinkage strains (indicated by bold lines) and the final recorded movements.

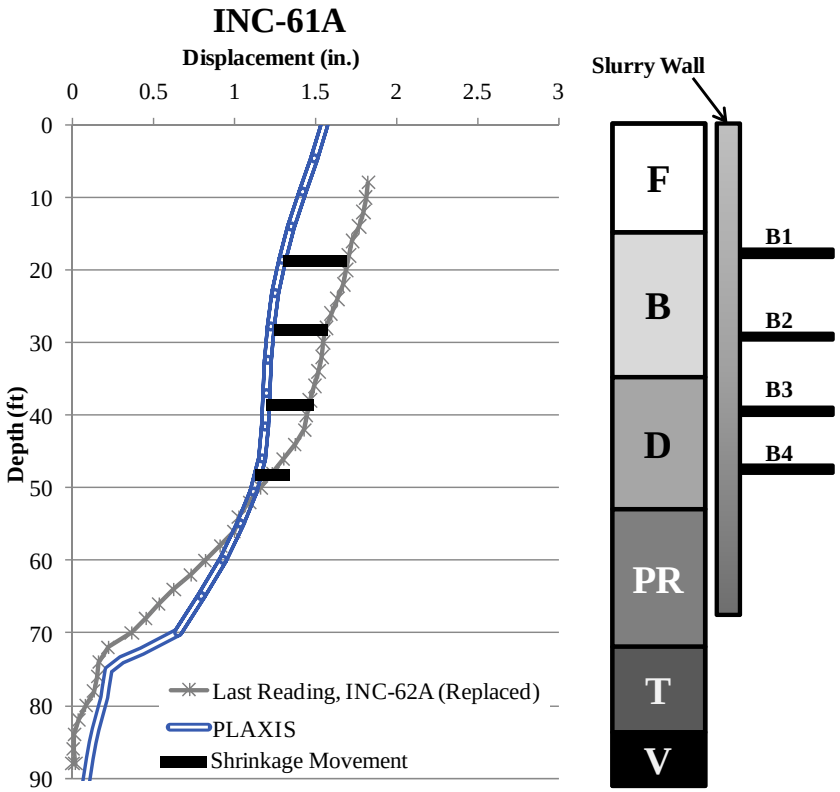

Figure 5-3: Cross Section A Baseline PLAXIS Simulation and INC-61A with Creep and Shrinkage

The movements from the PLAXIS simulations with the addition of the creep and shrinkage movements appeared to match well with the movements recorded by the inclinometers for both cross sections. One explanation for the discrepancy in the PLAXIS results with the inclinometers movements was the shrinkage strains. The use of concrete lateral supports is unique to top-down construction, while the use of steel bracing or ground anchors are used in conventional excavations. Therefore, shrinkage is primarily a concern for top-down construction.

5.3 Bending Moments

The moments in the wall for Cross Section A after the installation of each basement slab are shown in Figure 5-4. One can see that the maximum negative and maximum positive bending moments increased as the excavation progressed from (a) to (d). At each stage of construction, the maximum negative moment was located at the lowest level of lateral support with the exception of the first stage (a). The maximum positive moment for each stage was located at the base of the excavation.

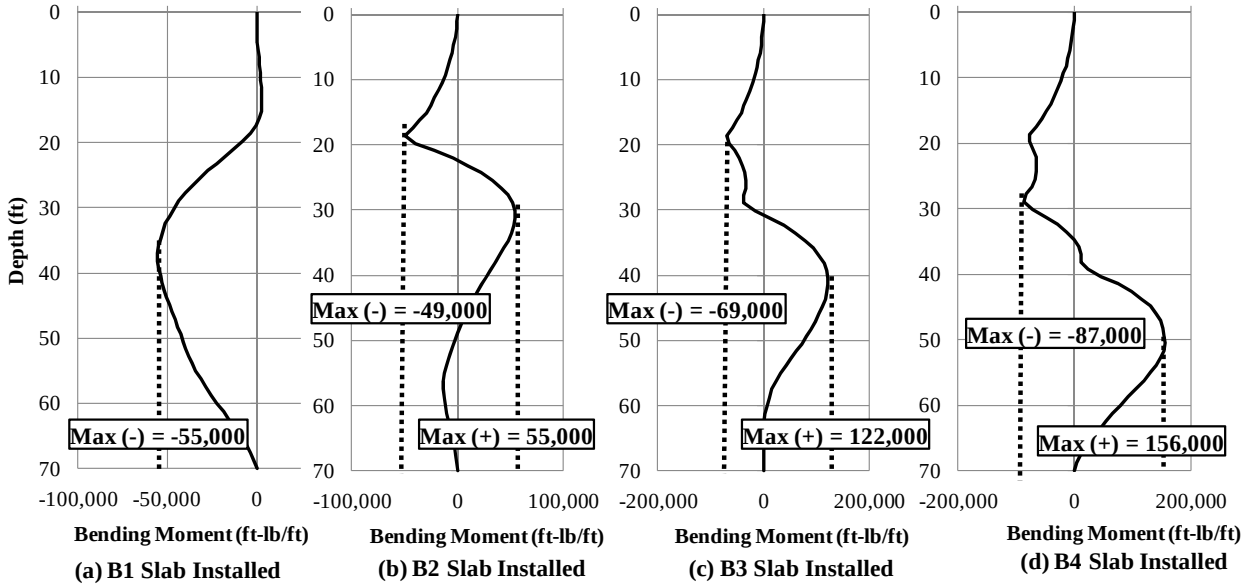

Figure 5-4: Bending Moments in Cross Section A PLAXIS Simulation

The maximum bending moments at these stages are compared to the cracked moment of the slurry wall to determine if the slurry wall had likely cracked during construction. The cracked moment, M_{cr}, is calculated by the following equation:

$$M_{cr} = f_r \frac{I_g}{y_t} \qquad \textbf{5-11}$$

where f_r is the modulus of rupture of the concrete slurry wall, I_g is the moment of inertia and y_t is the distance from the neutral axis to the extreme fiber. The modulus of rupture is calculated by the equation:

$$f_r = 7.5\sqrt{f'_c}\ \text{(psi)} \qquad \textbf{5-12}$$

where f_c' is the compressive strength of concrete. The slurry wall had a compressive strength of 5,000 psi. The moment of inertia/ft was 2.25 ft^4/ft and the distance to the neutral axis was 1.5 ft. Using these values, the cracked moment was calculated as 115,000 lb-ft/ft. One may see that the maximum positive moments computed in PLAXIS for (c) and (d) were larger than the cracked moment. These results indicate that the maximum bending moment in the slurry wall likely exceeded the cracked moment in the last two stages of construction.

5.4 Undrained Simulation

An undrained simulation was performed to determine the impact the consolidation stages had on the computed results. The consolidation phase results in a partially drained condition which depends on the hydraulic conductivity of the soils. The hydraulic conductivity values presented in Chapter 4 were based on analyses by Calvello (2002), who chose the values based on typical values for clays and not on site-specific laboratory test results. Therefore, a completely undrained simulation was performed on Cross Section A and compared to the baseline simulation in Figure 5-5.

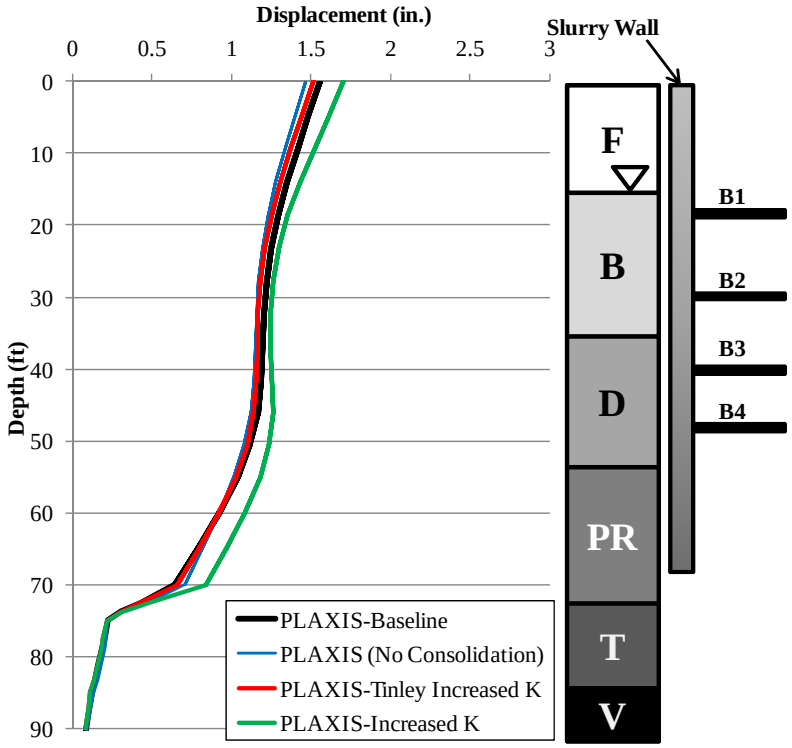

Figure 5-5: Cross Section A PLAXIS with and without Consolidation

Two other simulations were also included in Figure 5-5. The first included an increase in the hydraulic conductivity for all the clay soil layers (PLAXIS-Increased K). The hydraulic conductivity in the horizontal direction was 0.005 ft/day and 0.003 ft/day in the vertical direction for this simulation. These values represent maximum values for clay materials and should represent the "most flow" possible scenario. The second simulation that was included was an increase in the hydraulic conductivity of the Tinley soil layer (PLAXIS-Tinley Increased K). The Tinley clay is the first soil layer underlying the soft compressible clay layers. Increasing the hydraulic conductivity of this layer should represent a condition of two-way drainage within the soft clay layers whereas the baseline simulation represents a one-way drainage condition.

Results of the undrained simulation indicated that excluding the consolidation phases resulted in slightly less wall movements than when the partial consolidation was included in the analysis. The scenario which increased the hydraulic conductivities of all the clay soils resulted in the greatest wall movements, approximately 0.2 inches greater than the baseline scenario. The increase in hydraulic conductivity for the Tinley layer resulted in nearly identical movements as the baseline scenario. Overall the variation in maximum wall movements between the different drainage scenarios amounted to approximately 0.3 inches.

Careful consideration of drainage condition is needed when evaluating excavation behavior when relatively small movements are expected. This effect may be as large as the effect of shrinkage-induced wall movements at least for conditions at Block 37. However, the baseline solution is the most realistic for the Block 37 conditions and shrinkage-induced movements are considered to have an important effect at this site.

5.5 Lateral Support Lengths

The lateral supports (i.e., basement floor slabs) spanned different lengths, depending on the basement level. In the baseline simulation, the middle slabs (B1 and B2) which abutted the tunnel wall were

assigned anchor lengths equal to the actual length of the slab, while slabs B1 and B4 were assigned lengths equal to half the actual length of each slab. To evaluate the effects of this assumption, two simulations were made that considered the full length of all slabs and the half length of all the slabs. The results of the simulations are shown in Figure 5-6.

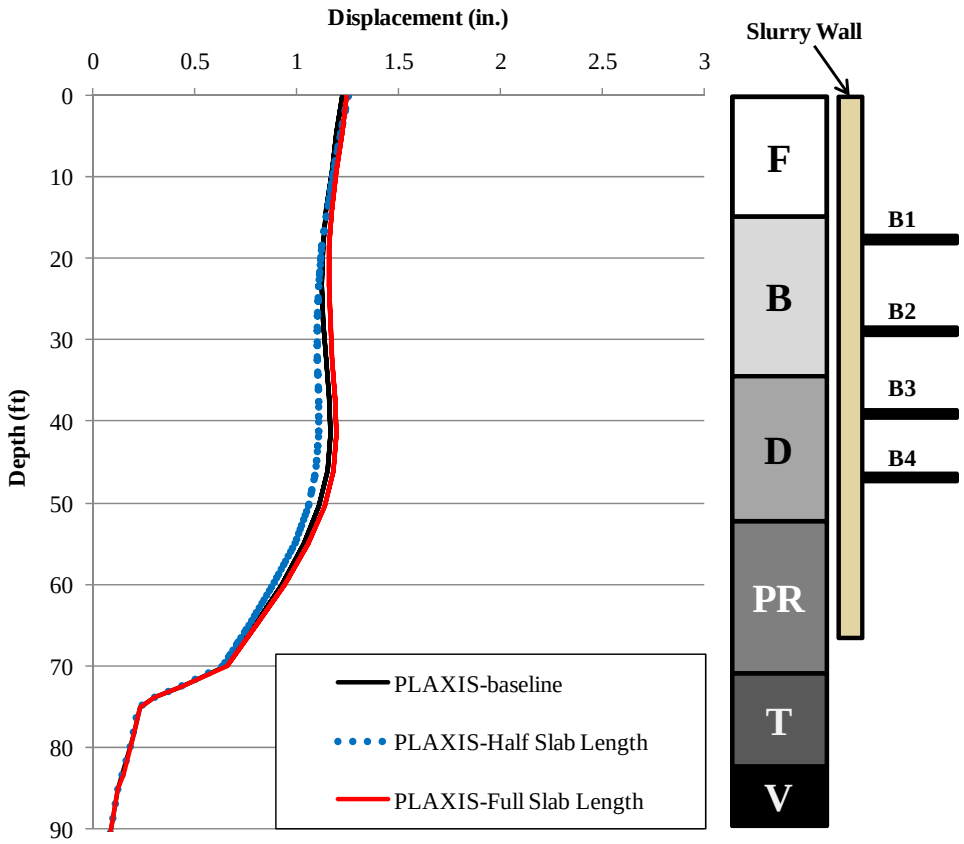

Figure 5-6: Cross Section A PLAXIS with varying Slab Lengths

The varying slab lengths and hence the stiffness of the supports, appeared to have little effect on the movements. Therefore, for the stiff support system at Block 37, variation in stiffness of ± 50% had little effect on the computed lateral wall deformations.

5.6 Summary and Conclusions

Chapter 5 presented the results of the various finite element simulations performed on Cross Section A of the Block 37 construction activities. A baseline simulation was first presented and the wall movements,

settlements, and bending moments calculated by PLAXIS were presented and compared to observed movements. In general, movements calculated by PLAXIS were less than the observed lateral movements at the wall and ground surface settlement. One possible explanation for the discrepancies in movements was that the creep and shrinkage experienced by the concrete basement slabs was not captured by the PLAXIS simulation. The creep and shrinkage of the basement floor slabs were calculated according to ACI recommendations and added to the lateral wall movements based on the baseline PLAXIS simulation. These movements were compared to the observed lateral movements at the wall. The shrinkage movements appeared to account for much of the disparity between the PLAXIS-computed movements and the recorded movements. The PLAXIS-computed bending moments were summarized for four stages of construction and compared to the cracked moment. Calculations indicate that the bending moments in the slurry wall likely exceeded the cracked moment near the end of construction. Therefore, a reduction in the stiffness of the slurry wall would seem reasonable for later stages of construction that produce bending moments exceeding the cracked moment. Since the cracked moment is only exceeded near the end of construction when numerous lateral supports were in place, the reduction in slurry wall stiffness would likely have little effect on lateral wall movements.

Chapter 5 also presented two analyses looking at the drainage effects and anchor length effects. First, several drainage conditions were modeled in PLAXIS to compare to the baseline analysis. The completely undrained analysis resulted in the smallest movements, while the analysis with the increased hydraulic conductivities for the clay layers resulted in the greatest movements. Overall the variation in movements across the four different drainage scenarios amounted to approximately 0.3 inches. The second analysis focused on the basement floor slab lengths assigned to the anchors. The anchor lengths were varied to analyze the effect of the anchor length on the computed movements. The simulations resulted in very similar results to the baseline simulation. Therefore, it appears that the assumption of the anchor lengths made in Chapter 4 had minimal impact on the final PLAXIS movements.

Chapter 6: Conclusions and Recommendations for Future Work

Based on results of the performance data and finite element simulations, several conclusions and recommendations for future work are presented. The following conclusions can be drawn:

- Potholing activities can cause significant lateral movements in the excavation support system. The removal of existing foundations should be considered in the design process as a possible source of lateral movements in the excavation support system. Contractors should consider potholing in sections and progressing across the site, refilling sections before moving to the next section instead of potholing the entire site at once to minimize lateral wall movements.

- Shrinkage of concrete lateral supports may impact lateral ground movements. This case study showed that lateral movements not accounted for in finite element models may be due to shrinkage.

- Omission of the top lateral support in a top-down constructed building may result in significant cantilever movements in the excavation support system. The benefit of small wall movements in top-down construction cannot be achieved unless a lateral brace is constructed close to the ground surface.

- Reduction in stiffness of the slurry wall should be considered when the calculated bending moments within the wall exceed the cracked moment.

The analyses presented in this thesis resulted in several recommendations for future work:

- Instrument concrete lateral supports with strain gauges to monitor actual strains in the members. Recorded strains within the lateral supports may be compared to creep and shrinkage calculations to verify these calculations.

- Install redundant inclinometers to verify lateral movements and for additional insurance against loss of data due to damage. Protect installed inclinometers so loss of data is minimized.

Chapter 7: References

ACI Committee 209. Prediction of Creep, Shrinkage, and Temperature Effects in Concrete Structures, ACI 209R-92. 1992.

Calvello, M. (2002). Inverse analysis of a supported excavation through Chicago glacial clays. PhD thesis, Northwestern University, Evanston, Illinois, 2002.

Chao, H. C., Hwang, R. N. and Chin, C. T. Influence of Tip Movements on Inclinometer Readings and Performance of Diaphragm Walls in Deep Excavations. ASCE Conference: Proceedings of the 2010 Earth Retention Conference, ASCE, ISBN: 978-0-7844-1128-5. 2010.

Clough, G. W., and O'Rourke, T. D. (1989). Construction induced movements of in situ walls. Geotechnical Special Publication No. 25: Proceedings of Conference on Design and Performance of Earth Retaining Structures held at Cornell University, Ithaca NY, edited by Pc C. Lambe and L. A. Hansen, 439-470. New York, NY: ASCE.

Finno, R.J. and Calvello, M., "Supported Excavations: the Observational Method and Inverse Modeling," Journal of Geotechnical and Geoenvironmental Engineering, ASCE, Vol. 131, No. 7, July, 2005, 826-836.

Finno, R.J. and Chung, C.K. (1992). Stress-strain-strength responses of compressible Chicago glacial clays. Journal of Geotechnical Engineering, ASCE, Vol.118, No. 10, p. 1607-1625.

Finno, R. J., Wang, J. Earth Pressure on Cantilever Sheet-Pile Walls with Retained Slopes, Evanston, Illinois, 2006

Hill, John. "A Pile of Dirt Takes Shape." Web log post. A Daily Dose of Architecture. Blogger, 14 Feb. 2006. Web. 1 June 2011. <http://archidose.blogspot.com/2006/02/pile-of-dirt-takes-shape.html>.

Hsieh, P.-G., and Ou, C.-Y., (1998). Shape of ground surface settlement profiles caused by excavation. Canadian Geotechnical Journal, June 1998, Vol. 35, 1004-1016.

Morgan A. (2006). A Parametric Study of a Supported Excavation and Tunnel Connection through Chicago Glacial Clays. MS thesis. Department of Civil Engineering, Northwestern University, Evanston, IL.

Mu, L, Finno, R.J., et al. (2011). Defining soil parameters for computing deformations caused by braced excavation.

PLAXIS manual. 2D-2010. Edited by R.B.J. Brinkgreve, Delft University of Technology & PLAXIS bv, The Netherlands, W.M. Swolfs, E. EnginA.A. Balkema Publishers, 2011. ISBN 978-90-76016-08-5.

Roboski, J.F. (2004). Three-dimensional ground movements caused by deep excavations. PhD thesis. Department of Civil Engineering, Northwestern University, Evanston, IL.

STS Consultants. STS Consultants Project No 25337-H, August 2004, Chicago, IL

Wang, Chu-Kia, Charles G. Salmon, and José A. Pincheira. Reinforced Concrete Design. Hoboken, NJ: John Wiley & Sons, 2007. Print.

"Weather History." Best Places To Live - CityRating.com. Web 31 May 2011. <http://www.cityrating.com>.